Imperial College London
Department of Earth Science and Engineering

2023

Modelling of Rock Spalling in a Geological Disposal Facility for Nuclear Waste

Maria-Cristina Saceanu

Supervisors: Dr. Adriana Paluszny and Prof. Robert W. Zimmerman

A thesis submitted in fulfillment of the requirements for the degree of
Doctor of Philosophy

Abstract

Geologic Disposal Facilities (GDFs) are the preferred long-term solution for the safe disposal of radioactive waste. The construction and subsequent performance of deep geologic repositories may create damage and fractures in the rocks surrounding the waste-bearing boreholes, compromising the integrity of the geological barrier that is intended to prevent radionuclides from escaping into the biosphere.

In this work, the processes that lead to the fracturing and damage of the host rock are numerically modelled in three dimensions with a finite element-based, monolithically-coupled thermo-mechanical simulator. Previous fracture growth methodology is extended, by incorporating continuum damage mechanics to simulate the nucleation of fractures. A novel lofting algorithm improves the meshing efficiency of fracture mechanics models, and enhances the generation of detailed three-dimensional geometries. The simulations explicitly capture the initiation and growth of new fractures, due to the changing thermo-mechanical loading. Validations of the simulation approach are conducted at borehole and tunnel scales, based on comparisons against analytical models, and experimental measurements made at several sites.

The impact of borehole drilling, and subsequent heating and cooling, is investigated specifically for the Swedish Forsmark GDF site, using realistic properties and timelines. Single and multiple borehole geometries of varying characteristics are considered, including varying borehole shapes and spacings, tunnel effects, and *in situ* stress variations. Borehole spacing has a significant effect on the fracture pattern formed across interacting boreholes, whereas heating has a secondary effect on fracture growth. Material property variations are found to induce less uniform nucleation and fracture growth extension. The effect of long-term evolution of glacial cycle stresses is also evaluated for initially intact rocks. These glaciation-induced stresses are shown to also induce spalling patterns with variations in orientation and extension, depending on the loading scenario.

Declaration

I declare that the thesis titled *"Modelling of Rock Spalling in a Geological Disposal Facility for Nuclear Waste"* is my own work, except where explicitly stated otherwise. I confirm that this work was done while in candidature for a research degree in the Department of Earth Science & Engineering at Imperial College London. This thesis has not been previously submitted in whole or in part for any other degree or professional qualification at this university or any other institution. Where the thesis is based on previous work of others within the research group, their contributions have been indicated clearly in the text and acknowledged. Consulted literature and supporting resources have been referenced in the text and accredited.

Maria-Cristina Saceanu
March 2023

© The copyright of this thesis rests with the author. Unless otherwise indicated, its contents are licensed under a Creative Commons Attribution-Non Commercial 4.0 International Licence (CC BY-NC).

Under this licence, you may copy and redistribute the material in any medium or format and you may also create and distribute modified versions of the work. This is on the condition that you credit the author and do not use this work, or any derivative works, for a commercial purpose.

When reusing or sharing this work, ensure that you make the licence terms clear to others by naming the licence and linking to the licence text. Where the work has been adapted, you should indicate that the work has been changed and describe those changes.

Please seek permission from the copyright holder for uses of this work that are not included in this licence or permitted under UK Copyright Law.

Acknowledgements

Completing a PhD is a challenging endeavour and I am very grateful to everyone who has supported me in this journey. I am thankful for the chance to explore a research area that will continue to hold increasing relevance in the future, and I would like to acknowledge the Swedish Nuclear Fuel and Waste Management Company (SKB) for funding this project, and Dr. Diego Mas Ivars for his constructive feedback from a practical perspective. His contributions have enriched this work and made it highly relevant and applicable in a real-world context.

I am deeply grateful to my supervisors, Dr. Adriana Paluszny and Prof. Robert W. Zimmerman, whose guidance, support, and encouragement were instrumental in steering this research project to completion. Not only are they experts in their respective fields, but also great teachers and mentors. They fostered the technical, programming, and research skills I needed to complete this project. Adriana's hands-on guidance on numerical modelling and simulation, coupled with Prof. Zimmerman's deep insights into the field of rock mechanics, are the two main pillars upon which this work has relied.

This work would also not have been possible without the past and present researchers from the Rock Mechanics group, who have contributed to the development of the ICGT. Special thanks to all of them, for providing me with a powerful numerical tool to use and further develop during my project.

I would also like to gratefully acknowledge my thesis examiners, Prof. Gareth Collins and Dr. Chin-Fu Tsang, for their constructive comments during the viva, which helped me further refine the thesis to this final version.

Finally, I wish to express my gratitude to my family and friends, for being there for me, patiently understanding and encouraging me on this journey. I would not have reached the final milestone without your unwavering support, friendship and companionship.

Contents

Abstract i

Declaration ii

Copyright ii

Acknowledgements iii

List of Figures viii

List of Tables xii

Abbreviations xiii

Symbols xiv

1 Introduction 1

1.1 Background . . . 1
1.2 Motivation . . . 1
1.2.1 Radioactive waste disposal . . . 1
1.2.2 Subsurface fracture growth . . . 2
1.3 Thesis overview . . . 3
1.4 Imperial College Geomechanics Toolkit . . . 5
1.4.1 Pre-existing functionality and validations . . . 5
1.4.2 Added functionality and validations . . . 6
1.5 Publications and Conferences . . . 8

2 Literature Review 10

2.1 Deep Geological Repositories . . . 10
2.2 Excavation Damage Zones . . . 12
2.3 Stresses around subsurface excavations . . . 13
2.4 Failure around deep-drilled boreholes . . . 16
2.4.1 Borehole breakouts vs. spalling . . . 16
2.4.2 Field observations . . . 18
2.4.3 Spalling mechanism and spalling strength . . . 19

2.5 Analytical methods . . . 21
2.5.1 Rock failure criteria . . . 21
2.5.1.1 Shear strength-based: Mohr-Coulomb . . . 21
2.5.1.2 Empirical: Hoek and Brown . . . 22
2.5.1.3 Tensile strength-based: Griffith . . . 22
2.5.1.4 Strain energy-based: Stacey . . . 23
2.6 Numerical methods . . . 23
2.6.1 Continuum methods . . . 23
2.6.2 Discontinuum methods . . . 24
2.6.3 Hybrid methods . . . 25
2.6.4 Limitations of existing models . . . 27

3 Methodology 28

3.1 Introduction . . . 28
3.1.1 Imperial College Geomechanics Toolkit (ICGT) . . . 28
3.2 Governing equations . . . 30
3.2.1 Mechanical deformation . . . 30
3.2.2 Thermo-mechanical deformation . . . 30
3.3 Model geometry and discretisation . . . 32
3.3.1 Finite element method . . . 34
3.3.2 Remeshing and mapping of variables . . . 36
3.3.3 Fracture geometry . . . 38
3.3.4 Fracture surfaces as lofted NURBS . . . 40
3.4 Fracture initiation around a circular borehole . . . 42
3.4.1 Mazars damage model . . . 43
3.4.2 From continuum damage to discrete fractures . . . 46
3.4.2.1 Total number of initial disks . . . 47
3.4.2.2 Initial disk size and orientation . . . 47
3.4.2.3 Initial disk spacing . . . 47
3.5 Fracture growth leading to spalling . . . 48
3.5.1 Linear elastic fracture mechanics . . . 48
3.5.2 Fracture tip stress intensity factors . . . 50
3.5.3 Growth criteria . . . 51
3.5.3.1 Propagation criterion . . . 51
3.5.3.2 Length criterion . . . 52
3.5.3.3 Angle criterion . . . 54
3.5.4 Fracture surface contact . . . 54
3.5.5 Fracture-borehole interaction and fracture arrest . . . 54
3.5.6 Simulation parameters involved in fracture growth . . . 55
3.5.6.1 Fracture propagation exponents . . . 55
3.5.6.2 Maximum extension length . . . 56
3.6 Summary . . . 56

4 Validations **58**
4.1 Introduction . . . 58
4.2 FEM validations . . . 58
4.2.1 Borehole mechanical stresses . . . 58
4.2.1.1 Single borehole . . . 59
4.2.1.2 Multiple boreholes . . . 61
4.2.2 Borehole damage modelling . . . 63
4.2.3 Borehole temperature . . . 66
4.2.4 Borehole thermal stresses . . . 68
4.3 Fracture growth validations . . . 69
4.3.1 Numerical computation of SIFs . . . 69
4.3.2 Spalling around a single borehole . . . 72
4.3.3 Simulation parameters involved in nucleation and growth . . . 75
4.3.3.1 Initial disk size and orientation . . . 75
4.3.3.2 Total number of fractures . . . 77
4.3.3.3 Fracture propagation exponents . . . 78
4.3.3.4 Maximum extension length . . . 82
4.4 Conclusions . . . 82

5 Mechanical Spalling **84**
5.1 Introduction . . . 84
5.1.1 Forsmark repository site . . . 84
5.2 Numerical model set-up . . . 86
5.2.1 Rock properties . . . 86
5.2.2 Model geometry and boundary conditions . . . 88
5.2.3 Model sizes and simulation costs . . . 92
5.3 Effect of the deposition tunnel . . . 95
5.3.1 Fracturing around a deposition borehole–deposition tunnel system . . . 95
5.3.2 Fracturing around a single borehole . . . 100
5.3.3 Effect of tunnel orientation . . . 102
5.4 Effect of the *in situ* stresses . . . 103
5.5 Effect of borehole geometry . . . 106
5.6 Effect of neighbouring boreholes . . . 108
5.6.1 Number of boreholes . . . 108
5.6.2 Borehole spacing . . . 111
5.7 Discussion . . . 113
5.8 Conclusions . . . 115

6 Thermo-mechanical spalling **117**
6.1 Introduction . . . 117
6.2 Thermo-mechanical spalling of a single borehole . . . 119
6.2.1 Rock properties . . . 119

6.2.2 Model geometry and boundary conditions . . . 119
6.2.3 Borehole temperature and thermal stress . . . 120
6.2.4 Fracture patterns and spalling extent . . . 124
6.3 Thermo-mechanical spalling of multiple boreholes . . . 129
6.4 Effect of *in situ* heterogeneities . . . 132
6.5 Discussion . . . 136
6.6 Conclusions . . . 138

7 Effect of glaciation on long-term repository stability 139
7.1 Introduction . . . 139
7.2 Numerical model set-up . . . 140
7.2.1 Modelling Assumptions . . . 142
7.3 Fracture patterns and spalling extent . . . 143
7.4 Conclusions . . . 146

8 Conclusions 147
8.1 Summary of thesis . . . 147
8.2 Future work . . . 149

References 152

List of Figures

2.1 Schematic diagram of the multiple barrier concept for deep geological disposal of nuclear waste . . . 11

2.2 Schematic diagram of the main excavation damage zones (EDZs) around a circular excavation . . . 13

2.3 Analytical stresses around subsurface excavations assuming isotropic elasticity and plane strain conditions . . . 15

2.4 *In situ* measurements of spalling depth compiled by Martin et al. (1999) . . . 17

2.5 Spalling mechanism inferred from a polarised light cross-section of a stabilised borehole showing spalling-inducing fractures . . . 20

2.6 Numerical models of spalling, using continuum, discontinuum, and hybrid methods . . . 26

3.1 Schematic diagram showing the interaction between the ICGT, the geometry-handling software (Rhino7) and the mesher (ICEM CFD) . . . 32

3.2 Example of unfractured model geometry created with Rhino3D and its corresponding mesh created with Ansys ICEM CFD . . . 33

3.3 Nodal stress averaging effect on the maximum principal stress at the borehole wall . . . 36

3.4 Mapping of variables between successive meshes . . . 37

3.5 Tessellated fracture surface . . . 38

3.6 Comparison between tessellated and lofted fracture geometries and their corresponding meshes . . . 39

3.7 Lofted fracture surface . . . 41

3.8 Effect of the Mazars damage parameters on stress-strain curves . . . 46

3.9 Stresses at the tip of a two-dimensional fracture . . . 49

3.10 The three main loading modes of a fracture surface . . . 50

3.11 Schematic representation of an elliptic crack surface in three dimensions and its tip propagation vectors . . . 51

3.12 Trimming of a fracture surface against an excavation wall . . . 55

4.1 Validation of the stress field around a vertical circular borehole . . . 59

4.2 Mesh convergence test showing the numerical stress error at different levels of mesh refinement . . . 62

4.3 Validation of the tangential stresses in a two-borehole model under uniaxial and biaxial tension . . . 63

4.4 Damage model parameters for the Forsmark site derived from uniaxial tension and compression curves . . . 65

4.5 Validation of the temperature distribution around a circular heat-emitting borehole . . . 67

4.6 Thermo-mechanical stress at the borehole wall when the borehole is heated by 100 °C . . . 68

4.7 Schematic diagram of the initial fracture disk used for SIF validation in three dimensions . . . 70

4.8 Validation of stress intensity factors around an isolated fracture under uniaxial tension . . . 71

4.9 Validation of stress intensity factors around an isolated fracture under uniaxial compression . . . 72

4.10 Validation of mechanical spalling, comparing the radial and axial views of the numerical fracture patterns with *in situ* observations . . . 73

4.11 Young's modulus distribution along a 3.5 m diameter circular tunnel . . . 74

4.12 Effect of the initial disk size on nucleation patterns . . . 76

4.13 Effect of the total number of fractures on growth patterns . . . 77

4.14 Effect of the Paris exponents on fracture interaction and growth patterns: radial view $(x - y)$ . . . 79

4.15 Effect of the Paris exponents on fracture interaction and growth patterns: axial view $(z - y)$ . . . 80

4.16 Effect of the Paris exponents on fracture area per growth step . . . 81

5.1 Location and general tectonic setting of the Forsmark site . . . 85

5.2 Geological map of the Forsmark site . . . 88

5.3 Schematic representation of typical deposition borehole and deposition tunnel geometries . . . 90

5.4 Model geometry and boundary conditions corresponding to the simulation cases investigating mechanical spalling . . . 91

5.5 Computational costs associated with the different numerical models of mechanical spalling . . . 93

5.6 Maximum principal stress in the *deposition tunnel model* and in the *simplified borehole and tunnel model* . . . 94

5.7 Damage and initial fracture disks nucleation loci in the *deposition tunnel model* . . . 96

5.8 Sectional ($z-y$) view of damage and fracture development around a horseshoe-shaped deposition tunnel and ramped deposition boreholes 97

5.9 Sectional ($z-y$) view of stress intensity factors around a horseshoe-shaped deposition tunnel and ramped deposition boreholes 98

5.10 Sectional ($x-y$) view of damage and fracture development around a horseshoe-shaped deposition tunnel and ramped deposition boreholes 99

5.11 Effect of the deposition tunnel on borehole stress and orientation of the initial fracture disks during nucleation 100

5.12 Effect of the deposition tunnel on fracture growth 102

5.13 Effect of *in situ* stress magnitude and tunnel orientation on simulated fracture patterns around a single deposition borehole 104

5.14 Effect of *in situ* far-field stress magnitude at Forsmark on the tangential stress at the borehole wall, prior to fracture nucleation 105

5.15 Effect of borehole geometry on simulated fracture patterns, showing final fracture extent for a circular, cone-shaped, and wedge-shaped borehole . . . 107

5.16 Principal stresses magnitudes and orientations around circular boreholes spaced 4 m and 6 m apart, in 3- and 5-borehole models, respectively 110

5.17 Axial ($z-x$) cut planes showing the damaged Young's modulus after fracture growth has arrested in four cases, where three interacting boreholes are spaced 2.5, 3.0, 3.5, and 4.0 m apart 111

5.18 Radial ($x-y$) and axial ($z-x$) cut planes showing the final fracture patterns that develop around three interacting boreholes spaced 2.5, 3.0, 3.5, and 4.0 m apart 112

6.1 Forsmark repository layout and host rock temperature estimations at the central borehole wall in several locations within the repository (SKB TR-10-23 2010) 118

6.2 Model geometry and boundary conditions corresponding to the single borehole thermo-mechanical case 120

6.3 Temperature field in the single borehole model with a prescribed initial constant temperature of 100 °C 121

6.4 Comparison of the thermo-mechanical stress in the single borehole model after 8 weeks of heating with a prescribed initial constant temperature of 100 °C vs. the mechanical only stress 122

6.5 Maximum principal stress field in the single borehole model comparing mechanical and thermo-mechanical stresses after 1 day, 2 weeks, 4 weeks and 8 weeks of heating 123

6.6 Comparison of spalling patterns and fracture growth extent in the mechanical and thermo-mechanical simulation cases 125

6.7 Fracture geometries and apertures developing in response to thermo-mechanical loading, after 1 day, 2 weeks, 4 weeks and 8 weeks of heating 127

6.8 Maximum principal stress distribution in the fractured zone and simulated fracture apertures at maximal growth extent 128

6.9 Temperature field in a three-borehole repository model after approximately five years, compared with SKB's analytical calculations 131

6.10 Maximum principal stress field and corresponding fracture patterns in a three-borehole repository model 132

6.11 Heterogeneous model: elastic modulus distribution (boxes) 133

6.12 Heterogeneous model: elastic modulus distribution (clusters) 134

6.13 Comparison of the maximum principal stress contours in a three-borehole model in the homogeneous vs heterogeneous cases 136

7.1 Evolution of the ice sheet thickness and the glacially induced stress components at repository depth, *i.e.*, 500 m depth, at Forsmark 140

7.2 Model geometry, boundary conditions, and predicted temporal evolution of the total remote stress at Forsmark throughout the next glaciation 141

7.3 Top and side views of the fracture nucleation loci during the six main glacial events 144

7.4 Top and side views of the fracture patterns that develop during the six main glacial events 145

List of Tables

4.1 Typical values of Mazars parameters from literature on concrete and rock damage. 64

4.2 Thermal properties and time step used in the transient simulations for temperature validation 66

5.1 Rock properties (SKB TR-08-05 2007), damage parameters and *in situ* stress magnitudes (SKB R-08-116 2009) defined for the numerical simulations of deformation, fracture and damage of the Forsmark case. 87

5.2 Effect of different repository configurations on the maximum fractured depth, width and surface area. Simulation parameters and boundary conditions are those from Forsmark (Table 5.1). 114

6.1 Average values of the host rock thermal properties at Forsmark (SKB TR-08-05 2007), considered in the thermo-mechanical simulations of spalling in this chapter. 119

7.1 Rock properties in the glaciation simulations 141

7.2 *In situ* stresses used in the glaciation simulations. 141

Abbreviations

AECL Atomic Energy of Canada Limited

APSE Äspö Pillar Stability Experiment

BDEM Boundary-discrete element method

BEM Boundary element method

CAD Computer-aided design

CAPS Counterforce Applied to Prevent Spalling

CSMP++ Complex Systems Modelling Platform

CWFS Cohesion Weakening Friction Strengthening

DGR Deep Geological Repository

DISL Damage Initiation Spalling Limit

DLL Dynamic Link Library

EdZ Excavation disturbed zone

EDZ Excavation damaged zone

EDZs Excavation damage zones

FDEM Finite-discrete element method

FDM Finite difference method

FEM Finite element method

GDF Geological Disposal Facility

HDZ Highly damaged zone

HRL Hard Rock Laboratory

ICGT Imperial College Geomechanics Toolkit

KBS-3 The Swedish "multiple barrier" disposal method

LEFM Linear elastic fracture mechanics

NMM Numerical manifold method

NURBS Non-uniform rational B-splines

SIF Stress intensity factor

SKB Swedish Nuclear Fuel and Waste Management Company

XFEM Extended finite element method

Symbols

Symbol	Description	Unit
Ω	Rock volume domain	m^3
$\mathcal{B}$	Borehole volume domain	m^3
Γ	Fracture surface domain	m^2
σ_{rr}	Radial stress	Pa
$\sigma_{\theta\theta}$	Tangential stress	Pa
σ_{zz}	Axial stress	Pa
$\tau_{r\theta}$	Shear stress	Pa
σ_H	Maximum horizontal far-field stress	Pa
σ_h	Minimum horizontal far-field stress	Pa
σ_v	Vertical far-field stress	Pa
r	Radial distance from the borehole center	m
R_b	Circular borehole radius	m
R_f	Spalling depth measured from the centre of the borehole	m
θ	Angular rotation from the direction of σ_H	$^\circ$
σ_{UCS}	Uniaxial compressive strength	Pa
σ_{TS}	Uniaxial tensile strength	Pa
C_o	Cohesion	Pa
φ	Friction angle	rad
α	Coefficient of volumetric thermal expansion	K^{-1}
C_m	Heat capacity	J kg^{-1} K^{-1}
κ	Thermal conductivity	W m^{-1} K^{-1}
ρ_m	Density	kg/m^3
K	Bulk modulus	Pa

Symbol	Description	Unit
ν	Poisson's ratio	–
E	Young's modulus	Pa
$\tilde{E}$	Damaged Young's modulus	Pa
$\boldsymbol{\sigma}$	Cauchy stress tensor	Pa
$\boldsymbol{\varepsilon}$	Strain tensor	–
σ_0	Initial stress	Pa
ε_0	Initial strain	–
$\boldsymbol{D}$	Linear elastic stiffness matrix	Pa
$\boldsymbol{I}$	Identity matrix	–
$\boldsymbol{u}$	Displacement vector	m
$\boldsymbol{F}$	Body forces applied to the numerical domain	N
T_m	Rock matrix temperature	°C
$\boldsymbol{\lambda_m}$	Thermal conductivity tensor	W m^{-1} K^{-1}
λ_n	Thermal conductivity in the direction normal to the fracture surface	W m^{-1} K^{-1}
β_f	Fracture growth rate exponent	–
β_n	Fracture tip growth rate exponent	–
Δl_f	Maximum extension of a fracture f	m
Δl_n	Maximum extension of a node n	m
Δl_v	Maximum extension of all fractures within a volume v	m
$\mathcal{G}_n$	Energy release rate at a tip node n	J m^{-2}
$\mathcal{G}_f$	Maximum energy release rate on a fracture f	J m^{-2}
$\mathcal{G}_v$	Maximum energy release rate in a fractured volume v	J m^{-2}
K_{II}	Mode II stress intensity factor	Pa m$^{1/2}$
K_{III}	Mode III stress intensity factor	Pa m$^{1/2}$
K_{IIC}	Mode II fracture toughness	Pa m$^{1/2}$
K_{IIIC}	Mode III fracture toughness	Pa m$^{1/2}$

Symbol	Description	Unit
$\delta \boldsymbol{u}$	Virtual displacement vector	m
$\delta \boldsymbol{\varepsilon}$	Virtual strain vector	–
$\boldsymbol{\Phi}$	Surface tractions	Pa
$\boldsymbol{N}$	Finite element shape functions	–
$\boldsymbol{B}$	Derivatives of the finite element shape functions	–
$\boldsymbol{k}^{(e)}$	Element stiffness matrix	–
$\boldsymbol{C}_k^w(\mathrm{u})$	NURBS curve	–
$\boldsymbol{P}_{i,k}^w$	Weighted control points of a NURBS curve	–
$N_{i,p}$	Basis functions of a NURBS curve	–
K_v	Mixed-mode critical stress intensity factor	Pa $\mathrm{m}^{1/2}$
K_{IC}	Mode I fracture toughness	Pa $\mathrm{m}^{1/2}$
d	Mazars damage variable	–
$\langle \boldsymbol{\varepsilon} \rangle_+$	Positive part of the strain tensor	–
$\tilde{\boldsymbol{\varepsilon}}$	Mazars equivalent strain	–
ε_{ti}	Principal strain component due to tensile stresses	–
ε_{ci}	Principal strain component due to compressive stresses	–
s	Inter-borehole spacing, measured between two adjacent borehole centres	m
P_w	Rock pillar width, measured between two adjacent borehole surfaces	m
J_0	Bessel function of the first kind	–
Y_0	Bessel function of the second kind	–
c_p	Specific heat capacity	J kg^{-1} K^{-1}

Chapter 1

Introduction

1.1 Background

Long-term management of nuclear fuel waste is becoming an increasingly pressing issue, as around 370,000 tonnes of high level waste have accumulated since the first commercial nuclear reactors started operating in the early 1960s (IAEA 2018). Additionally, the nuclear power industry currently produces between 11,000 and 18,000 tonnes of spent fuel every year, and nuclear power's share in the global energy mix is likely to increase in the future, based on growing energy demand and the on-going transition from fossil fuels to alternative low-carbon energy sources (Abousahl et al. 2021).

1.2 Motivation

1.2.1 Radioactive waste disposal

Nuclear waste is classified, based on its radioactive content, into low-, intermediate- and high-level waste. Most low-level and intermediate-level wastes, such as contaminated tools and filters, are usually sent to land-based disposal and do not generally require long-term management. In contrast, high-level waste, comprising disused nuclear fuel, requires a more complex storage and disposal procedure, as it remains radioactive for thousands of years (Long & Ewing 2004).

In the first instance, disused fuel is stored at the reactor site in cooling pools, where water is circulated for several years, to prevent overheating and make its further handling safer. Waste that has been cooled sufficiently is eventually moved in dry casks at ground level, or shallow underground facilities (IAEA Tecdoc Series 2005). Although these near-surface storage facilities are designed to safely contain and isolate the waste, they are prone to

natural hazards and human interference, and thus are only viewed as a temporary storage solution (Macfarlane 2001). The consensus is that in the long term, high level waste should be stored in deep-mined geological repositories (IAEA 2012), which require less maintenance and surveillance than over-ground options, once the deposition boreholes and tunnels have been backfilled.

Another reason why deep underground disposal is considered the safer option is because the final repositories are based on a "multiple barrier concept" (Bodansky 1996), which introduces additional protective layers separating the hazardous waste from the environment. The barriers are both engineered (the waste assembly, canister and buffer) and natural (the host rock), and on-going research is being conducted to determine their optimal configurations, *e.g.* type of canister, composition of the buffer, shape of the borehole, suitability of different host rock types, such as evaporites, crystalline rocks, argillaceous rocks, etc. (SKB 1978, ANDRA 2005, NAGRA 2002, Faybishenko et al. 2017).

The construction of a nuclear waste repository will involve drilling and excavating a range of underground structures of different geometries and sizes, such as access tunnels, ramps, deposition tunnels, and deposition boreholes. One of the risks that arises is the development of fractures and loss of host rock integrity in the vicinity of the waste-bearing boreholes (Martin & Christiansson 2009). To evaluate the viability of deep underground disposal, one must assess the potential extent of these subsurface fractures.

1.2.2 Subsurface fracture growth

Fractures are rock mass discontinuities. They can occur naturally in the subsurface as a result of Earth's tectonic activity (e.g. faults, joints, vugs, veins). Such discontinuities can also develop around man-made excavations due to perturbations of the initially undisturbed *in situ* stress field. High stress concentrations at excavation boundaries cause brittle rock to fail when the rock mass strength is exceeded, ultimately resulting in localised enlargements of the borehole diameter (e.g. spalling, borehole breakouts, washouts). Nucleation and growth of fractures significantly alter the geomechanical and flow properties of the subsurface host rock (Tsang et al. 2005), providing pathways for radionuclide transport beyond the visible failure at the borehole wall.

Spalling is a common type of stress-induced failure that occurs around deep excavation boundaries in crystalline rock, in the absence of confining pressure (Perras & Diederichs 2016). The failure often appears as rock splitting or slabbing in hard rocks, but can also manifest itself through shearing in weaker rocks (Amadei & Stephansson 1997). Fairhurst & Cook (1966) first described spalling failure as the development of extension fractures under compressive loading. Spalling is challenging to model - conventional failure criteria and their numerical implementations have thus far been unable to capture the failure ex-

tent observed in the field (Hajiabdolmajid et al. 2002*b*, Hamdi et al. 2014). Additionally, numerical studies that successfully replicate spalling in two dimensions cannot represent complex three-dimensional fracture growth and interaction in large scale repository models.

1.3 Thesis overview

The main objective of this thesis is to study fracture initiation and propagation in response to the mechanical and thermal stresses that arise at underground deposition boreholes and tunnels walls, and to conduct numerical simulations that accurately capture the fracturing processes leading to spalling failure. More specifically, this can be divided into smaller objectives:

- Increase the understanding of the concept of spalling and spalling strength, by performing a cross-comparison of analytical, experimental, and numerical models of spalling in order to assess their predictive capabilities;
- Integrate existing experimental data generated from field studies to validate the numerical models;
- Investigate the effect of potential repository configurations, rock heterogeneity, pre-existing fractures, and changing *in situ* stresses on predictions of spalling strength and extent, using analytical and numerical methods;
- Assess the long-term evolution of the repository throughout its excavation (M), thermal (M⇒TM) and glacial (M⇒TM⇒M) phases.

This thesis is split into eight chapters, as follows:

- Chapter 1 introduces the PhD project and outlines the main objectives and structure of the thesis. The numerical tool that was used for the spalling simulations is then shortly reviewed, emphasising the pre-existing modeling capabilities, as well as the enhancements and additional features that were implemented specifically for modelling spalling.
- Chapter 2 introduces key concepts related to geological disposal of nuclear waste, which are used or referenced throughout the thesis. Excavation damage zones and spalling are defined and the differences between spalling and other types of borehole failure are presented. The chapter also gives an overview of the existing analytical and numerical approaches to simulate spalling, and analyses their predictive capabilities.

- Chapter 3 presents a geometric fracture growth approach to model spalling. The governing equations and the main algorithms involved in fracture initiation and growth are presented. This chapter also explains how the geometric model is built and discretised, and how the fracture tip loops and surfaces are constructed as non-uniform rational B-splines (NURBS). The methods for computing mechanical and coupled thermo-mechanical deformation, fracture surface contact, stress intensity factors, and fracture growth are presented. The chapter highlights specific simulation parameters that are validated for spalling in the following chapter.

- Chapter 4 contains validations of the FEM-computed variables, SIFs, and fracture growth patterns, to determine the effectiveness of the modelling approach in reproducing fracture mechanisms associated with mechanical spalling. This chapter shows that the borehole deformation and ensuing fractures respond realistically to the applied mechanical and thermal loads after the borehole drilling and borehole heating stages. Method- and simulation-specific parameters such as number of nucleated fractures, their initial disk size and spacing, are varied to assess their influence on the final fracture patterns, and ensure that the fractures match field observations from tunneling experiments.

- Chapter 5 focuses on mechanical (M) evolution of spalling fractures that are expected to develop in the vicinity of deposition boreholes and tunnels of a typical repository for nuclear waste. The Forsmark candidate area is chosen to investigate the impact of *in situ* stresses, deposition tunnel and its orientation, borehole geometry and borehole spacing, on the modelled damage and fracture extent. Since no deposition boreholes have yet been drilled at Forsmark, this chapter also presents the first numerical predictions of fracture growth leading to spalling at the future GDF site.

- Chapter 6 investigates the impact of borehole heating and cooling on the surrounding host rock and its influence on the nucleation and growth of new fractures under coupled thermo-mechanical (TM) loading. This chapter also examines the effect of borehole heat on pre-existing spalling patterns that had developed around the borehole after the mechanical excavation phase, and stabilised prior to the thermal heating phase. Finally, a realistic timeline is implemented, where the borehole heat flux varies based on a typical spent fuel canister decay rate. The results obtained for a multiple borehole model are then discussed in relation to those presented in Ch. 5.

- Chapter 7 examines the long-term evolution of the repository, considering the changes in *in situ* stresses on the timescales of a glacial cycle. The thermal (TM) phase of the repository is assumed to be completed and several geo-mechanical (M) scenarios are investigated, corresponding to distinct *in situ* stress evolution paths at different repository locations relative to the ice sheet during the glacial cycle.

- Chapter 8 highlights the key results and contributions of this work, and proposes several ideas on how this work can be improved and extended.

1.4 Imperial College Geomechanics Toolkit

The Imperial College Geomechanics Toolkit (ICGT) is a finite element-based discrete fracture growth simulator, which possesses the capability to conduct fully coupled poro-thermo-elastic simulations in addition to single and multi-phase flow simulations. The ICGT employs a three-dimensional geometric fracture growth approach, in which fractures are explicitly represented as surfaces and curves, and treated as distinct meshed entities. These undergo extension and interaction based on Linear Elastic Fracture Mechanics (LEFM) theory. The ICGT was initially developed from the Complex Systems Modelling Platform (CSMP++), a finite element-based library that was developed to simulate multi-physics geologic processes such as single-phase and multi-phase flow, reactive transport, and heat transfer in two and three dimensions (Matthäi et al. 2007).

1.4.1 Pre-existing functionality and validations

The existing functionality of ICGT has been gradually implemented and validated by present and past members of the Rock Mechanics Research Group. The simulator capabilities on which this work relies are documented in the following chronological list of publications related to ICGT:

- Paluszny et al. (2007) implemented the discretisation of discrete fractures within CSMP++ and showed that resulting meshes can accurately represent free-form material interfaces, adapt the mesh resolution to the solution variations, and handle large deformations of the mesh.
- Paluszny & Matthäi (2009) introduced an iterative algorithm to simulate simultaneous quasi-static propagation of multiple fractures. They showed that the simulator can capture fracture growth patterns in 2D, including *en-echelon* fracture linkage, fracture hooking, and orthogonal tip approximation.
- Paluszny & Matthai (2010) incorporated steady state single-phase flow in 2D and computed and validated the effective permeability and fracture-matrix flux ratio of a fractured porous domain.
- Paluszny & Zimmerman (2011) extended the fracture growth implementation to three dimensions, decoupling the geometric representation of the cracks from the mesh, and used a reduced virtual integration technique to compute stress intensity factors (SIFs) on arbitrary meshes.

- Paluszny & Zimmerman (2013*a*) introduced a novel algorithm that uses smooth surface representations of the fractures, rather than faceted or discrete representations, allowing for more accurate and efficient modelling of the fracture geometry as it evolves during growth.

- Lang et al. (2014) implemented a pressure gradient and flux averaging technique to compute the full permeability tensor of three-dimensional discrete fracture and matrix models. They also validated permeability in three dimensions, comparing equivalent permeabilities with analytical solutions for sugar cube models.

- Nejati et al. (2015*a*) developed a disk-shaped domain integral method for the accurate computation of the J-integral and SIFs of three-dimensional planar fractures, using tetrahedral elements.

- Nejati et al. (2015*b*) proposed and validated the use of corner-based and edge-based quarter-point tetrahedral elements in order to increase the displacement field accuracy and capture the high stress gradients at the fracture tips. They also implemented the displacement correlation method for quarter-point tetrahedral elements to extract the stress intensity factors from unstructured meshes.

- Nejati et al. (2016) implemented a gap-based Augmented Lagrangian method with Uzawa algorithm that resolves the frictional forces on the surface of the fractures and captures propagation under compressive loading.

- Thomas et al. (2017) validated SIFs for an isolated penny-shaped fracture under tension and SIF perturbation for two coplanar interacting fractures. They also proposed three measures to quantify fracture interaction: the circumferential and maximum SIF perturbation, and the amplification to shielding ratio.

- Salimzadeh et al. (2018) implemented a three-dimensional fully coupled thermo-hydro-mechanical (THM) model for deformable fractured geothermal systems and validated advective-diffusive heat transfer through a single fracture, and for the single-phase fluid flow problem in a deformable fracture.

- Thomas et al. (2020) implemented a modified two-step formulation of the Paris extension criterion. They used two growth rate exponents, one for the fracture level and one for the tip level, to control the relative propagation of different fractures within an array and different tip nodes along the fracture edge, respectively.

1.4.2 Added functionality and validations

- **Nucleation of initial disks based on damage**
  The studies outlined in Section 1.4.1 simulated the growth of individual fractures as

well as interacting fracture arrays from penny-shaped initial fracture disks, which were positioned randomly and oriented in arbitrary directions within the computational domain. The numerical simulations presented in this thesis required the implementation of a novel approach to model fracture nucleation, based on the damage occurring in the unfractured and homogeneous domain after the borehole excavation stage. This work extended the simulator to nucleate the initial distribution, orientations, and sizes of fractures in a more deterministic manner.

- **Integration and automation of Rhino3D plug-ins for handling geometry**
  Prior to initiating the fracture disks and the discontinuous modelling, stress concentrators such as the free excavation surfaces needed to be incorporated into the model. This work extended the ICGT simulator by integrating a commercial CAD software to dynamically manipulate NURBS geometry at runtime. This includes automatic operations for creating and modifying excavations and fracture surfaces within the simulation domain. Different types of excavation geometries, such as circular boreholes, ramped boreholes, horse-shoe shaped tunnels were also parametrised and can now be accurately represented and interacted with in the simulation.

- **Bespoke boundary conditions**
  - Implemented triaxial compression boundary conditions to impose the remote stresses and validated the resulting mechanical stress field around single and multiple boreholes under triaxial compression.
  - Extended the triaxial compression boundary conditions by introducing a free surface at the upper boundary of the computational domain. This emulated the effect of a deposition tunnel floor, without needing to incorporate the whole deposition tunnel in the numerical domain.
  - Implemented thermal boundary conditions where either a constant temperature, or a variable heat flux based on the typical decay rate of a spent fuel canister is applied to the borehole surface to simulate borehole heating and cooling. Validated the resulting temperature and thermal stress fields around a single borehole.

- **k-means clustering algorithm for heterogeneity**
  ICGT possessed pre-existing functionality to introduce heterogeneities by partitioning the domain into distinct boxes. However, real-world heterogeneities do not exhibit sharp boundaries. To address this limitation, an enhanced approach was developed using a k-means clustering algorithm to capture heterogeneity more accurately. This involved grouping the integration points into random clusters, with each cluster assigned physical properties sampled from a distribution of values, to better represent the true variations observed in natural rock heterogeneities.

1.5 Publications and Conferences

Journal articles

- **Saceanu, M. C.**, Paluszny, A., Zimmerman, R. W. & Mas Ivars, D. (2022), "Fracture growth leading to mechanical spalling around deposition boreholes of an underground nuclear waste repository", *International Journal of Rock Mechanics and Mining Sciences*, **152**, 105038. https://doi.org/10.1016/J.IJRMMS.2022.105038
- Paluszny A., Thomas, R. N., **Saceanu, M. C.** & Zimmerman, R. W. (2020), "Hydro-mechanical interaction effects and channelling in three-dimensional fracture networks undergoing growth and nucleation", *Journal of Rock Mechanics and Geotechnical Engineering*, **12**, 707-719. doi.org/10.1016/j.jrmge.2020.04.004

Journal articles in preparation for submission

- **Saceanu, M. C.**, Paluszny, A., Zimmerman, R. W., & Mas Ivars, D., "Thermo-mechanical modelling of spalling around the deposition boreholes of an underground nuclear waste repository during its thermal phase".
- **Saceanu, M. C.**, Paluszny, A., Zimmerman, R. W., & Mas Ivars, D., "Effect of *in situ* heterogeneities and pre-existing flaws on rock spalling around underground excavations".

Peer-reviewed conference papers

- **Saceanu, M. C.**, Paluszny A., Zimmerman R. W. & Mas Ivars D. (2023), "Evolution of spalling-inducing fractures around a deep geological repository for nuclear waste during glaciations and their effect on the long-term repository stability", *15^{th} ISRM Congress 2023 & 72^{nd} Geomechanics Colloquium*, 8-11 October 2023, Conference paper.
- **Saceanu, M. C.**, Paluszny A., Zimmerman R. W. & Mas Ivars D. (2020), "Numerical modelling of spalling around a nuclear waste storage deposition borehole using a fracture mechanics approach", *54^{th} U.S. Rock Mechanics/Geomechanics Symposium, Virtual*, Conference paper ARMA-2020-1396. https://onepetro.org/ARMAUSRMS/proceedings/ARMA20/All-ARMA20/ARMA-2020-1396/447613

Conference Presentations

- Paluszny A., **Saceanu, M. C.** & Zimmerman, R. W. (2023), "Numerical Modelling of the Nucleation and Growth of Multiple Three-Dimensional Dense Fracture Sets", *14^{th} International Conference on Large-Scale Scientific Computations (LSSC23)*, Sozopol, Bulgaria, 5-9 June 2023, Oral presentation.

- Paluszny, A., Suchoy, L., **Saceanu, M. C.** & Zimmerman, R. W. (2023), "Coupled thermo-mechanical growth of multiple fractures in brittle heterogeneous rocks during thermal shock and resulting aperture distributions", *EGU General Assembly*, Vienna, Austria, 24–28 April 2023, Oral presentation EGU23-7515, https://doi.org/10.5194/egusphere-egu23-7515,2023.

- **Saceanu, M. C.**, Paluszny, A., Zimmerman, R. W. & Mas Ivars, D. (2022), "Thermo-mechanical modelling of borehole spalling and host rock damage in deep geological repositories for nuclear waste disposal" *International Conference on Coupled Processes in Fractured Geological Media (CouFrac)* 11-13 November 2022, Oral presentation and extended abstract.

- **Saceanu, M. C.**, Paluszny, A., Zimmerman, R. W. & Mas Ivars, D. (2022), "Effect of in-situ heterogeneities and pre-existing flaws on rock spalling around underground excavations", *15th World Congress on Computational Mechanics (WCCM-APCOM), Online*, 31 July - 5 August 2022, Oral presentation.

- Paluszny A., Thomas R. N., **Saceanu, M. C.** & Zimmerman, R. W. (2021), "Thermo-(hydro)-mechanical effects on fracture growth and apertures in three dimensional subsurface fractured rocks", *EGU General Assembly, Online*, 19-30 April 2021, Oral presentation EGU21-14418, https://doi.org/10.5194/egusphere-egu21-14418

- Paluszny A., **Saceanu, M. C.**, Paluszny M. (2021), "Three-dimensional lofted spatial B-Splines for isogeometric fracture growth modelling", *International Conference of the Engineering Mechanics Institute, Online*, 22-24 March 2021, Oral Presentation.

- **Saceanu, M. C.**, Paluszny, A., Zimmerman, R. W. & Mas Ivars, D. (2020), "Thermo-mechanical modelling of spalling failure around deposition boreholes in underground nuclear waste repositories", *International Conference on Coupled Processes in Fractured Geological Media (CouFrac), Online* 11-13 November 2020, Oral presentation and extended abstract.

- **Saceanu, M. C.**, Paluszny, A., Zimmerman, R. W. & Mas Ivars, D. (2020), "Impact of deposition borehole geometry on mechanical spalling in nuclear waste repositories", *EGU General Assembly, Online*, 4–8 May 2020, Oral presentation EGU2020-5936, https://doi.org/10.5194/egusphere-egu2020-5936

- **Saceanu, M. C.**, Paluszny, A., Zimmerman, R. W. & Mas Ivars, D. (2022), "Finite element modelling of thermo-mechanical spalling around deposition boreholes in a GDF" *Nuclear Waste Services Research Support Office (RSO) Webinar: Mathematical Modelling of Coupled Processes relevant to a GDF*, 23 June 2022, Invited talk. https://www.youtube.com/watch?v=q_B4feNdUU8

Chapter 2

Literature Review

The construction of an underground geological repository will involve drilling a range of structures at depths of several hundreds of meters, including access tunnels, ramps, deposition tunnels, and deposition boreholes, in which the spent fuel will be emplaced. It is important to understand how the overstressed rock will behave following the excavation of these structures, in order to ensure an effective repository design and its long-term stability. This chapter introduces the concept of underground nuclear waste storage in geological repositories and the fracturing processes that occur in the vicinity of deep-drilled excavations. Analytical and numerical methods that have been formerly employed to model borehole deformation and failure are presented in the context of deep geological disposal.

2.1 Deep Geological Repositories

Early strategies in the field of long-term nuclear waste management included potential disposal in salt mines (Parker et al. 1978), ice sheets (Zeller et al. 1973, Philberth 1977), deep-sea sediments (Hollister et al. 1981), subsoil (Morton & Struxness 1956), and even outer space (Burns et al. 1978). Most of these have since been discarded, and deep geological repositories are now considered the most appropriate solution for final disposal and isolation of high-level nuclear waste (Long & Ewing 2004).

Although research on deep geological disposal began as early as the 1970s (SKB TR-01-03 1978), no such repository has yet been completed. The most advanced programmes are in Finland, where excavation work is underway, and a trial run for final disposal is planned to be performed in 2023 (Makkonen 2022), and Sweden, where the Forsmark site has recently been approved, and construction is expected to begin this decade (SKB 2022).

The planned nuclear waste repository at Forsmark is designed based on the Swedish KBS-3 concept (SKB TR-10-12 2010), which is more generally known as a multiple barrier concept. KBS-3 isolates the spent fuel in a deposition sequence comprised of several steps. Firstly, the spent fuel is processed into solid form and emplaced in cast iron inserts, which may accommodate multiple fuel assemblies. Subsequently, the cast iron is encapsulated in noncorrosive copper canisters, which will eventually be deposited deep underground in crystalline rock, inside vertical boreholes. Afterwards, the boreholes will be buffered with bentonite clay, which will pad the canister and provide support pressure to the borehole wall. The method of borehole confinement with bentonite clay has been shown to reduce the severity of spalling (SKB TR-10-37 2010, Andersson 2007). Finally, the deposition tunnels will be backfilled (Figure 2.1).

One of the reasons that no deep geological repository has yet been completed is the challenge in identifying and characterising a potential site (Kuppler & Hocke 2018). Site investigation and characterisation is laborious work, requiring an integrated understanding of bedrock geology, hydrogeology, rock mechanical and thermal properties, *in situ* stresses, existing fracture domains and deformation zones, as well as accurate predictions of how the rock mass will react to long-term changes in all these variables (SKB TR-08-05 2008).

When drilling the underground structures that will form the deep geological repository, development of potential fractures is a risk. These fractures can cause a loss of borehole structural integrity. With both mechanical (after drilling) and thermal (after emplacement of the canisters) stresses acting on the borehole wall, fracture initiation and growth is promoted by the alteration of the natural stress state in the previously undisturbed rock.

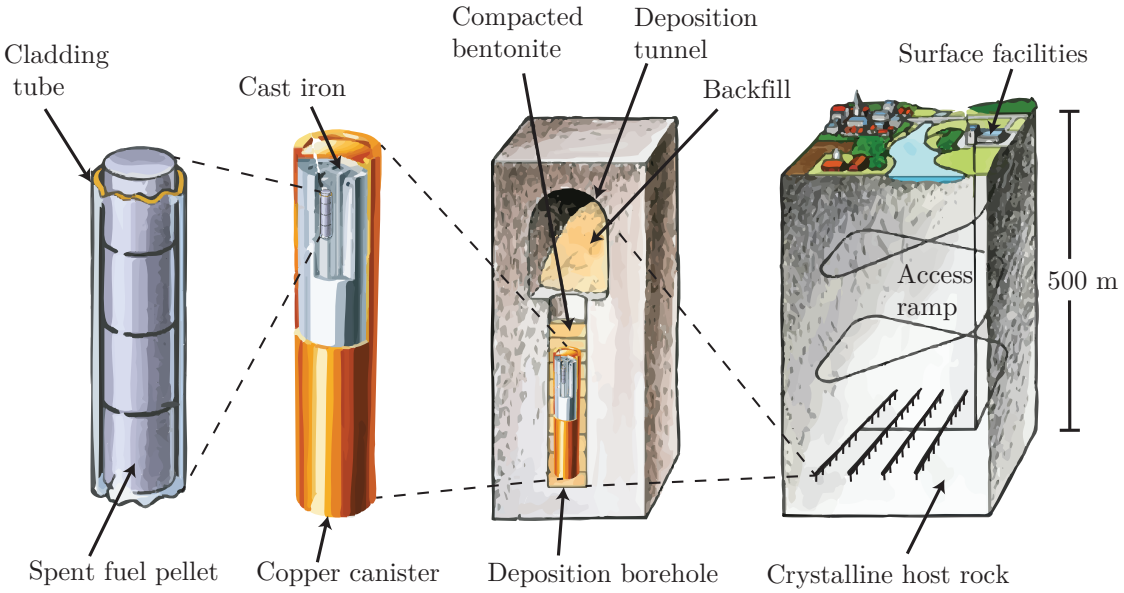


Figure 2.1: Schematic representation of the KBS-3 repository, illustrating the multiple barrier concept. Adapted from SKB TR-12-01 (2012).

2.2 Excavation Damage Zones

The extent and nature of the damage surrounding underground excavations has been the topic of interest of many researchers (Martino & Chandler 2004, Hudson et al. 2009, Vazaios et al. 2019, Behera et al. 2021) and is a significant prerequisite for the design considerations of a DGR (Kwon et al. 2009, Siren et al. 2015). Damaged or fractured rock presents increased permeability and hydraulic conductivity (Tsang et al. 2005), potentially enhancing radionuclide escape into the host rock in the event of canister leakage.

There are numerous definitions and terminologies used in the literature to describe the different excavation damage zones (EDZs) that occur in the vicinity of underground excavations (Siren et al. 2015). The ones used throughout this thesis are illustrated in Figure 2.2 and were summarised based on the classifications from Tsang et al. (2005) and Siren et al. (2015) as follows:

- Highly damaged zone (HDZ) is the closest zone around the excavation. In the HDZ, fractures nucleate and propagate as a result of *in situ* stress redistribution after drilling. The rock mass properties are significantly altered. This zone contains visible, connected fractures which may cause spalling of the borehole wall and form a failed zone. Hudson & Harrison (2000) noted that spalling damage is stress-induced and should be differentiated from excavation damage, which is also present around the borehole, but can be minimised during the excavation. In this thesis, the HDZ is therefore referred to as the "spalled zone".
- Excavation damaged zone (EDZ)[1] encompasses the "spalled zone" and contains irreversible damage in the form of connected fractures, which become progressively disconnected further away from the borehole wall. This zone is also characterised by changes in the rock geomechanical properties, but the deeper fractures do not interact with the borehole wall directly and are not involved in spalling.
- Excavation disturbed zone (EdZ), is the furthest zone influenced by the stress redistribution after drilling. However, in the EdZ, deformation is reversible and the rock remains intact, *i.e.* no fracturing occurs. To avoid confusion with the EDZ, EdZ will be referred to as excavation influenced zone in this work. Beyond the EdZ the rock remains elastically undisturbed.

The depths of the EDZs can estimated by direct measurement, *e.g.* monitoring fracture development with a digital optical televiewer (Li et al. 2013), recording acoustic emission (Spies & Eisenblätter 2001), seismicity (Schuster et al. 2001), or resistivity changes (Kruschwitz & Yaramanci 2004) in the near borehole region. Alternatively, many authors

[1] Note the distinction with its hypernym - excavation damage zones (EDZs). In other words, EDZ is a subset of EDZs (EDZs = HDZ ∪ EDZ ∪ EdZ).

have developed empirical, analytical and numerical methods, to facilitate predictions of the EDZs based on the stress state around the underground excavation and the physical properties of the rock mass hosting the excavation. These will be presented in more detail in the following sections.

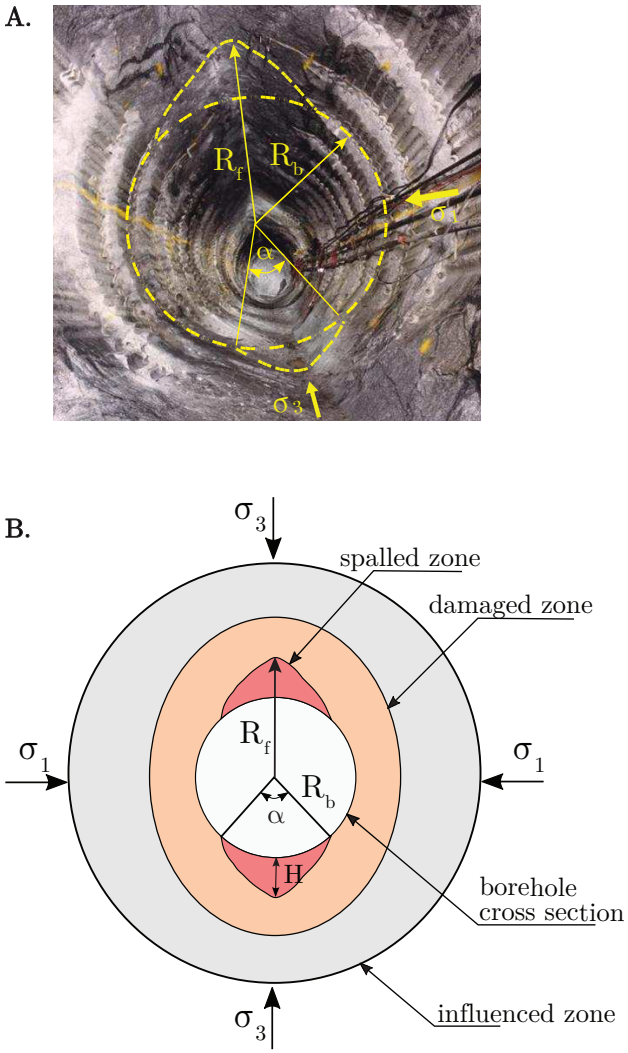


Figure 2.2: A. Spalled notch observed *in situ* [modified from Zhao et al. (2010)] and **B.** schematic representation of the three stress-induced damage zones around a circular excavation [modified from Read (2004)]. R_b, α and H denote the borehole radius, spalling angle (or spalling width), and spalling depth, respectively. The spalling depth is also frequently defined as the distance measured from the centre of the borehole, labeled as R_f.

2.3 Stresses around subsurface excavations

The undisturbed *in situ* tectonic stresses redistribute around the walls of a subsurface excavation, resulting in a locally disturbed stress field controlled by magnitude of remote

stresses and shape of excavation. In a homogeneous, isotropic, and linear elastic medium, assuming far-field vertical stress parallel to borehole axis and negligible vertical plane deformation, the stress field around a circular borehole is (Jaeger et al. 2007):

$$\sigma_{\theta\theta} = \frac{\sigma_H + \sigma_h}{2}\left(1 + \frac{{R_b}^2}{r^2}\right) - \frac{\sigma_H - \sigma_h}{2}\left(1 + 3\frac{{R_b}^4}{r^4}\right)\cos 2\theta \tag{2.1a}$$

$$\sigma_{rr} = \frac{\sigma_H + \sigma_h}{2}\left(1 - \frac{{R_b}^2}{r^2}\right) + \frac{\sigma_H - \sigma_h}{2}\left(1 - 4\frac{{R_b}^2}{r^2} + 3\frac{{R_b}^4}{r^4}\right)\cos 2\theta \tag{2.1b}$$

$$\sigma_{zz} = \sigma_v - 2\nu(\sigma_H - \sigma_h)\frac{{R_b}^2}{r^2}\cos 2\theta \tag{2.1c}$$

$$\tau_{r\theta} = -\frac{\sigma_H - \sigma_h}{2}\left(1 + 2\frac{{R_b}^2}{r^2} - 3\frac{{R_b}^4}{r^4}\right)\sin 2\theta \tag{2.1d}$$

where σ_{rr}, $\sigma_{\theta\theta}$, $\tau_{r\theta}$ are the radial, tangential and shear stresses around the borehole, σ_H and σ_h are the maximum and minimum horizontal far-field stresses, σ_v is the vertical far-field stress, R_b is the radius of the borehole, r is the radial distance from the borehole center, θ is the angular rotation from the direction of σ_H, and ν is the Poisson's ratio.

Figure 2.3a exemplifies the analytical tangential (Equation 2.1a), radial (Equation 2.1b), vertical (Equation 2.1c) and shear stress (Equation 2.1d) variation around a circular borehole as a function of azimuth and radial distance. At the borehole wall (Figure 2.3b), the tangential stress is maximum at $\theta = [90°, 270°]$, and minimum at $\theta = [0°, 180°]$ wrt. σ_H direction. This variation may cause compressive failure at $\theta = [90°, 270°]$ if the rock compressive strength is exceeded, and tensile failure at $\theta = [0°, 180°]$ if the tensile strength is exceeded and if $\sigma_{\theta\theta}$ is tensile ($\sigma_{\theta\theta} = 3\sigma_h - \sigma_H \geq 0$). Compressive failure at $\theta = [90°, 270°]$ (in the direction of σ_h) manifests through borehole breakouts, which generally develop by shear fracturing and cause enlargements of the borehole. Alternatively, tensile failure at $\theta = [0°, 180°]$ typically results in narrow, radial fractures, which do not cause significant deformation of the borehole wall in this direction. Equations 2.1b—2.1c explain the shear fractures found in the direction of the minimum horizontal stress, but not tensile fractures, which have also been observed to form at borehole azimuths with entirely compressive stress field (Fairhurst & Cook 1966).

As the radial distance increases beyond five borehole radii, the tangential, radial, and vertical stresses approach the magnitudes of the undisturbed, far-field horizontal and vertical principal stresses (Figure 2.3c). This implies that adjacent boreholes, and the boundaries of the numerical domain should be placed at least $5R_b$ away, to minimise stress interactions and boundary effects. It should be noted that the specific requirements for minimum borehole separation from other boreholes or free boundaries depends on the rock properties, heterogeneity distribution and far-field stress anisotropy. $5R_b$ is the area of influence that a single borehole has on its own surrounding stress field in the absence of neighbouring boreholes and under the assumptions that: 1. the borehole is placed in a homogeneous,

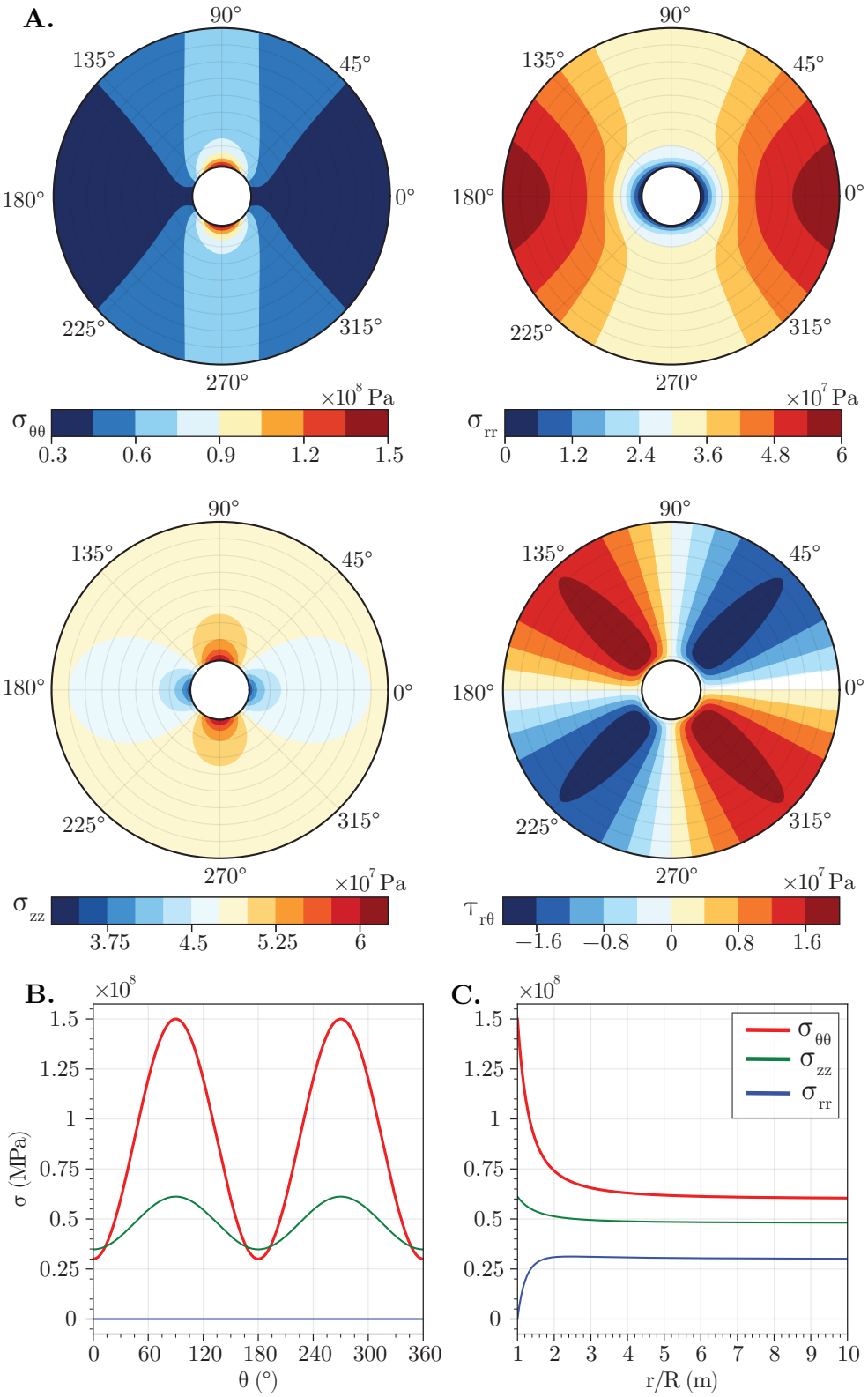


Figure 2.3: **A.** Stress contours around a circular borehole assuming isotropic elasticity (Eqs. 2.1b—2.1c). The radial grid increment is 1 m, $\sigma_H = 60$ MPa, $\sigma_h = 30$ MPa, $\sigma_v = 48$ MPa, $R_b = 1.75$ m, $\nu = 0.22$. **B.** Magnitude of $\sigma_{\theta\theta}$, σ_{zz} and σ_{rr} as a function of angle θ with the direction of the maximum horizontal stress σ_H. **C.** Magnitude of $\sigma_{\theta\theta}$, σ_{zz} and σ_{rr} as a function of radial distance r/R in the direction of the minimum horizontal stress σ_h.

isotropic, and linear elastic medium; 2. the far-field vertical stress is parallel to borehole axis; 3. the borehole is infinitely long (plane strain conditions).

2.4 Failure around deep-drilled boreholes

Fracture development in the highly damaged zone causes rock failure that can take several forms, among which spalling, slabbing, and rock bursting are most commonly encountered around boreholes and tunnels drilled in hard, brittle rock (Kaiser & McCreath 1994, Diederichs et al. 2004, Read 2004). Depending on the loading conditions and the rock mechanical properties, one or more of these types of failures may occur (Hoek 1968, Hills et al. 1996).

2.4.1 Borehole breakouts vs. spalling

The terms "spalling" and "borehole breakout" have been used interchangeably to denote cross-sectional elongations of boreholes, due to loss of integrity of the neighbouring host rock in two diametrically opposite failed zones (Amadei & Stephansson 1997). Spalling is the preferred term in tunneling literature to describe brittle failure in hard, crystalline rocks in the immediate vicinity of an unconfined excavation (where $\sigma_{rr} \rightarrow 0$), and was first observed by Leeman (1958) in Witwatersrand gold mines in South Africa. More recent observations of spalling arised from field studies of test boreholes and tunnels, which were excavated as part of the site characterisation studies for deep geological repositories (Martin & Kaiser 1996, Read 2004, Andersson & Martin 2009, Andersson et al. 2009*a*).

Spalling failure mechanism is caused by tensile fracture development in brittle rock under high compressive *in situ* stresses (Martin 1997). Diederichs (2007*a*) differentiates spalling from rock bursting, noting that spalling may be nonviolent, whereas rock bursting involves the violent collapse of a large volume of spalled rock. It is generally agreed that spalling initiates in tension, but how much of the failure results from fractures propagating in tension vs. shear is still a matter open to active research (Wesseloo & Stacey 2016, Barton & Shen 2017).

Spalling can thus be regarded as a particular case of borehole breakouts, which have been extensively studied in petroleum-related literature. Although the two concepts overlap, the literatures from the two fields remain isolated, mainly due to the different lithologies and *in situ* conditions involved. Some authors may also refer to the process of breakout formation in weaker rocks as "spalling" (Haimson 2007), however, the failure mechanism by which a borehole breakout initiates can be tensile or shear (Hudson & Harrison 2000), whereas spalling initiation is associated with tensile cracking only (Martin et al. 1997).

A number of early field (Bell & Gough 1979, Gough & Bell 1982, Fordjor et al. 1983) and laboratory (Haimson & Song 1993, Lee & Haimson 1993) studies have recorded that the direction in which spalling and borehole breakouts develop in vertical boreholes is along the springline of the minimum horizontal stress, and the final breakout can have different shapes such as "v-shaped notch", "dog ear" or "cusp" (Zheng et al. 1989, Amadei & Stephansson 1997). Consequently, *in situ* stresses are commonly estimated from breakouts, as stress directions and magnitudes correlate with breakouts orientations and depths (Zoback et al. 2003, 2010, Lin et al. 2020, Setiawan & Zimmerman 2022).

The extent of the breakout, or the "spalled zone" that forms around an underground opening, is a function of the geometry of the opening, the *in situ* stresses, and the strength of the rock mass. Martin et al. (1999) developed an empirical relationship to fit the data from a number of field studies (Figure 2.4) by relating the radial extent of the "v-shaped" notch, *i.e.* the spalling depth, to the maximum tangential stress acting on a circular tunnel boundary, the uniaxial compressive strength of the rock, and the size of the opening:

$$\frac{R_f}{R_b} = 0.49(\pm 0.1) + 1.25\frac{\sigma_{\theta\theta}}{\sigma_{UCS}} \tag{2.2}$$

where R_f is the spalling depth measured from the centre of the borehole, as illustrated in Figure 2.2, R_b is the radius of the circular tunnel, $\sigma_{\theta\theta}$ is the tangential stress at the borehole wall prior to fracturing, equal to $3\sigma_H - \sigma_h$, and σ_{UCS} is the laboratory uniaxial compressive strength. Equation 2.2 was later adapted by Diederichs (2007*a*) to use the *in*

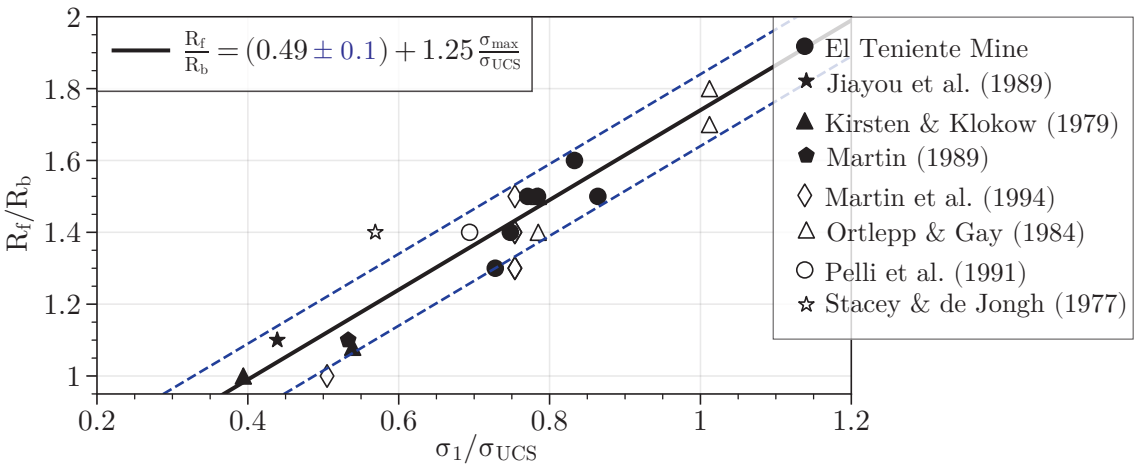


Figure 2.4: *In situ* measurements of spalling depth compiled by Martin et al. (1999) and the empirically determined equation fitting the field data.

situ strength of the rock in the vicinity of excavations, instead of the uniaxial compressive strength. Similar equations were proposed by Perras & Diederichs (2016), who used a modified version of the Hoek-Brown criterion to model EDZs numerically in granites, limestones, and mudstones. They delineated not only the extent of the highly damaged, or "spalled zone", but also the excavation damage zones further away from the borehole

wall, where the rock becomes progressively less damaged.

2.4.2 Field observations

The Mine-By Experiment

Between 1989 and 1995, the Atomic Energy of Canada Limited (AECL) carried out the "Mine-by tunnel experiment" with the aim to understand brittle rock behaviour around a circular borehole under high stresses. The experiment consisted of drilling a 3.5 m diameter circular tunnel in the a relatively unfractured granitic rock (Lac du Bonnet granite) at approximately 500 m depth. To minimise construction damage, AECL used line drilling and non-explosive rock-splitting techniques. An acoustic emission/microseismic (AE/MS) monitoring system was installed to monitor the stress-induced damage of the rock mass after drilling (Martin & Kaiser 1996).

The tunnel was excavated subparallel to the direction of the minimum horizontal stress σ_h, to maximise the ratio between the other two principal stresses acting on the roof and floor of the tunnel. The *in situ* stresses were estimated to be: $\sigma_H = 60 \pm 3$ MPa, $\sigma_h = 45 \pm 4$ MPa, $\sigma_v = 11 \pm 2$ MPa. Spalling became apparent in both the roof and the floor of the tunnel and the depth of spalling was estimated to be approximately 1.3 times the tunnel radius (Figure 2.2). When the spalled material was removed through scaling, additional fracturing was triggered, which revealed the importance of borehole reinforcement to contain spalling (Martin et al. 1999, Read 2004). Borehole reinforcement was tested and was demonstrated to be effective for suppressing spalling damage in the CAPS (Counterforce Applied to Prevent Spalling) experiment (SKB TR-10-37 2010), conducted a few years later.

The Äspö Pillar Stability Experiment

The Äspö Pillar Stability Experiment (APSE) was conducted between 2002 and 2006 in SKB's Äspö Hard Rock Laboratory (HRL), located near Oskarshamn in southern Sweden, at 450 m depth, where the geological conditions and *in situ* stress magnitudes were already determined from telescopic boreholes. The experiment consisted of drilling two 8 m long and 1.75 m diameter boreholes separated by a 1 m thick pillar of diorite rock (Andersson & Martin 2009).

The experiment was particularly valuable because in addition to mechanical spalling, it also studied the effect of thermal spalling, by coupling electrical heaters to the borehole wall and creating the conditions expected to occur during the radioactive decay of the spent fuel. At a maximum thermal stress induced by 38.8 °C temperature increase, new fracturing events were recorded (Andersson 2007, Andersson et al. 2009*a*). It was also

found that thermal spalling may be prevented if a small confining stress supporting the excavation wall is added through borehole reinforcement (Andersson et al. 2009*a*).

2.4.3 Spalling mechanism and spalling strength

Drilling experiments on cm-scale cores, in different rock types, e.g. granites, limestones, sandstones, have brought insights into the fracture mechanisms leading to spalling. Haimson (2007) noted that the spalled notches obtained in the laboratory in the granite specimens are very similar to those observed in the metre-scale circular tunnel excavated as part of the Mine-By Experiment. The experiments on the granite specimens showed extensile micro-cracks nucleating subparallel to the maximum compressive stress and along the direction of the minimum compressive stress. At increased compressive stresses, the micro-cracks grew in length and density, and approached the free surface of the borehole forming thin, subparallel rock slabs. The slabs closest to the borehole buckled and collapsed into the borehole, triggering the spalling process, which continued until the remaining cantilevers from the previous spalled fragments provided enough containment to stabilise the fracturing process (Figure 2.5a).

Song (1998) pointed out that the stabilised edge of the breakout resembles a set of conjugate shear fractures formed after the coalescence of the tensile micro-cracks. Recent experiments of spalling and rock burst on granite specimens performed by Hu et al. (2019) also support the idea that tensile micro-cracks coalesce into macro-fractures, which fail in shear, as most of the damage monitored as acoustic emission events was due to the growth of the macro-fractures. Figure 2.5b shows a schematic representation of the spalling mechanism inferred from the interpreted petrographic microscope image, where multiple tensile micro-cracks coalesce *en échelon* to trigger macroscopic shearing.

Similar-shaped breakouts have also been observed to form in other rock types, such as strong limestones and sandstones but the initiation and failure mechanisms are different, depending on the rock properties. For example, the dilatant micro-cracks preceding spalling in granite are intra- and trans-granular. Alternatively, those observed in limestones are predominantly inter-granular and they follow the least resistive paths prescribed by porosity. In weaker rocks, the micro-cracks initiate and propagate in shear, rather than in tension (Zheng et al. 1989, Zhou 1994). This implies that the rock mass strength plays an important role in the spalling process.

The "spalling strength" is commonly defined as the minimum tangential stress at which tensile cracks nucleate in hard rocks in highly compressive environments. Multiple field observations of spalling around underground excavations showed that the *in situ* spalling strength can be estimated to be 40%-60% the uniaxial compressive strength (σ_{UCS}) measured in laboratory on rock cores. Several theories have been proposed to explain the

difference between the laboratory and field values of spalling strength. These include: different loading and unloading stress paths during laboratory testing, compared with the *in situ* excavation process (Martin 1997); different loading rates (Zhang et al. 2011); damage accumulation ahead of the tunnel face during excavation, which may lower the *in situ* cohesive strength of the rock (Read et al. 1998); rugosity of the excavation wall, causing higher local stress concentrations at the excavation boundary (Cai & Kaiser 2014); scale effects and sample bias - the core samples from which the σ_{UCS} is experimentally determined are likely to contain fewer defects as they originate from parts of the rock mass of better quality (Cai & Kaiser 2014, Wang et al. 2022).

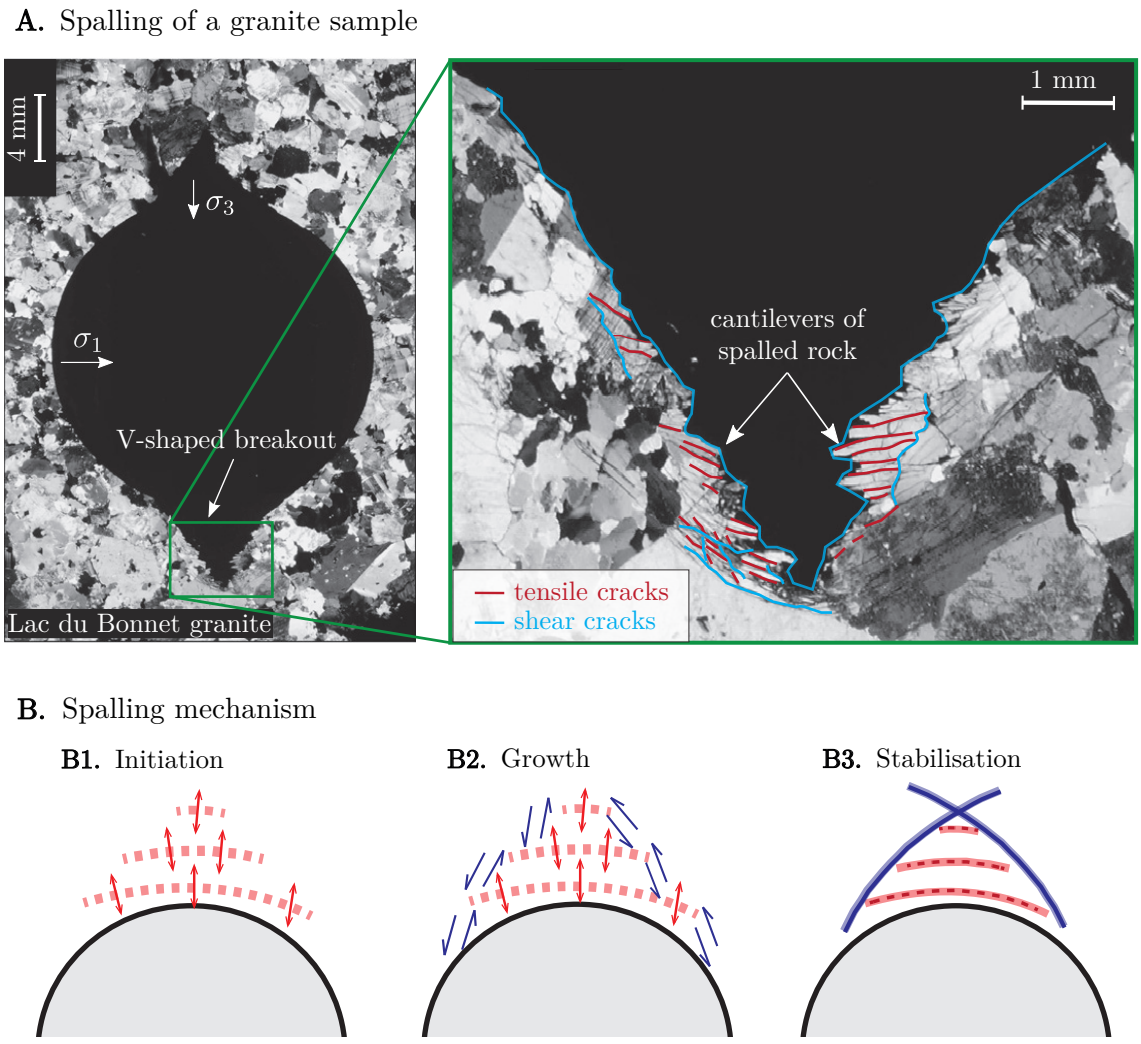


Figure 2.5: **A.** Polarised light cross-section of a stabilised borehole showing spalling-inducing fractures and the remnant cantilevers of spalled rock, which play a role in stabilising the breakout. Adapted from Haimson (2007), with an auxiliary interpretation of the imaged fractures. **B.** Spalling mechanism inferred from *A*, consisting of three stages: **b1.** nucleation of tensile micro-cracks along σ_3 and oriented subparallel to σ_1; **b2.** interaction and coalescence of the micro-cracks; **b3.** arrest of the fracturing process, showing stabilised notch geometry.

2.5 Analytical methods

2.5.1 Rock failure criteria

Failure criteria have been developed to determine if materials will break under specific applied loads and material strength conditions, e.g. Mohr-Coulomb (Jaeger et al. 2007), Hoek-Brown (Hoek & Brown 1980), Mogi (Mogi 1971), Drucker-Prager (Drucker & Prager 1952). These are widely used in rock mechanics, as they can provide quick failure predictions, but their applicability is constrained to specific cases, and more recent modifications are needed to account for the full triaxial stress state (Al-Ajmi & Zimmerman 2005). Additionally, shear-strength based criteria do not capture the correct mechanism of spalling fracture initiation in tension (Stacey & Wesseloo 2022), and they underestimate the failure extent in brittle rocks such as granites (Martin et al. 1999).

2.5.1.1 Shear strength-based: Mohr-Coulomb

The Mohr-Coulomb criterion relates the shear stress, $\tau_{\max}$, needed to cause failure along a plane to the rock cohesive strength, the coefficient of internal friction and the normal stress acting on the plane σ_n:

$$\tau_{\max} = C_o + (\tan \varphi)\, \sigma_n \tag{2.3}$$

where C_o and φ are the cohesion and friction angle, respectively. This criterion neglects the effect of the intermediate principal stress, σ_2, on rock strength, but has been widely used in early models of borehole breakouts (Zoback et al. 1985) due to its simplicity.

Martin & Chandler (1994) carried out a series of laboratory studies on granite, to show that cohesion is lost and friction is mobilised at different strains. The cohesive strength dominates the rock behaviour before damage initiates, and it reduces as tensile microcracks accumulate. Once the cohesion is lost and macro-failure is visible, the frictional component of the strength gets mobilised. Consequently, Martin et al. (1999) proposed that the Mohr-Coulomb criterion in its original form cannot adequately predict spalling failure, and a modified criterion should be used.

Hajiabdolmajid et al. (2002*b*, 2003) proposed a cohesion weakening-frictional strengthening approach (CWFS), where the cohesive and frictional strength components are mobilised as a function of remotely measured plastic strain ε:

$$\tau_{\max} = C(\varepsilon) + \sigma_n(\varepsilon) \tan \varphi \tag{2.4}$$

Using this modified approach, they obtained improved predictions of the spalling failure extent. However, the failure mechanism in this case is shear, and does not predict extensional fracturing that has been observed to occur during spalling.

2.5.1.2 Empirical: Hoek and Brown

One of the most frequently used criteria to predict failure in both intact and fractured rock is the Hoek-Brown criterion. The general expression of the criterion can be written as:

$$\sigma_1 = \sigma_3 + \sigma_{UCS}\left(m_b\frac{\sigma_3}{\sigma_{UCS}} + s\right)^a \tag{2.5}$$

where σ_1 and σ_3 are the maximum and minimum principal stresses, σ_c is the uniaxial compressive strength of the intact rock, m_b is the Hoek-Brown constant of the rock mass, s and a are constants determined from the characteristics of the rock mass.

Similarly to the CWFS modification needed to model spalling with the Mohr-Coulomb criterion, Diederichs (2007*b*) developed the Damage Initiation Spalling Limit (DISL) approach to capture brittle spalling behaviour by specifying peak and residual values for the Hoek-Brown input parameters m_b, s and a. The two set of values are used to define the damage initiation and spalling limit envelopes and capture the transition from elevated cohesion and low friction to cohesion loss and friction mobilization.

2.5.1.3 Tensile strength-based: Griffith

Griffith (1921, 1924) introduced the concept of materials containing pre-existing micro-flaws. In a two-dimensional setting, he assumed a linear-elastic material to have micro elliptical cracks of random orientations. Fracturing occurs when the maximum stress at the boundary of an arbitrarily oriented flaw arrives at a certain critical value. Among all cracks, fracturing would initiate from the crack in the orientation that causes the greatest maximum tensile stress at its boundary. Under biaxial stresses, Griffith proposed that failure occurs if the following condition is satisfied:

$$(\sigma_1 - \sigma_3)^2 = 8\sigma_t\,(\sigma_1 + \sigma_3) \tag{2.6}$$

where σ_1 and σ_3 are the maximum and minimum principal stresses and σ_t is the rock uniaxial tensile strength.

2.5.1.4 Strain energy-based: Stacey

Stacey (1981) proposed an extensional strain criterion, which also takes into account the intermediate principal stress, to explain fracture initiation in a fully compressive stress field:

$$\varepsilon_3 = \frac{1}{E}\left[\sigma_3 - \nu(\sigma_1 + \sigma_2)\right] \tag{2.7}$$

where σ_1, σ_2, σ_3 are the maximum, intermediate, and minimum principal stresses, ν is the Poisson's ratio and E is the Young's modulus.

Using this extensional strain criterion in 2D, Barton & Shen (2017) suggested that the reason *in situ* spalling strength is $0.4 \pm 0.1 \times \sigma_{UCS}$ may be a natural consequence of typical rock deformability properties. Rewriting Equation 2.7 in terms of the radial and tangential stresses:

$$\varepsilon_{rr} = \frac{1}{E}(\sigma_{rr} - \nu\sigma_{\theta\theta}) \tag{2.8}$$

where ε_{rr} is the radial strain, σ_{rr} is the radial stress, $\sigma_{\theta\theta}$ is the tangential stress at the borehole wall, and assuming that tensile failure occurs when ε_{rr} reaches a critical strain $\varepsilon_c = \frac{\sigma_{TS}}{E}$, where σ_{TS} is the rock uniaxial tensile strength:

$$\frac{1}{E}(\sigma_{rr} - \nu\sigma_{\theta\theta}) = -\frac{\sigma_{TS}}{E} \tag{2.9}$$

they pointed out that for typical values of uniaxial compressive strengths and Poisson's ratios, *e.g.* $\sigma_{\mathrm{UCS}} \simeq 10\sigma_{TS}$ and $\nu = 0.25$, the tangential stress at which fracturing initiates in the proximity of an excavation wall where $\sigma_{rr} \approx 0$ is:

$$\sigma_{\theta\theta} = \frac{\sigma_t}{\nu} = \frac{\sigma_{UCS}}{10 \times 0.25} = 0.4\sigma_{UCS} \tag{2.10}$$

2.6 Numerical methods

From a computational perspective, numerical methods for simulating rock fracturing can be divided into three main categories: continuum, discontinuum and hybrid approaches (Figure 2.6). The failure criteria described in the previous section are usually implemented in continuum models, which are used to simulate borehole failure in the form of spalling or borehole breakouts.

2.6.1 Continuum methods

In continuum models, the rock domain is regarded as one continuous body, where deformation is computed based on a constitutive relationship, and fractures are treated as

changes in the assigned constitutive criterion, *i.e.* material weakening. Rabczuk (2013) provided an extensive overview of continuum methods and how they represent fractures.

Continuum models of spalling can be either elastic-plastic—where strain is split into elastic and plastic strain; or damage-based—where accumulating damage accounts for a progressive degradation of the material stiffness. Such models are conventionally implemented using the finite element method (FEM) (Cai & Kaiser 2014, Edelbro 2010, Germanovich & Dyskin 2000, Diederichs 2007*a*), finite difference method (FDM) (Hajiabdolmajid et al. 2002*b*, 2003), or boundary element method (BEM) (Martin et al. 1999, Zheng et al. 1989).

Hajiabdolmajid et al. (2002*b*, 2003) showed that continuum models of spalling based on conventional constitutive laws, such as elastic perfectly-plastic or elastic brittle-plastic, have not been able to replicate the shape and depth of the spalled notch in brittle rock. This is because the traditional failure criteria, Mohr-Coulomb and Hoek-Brown, assume that cohesion and friction are simultaneously mobilised. To overcome this limitation, modified modeling approaches such as Cohesion Weakening Friction Strengthening (CWFS) (Hajiabdolmajid et al. 2003), and Damage Initiation Spalling Limit (DISL) (Diederichs 2007*a*) were introduced. In CWFS and DISL, the cohesion and friction angle are mobilised independently, depending on the accumulated plastic strain, or damage. These modified approaches also consider the plastic strain required for 1) the cohesive component to reach its residual value, and 2) the frictional component to reach its peak value is dependent on grain size and heterogeneities.

While the Cohesion Weakening Friction Strengthening (CWFS) criterion used in continuum approaches generates results in agreement with field observations, it requires an *a priori* estimation of the plastic strain limit—the point at which the cohesion component reaches its residual value and the frictional component becomes fully mobilised.

One powerful continuum approach is a continuum model with discrete fractures in which fractures are represented as separate entities from the mesh. This model was introduced by Belytschko & Black (1999) in 2D and is now known as the extended finite element method (XFEM). The main advantage of this method is that the shapes and locations of the fractures are not embedded in the mesh. However, the fractures are limited by the mesh refinement of the domain. The vast majority of spalling models which simulate discrete fracture processes are based on discontinuum or hybrid methods.

2.6.2 Discontinuum methods

Martin (2014) highlighted that the existing numerical studies of spalling using continuum methods may only provide an approximation of the spalling fracturing mechanism, which is inherently discrete. Another set of methods suitable for modelling spalling are the discontinuum numerical methods. Cundall & Hart (1993) provided a detailed account

of discrete element methods (DEM) and their various implementations, alongside their applicability in modeling discrete fracture initiation and growth.

An advantage of the discrete element method is that it does not depend on the previously described constitutive criteria to define where fracturing occurs. Instead, particle contact (Cundall 2001) is used to replicate failure. The numerical domain is discretised, each particle contact given a local micro–strength. When the tensile or shear strength at the contact is overcome, it breaks. The progressive micro–failure process continues with subsequent bonds breaking, eventually causing macro–failure. A disadvantage of this method is that the assigned contact strengths, as well as particle shapes, sizes and clustering are not geomechanically informed, and so the accuracy of the fracturing mechanism cannot be verified.

Similar to continuum modelling, classical DEM implementations fail to simulate spalling fractures in compressive stress fields, as they overestimate the spalling strength of brittle rock around excavations. To obtain realistic macroscopic fracturing behaviour, numerical studies using discontinuum methods showed that additional factors such as grain clustering (Potyondy & Cundall 2004, Ding & Zhang 2014, Tuckey 2020), micro-scale heterogeneity (Lan et al. 2010) or grain interlocking (Scholtès & Donzé 2013) need to be introduced.

Potyondy & Cundall (2004) used a two-dimensional bonded particle model to simulate spalling failure around the "Mine-By" tunnel and were able to reproduce the spalling depths and widths observed in the field experiment. Their model also captures tensile micro-cracking, but the obtained macro-fracture patterns also resemble shear bands that usually form in much weaker rocks.

Lan et al. (2010) introduced the effect of small scale heterogeneities in a grain-based model, using polygonal grains of variable sizes, which were bonded together through contacts that accounted for the micro–heterogeneity, but also allowed simulation of intra-element fracturing. Using this enhanced DEM approach, the depth and shape of spalling observed around boreholes drilled as part of the Äspö Pillar Stability Experiment was reproduced (Lan et al. 2013).

2.6.3 Hybrid methods

Hybrid methods such as Finite / Discrete Element Method (FDEM), Boundary / Discrete Element Method (BDEM), or Numerical Manifold Method (NMM) combine aspects of both continuum and discontinuum methods. The domain of each DEM is modelled as a continuum, in general as elastic or elasto-plastic domains. During deformation, if the failure criterion is reached, a small fracture is introduced in the element where this happens and the model evolves into a DEM (Martin et al. 1999, Cai et al. 2004). However, DEM methods require micro- to macro- calibration of properties, which further requires direct

comparison of experimental results against simulations at a specific resolution. These approaches also generally model fracture along pre-existing internal boundaries in the model, which limits their predictive capability.

The suitability of using a combined finite/discrete element method (FDEM) to simulate brittle fracturing has been investigated by several researchers (Martin et al. 1999, Cai et al. 2004, Mitelman & Elmo 2014, Hamdi et al. 2014, Vlachopoulos & Vazaios 2018, Vazaios et al. 2019). This method is based on modelling fracturing and fragmentation processes explicitly. This allows the model to simulate the transition from a continuous to a discontinuous domain, and hence replicate the fracture initiation and propagation more accurately than continuum or discontinuum methods on their own.

Hamdi et al. (2014) simulated spalling damage using a combined finite–discrete element method (FDEM) in their model, under both static and dynamic loading. Using the FDEM method, they were capable of simulating fracture initiation, coalescence and propagation in 2D, applying progressively increasing stresses to the borehole. In their work, the intact rock was initially represented as a continuum, and when the failure criterion within the intact rock was exceeded, a fracture was introduced at that particular location. From then on, the model evolved into a discrete element model, where fractures propagated around boundaries of the meshed elements (inter-element fracturing), or cut through the elements themselves (intra-element fracturing).

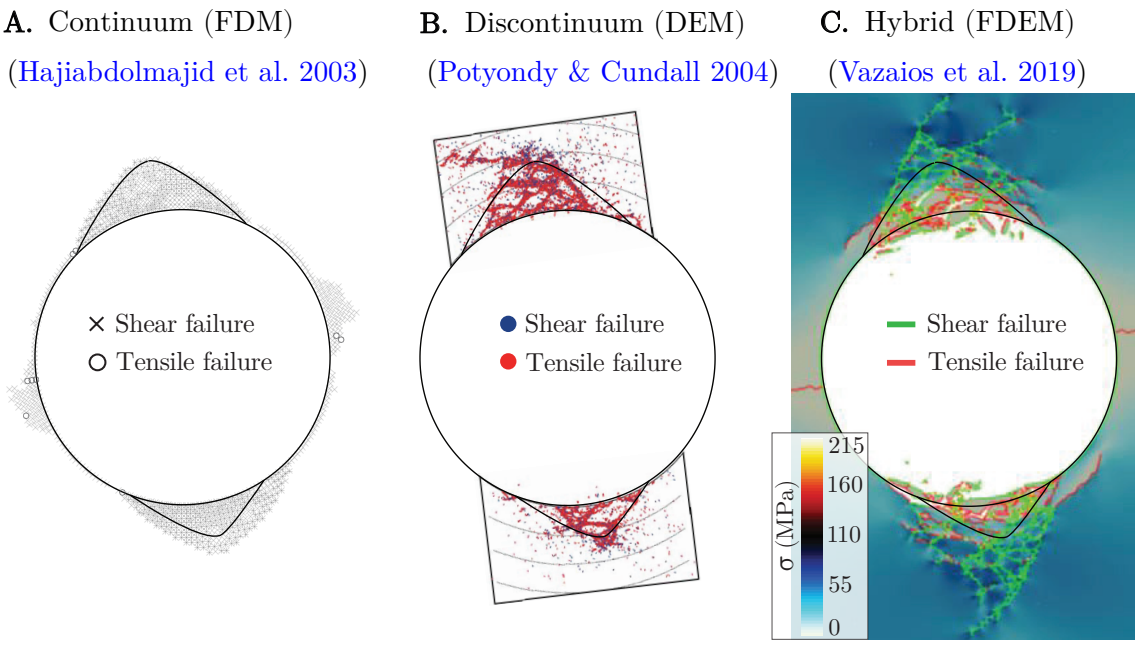


Figure 2.6: Examples of three distinct numerical spalling simulations, using continuum (**A**), discontinuum (**B**) and hybrid (**C**) methods, respectively.

Vlachopoulos & Vazaios (2018) investigated the effectiveness of two distinct numerical models, namely the finite element method (FEM) and the hybrid finite-discrete element method (FDEM)in simulating rock fracturing during excavation in hard rock masses. The two numerical models were based on data and observations collected from the Underground Research Laboratory (URL) Test Tunnel in Manitoba, Canada. They analysed the mechanical response of the underground excavation situated in a highly interlocked and hard rock mass predicted by both models and concluded that the FDEM method outperformed the continuum method in capturing the highly damaged zone (HDZ) and the excavation damaged zone (EDZ) associated with such excavations in hard rock masses.

2.6.4 Limitations of existing models

Most numerical studies of spalling mentioned in this section were conducted using proprietary simulators, and are generally limited to two-dimensional analyses. As a consequence, they inherently fail to capture the complex fracture interaction and growth patterns along the borehole wall, in the third dimension.

The numerical modelling approaches implemented in the commercial simulators succeed, in various extents, to match the observed locations of spalling failure and spalling depths. They require, however, a significant number of input parameters and extensive calibration to produce accurate results. For example, FEM models using the Mohr-Coulomb (Hajiabdolmajid et al. 2002*a*) or the Hoek–Brown (Vlachopoulos & Diederichs 2014, Vlachopoulos & Vazaios 2018) criteria to represent spalling failure criterion did not capture the brittle failure mechanism in a realistic manner, as they under- or overestimate the spalling strength and predict a incorrect damage extent when compared with in situ studies.

Models using shear-based criteria to simulate spalling do not initiate tensile fractures in entirely compressive stress regimes, although this was shown to occur when a critical extensional strain is exceeded at the borehole wall (Fairhurst & Cook 1966, Stacey 1981, Stacey & Wesseloo 2022). Additionally, FEM with additional modifications is able to capture the highly damaged zone (HDZ) around the excavation, where the material is damaged due to extensile fracturing, but it underestimates the excavation damaged zone (EDZ), where the rock is fractured, but still maintains its integrity. FDEM models were shown to capture both the HDZ and the EDZ around excavations in brittle rock, as they capture fracture initiation, propagation, and interaction based on fracture mechanics principles (Vlachopoulos & Vazaios 2018, Shen & Barton 2018).

The work presented in this thesis differs from those described above, as it investigates spalling in three dimensions, and applies a first-principle geometric fracture growth approach to model spalling/failure patterns efficiently. The next chapter provides a comprehensive description of the methodology used.

Chapter 3

Methodology

3.1 Introduction

As presented in Chapter 2, numerous approaches have been developed to study spalling analytically and numerically. Many of these approaches rely on simplified 2D assumptions and do not model individual fracture interactions and growth, but rather focus on predicting the extent of the various damage zones around subsurface excavations. Additionally, many studies that do succeed to reproduce the correct *failure extent*, fail to capture the actual *failure mechanism*.

"Spalling fractures", *i.e.* fractures that lead to the formation of spalled / highly damaged zones around boreholes, are particularly challenging to model numerically because of the range of scales and processes involved. The most advanced numerical models of spalling in which fracture growth is explicitly modelled require a significant number of input parameters, and extensive calibration, to produce accurate results. This chapter describes an alternative approach, in which principles of damage mechanics and linear elastic fracture mechanics are complementarily integrated into a unified numerical workflow to capture the spalling process, from fracture nucleation, to interaction with the borehole and growth arrest.

3.1.1 Imperial College Geomechanics Toolkit (ICGT)

All simulations are conducted in the ICGT, a 3D discrete fracture growth simulator, which can model a range of physical processes, including coupled poro-thermo-elastic deformation and multi-phase fluid flow. The ICGT models fracture growth as a function of deformation, which is numerically computed using the finite element method (Section 3.3.1), taking into account the physical properties of both the rock domain and the fracture surfaces.

Stress-induced spalling fractures nucleate from the damage that the host rock incurs in the proximity of the borehole, following its excavation (Section 3.4) in an initially isotropic, homogeneous, and linear elastic brittle rock domain. Fractures are represented discretely using smooth parametric surfaces (Section 3.3.3) and their growth is evaluated at the fracture front, where three modal stress intensity factors (SIFs) are calculated, capturing both tensile and shear fracture tip propagation (Section 3.5.2). SIFs are related to the energy necessary to extend the fracture, and they determine the magnitude and orientation of growth vectors at the fracture tip (Section 3.5.3). The stress intensity factor computation has been validated by Nejati et al. (2015*b*) for displacement correlation using quarter points, and Nejati et al. (2015*a*) for the disk-shaped domain integral method.

During the simulations, fracture geometry is always stored independently from the mesh (Paluszny & Zimmerman 2013*b*), and the volumetric discretisation of the domain conforms to the evolving fracture geometry, not *vice versa* (Section 3.3.2). Fracture extension is thus not influenced or constrained by the mesh. Multiple discontinuities of varying radii and evolving non-planar surface geometry grow in response to the local stress state at their tip nodes, with growth being influenced by the distribution of stress intensity factors, which capture the effect of *in situ* stresses, fracture interaction, and variations in material properties due to ensuing damage. This approach avoids a significant problem in many numerical studies of spalling, which rely on very refined meshes in order to ascertain that the generated fracture patterns are relatively independent from the mesh topology (Gao & Stead 2014, Tatone & Grasselli 2015).

The methodology and its implementation in ICGT has been validated by Paluszny & Matthäi (2009) in two-dimensions on interacting fractures, and in three-dimensions for isolated fractures under uniaxial tension and compression (Thomas et al. 2020). The ICGT has also been used in studies of fracture interaction (Thomas et al. 2017), hydraulic fracturing, where growth and aperture evolution of hydraulic fractures was validated (Salimzadeh et al. 2017), and THM fracture growth in the context of geothermal energy (Salimzadeh et al. 2018).

The present work presents extensions to the fracture growth methodology and its implementation in ICGT by considering the nucleation of fractures around underground excavations based on continuum damage mechanics, and the use of lofting to update geometric descriptions of fractures during growth. Additional validations relevant to modelling spalling-inducing fractures are presented in Chapter 4, including unit testing the SIF computation for an isolated fracture and validations of the major field variables (stress, damage and temperature) in single borehole and multiple boreholes models against closed-form solutions.

3.2 Governing equations

3.2.1 Mechanical deformation

Initial deformation of the intact rock domain is computed in response to the applied boundary stresses, as linear elastic deformation (Jaeger et al. 2007). For a homogeneous and isotropic rock matrix, the linear elastic stress-strain equation is

$$\boldsymbol{\sigma} = \boldsymbol{D}(\boldsymbol{\varepsilon} - \boldsymbol{\varepsilon_0}) + \boldsymbol{\sigma_0} \tag{3.1}$$

where $\boldsymbol{\sigma}$ and $\boldsymbol{\varepsilon}$ are the stress and strain tensors, σ_0 and ε_0 represent the initial stress and strain, and $\boldsymbol{D}$ is the linear elastic stiffness matrix, which accounts for the rock mechanical properties. Assuming infinitesimal deformation, strain is related to the displacement vector by:

$$\boldsymbol{\varepsilon} = \frac{1}{2}\left[\boldsymbol{\nabla u} + (\boldsymbol{\nabla u})^T\right] \tag{3.2}$$

Finally, Equations 3.1 and 3.2 are incorporated into an equilibrium equation that relates the forces applied to the numerical domain, to the stresses that develop inside the domain:

$$\boldsymbol{\partial \sigma} + \boldsymbol{F} = 0 \tag{3.3}$$

3.2.2 Thermo-mechanical deformation

Coupled thermal-hydraulic-mechanical (THM) behaviour is a significant research topic in nuclear waste disposal, as the fractured rock will also experience thermal loads due to the heat-emitting nuclear waste canisters. In ICGT, the fully coupled THM response is computed taking into account thermoelastic deformation, fluid flow through fractures and the rock matrix, and heat transfer through fractures and the rock matrix (Salimzadeh et al. 2018).

In this work, it is assumed that there is no fluid residing inside the rock matrix and/or the fractures. This is a reasonable assumption in the nuclear waste disposal context, where the most advanced programs consider disposal in relatively unfractured (low permeability), crystalline (no porosity) host rock. In the absence of fluid, the thermoelastic stress-strain relationship (Zimmerman 2000, Khalili & Selvadurai 2003) is

$$\boldsymbol{\sigma} = \boldsymbol{D}(\boldsymbol{\varepsilon} - \varepsilon_0) + \sigma_0 - \alpha K(T_m - T_0)\boldsymbol{I} \tag{3.4}$$

where $\boldsymbol{\sigma}$ and $\boldsymbol{\varepsilon}$ are the stress and strain tensors, respectively, $\boldsymbol{D}$ is the linear elastic stiffness matrix, α is the coefficient of volumetric thermal expansion, K is the bulk modulus, T_m is the rock temperature and $\boldsymbol{I}$ is the identity matrix.

Heat transport, in the absence of fluid flow (advection), occurs by conduction through the rock matrix (Equation 3.5a) and through the fracture surfaces (Equation 3.5b) respectively:

$$\boldsymbol{q}_{mc} = -\boldsymbol{\lambda_m} \nabla T_m \tag{3.5a}$$

$$\boldsymbol{q}_{mf} = \lambda_n \frac{\partial T}{\partial \boldsymbol{n_c}} \tag{3.5b}$$

where $\boldsymbol{\lambda_m}$ is the thermal conductivity tensor of the rock, ∇T_m is the temperature gradient driving conductive heat flux through the rock matrix, λ_n is the thermal conductivity in the direction normal to the fracture surface, and $\frac{\partial T}{\partial \boldsymbol{n_c}}$ is the temperature gradient in the direction normal to the fracture.

Under transient conditions, the rock may also store thermal energy. Assuming zero porosity, the matrix heat capacity is equal to that of the solid rock and the stored heat is given by:

$$\boldsymbol{q}_{ms} = \rho_m C_m \frac{\partial T_m}{\partial t} \tag{3.6}$$

where ρ_m is the rock density and C_m is the rock heat capacity.

Finally, the thermal energy change due to the bulk deformation of the rock skeleton can be expressed as:

$$q_{mu} = \alpha K T_m \frac{\partial \left(\boldsymbol{\nabla} \cdot \boldsymbol{u} \right)}{\partial t} \tag{3.7}$$

The general equation for heat transfer through the fractured rock is obtained by combining Equations 3.5–3.7 and integrating them over the rock volume Ω and fracture surfaces Γ respectively:

$$\int_\Omega \boldsymbol{\nabla} \cdot \left(\boldsymbol{\lambda_m} \nabla T_m \right) d\Omega = \int_\Omega \left[\rho_m C_m \frac{\partial T_m}{\partial t} - \alpha K T_m \frac{\partial \left(\boldsymbol{\nabla} \cdot \boldsymbol{u} \right)}{\partial t} \right] d\Omega + \int_\Gamma \left[\lambda_n \frac{\partial T}{\partial \boldsymbol{n_c}} \right] \mathrm{d}\Gamma \tag{3.8}$$

3.3 Model geometry and discretisation

While rock spalling in the proximity of the boreholes and tunnels of a deep geological repository is a geomechanical process that occurs in a semi-infinite medium, numerically, it is simulated in a finite computational domain. The first step in the numerical modelling approach is to build the initial geometric model and define the boundaries of the major volumetric objects, such as the host rock domain and the borehole domain (Figure 3.2a–3.2b). These are defined in a computer-aided design (CAD) software (Rhino3D 2020) as non-uniform rational B-spline (NURBS) curves and surfaces.

CAD geometry is automatically generated at every simulation step and fully integrated with the ICGT, through a plugin built with the Rhino C/C++ Software Development Kit (SDK). The plugin is a dynamic link library (DLL), which interacts with both the ICGT and Rhino at run-time (Fig. 3.1). It takes input parameters from ICGT, *e.g.* borehole radius, borehole length, number of boreholes, fracture tip locations and constructs the parametric borehole and fracture surfaces. The 3D model geometry data is stored in openNURBS format (.3dm).

CAD geometry is subsequently discretised using the ICEM CFD octree mesher (ANSYS 2020). Surfaces and volumes are represented by higher-order isoparametric quadratic triangles and tetrahedra, respectively (Figure 3.2c). During the simulation, fracture geometry is stored independently from the mesh (Paluszny & Zimmerman 2013*b*). After each iteration, a new optimised mesh is created at modest computational cost, using a fully parallel octree-based volumetric algorithm (Figure 3.2a– 3.2b).

The mesh is stored in unstructured grid format (.uns) used by Ansys. Figure 3.1 illustrates the interaction between the three pieces of software. The DLL plugin acts as a bridge between ICGT and Rhino7, allowing them to interact during runtime. After the CAD geometry is generated in Rhino7, it is passed to ICEM CFD for meshing. Once the mesh is generated, the geometry data is stored separately from the mesh, and ICGT uses it in the following simulation step. This process repeats until the simulation is completed.

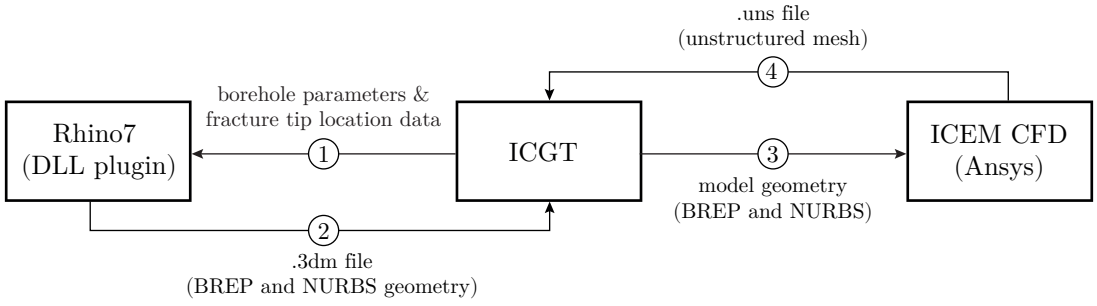
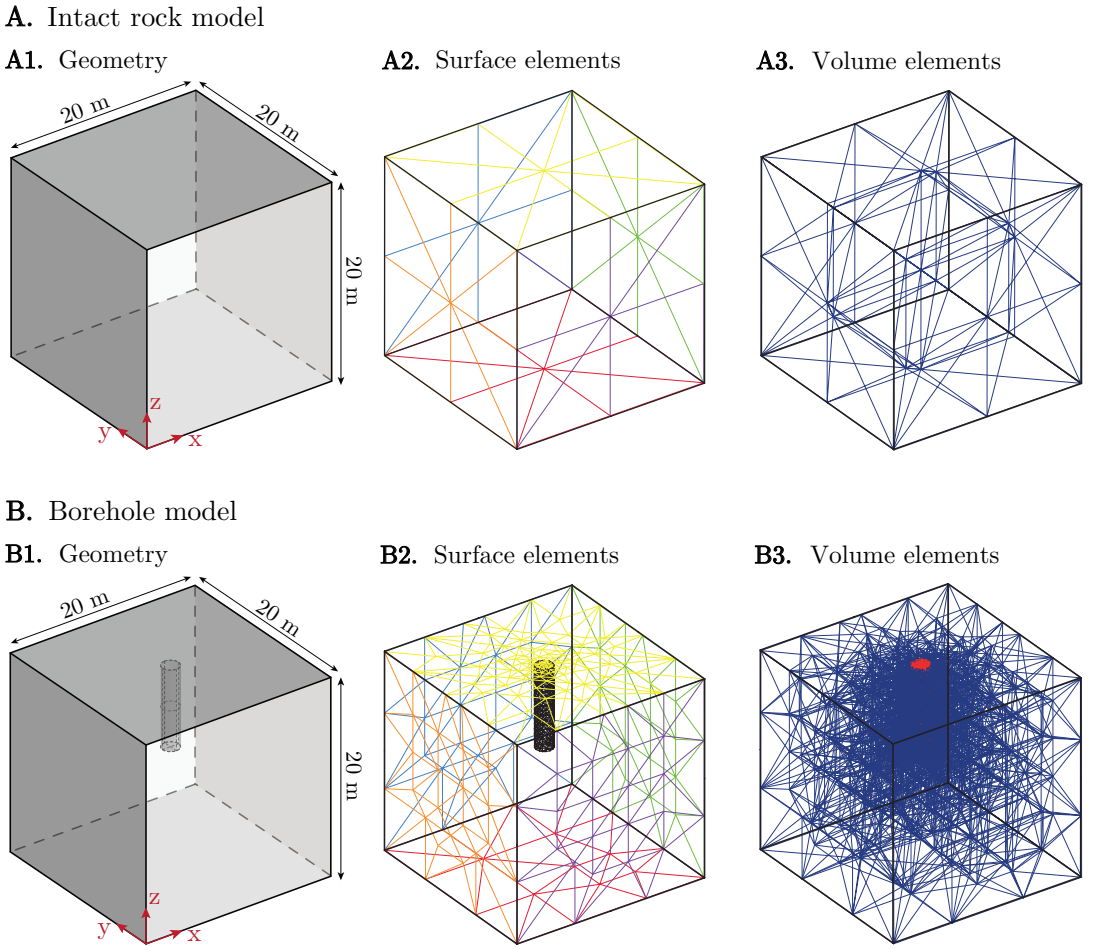
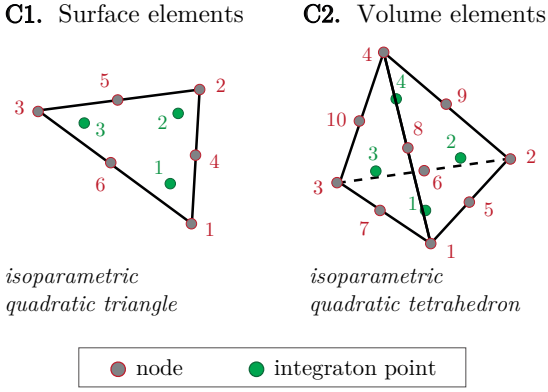


Figure 3.1: Schematic diagram showing the interaction between the ICGT, the geometry-handling software (Rhino7) and the mesher (ICEM CFD).





Mesh details

Elmt. group		No. of elmts. **A.**	**B.**
	Domain boundaries	48	452
	Excavation boundary	0	768
	Rock volume	96	11015
	Excavation volume	0	2718
Total no. of elements		144	14953
Total no. of nodes		189	18874

Figure 3.2: Example of unfractured model geometry created with Rhino3D and its corresponding mesh created with Ansys ICEM CFD, showing: **A.** the initial "intact rock" model before borehole excavation; **B.** the new model after the borehole surface is added; **C.** the finite element types used to represent the surface and volumetric meshes throughout this work. The rock domain and borehole elements have initial refinements of 5 m and 0.5 m, respectively.

3.3.1 Finite element method

The governing equations for mechanical or thermo-mechanical deformation are discretised in their weak form (Zienkiewicz et al. 2013), using the principle of virtual work, which states that, for any given infinitesimal virtual displacement $\delta\boldsymbol{u}$, a body remains in equilibrium if the work of internal forces equals the work of external surface tractions applied to its surface. Considering mechanical deformation, Equations 3.1, 3.2 and 3.3 can be rewritten as:

$$\int \{\delta\boldsymbol{\varepsilon}\}^T \{\boldsymbol{\sigma}\}\, dV = \int \{\delta\boldsymbol{u}\}^T \{\boldsymbol{F}\}\, dV + \int \{\delta\boldsymbol{u}\}^T \{\boldsymbol{\Phi}\}\, dS \tag{3.9}$$

where δ is a virtual differential, such that $\delta\boldsymbol{\varepsilon}$ is the vector of virtual strain components and $\delta\boldsymbol{u}$ is the vector of virtual displacements, $\{\boldsymbol{F}\}$ are the body forces and $\boldsymbol{\Phi}$ are the surface tractions.

For every element, displacement $\{\boldsymbol{u}\}$ is interpolated from the set of nodal displacements $\{\boldsymbol{d}\}$ as below:

$$\{\boldsymbol{u}\} = \boldsymbol{N}\{\boldsymbol{d}\} \tag{3.10}$$

where $\boldsymbol{N}$ is the vector of finite element shape functions, specific to the type of finite element used for discretisation, and $\boldsymbol{d}^T = \left\{u_x^1, u_y^1, u_z^1, \ldots, u_x^{\mathrm{n}}, u_y^{\mathrm{n}}, u_z^{\mathrm{n}}\right\}$.

The relationship between strain and displacement (Equation 3.2) can thus be rewritten in discretised form as:

$$\{\boldsymbol{\varepsilon}\} = \boldsymbol{\partial}\{\boldsymbol{u}\} = \boldsymbol{\partial N}\{\boldsymbol{d}\} = \boldsymbol{B}\{\boldsymbol{d}\} \tag{3.11}$$

where $\boldsymbol{B}$ is the vector containing the derivatives of the finite element shape functions. From Equation 3.11, one can rewrite the virtual displacements and strains in terms of the nodal displacements and the finite element interpolation matrices $\boldsymbol{N}^T$ and $\boldsymbol{B}^T$:

$$\{\delta\boldsymbol{u}\}^T = \{\partial\boldsymbol{d}\}^T \boldsymbol{N}^T \tag{3.12}$$

$$\{\delta\boldsymbol{\varepsilon}\}^T = \{\partial\boldsymbol{d}\}^T \boldsymbol{B}^T \tag{3.13}$$

Substituting Equations 3.1, 3.12 and 3.13 into the integral from Equation 3.9, the force equilibrium can be written as:

$$\begin{aligned} \int \boldsymbol{B}^T\boldsymbol{D}\boldsymbol{B}dV\,\{\boldsymbol{d}\} + \int \boldsymbol{B}^T\{\boldsymbol{\sigma_0}\}\, dV \\ - \int \boldsymbol{B}^T\boldsymbol{D}\{\boldsymbol{\varepsilon_0}\}\, dV \\ - \int \boldsymbol{B}^T\{\boldsymbol{F}\}\, dV \\ - \int \boldsymbol{B}^T\{\boldsymbol{\Phi}\}\, dS = 0 \end{aligned} \tag{3.14}$$

where $\boldsymbol{D}$ is the linear elastic stiffness matrix for an isotropic material in three dimensions:

$$\boldsymbol{D} = \frac{E(1-\nu)}{(1+\nu)(1-2\nu)} \begin{bmatrix} 1 & \frac{\nu}{1-\nu} & \frac{\nu}{1-\nu} & 0 & 0 & 0 \\ \frac{\nu}{1-\nu} & 1 & \frac{\nu}{1-\nu} & 0 & 0 & 0 \\ \frac{\nu}{1-\nu} & \frac{\nu}{1-\nu} & 1 & 0 & 0 & 0 \\ 0 & 0 & 0 & \frac{1-2\nu}{2(1-\nu)} & 0 & 0 \\ 0 & 0 & 0 & 0 & \frac{1-2\nu}{2(1-\nu)} & 0 \\ 0 & 0 & 0 & 0 & 0 & \frac{1-2\nu}{2(1-\nu)} \end{bmatrix} \tag{3.15}$$

where E is the elasticity modulus and ν is the Poisson's ratio. Equation 3.14 is defined for each element in the domain and it has the general form:

$$\boldsymbol{k}^{(e)} \{\boldsymbol{d}\} = \{\boldsymbol{rhs}\} \tag{3.16}$$

where $\boldsymbol{k}^{(e)} = \int \boldsymbol{B}^T \boldsymbol{D} \boldsymbol{B} dV$ represents the element stiffness matrix and $\{\boldsymbol{rhs}\}$ the right-hand side of the system.

To compute the displacement field across the whole domain, all individual element stiffness matrices $\boldsymbol{k}^{(e)}$ are assembled into a global stiffness matrix $\boldsymbol{K}$ of size depending on the number of nodes in the numerical domain and the number of dimensions of $\{\boldsymbol{u}\}$. The resulting system of equations is solved for the nodal displacements $\{\boldsymbol{d}\}$, using an algebraic multigrid solver (Stüben 2001). The governing equations in the case of the thermo-mechanically coupled problem are discretised in a similar manner. ICGT employs a monolithic approach to solve the coupled displacement and temperature fields simultaneously (Salimzadeh et al. 2018). This approach is generally more stable and it better handles coupling effects than do staggered algorithms (Danowski et al. 2013).

Displacements are computed at the nodes and then interpolated at the integration points where the material properties are defined. The interpolations are done in the finite element natural coordinate space, and computed values are mapped back to global space using Jacobian transformations (Zienkiewicz et al. 2013). Stresses and strains, which are defined at the integration points, are subsequently computed using Equations 3.11–3.13 and eventually extrapolated from the integration points to the nodes.

The stress field at each node is obtained by averaging the stresses from all the elements that have the node as a vertex, except for the elements that belong to the borehole wall. This smoothing technique enhances the continuity of the stress field across neighbouring elements. As shown in Figure 3.3, the nodal stress at the borehole wall matches well with the analytical solution (Equation 2.1a), as long as the averaging is done separately for the borehole and rock elements, *i.e.* no stress averaging is performed across material boundaries and interfaces. A more thorough validation of the borehole stresses is further presented in Chapter 4.

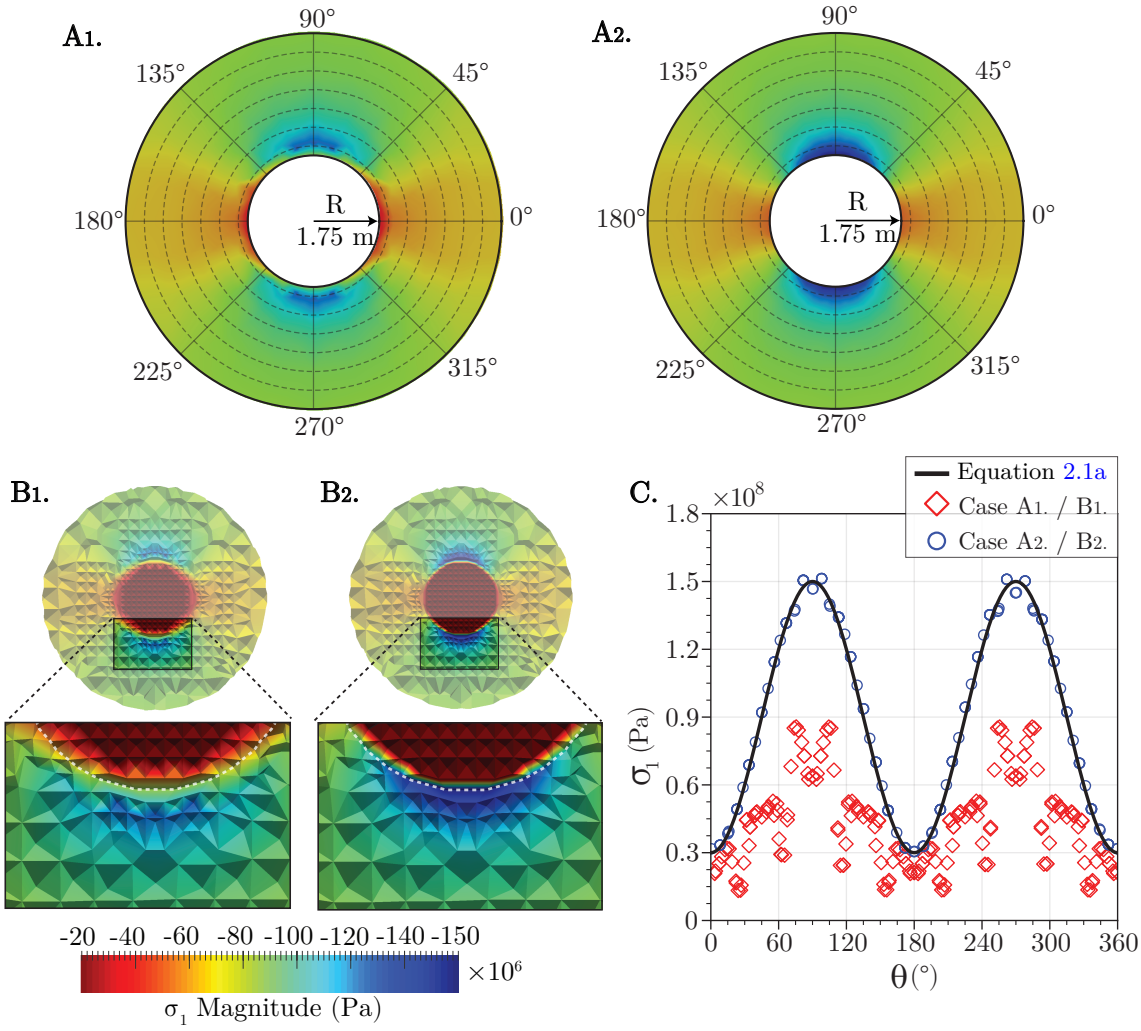


Figure 3.3: Maximum principal stress at the borehole wall, extrapolated from the integration points to the nodes (nodal stress). **A_1.** The stress value at a particular node is computed by averaging values from all parent elements contributing to that node. **A_2.** If the parent elements are part of the borehole wall, their contributions are averaged separately, material by material. **B_1.** Mesh corresponding to A_1, showing incorrect stress averaging across the borehole boundary. **B_2.** Mesh corresponding to A_2, showing correct sharp transition from highly stressed rock material to unstressed borehole material. **C.** Comparison of the two cases with the analytical solution (Equation 2.1a).

3.3.2 Remeshing and mapping of variables

The volumetric discretisation of the domain conforms to the evolving geometry and the mesh is regenerated at each growth step to follow the new internal geometry. After each remeshing step, the "new" mesh is void of any information from the previous step, and the internal variables involved in the current iteration need to be either reloaded, or mapped from the previous mesh. Material properties that are homogeneous throughout the computational domain and do not change as the simulation progresses, are reloaded onto the

new mesh, by assigning their uniform value everywhere in the new mesh. In contrast, heterogeneous properties and evolving variables such as displacement, temperature, or damage need to be mapped from the previous mesh before their new state is computed.

To preserve continuity, the mapped variable needs to be stored at the nodes before it is transferred to the new mesh. Therefore, properties which are stored at the integration points, such as material properties or the stress tensor, are first extrapolated to the nodes of the old mesh. Figure 3.4 illustrates the mapping of a heterogeneous Young's modulus distribution between two meshes of different densities. The nodal values are obtained as

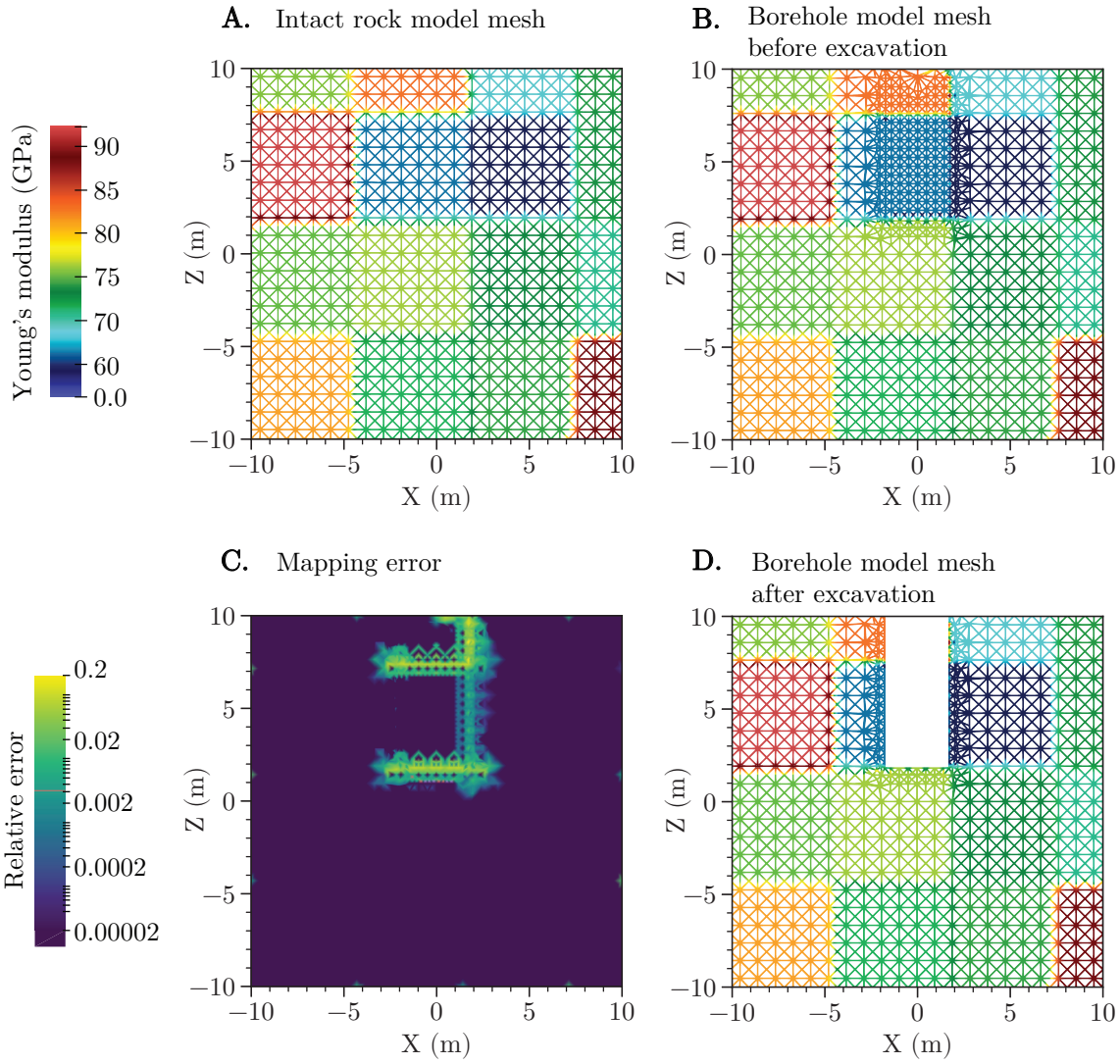


Figure 3.4: **A.** Cut plane through a 20×20×20 m computational domain, where the elastic modulus is randomly distributed in a checkerboard pattern. **B.** Young's modulus pattern from the intact rock model (Figure 3.4a) mapped onto a newly generated mesh, which contains a vertical borehole centered at $x = 0\ m$. The borehole material is not excavated yet, but the new mesh is locally refined around the borehole. **C.** Relative error introduced by the mapping algorithm. Note that the error scale is logarithmic for visualisation. **D.** Young's modulus pattern from the borehole model (Figure 3.4b) showing the borehole material excavated after mapping.

detailed in the previous section, by averaging the extrapolated values from all the parent elements.

The heterogeneity distribution is randomly generated at the beginning of the simulation on the initial mesh (Figure 3.4a), and mapped onto the borehole mesh in two steps: firstly, every node in the new mesh is searched among the elements of the old mesh, to find the element in the old mesh containing the new node. Next, the old nodal value of the Young's modulus is interpolated at the new node. As the mesh becomes more refined (Figure 3.4b), through the addition of the borehole (and later fracture surfaces), the search for new nodes in old elements and subsequent mapping from a coarser mesh to a finer mesh is generally unproblematic and accurate. The relative error between meshes A and B (Figure 3.4c) is low when values are mapped between similar-sized elements, away from the borehole wall. The error increases at the borehole wall, and is highest at the elements across which the Young's modulus changes abruptly (between the squares of the checkerboards).

3.3.3 Fracture geometry

Fractures are modelled as discontinuities within the volumetric rock domain. Their geometry consists of an ensemble of points (fracture tip nodes), curves (fracture tip loops) and surfaces (leader/follower), and it evolves as a function of deformation. Fracture surfaces in ICGT have been routinely represented through tessellated triangles.

Figure 3.5 illustrates fracture growth from an initial disk using geomechanically-computed propagation vectors, as described in Section 3.5. In this case, the fracture surface is constructed by connecting the old (prior to growth) and new (after growth) sets of fracture tips through triangles at every growth step. During the first growth step, the initial disk boundary becomes a set of polylines, connected at the fracture tips. At subsequent growth steps, the fracture surface is extended through triangulations.

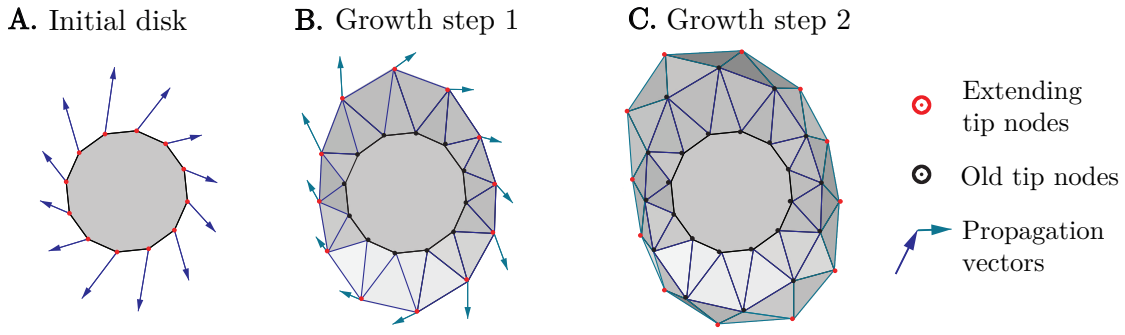


Figure 3.5: Schematic illustration showing the process of constructing a tessellated fracture surface through triangulation between successive growth steps.

The triangulation approach of constructing the fracture surface introduces additional geometrical complexity (Figure 3.6a) and cause a high density mesh (Figure 3.6c) to be generated around the fracture to conform with the convoluted fracture geometry. This is due to additional mesh nodes that are introduced for each triangle vertex. The convoluted fracture geometry, in turn, introduces mesh artifacts such as gaps, overlaps, or sharp angles, in particular when the extending fracture tip loop is in close proximity of another surface, such as the borehole boundary. Additionally, when multiple fracture tips propagate along the free borehole surface, the mesher does not always distinguish the fracture tip from the borehole surface. This results in misrepresentations of the actual geometries, which increase numerical instabilities, as the fracture mechanics parameters involved in growth (Section 3.5) cannot be accurately computed.

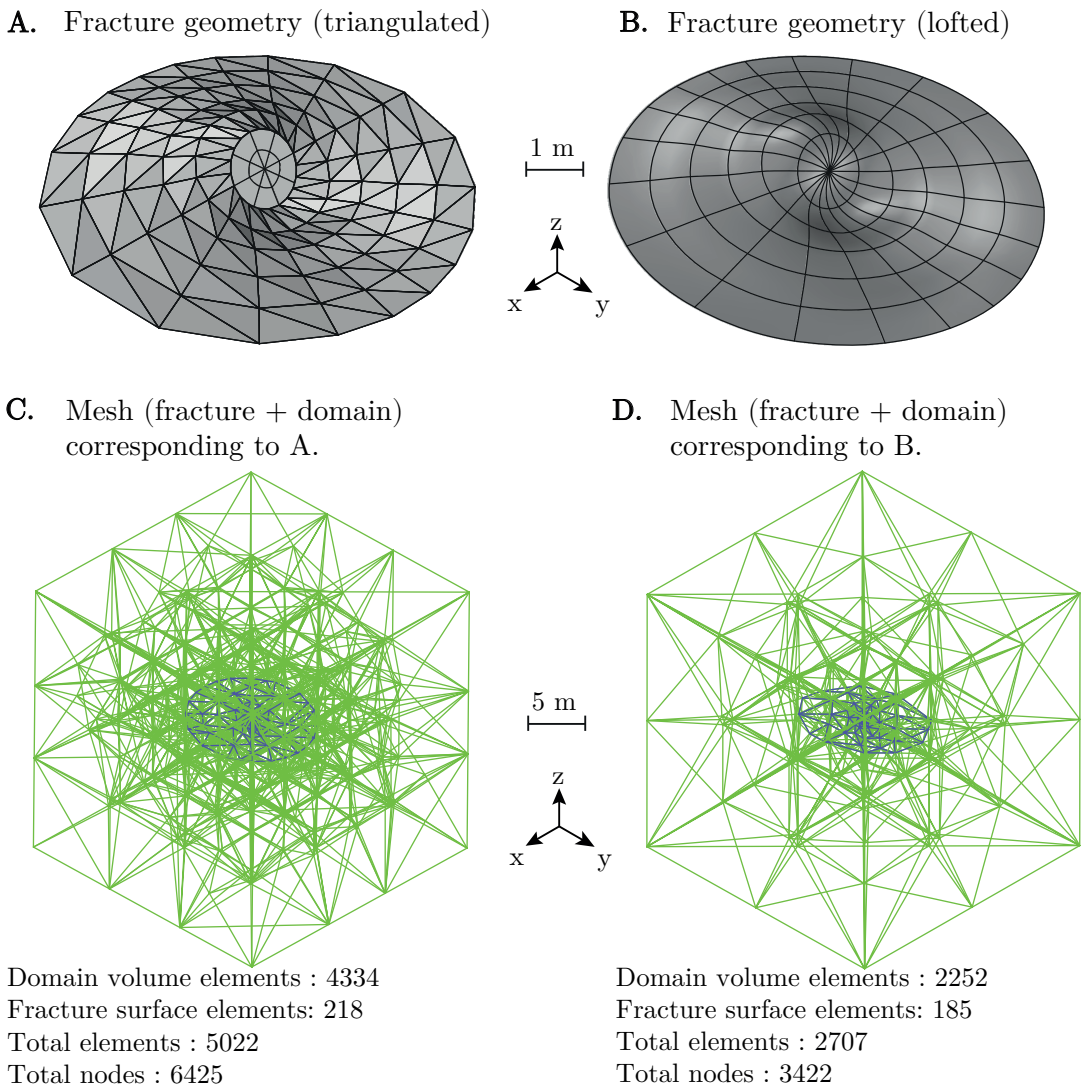


Figure 3.6: Fracture geometries (**A**, **B**) and corresponding mesh densities (**C**, **D**) after five growth steps, when the fracture surface is constructed through triangles (**A**) versus lofting (**B**). Triangular fracture surface elements are shown in blue, and tetrahedral volume elements are shown in green. In both cases, the fracture has 20 tip segments, *i.e.* 21 tip nodes.

3.3.4 Fracture surfaces as lofted NURBS

In this work, fractures are geometrically constructed as non-uniform rational basis splines (NURBS). NURBS have been increasingly used in representing fracture domains (Martha et al. 1993) and modelling their growth (Ghorashi et al. 2012, Dimitri et al. 2014, Yadav et al. 2020), because they can accurately describe a wide range of shapes: from simple 2D lines and curves, to more complex 3D free-form surfaces and volumes. Piegl & Tiller (1997) give a general overview of NURBS and Paluszny & Zimmerman (2013*b*) show the advantages of using NURBS in the context of fracture mechanics with explicit geometric representation of fracture shapes.

An improved approach in constructing the fracture surface is through lofting. Compared to the triangulation approach, lofting produces a smooth surface (Figure 3.6b), which is watertight and presents less geometric complexity. Meshing the lofted surface results in a coarser mesh that adapts to the smooth representation of the geometry, while maintaining fidelity to the fracture geometry and reducing the risk of mesh artifacts (Figure 3.6d). Similar to the triangulation approach, the fracture tip nodes are used in lofting to define the fracture front during growth. Instead of connecting them through a set of segments, they become the control points of the curves that will interpolate the fracture surface.

Figure 3.7 illustrates the process of constructing a fracture surface from an initial disk, by lofting a NURBS surface through the fracture tip loops. At each growth step, a smooth NURBS curve, representing the fracture tip loop, *i.e.* fracture front, is constructed through the newly extended fracture tip nodes.

A NURBS curve of degree p is a piece-wise polynomial curve, that can be represented in the parametric u space as:

$$\boldsymbol{C}_k^w(u) = \sum_{i=0}^{n} N_{i,p}(u)\boldsymbol{P}_{i,k}^w \tag{3.17}$$

where $\boldsymbol{P}_{i,k}^w = (w_{i,k}x_{i,k}, w_{i,k}y_{i,k}, w_{i,k}z_{i,k}, w_{i,k})$ are the weighted control points of the curve and $N_{i,p}$ are the basis functions of the curve. All the basis functions are defined over the same knot vector $U = \{\underbrace{a, ...a}_{\text{p+1}}, u_{p+1}, ...u_n, \underbrace{b, ..., b}_{\text{p+1}}\}$, where a and b are usually 0 and 1, respectively.

The successive NURBS curves representing the fracture front at consecutive growth steps become the section curves through which the fracture surface will be lofted. The lofting technique consists of mathematically blending the section curves together to form a smooth surface (Koch 2009). Similar to the definition of a NURBS curve, a NURBS surface of degree $p \times q$ in the $u - v$ parametric space is defined as:

$$\boldsymbol{S}^w(u, v) = \sum_{i=0}^{n}\sum_{j=0}^{m} N_{i,p}(u)N_{i,q}(v)\boldsymbol{P}_{i,j}^w \tag{3.18}$$

where $\boldsymbol{P}^w_{i,j} = (w_{i,j}x_{i,j}, w_{i,j}y_{i,j}, w_{i,j}z_{i,j}, w_{i,j})$ are the control points of the surface, and $N_{i,p}(u)$ and $N_{j,q}(v)$ are the basis functions of the surface. The NURBS surface can be thought of as the tensor product of two NURBS curves. The two sets of surface basis functions are defined over their corresponding knot vectors:

$$U = \{u_0, ..., u_r\}, i = 0, ..., r-1 \tag{3.19a}$$

$$V = \{v_0, ..., v_s\}, j = 0, ..., s-1 \tag{3.19b}$$

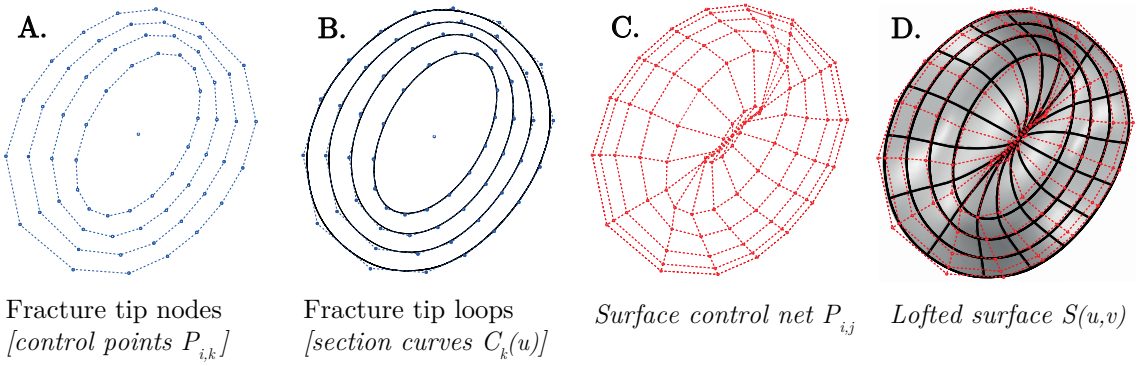


Figure 3.7: Schematic representation of the lofting process showing four growth steps in a single fracture: **A.** The four successive fracture fronts are constructed through 16 control points ($P_{i,k}$), which correspond to the tip nodes of fracture i at growth step k. **B.** The fracture tip loops are represented through NURBS curves ($C_k(u)$) in parametric space. **C.** The control net of the fracture surface ($P_{i,j}$) is obtained by interpolating in the direction of fracture growth between the fracture fronts at successive growth steps. **D.** The fracture surface ($S(u,v)$) is constructed through the control net in parametric space.

Algorithm 1: NURBS lofting algorithm from Piegl & Tiller (1996)

Input:
Fracture tip loops at every growth step as NURBS curves $\boldsymbol{C}^w_k(u)$
Degree q of the lofted surface in the direction of interpolation
Output:
Lofted surface $\boldsymbol{S}^w(u,v)$

$n \leftarrow$ highest index in control point arrays
$U \leftarrow$ knot vector of any $\boldsymbol{C}^w_k(u)$
compute $v_0, ..., v_k$ for curve interpolation
compute V by averaging v parameters
for *i=0 to n* **do**
  for *i=0 to k* **do**
    $\boldsymbol{Q}^w_j \leftarrow i^{th}$ control point of $\boldsymbol{C}^w_j$
  $\left\{\boldsymbol{P}^w_{i,j}\right\}_{j=0}^{k} \leftarrow$ interpolate $\left\{\boldsymbol{Q}^w_j\right\}_{j=0}^{k}$ with a degree q curve

The geometric process of lofting consists of performing curve interpolations across the control points of all the section curves, resulting in the control net of the surface (Algorithm 1).

The surface control points do not necessarily always lie on the physical location of those of the curves, but rather describe their domain through a series of recursive operations that translate a local reference space into a curve or surface that exists in physical space. The newly constructed surface is called a lofted surface, as it lofts or approximates the region between a pair of two curves, each described by a set of control points of equal size. These cross-sectional curves become isoparametric curves of the lofted surface as shown in Figure 3.7. The final surface shape will depend on the number, shape and positioning of the section curves, and will evolve as in the natural system by adding new surfaces to the existing surface object. Piegl & Tiller (1997) provide an in-depth description of NURBS geometries and relevant operations.

In the context of modelling fracture growth leading to spalling, NURBS representations of fractures are advantageous for several reasons: they capture details at many scales, since they are not limited by a specific resolution; they do not require large storage memory, which would be problematic if hundreds of fractures are generated; they are consistent with emerging isogeometric methods (Hughes et al. 2005, Proserpio et al. 2020, Lazzari et al. 2021, Xia et al. 2022). The gains from representing complex geometries using parametric surfaces, such as NURBS, are significant, allowing for substantially higher quality meshes to be generated in an efficient manner for their use in both mechanics and flow numerical simulations (Paluszny et al. 2007).

3.4 Fracture initiation around a circular borehole

Failure of an initially intact and brittle rock begins with inelastic degradation (damage), that occurs locally around microscopic defects at the pore- or grain-scale. Stress concentrations around these defects lead to the formation of a “process zone” or “damage zone”, where a local reduction in the rock strength occurs (Boukharouba et al. 2009). The size of this damage zone is influenced by the rock properties, heterogeneity distribution and the proximity of other pre-existing micro-cracks (Bazant & Kazemi 1990, Fakhimi & Tarokh 2013). Continuum damage mechanics (CDM) theory was first developed to capture brittle creep damage in metals (Kachanov 1999) and has since branched into a variety of damage phenomena including elastic-plastic damage, elastic-brittle damage, fatigue damage, etc. (Lemaitre 1984, Voyiadjis & Kattan 2008). In general, damage mechanics theory provides a framework to represent the damaged state of a material in terms of one or several damage variables. The damage variables influence the mechanical behavior of the damaged material, accounting for the micro-defects present within the material (Krajcinovic 2000).

Micro-cracking is conventionally modelled in CDM as the progressive degradation of the elastic stiffness. The evolution and propagation of the micro-defects eventually result in macroscopic failure, which is represented as a sudden localisation of damage (Chaboche

1988*a*,*b*). However, the progressive transition from diffuse damage to strain localisation caused by strain-softening cannot be accurately captured with continuum approaches, such as FEM, without extensive modifications. This is because in continuum implementations of classical damage theory, "fast" damage localisation, *i.e.* fracture growth, is highly sensitive to the spatial discretisation (Bažant 1986), and will tend to localise in the smaller sized elements, or even at the integration points, where the material properties are defined. This results in strong mesh bias and also wrongly implies that the fracturing process occurs without dissipation of energy, as the volume over which energy is dissipated at an integration point is zero (Bažant 1986, Krajcinovic & Mastilovic 1995).

Many numerical approaches have been proposed in order to make CDM theory thermodynamically consistent in its numerical implementations and regularise the damage evolution. The most commonly implemented are non-local models, such as smeared crack models (Bažant & Oh 1983, Jirásek 2011), in which the damage value at each integration point is replaced with a weighted average over an arbitrary spatial neighborhood around each integration point and gradient-enhanced models, which incorporate the effect of gradients of internal variables, such as the equivalent strain, into the constitutive equations governing material behaviour (Frémond & Nedjar 1996, Geers et al. 1998, Simone et al. 2003, Saroukhani et al. 2013). These implementations require either *a priori* knowledge of the width (or volume) over which energy will dissipate during fracture growth, or additional boundary conditions and modifications necessary to model damage evolution along material interfaces, leading to untypical formulations of the governing differential equations. Therefore, in this work, damage mechanics is used to model the initial diffuse damage that the host rock sustains in the proximity of an excavation and nucleate the initial fracture disks from which spalling initiates.

Once the locations of the critical disks have been determined, fractures are not modelled as strain localisation in the continuum, but as discrete entities, whose behaviour is governed by linear elastic fracture mechanics (Section 3.5.1). In this context, the term "fracture nucleation" refers to the micro-structural processes that lead to the formation of discrete macro-cracks. It is important to distinguish this concept from "nucleation" which occurs from an existing discrete crack tip.

3.4.1 Mazars damage model

Mazars's (1984) damage model was originally developed to describe strain softening of quasi-brittle materials, such as concrete, and it was shown to predict such behaviour accurately. The numerical implementation in ICGT is based on linear elasticity coupled with isotropic damage. The stress-strain equation is modified to account for the elastic stiffness degradation and softening behavior due to micro-defects using an isotropic scalar damage variable d, which is introduced to scale the stiffness matrix $\boldsymbol{D}$.

The stress-strain relationship (Equation 3.1) now becomes:

$$\boldsymbol{\sigma} = (1 - d)\boldsymbol{D}\boldsymbol{\varepsilon} \tag{3.20}$$

This model is implemented under two simplifying assumptions. The first assumption is that the stiffness is damaged proportionally in all directions (isotropy), and the second assumption is that the Poisson's ratio is not affected by damage.

The damage parameter d is found by calculating the equivalent strain, $\tilde{\boldsymbol{\varepsilon}}$, which is the Euclidean norm of the positive part of the strain tensor (Lemaitre 1984):

$$\tilde{\boldsymbol{\varepsilon}} = \|\langle\boldsymbol{\varepsilon}\rangle_+\|_2^2 \tag{3.21}$$

The positive part of the strain tensor $\boldsymbol{\varepsilon}$ is given by:

$$\langle\boldsymbol{\varepsilon}\rangle_+ = \sum_{i=1}^{3}\langle\varepsilon_i\rangle_+\boldsymbol{n_i}\otimes\boldsymbol{n_i} = \sqrt{\sum_{i=1}^{3}\left(\langle\varepsilon_i\rangle_+\right)^2} \tag{3.22}$$

where ε_i and $\boldsymbol{n_i}$ are the eigenvalues and eigenvectors of the strain tensor and $\langle\varepsilon_i\rangle_+$ is defined as

$$\langle\varepsilon_i\rangle_+ = \begin{cases} \varepsilon_i & \text{if } \varepsilon_i > 0 \\ 0 & \text{if } \varepsilon_i \leq 0 \end{cases} \tag{3.23}$$

The equivalent strain $\tilde{\boldsymbol{\varepsilon}}$ quantifies the amount of extension during the loading of the borehole and is used to decide if and where the spalling fractures may nucleate. The initial disks loci are found by comparing $\tilde{\boldsymbol{\varepsilon}}$ with a critical strain threshold, $\tilde{\varepsilon}_c$, which is the ratio of the rock tensile strength and the undamaged Young's modulus:

$$\tilde{\boldsymbol{\varepsilon}} \geq \tilde{\boldsymbol{\varepsilon}}_{\boldsymbol{c}} \tag{3.24}$$

For a general stress state, the damage variable d is calculated as a linear combination of damage under tension and under compression, to represent the differing behavior of the rock in the two damage modes:

$$d = \alpha_t d_t + \alpha_c d_c \tag{3.25}$$

where α_t and α_c are two dimensionless coefficients accounting for the contribution of tensile and compressive stress states to damage, respectively. These coefficients are evaluated as:

$$\alpha_t = \left(\sum_{i=1}^{3}\frac{\varepsilon_{ti}\langle\varepsilon_i\rangle}{\tilde{\varepsilon}^2}\right)^{\beta} \tag{3.26a}$$

$$\alpha_c = \left(\sum_{i=1}^{3}\frac{\varepsilon_{ci}\langle\varepsilon_i\rangle}{\tilde{\varepsilon}^2}\right)^{\beta} \tag{3.26b}$$

where ε_{ti} and ε_{ci} are the principal strains due to tensile and compressive stresses, respec-

tively, and the exponent β is a damping factor, here assumed to be equal to 1. α_t and α_c take values between 0 and 1, such that $\alpha_t = 1$ and $\alpha_c = 0$ under uniaxial tension, and conversely, $\alpha_t = 0$ and $\alpha_c = 1$ under uniaxial compression.

Both the tensile and compressive parts of the damage are computed from the same equivalent strain (Equation 3.21), using the following equations:

$$d_t = \begin{cases} 0 & \text{if } \tilde{\varepsilon} \leq \varepsilon_0 \\ 1 - \frac{(1-A_t)\varepsilon_0}{\tilde{\varepsilon}} - A_t e^{-B_t(\tilde{\varepsilon}-\varepsilon_0)} & \text{if } \tilde{\varepsilon} \geq \varepsilon_0 \end{cases} \tag{3.27}$$

$$d_c = \begin{cases} 0 & \text{if } \tilde{\varepsilon} \leq \varepsilon_0 \\ 1 - \frac{(1-A_c)\varepsilon_0}{\tilde{\varepsilon}} - A_c e^{-B_c(\tilde{\varepsilon}-\varepsilon_0)} & \text{if } \tilde{\varepsilon} \geq \varepsilon_0 \end{cases} \tag{3.28}$$

where ε_0 is the strain threshold and A_t, B_t, A_c, and B_c are material parameters that determine the post peak shapes of the uniaxial stress-strain curves in tension and compression, respectively. A_t and A_c affect the residual strength component of the curve, and B_t and B_c modulate the slope of the curve in the strain-softening region, as illustrated in Figure 3.8.

Based on the concept of strain equivalence (Lemaitre 1984), which relates the damage state to the elastic modulus change, the Young's modulus in the spalling simulations is subsequently degraded (Eq. 3.29):

$$\tilde{E} = E\ (1 - d) \tag{3.29}$$

where d is the damage variable from Equation 3.25, and $\tilde{E}$ is the damaged Young's modulus.

The damaged Young's modulus is stored numerically as an integration point variable, with one value computed per integration point of the finite element. This captures the variation of the material within the volumetric element, and ensures a continuous loss of rock strength across the element. Therefore, the variation of the material properties occurs at a finer level than the actual dimension of the mesh. For visualisation purposes, throughout this thesis, the Young's modulus is extrapolated to the element to simplify its graphical representation. To ensure the numerical stability of the simulations, the minimum value of Young's modulus is capped at a small non-zero value (for most simulations herein, 10 Pa), which effectively corresponds to a substantial reduction of the material stiffness, and indicates that the rock has completely lost its integrity.

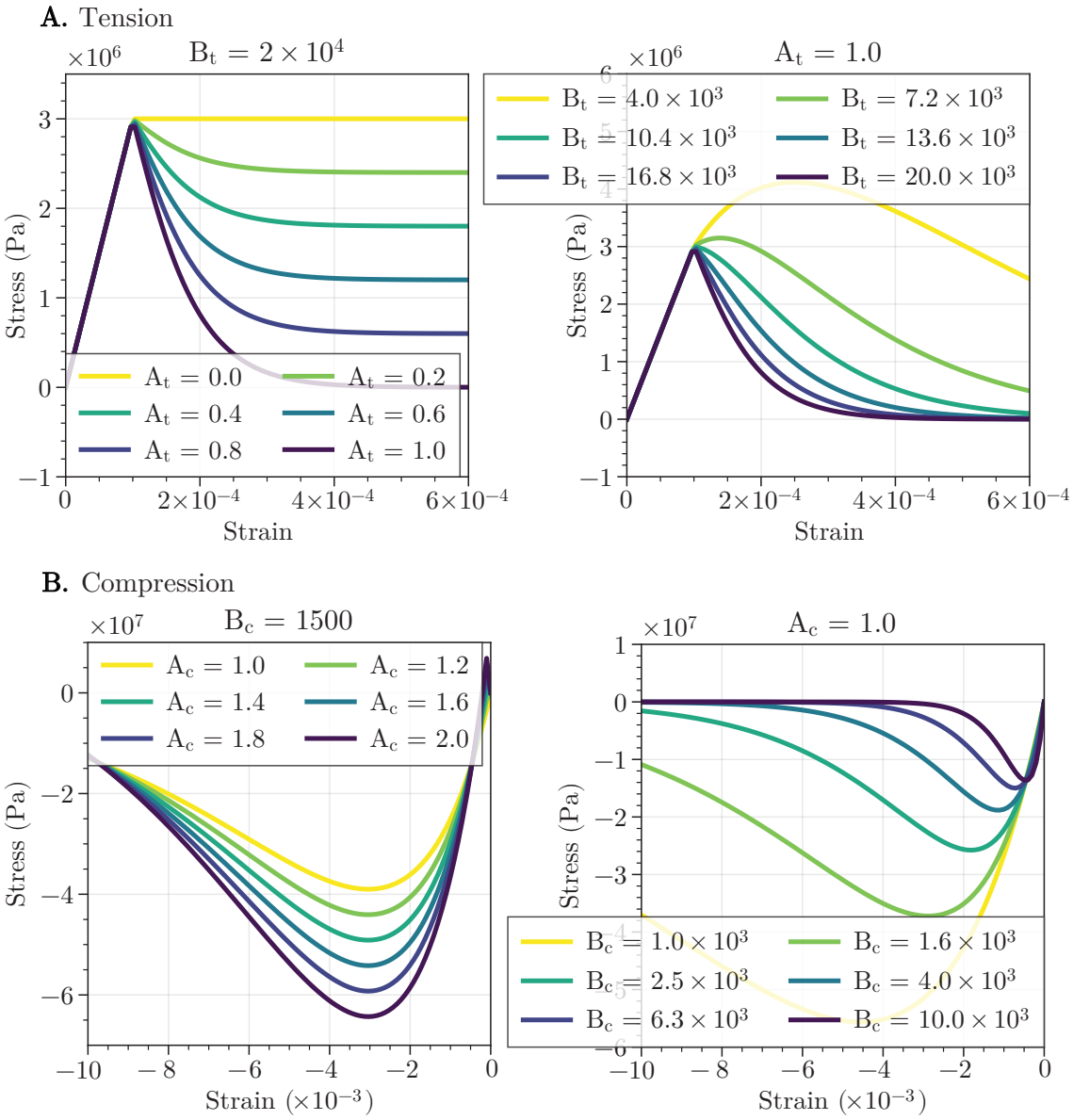


Figure 3.8: Effect of the A_t, B_t, A_c, and B_c parameters on the post-peak shapes of stress-strain curves under tension (**A**) and compression (**B**). The shapes are representative for concrete, with critical strain threshold $\varepsilon_0 = 1 \times 10^{-4}$, elastic modulus $E = 3 \times 10^{10}$ Pa and $\nu = 0.155$.

3.4.2 From continuum damage to discrete fractures

Numerical studies, in which discrete fracture networks are grown geomechanically using LEFM, often start with an arbitrary number of randomly distributed nuclei of constant size. The initial nuclei grow concurrently to form the eventual networks. Despite starting out from random flaws, the fracture network properties match those of the natural system, as the initial random disks interact and reorient during growth, conforming with the new state of the deformation in the numerical domain (Olson 1993, Renshaw & Pollard 1994*a*,

Renshaw 2000). A similar approach is used in this work, as discrete fractures comprising the spalled material develop from a set of critical flaws/disks around the borehole. However, their initial locations and orientations are not random. The disks nucleate in the regions or elements with the largest damage, where the rock stiffness has been most degraded due to the stress redistribution around the borehole after drilling, as described in the previous section. The simulation parameters involved in fracture initiation are: the total number of initial disks, the initial disk size and the initial disk spacing.

3.4.2.1 Total number of initial disks

The number of initial fracture disks is the maximum number of fractures that may nucleate during a simulation. A flaw may nucleate in any element where the damage criterion is satisfied. When the damage criterion is not satisfied, additional fractures will not nucleate, regardless of whether the maximum number of fractures provided as input has been reached or not. This approach does not aim to model the nucleation of every individual fracture that may occur at the borehole wall. A small number of initial disks is inserted in locations where the damage is the highest, and they subsequently extend to the locations where the growth criteria are met (Section 3.5.3).

3.4.2.2 Initial disk size and orientation

The initial flaw sizes are normally distributed and scaled with the amount of damage present at the nucleation location. The largest disk size, corresponding to the highest damage present in the rock, is given an arbitrary value small enough as to not influence the final fracture patterns. The following disk sizes decrease sequentially, taking as a maximum value the size of the element in which damage is computed. Thus, for a damaged element in which a fracture is being nucleated, the maximum diameter of the fracture will be given by the maximum length of the element in the plane defined by the fracture normal. Since the damage model is isotropic, the initial disk orientation is determined from the stress tensor. Specifically, initial disks nucleate normal to the direction of the minimum principal stress.

3.4.2.3 Initial disk spacing

The initial fracture disks are prevented from nucleating inside the borehole, by assigning a minimum spacing between the centre of the initial disk and the borehole wall, but there is no artificial restriction on growth, as the fractures are allowed to evolve following fracture mechanics principles (Section 3.5). Because nucleation occurs in a finite volume of rock in the proximity of the borehole, where the damage criterion is met, initial disk spacing

affects the number of fractures that can nucleate around the borehole. A larger spacing translates into fewer fractures. During growth, however, fracturing dynamics cancels out the effect of initial disk spacing, as fracture growth involves the creation of new fracture surfaces.

Several cases are presented in Chapter 4, where different values for each simulation parameter involved in fracture initiation are presented to illustrate their effect on the spalling patterns around a circular borehole.

3.5 Fracture growth leading to spalling

Continuum damage mechanics is appropriate to model fracture initiation, but once the neighbouring micro-defects start to coalescence into macro-cracks, numerical results are strongly dependent on the specific damage model implementation and its calibration. Linear Elastic Fracture Mechanics (LEFM) is a well-established theory, suited for modeling the growth and interaction of fractures in brittle rock, assuming that the fracture process is linear elastic (Anderson 2017).

Fracture mechanics models derived from Griffith's (1921) theory rely on prerequisite defects embedded at known locations in the domain, from which fracture growth initiates. Fractures nucleation is thus handled by the damage mechanics model, but unlike the dynamic damage studies that simulate fracturing behaviour through damage, this work employs damage only for the initial disk nucleation phase and once the locations of the initial disks are determined, fracture mechanics replaces the continuum damage model and growth is considered a quasi-static process, occurring in short ruptures.

3.5.1 Linear elastic fracture mechanics

LEFM theory is based on the pioneering works of Griffith (1921) and Irwin (1956), who developed criteria for fracture growth based on the energy balance at the crack tip. Griffith (1921) showed that fracture growth, under conditions of fixed external stresses, is an energy-consuming process, and Irwin (1956) defined the energy release rate $\mathcal{G}$ as the change in potential energy due to the growing fracture surface:

$$\mathcal{G} = -\frac{d(U - F)}{dA} \tag{3.30}$$

where U is the strain energy stored in the system, F is the work done by external forces, and A is the fracture area. Irwin (1957) also showed that stresses occurring near a fracture tip can be quantified in terms of a parameter related to the energy release rate, known as stress intensity factor (SIF).

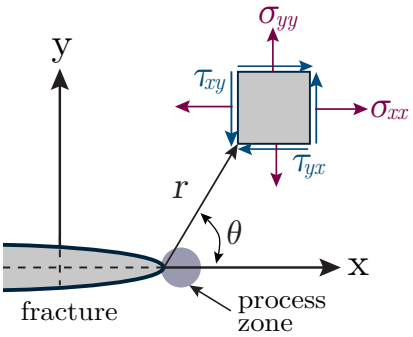


Figure 3.9: Stresses close to a fracture tip in an elastic material [adapted from Anderson (2017)].

Figure 3.9 shows the two-dimensional stress components acting on a square element located at a distance r ahead of a fracture tip, and their expressions are given in Equations 3.31–3.33.

$$\sigma_{xx} = \frac{K}{\sqrt{2\pi r}} \cos\left(\frac{\theta}{2}\right) \left[1 - \sin\left(\frac{\theta}{2}\right) \sin\left(\frac{3\theta}{2}\right)\right] \tag{3.31}$$

$$\sigma_{yy} = \frac{K}{\sqrt{2\pi r}} \cos\left(\frac{\theta}{2}\right) \left[1 + \sin\left(\frac{\theta}{2}\right) \sin\left(\frac{3\theta}{2}\right)\right] \tag{3.32}$$

$$\tau_{xy} = \frac{K}{\sqrt{2\pi r}} \cos\left(\frac{\theta}{2}\right) \sin\left(\frac{\theta}{2}\right) \cos\left(\frac{3\theta}{2}\right) \tag{3.33}$$

The stress in the proximity of the fracture tip is proportional to the stress intensity factor K and approaches infinity as $r \to 0$ if the material is assumed to be perfectly linear-elastic. In reality, the deformation of the process zone nearby the fracture tip is plastic and the stress is finite. To account for the plastic behaviour at the fracture tip, Rice (1968) introduced the $\mathcal{J}$ integral, which calculates the non-linear energy release rate as a line integral, evaluated along an arbitrary curve around the fracture tip:

$$\mathcal{J} = \int_{\Gamma} \left(w dy - T_i \frac{\partial u_i}{\partial x} ds \right) \tag{3.34}$$

where w is the strain energy density, defined as $w = \int_0^{\varepsilon_{ij}} \sigma_{ij} d\varepsilon_{ij}$, T_i are the components of the traction vector acting on the fracture, u_i are the components of the displacement vector, and ds is the length increment along the arbitrary contour around the fracture tip Γ (Anderson 2017).

Analytical solutions for the stress intensity factors have been proposed by many researchers, but these are subject to specific boundary conditions and fracture orientations. In this work, the SIFs are computed numerically by computing $\mathcal{J}$ along the fracture tips.

3.5.2 Fracture tip stress intensity factors

After the damage model determines the locations and orientations of the initial disks, the simulation computes three stress intensity factors (SIFs) K_I, K_{II}, and K_{III} at the fracture tips. The SIFs correspond to the three principal deformation modes of a fracture (Figure 3.10). They characterise the amplitude of the stress singularity at the fracture tip, and are conventionally used in fracture mechanics propagation criteria to determine fracture growth (Anderson 2017). SIFs are related to the strain energy release rate $\mathcal{G}$ at the advancing fracture front through:

$$\mathcal{G} = \frac{K_I^2 + K_{II}^2}{\tilde{E}} + \frac{K_{III}^2}{2\mu} \tag{3.35}$$

where $\tilde{E}$ is the elastic modulus and μ is the shear modulus of the rock. $\tilde{E} = E$ for plane stress conditions, and $\tilde{E} = E/(1-\nu^2)$ for plane strain, axisymmetry, or three dimensions, where ν is the Poisson's ratio.

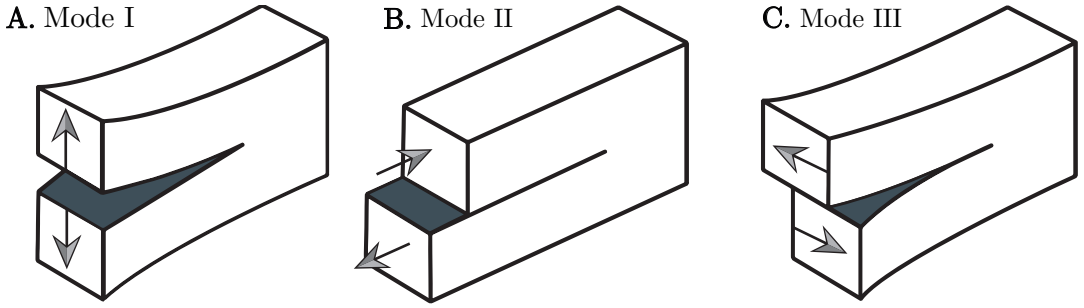


Figure 3.10: The three main loading modes of a fracture surface. Any arbitrary loading of a fracture can be decomposed into: mode I, corresponding to fracture opening in tension and modes II (sliding) and III (tearing) corresponding to in- and out-of-plane shear respectively [modified from Anderson (2017)].

In this work, numerical experiments are performed on brittle crustal rocks, where the size of the process zone is small compared with the size of the fracture, and hence the non-linear elastic $\mathcal{J}$ can be considered analogous to the linear elastic $\mathcal{G}$. SIFs are numerically evaluated by integrating energy in each growth mode independently, using Nejati et al.'s (2015*a*) virtual integration disk method. The method computes $\mathcal{G}$ based on a variant of Rice's (1968) $\mathcal{J}$-integral (Walters et al. 2005, Bremberg & Faleskog 2015), which is evaluated over a two-dimensional virtual disk domain sampling the region around the fracture tip (Figure 3.11). The values of K_I, K_{II}, and K_{III} are extracted assuming plane strain conditions close to the fracture tip (Nakamura & Parks 1989, Nejati et al. 2015*a*).

The main advantage of Nejati et al.'s (2015*a*) method is that it can be directly applied on unstructured tetrahedral meshes used in this work. The method computes SIFs accurately and efficiently even on coarse meshes. Similar energy-based methods, such as virtual

crack extension (Davis et al. 2014) and virtual crack closure (Okada et al. 2008), require refined structured meshes. Significantly slower, these alternate methods are unsuitable for modelling the simultaneous growth of multiple interacting fractures.

If a fracture grows too close to another fracture, or to a free surface, and the virtual disk domain around the fracture tip cannot be computed, SIFs are calculated directly from the FEM solution of the displacement field using the displacement correlation method (Henshell & Shaw 1975, Shih et al. 1976, Nejati et al. 2015*b*). Displacement accuracy around the fracture tips is increased with the quarter point technique (Nejati et al. 2015*b*).

3.5.3 Growth criteria

The energy-based growth criteria implemented in ICGT, using stress intensity factors, allow the numerical models to capture deformation at every tip along the fracture front. The fractures can thus grow in different directions and magnitudes in response to the local stresses. Figure 3.11 shows an initial flaw surface - at each fracture tip node, propagation vectors dictate how the fracture will extend after three iterations. The propagation vectors are determined as described below.

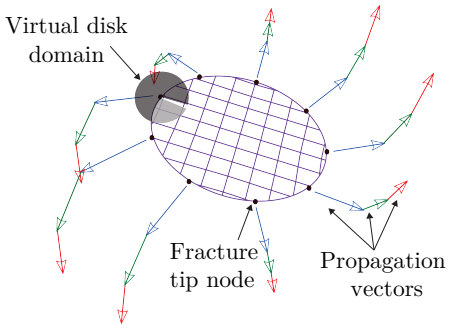


Figure 3.11: Schematic representation of an elliptic crack surface with nine fracture tips on its edge. The three sets of propagation vectors represent three progressive growth steps.

3.5.3.1 Propagation criterion

Computed SIFs are incorporated into a 3D mixed-mode criterion (Eq. 3.36) proposed by Richard et al. (2005). This criterion evaluates the projected stress intensity factor (K_v) onto the local coordinate system of the fracture. This criterion enables fracture growth when K_v exceeds the material toughness:

$$K_v = \frac{K_I}{2} + \frac{1}{2}\sqrt{K_I^2 + 4(\alpha_1 K_{II})^2 + 4(\alpha_2 K_{III})^2} \geq K_{IC} \tag{3.36}$$

where K_{IC} is the critical stress intensity factor for Mode I fractures, or material toughness, and α_1 and α_2 represent the material toughness ratios of Mode I to Mode II (1/1.3268) and Mode I to Mode III respectively (1/0.6297). These values have been experimentally determined by Chang et al. (2002) and Aliha et al. (2015) for brittle rocks, by testing specimen failure under pure mode II and mode III conditions, respectively.

When a discrete fracture tip node is subjected to a critical stress state for propagation ($K_v \geq K_{IC}$), a new location of the tip node is computed as per Sec. 3.5.3.2- 3.5.3.3. The new fracture front is then geometrically represented through a NURBS curve that is constructed through the new coordinates of the tip nodes, and the new fracture surface is then constructed through lofting all the historical fracture fronts up to and including the one just constructed during the current growth step.

If for a given static load fracture propagation ceases immediately after the introduction of the new tip loop and the lofting step, it is considered "stable fracture propagation", *i.e.* the fracture has grown one step under the static load and will not grow more unless the load is changed. During "unstable fracture propagation", the fracture will extend without an additional applied load after the critical level of stress for fracture propagation has been reached. If the fracture propagation ceases after current lofting step, the growth process is considered to be "stable". The majority of cases shown in this thesis are representative of the so called "unstable fracture propagation", where the fracture extends without any additional loads applied after the critical level of stress for fracture propagation has been reached.

3.5.3.2 Length criterion

Paris & Erdogan (1963) first extended the use of SIFs to quantify the rate at which a fracture advances during cyclical loading. Different forms of the "Paris law" have since then been employed to describe the growth rate of fractures. Renshaw & Pollard (1994*b*) showed that realistic spatial configurations of fracture arrays can be numerically reproduced in 2D, provided that the fracture fronts extend at different speeds. The general Paris criterion assigns fracture tip extension lengths that are proportional to the energy release rate $\mathcal{G}$ at individual tip nodes, *i.e.*, the fastest growing node is the node at which $\mathcal{G}$ is highest and vice versa (Pugno et al. 2006).

To capture the correct fracture tip propagation dynamics in 3D, the present method uses Thomas et al.'s (2020) implementation of a two-step Paris-type length criterion. This approach was shown to capture concurrent growth of multiple fractures at various growth rates both in tension and compression, by ensuring that growth is not numerically predisposed to occur only at the highest stressed tips. Thomas et al. (2020) achieved multiple fracture activation throughout the numerical domain and grew realistic discrete

fracture networks.

Given a set of fractures $\mathcal{F} = \{f_1, f_2, ...f_n\}$ that grow simultaneously in the same volume of rock, *e.g.*, the fracture array that forms the "spalled" zone in the proximity of an underground excavation, the maximum extension length Δl_f for each fracture is calculated:

$$\Delta l_f = \Delta l_v \left(\frac{\mathcal{G}_f}{\mathcal{G}_v} \right)^{\beta_f} \tag{3.37}$$

where $\mathcal{G}_f$ is the fracture energy release rate, corresponding to the largest value of $\mathcal{G}_n$ on fracture f; $\mathcal{G}_n$ is fracture tip energy release rate, calculated at each fracture tip node; $\mathcal{G}_v$ is the largest value of $\mathcal{G}_f$ in the whole fracture array; Δl_v is maximum extension length per growth step from all fractures in the domain and Δl_f is maximum individual fracture extension. Additionally, a second extension length is calculated per fracture tip n:

$$\Delta l_n = \Delta l_f \left(\frac{\mathcal{G}_n}{\mathcal{G}_f} \right)^{\beta_n} \tag{3.38}$$

where Δl_n is the extension of a local tip and $\mathcal{G}_n$ is the energy release rate at tip n. β_f and β_n correspond to fracture and tip growth rate exponents respectively.

Different β_f and β_n values influence how individual tips and interacting fractures grow with respect to one another. Δl_v, Δl_f andΔl_n are the maximum fracture extension lengths per growth step for the whole fracture array within the fractured volume, for each fracture within the fracture array, and for each tip node respectively. They control the extension lengths by: 1) setting an upper limit of growth amount in each step through Δl_v; 2) scaling the maximum extension of each fracture based on the ratio between the maximum energy release rate on the fracture $\mathcal{G}_f$ and in the volume $\mathcal{G}_v$, using β_f (Eq. 3.37); 3) scaling the local tip extension based on the ratio between the energy release rate at each tip node $\mathcal{G}_n$ and the energy release rate on the fracture $\mathcal{G}_f$, using β_n (Eq. 3.38).

This modified two-step Paris-type extension criterion was implemented by Thomas et al. (2020) in ICGT to improve concurrent fracture propagation in numerical domains containing multiple three-dimensional fractures. The modified criterion is based on the Paris law and introduces two values of the fracture growth rate exponent, β_f and β_n, which control the extent of growth for each fracture (Δl_f) and each tip node (Δl_n) respectively.

The main reason behind this implementation is to account for the variation in energy release rate among different fractures and different tip nodes and ensure that growth can be distributed across multiple fractures, while still weighted towards tips with higher energy release rate. Several β_f and β_n values are further analysed in Chapter 4 to assess the influence of the growth exponents on the spalled zones geometry in both radial and axial directions.

3.5.3.3 Angle criterion

Early criteria developed to predict the angle at which fracture tips extend, *e.g.*, the maximum tangential stress criterion (Erdogan & Sih 1963), the maximum principal stress criterion (Hussain et al. 1973), and the maximum energy release rate criterion (Maiti & Smith 1983), only consider the superposition of Mode I and Mode II (plane mixed mode) loading. To capture the fracture propagation path in three dimensions, this work uses Richard et al.'s (2005) angle criterion, which employs all three SIFs as follows:

$$\phi = \pm \left[A \frac{K_{II}}{K_I + K_{II} + K_{III}} + B \left(\frac{K_{II}}{K_I + K_{II} + K_{III}} \right)^2 \right] \tag{3.39}$$

where $A = 140°$ and $B = -70°$. The angle criterion has been validated by Richard et al. (2014), who compared the numerical predictions with experimental data for a number of materials and boundary conditions, and concluded that they can be applied to predict fracture growth accurately.

3.5.4 Fracture surface contact

Fractures are represented in ICGT by a set of edge curves, which contains all fracture tips, and two three-dimensional surfaces joined at the fracture edges. Fractures can either be open, with a varying aperture distribution, partially closed, or fully closed. The contact between the two fracture surfaces is computed using a gap-based Augmented Lagrangian method, with an iterative Uzawa algorithm (Nejati et al. 2016). This method resolves the frictional forces between the fracture leader and follower nodes, capturing both stick and slip regimes across the fracture surface (Nejati et al. 2016).

The contact algorithm in ICGT utilises three internal, and three external Uzawa iterations, a total of nine iterations per cycle to resolve the effect of the friction on the stress state, resulting in an aperture distribution across the surface of each fracture. In the simulations presented in this thesis, modelling of contact between fractures walls assumes a friction coefficient $\mu = 0.45$, which is representative of strong and brittle rocks, such as granites. The friction coefficient was estimated by SKB from tilt tests at Forsmark (SKB R-07-31 2007), designed for fracture parameter determination according to Barton & Bandis (1990).

3.5.5 Fracture-borehole interaction and fracture arrest

Intersections between fractures and the free borehole surface are handled using 3D Boolean operations. Fractures are prevented from growing into the borehole by assigning a high fracture toughness K_{IC} to the borehole material, which prohibits tip growth inside the

borehole. If a fracture tip located outside the borehole is predicted to extend inside the borehole at the current simulation step, it will proceed in doing so, and deactivate once it resides inside the borehole.

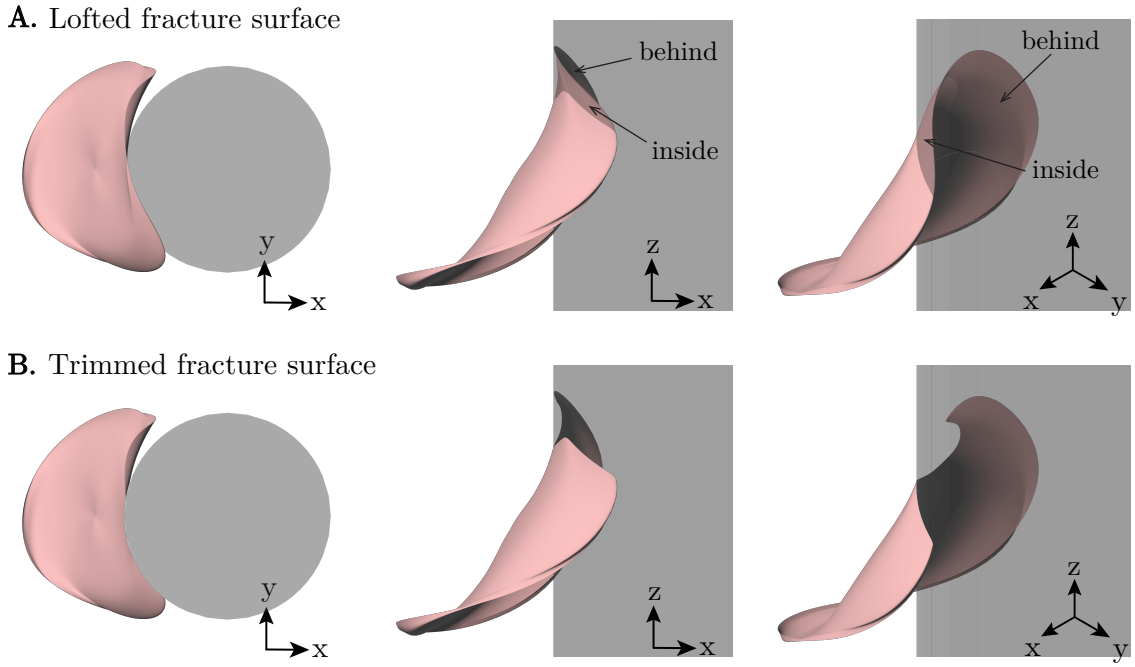


Figure 3.12: **A.** Example of a fracture surface growing inside the borehole. The borehole wall is transparent, allowing visualisation of the fracture surface both inside and behind the borehole. Fracture tips are deactivated if they grow inside the borehole, but their locations are used to construct the fracture surface through lofting. **B.** The lofted surface is split at the intersection with the borehole wall and the fracture fragments located inside the borehole are discarded. In subsequent steps, only the tips that are located outside of the borehole wall may extend.

Inactive tips are carried forward to future simulation steps, as part of the fracture tip loop, and they are used alongside the actively extending tips to construct the fracture surface in the next steps, as shown in Figure 3.12. The fracture extends as predicted by the propagation vectors, and if its lofted surface intersects the borehole wall, it is subsequently trimmed. This approach prevents artificially "snapping" the fracture tip to the borehole wall, so that the fracture-borehole intersection is dictated entirely by the geomechanically-computed growth vectors, and not by geometry-handling operations.

3.5.6 Simulation parameters involved in fracture growth

3.5.6.1 Fracture propagation exponents

Different β_f and β_n values influence how individual tips and interacting fractures grow with respect to one another. When a single fracture is considered (Lazarus 2003), an exponent smaller than 1 is used to model fatigue growth, whereas values much greater

than 1 are used for brittle fracture. Similarly, studies of multiple interacting fractures (Renshaw & Pollard 1994*a*, Lei et al. 2017, Thomas et al. 2017) showed that high values of the propagation exponents result in smaller growth increments in each growth step and more rapid localisation of fracture patterns.

3.5.6.2 Maximum extension length

The maximum extension length, Δl_v, is a simulation parameter used to scale the computed fracture extension per growth step. In this work, Δl_v values smaller than one borehole radius are used, to capture multiple growth increments before the fracture surfaces reach the borehole wall. Increasing Δl_v accelerates the time it would take a fracture array to reach a stable configuration. Several cases are analysed in Chapter 4 to assess the influence of the growth exponents and maximum extension length on the spalled zones geometry in both radial and axial directions around a single circular borehole, contributing to fracture pattern validation in the spalling context.

3.6 Summary

The fracture nucleation and growth processes described in this chapter are in line with the stages of spalling observed in experimental studies on cm-scale granite cores (Haimson 2007), as well as in field-scale excavations (Read 2004). These are: growth of tensile micro-cracks, modelled at the sub-element level as damage; coalescence of these micro-cracks into clusters, oriented subparallel to σ_1, modelled as the nucleation of the initial disks; growth of the initial disks under mixed-mode conditions until their intersection with the free borehole surface. Violent spalling, or rock bursting (Diederichs et al. 2004) caused by the buckling of the spalled rock is not explicitly modelled, but it can be inferred by examining the degradation of the elastic modulus at every growth step.

The numerical workflow is summarised in Algorithm 2, which describes fracture initiation and quasi-static growth under critical stress conditions. A boolean flag, FractureExtended, is set initially to False, to track fracture extension during processing. The fracture growth loop iteratively processes each fracture and its tip nodes. SIFs are computed for each tip node, and the critical value K_v is derived. If K_v exceeds the threshold K_{IC}, it signifies fracture extension at the respective tip node. Subsequently, the extension length, growth angle, and new tip location are computed. If at least one tip has extended during the current growth step, the FractureExtended flag is set to True. After processing all tip nodes for a fracture, a NURBS curve represents the new fracture front, and the fracture surface is constructed by lofting all historical fracture fronts. The process repeats for each fracture in the numerical domain, until no fracture extends (FractureExtended remains False)

and the algorithm terminates. The methodology presented in this chapter is validated against known analytical solutions for borehole stress, damage, and temperature in the next chapter.

Algorithm 2: Summary of numerical workflow

```
Define initial model geometry
Discretise initial geometry
Assign rock physical properties
Apply initial and/or boundary conditions
Compute displacement field
Compute geostatic strains and stresses
if with tunnel then
    Drill deposition tunnel
    Remesh
    Map variables from old mesh
    Compute deformation
Drill borehole(s)
Remesh
Map variables from old mesh
Compute deformation
if with nucleation then
    Compute damage
    Update elastic modulus and critical toughness
    while number of fractures < max number of fractures do
        Loop through elements in descending damage order
        Nucleate initial fracture disk
FractureExtended ← False
while True do
    for each fracture do
        for each fracture tip node do
            Compute SIFs K_I, K_II, K_III
            Calculate K_v
            if K_v > K_IC then
                Compute extension length
                Compute growth angle
                Determine new tip location
                FractureExtended ← True
        Loft fracture surface
    if FractureExtended = False then
        break
```

Chapter 4

Validations and Parameter Calibration

4.1 Introduction

This chapter contains validations of the FEM-computed field variables, SIFs and fracture growth patterns. The main objective of this chapter is to demonstrate the effectiveness of the modelling approach described in Chapter 3 in capturing fracture initiation and propagation mechanisms associated with spalling. Method-specific parameters that influence fracture nucleation and growth, *e.g.* number of initial fracture disks, their initial sizes and spacing, maximum extension length per growth step, and growth rate exponents are tested with different values to assess their influence on the final spalled zone metrics and ensure that the generated fracture patterns are in good agreement with field observations.

4.2 FEM validations

4.2.1 Borehole mechanical stresses

The accurate determination of the stress field in a medium containing multiple boreholes is of interest in the field of nuclear waste disposal as it constitutes a first step in understanding the mechanical behaviour of the repository host rock around the excavations. Particularly in this work, it is important to ascertain that the stress interactions between an arbitrary number of colinear boreholes and for any borehole spacing are correctly computed, before proceeding to simulate fracture nucleation and growth.

4.2.1.1 Single borehole

The stress field around a circular borehole subjected to far-field stresses σ_H, σ_h, and σ_v can be described using the concept of principal stresses. For a vertically-drilled borehole, the far-field horizontal stresses (σ_H and σ_h) apply perpendicular force on the borehole wall, resulting in the creation of tangential stress ($\sigma_{\theta\theta}$). The magnitude of the tangential stress varies around the borehole based on the angle of measurement, with the maximum value of $3\sigma_H - \sigma_h$ occurring at 90° and 270° *w.r.t.* σ_H, and the minimum value of $3\sigma_h - \sigma_H$ occurring at 0° and 180° *w.r.t.* σ_H.

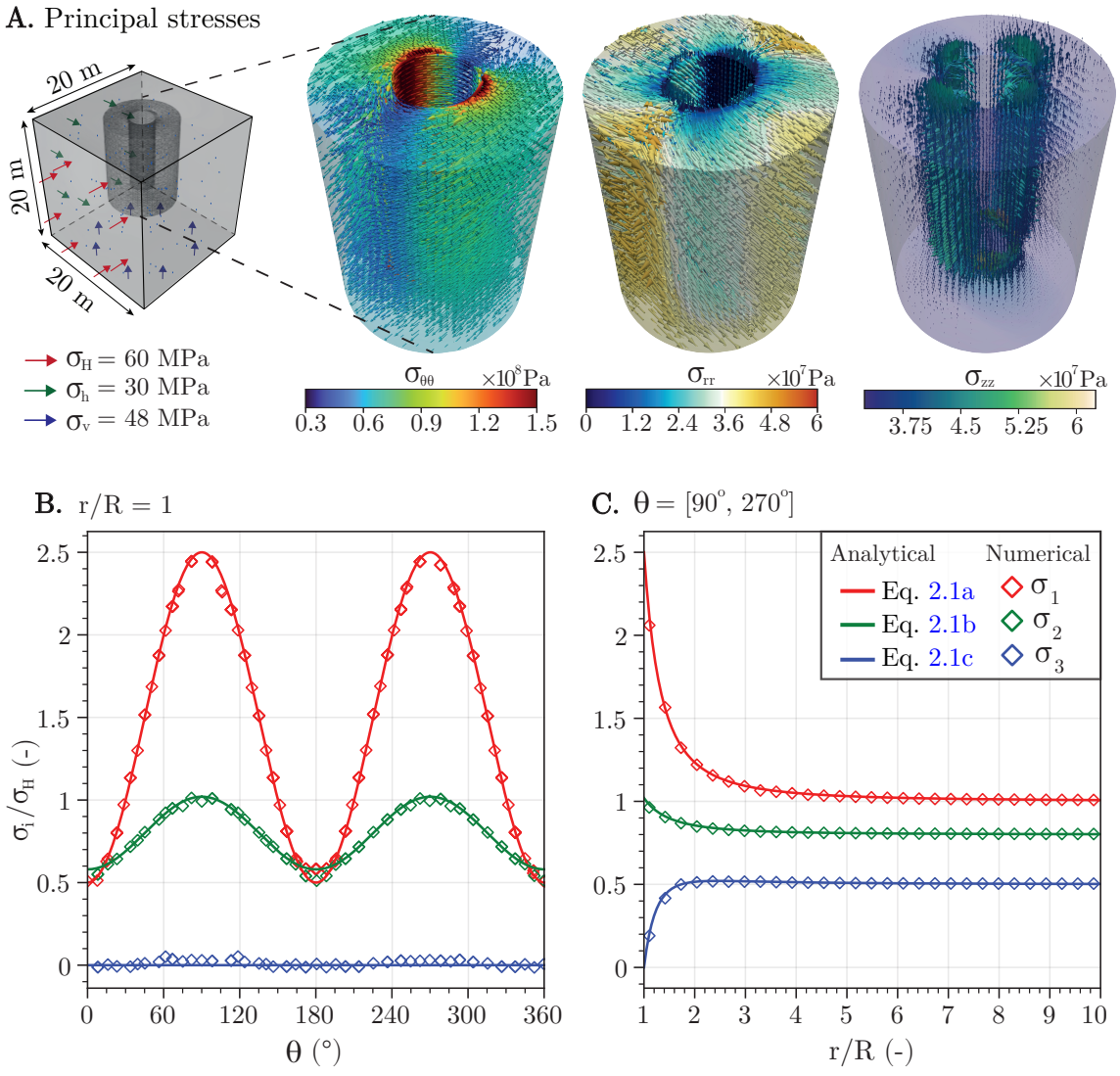


Figure 4.1: Validation of the stress field around a vertical circular borehole. **A.** Cut planes showing the magnitude and orientation of the principal stresses $\sigma_{\theta\theta}$, σ_{rr} and σ_{zz} around circular subjected to far-field stresses σ_H, σ_h and σ_v. **B.** Comparison of the principal stresses at the borehole wall with the Kirsch analytical solution. **C.** Comparison of the principal stresses in the radial direction (along the springline of σ_h) with the analytical solution.

In addition to the tangential stress, the far-field stresses also produce a vertical stress component (σ_{zz}) and a radial stress σ_{rr} at the borehole wall. The maximum magnitude of the vertical stress component occurs at the same azimuths as the maximum tangential stress and is generally lower, given by $\sigma_v + 2\nu(\sigma_H - \sigma_h)$. At the borehole wall, the third principal stress, *i.e.* the radial stress σ_{rr} is zero (Jaeger et al. 2007).

Figure 4.1a shows the stress field, represented through the three principal stresses, around a circular 1.75 m diameter borehole drilled vertically at the centre of a 20×20×20 m domain. The magnitudes of the far-field stresses applied to the domain edges are chosen such as $\sigma_h = 0.5 \times \sigma_H$ and $\sigma_v = 0.8 \times \sigma_H$. Figures 4.1b and 4.1c show each principal stress plotted against its corresponding analytical solution (Eqs. 2.1a–2.1c) at the borehole wall, and radially away from the borehole, respectively. The numerical stresses are sampled at borehole mid-height for comparison with the analytical solution, as the analytical solution does not capture the 3D stress effects at the bottom face of the borehole. The variation of the three principal stress components around and away from the borehole wall is consistent with the analytical solution, confirming that the selected geometry and mesh are stable, and that the size of the model is sufficient to prevent erroneous stress concentrations influenced by the domain edges.

The borehole in Figure 4.1 is refined with a surface element size of 0.5 m. The level of refinement required for the finite element simulation to accurately represent the stress field depends on a variety of factors, such as the complexity of the geometry, the type and magnitude of the applied loads, and the material properties within the numerical domain (Szabo & Babuska 2021). Typically, finer meshes produce more accurate stress field results, but at the expense of increased computational costs and time. Therefore, it is essential to balance the level of accuracy with computational efficiency when selecting an appropriate level of mesh refinement for a given problem. To identify the optimal level of refinement for the finite element mesh required to accurately compute the stress field around a typical nuclear waste disposal borehole, various borehole element sizes were tested, starting with a coarser mesh and then gradually increasing the refinement.

Figure 4.2a displays a set of 3D cut planes at the borehole mid-height, showing the nodal stress error for borehole wall refinements of 1 m (A1), 0.75 m (A2), 0.50 m (A3), 0.25 m (A4) and 0.10 m (A5). In all cases, the average error throughout the domain is below 2%, but errors as high as 14% concentrate in a few nodes at the borehole wall in the coarsest case (A1). This is because an element size of 1 m is not sufficient to represent the circular borehole geometry with radius of 0.875 m assumed in the analytical solution calculation. Figure 4.2b shows the distribution of relative errors across all nodes in the simulation, for the five refinement cases depicted in Figure 4.2a. The violin plot shows the full distribution of error values, where the wider region indicates a higher density of nodal stress data. The box plot shows the spread and skew of the error distribution, which is used to assess the sensitivity of the simulation results to the mesh size. As the

borehole wall is refined from 1 m to 0.25 m, the spread of the nodal error distribution decreases and the median error values become smaller. As the borehole wall size is further decreased from 0.25 m to 0.1 m, the error distribution remains relatively unchanged, and interestingly, the maximum error in the 0.1 m refinement case is larger than the maximum error in the 0.25 m refinement case. This suggests that the numerical stress computation for the given geometry and boundary conditions is not sensitive to mesh sizes finer than 0.25 m and the coarser mesh can be used without significantly affecting the accuracy of the results.

4.2.1.2 Multiple boreholes

A first validation of the stress field around multiple boreholes is done by considering two circular boreholes of equal radii, in an elastic rock domain. The centre-to-centre borehole separation is denoted s and the borehole surfaces, B_1 and B_2, are traction-free. The model is subjected to far-field tensile stress σ. Figure 4.3 shows the maximum principal stress at the borehole wall that arises when the two boreholes are subjected to transverse, longitudinal and biaxial tension respectively. For validation purposes, the maximum circumferential stress was plotted against the closed-form solutions derived for these cases by Ling (1948), showing a good match.

Figures 4.3a–4.3c display the maximum principal stress variation at the wall of borehole B1, subject to transverse, longitudinal, and biaxial tension, respectively. Figure 4.3d plots the maximum circumferential stress at the borehole wall, against the closed-form solutions, derived by Ling (1948) for the three different loading cases. The analytical solution considers two holes Γ_1 and Γ_2 on an infinite 2D plane under far-field stresses of σ^{∞}_{xx}, σ^{∞}_{yy}, and σ^{∞}_{xy}. Numerical stresses are sampled at the borehole mid-height, as in the previous section, allowing a direct comparison between the 3D numerical model and the 2D analytical solution. Figure 4.3d shows that the effect of neighboring boreholes decreases as the separation between them increases. Thus, the interaction between adjacent boreholes becomes insignificant and can be disregarded as long as the boreholes are spaced sufficiently far apart.

Furthermore, Figure 4.3 depicts that the minimum borehole separation required to significantly reduce stress interactions between them is dependent on the loading conditions. For example, in the case of biaxial tension, separations greater than 6 m are necessary to reduce stress concentration to that of a single borehole. This distance exceeds the area of influence that a single borehole would have on its own on the surrounding stress field (see Figure 4.1). Similarly, under transverse loading and for large borehole separations, the stress concentration at the borehole wall is non intuitively slightly lower than the single-borehole value of 3 (Zimmerman 1991).

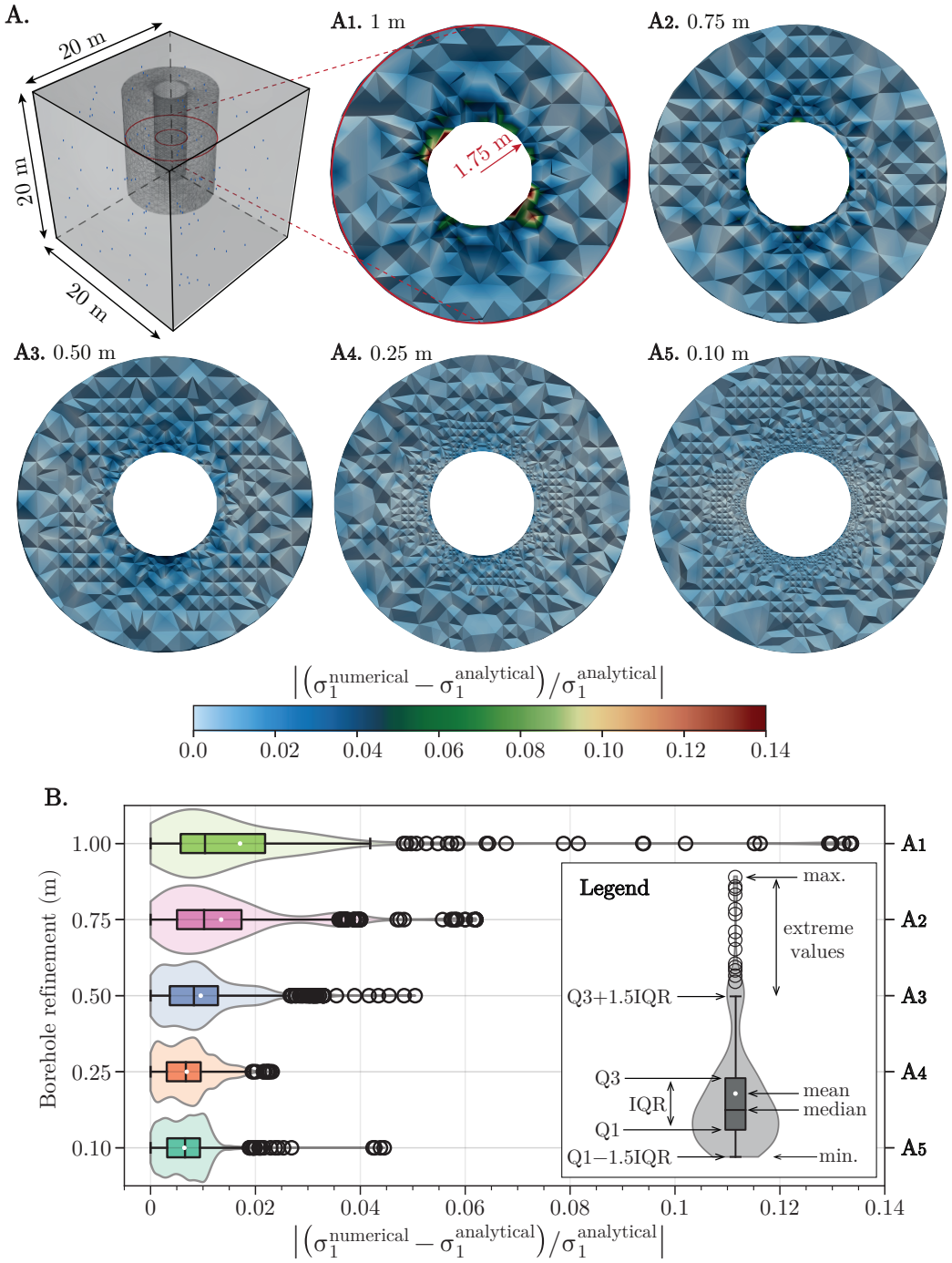


Figure 4.2: **A.** 3D cut planes at borehole mid-height showing the numerical error for different mesh refinements. The mesh resolution at the outer boundary is adaptively reduced to ensure a gradual increase in mesh size from the borehole wall to the domain boundaries. **B.** Violin plot, providing a visual comparison of the error distributions for the different mesh sizes shown in Figure 4.2a. Each set of errors is divided into four quartiles, with a line drawn at the median error value. The upper and lower quartiles are defined as the values above and below which 25% of the nodal error data points fall, respectively. The ends of the box plot indicate the range of data falling $1.5 \times IQR$ below and above the first and third quartiles, respectively. Nodal error data beyond this range are indicated as circles.

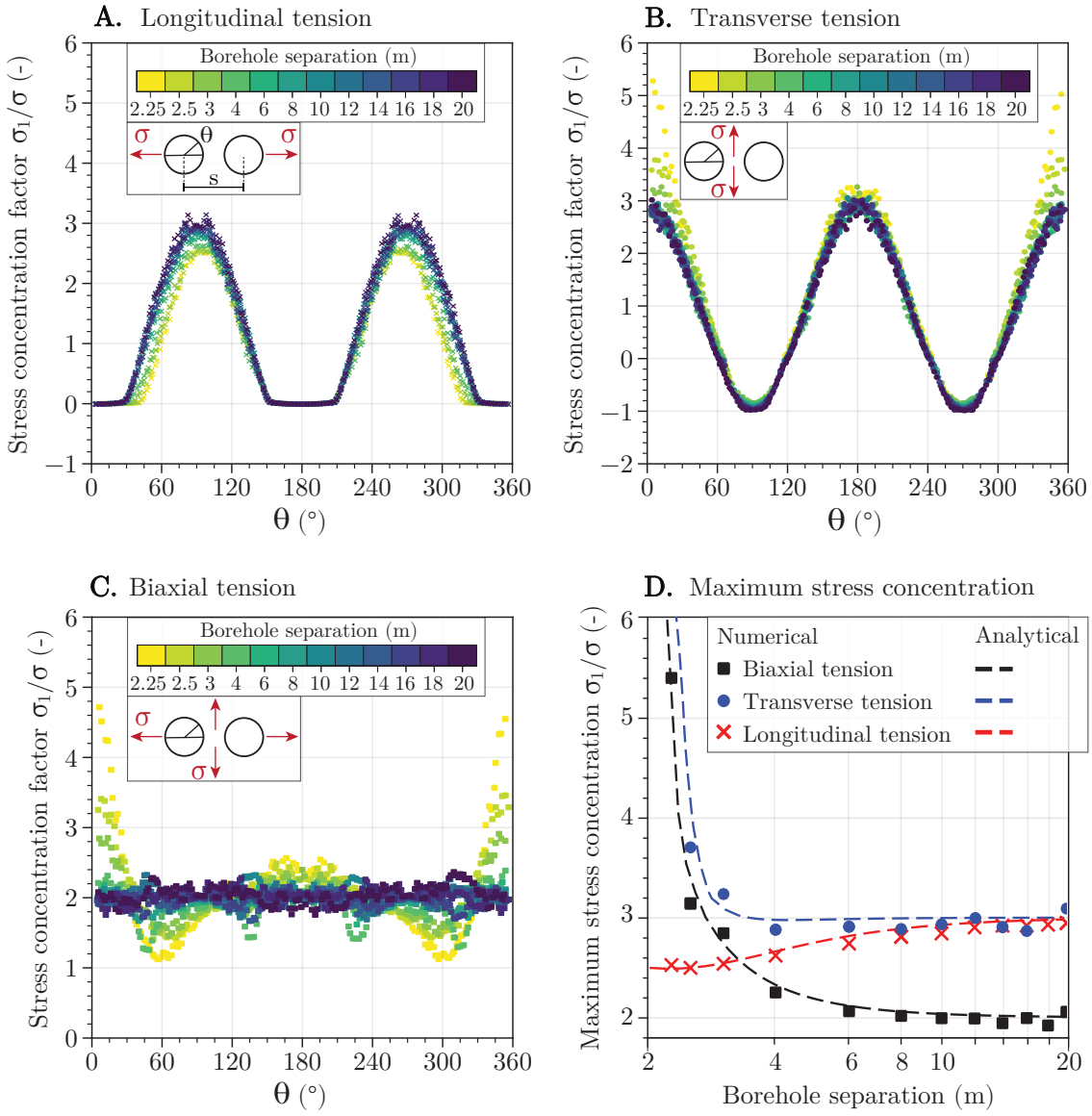


Figure 4.3: Variation of the tangential stress at the borehole wall, under longitudinal (**A.**), transverse (**B.**) and biaxial (**C.**) tensile loading. The stress values correspond to the nodal stresses from the borehole elements located at the borehole mid-height. Stresses are normalised to the applied load σ and coloured according to the specific spacing case. Effect of borehole spacing on the maximum principal stress at the borehole wall, in a two-borehole model, under uniaxial and biaxial loading (**D.**). The maximum tangential stress occurs at $\theta = 0°$ for uniaxial transverse and biaxial tension, and at $\theta = \pm 90°$ for longitudinal loading, in agreement with Ling's (1948) analytical solution.

4.2.2 Borehole damage modelling

Excavating boreholes in an initially intact rock mass not only causes stress augmentation around the excavations, but also a local degradation of the surrounding material, where

fractures preferentially nucleate and grow to develop into excavation damage zones (Tsang et al. 2005, Perras & Diederichs 2016). Chapter 3 motivated the suitability of using a damage mechanics approach to model fracture initiation and described the implementation of the Mazars damage model used in this work. In short, this work uses Kachanov's (1999) theory that the damage development of a material prior to localisation and brittle failure can be expressed as a scalar variable and Mazars's (1986) extension of this concept by determining a damage variable from damage in tension and compression respectively. However, Mazars's (1986) damage model and subsequent studies using this model are exclusively focused on concrete (Rabczuk & Belytschko 2004, Grassl & Jirásek 2006, Mazars & Grange 2017), and there is a limited number of studies on applying this model to brittle rock (Defoort et al. 2016, Souissi et al. 2017, Kim et al. 2020). This section describes how the damage parameters are derived from the experimental stress-strain curves obtained by SKB on rock samples from Forsmark.

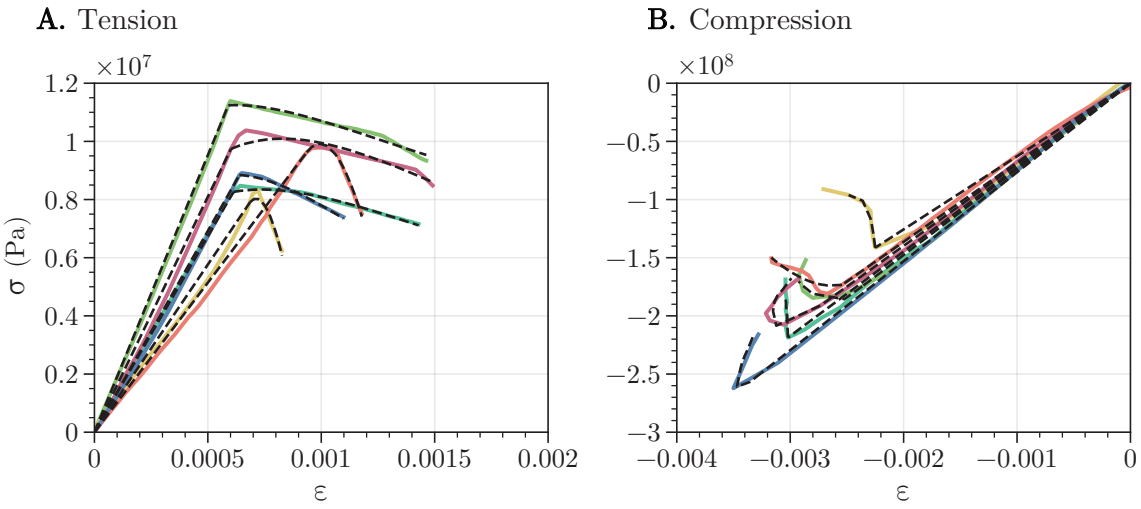
The stress-strain data used to determine the Mazars model constants A_t, A_c, B_t, B_c and ε_0 was obtained by SKB from indirect tensile tests (SKB P-05-212 2006), and uniaxial compression tests (SKB P-05-211 2005, SKB P-04-224 2004). The critical strain threshold ε_0 in the Mazars damage model represents the the maximum effective tensile strain that the rock can withhold. Parameters A_c, A_t and B_c, B_t are material constants governing the behaviour of the rock sample after peak stress, with A_c and A_t representing the asymptotic line after the peak and B_c and B_t determining the slope of the post-peak curve (see Fig. 3.8). For concrete samples, the values of the parameters A_c and A_t range from 1 to 2 and 0.7 to 1, respectively, and the values of B_c and B_t are within 1,000 to 2,000 and 9,000 to 21,000 respectively (Hamon 2013). Table 4.1 lists recent studies and their respective calibrated parameter values for A_t, A_c, B_t, B_c in damage models of concrete and rock.

Table 4.1: Typical values of Mazars parameters from literature on concrete and rock damage.

Rock Type	A_t	A_c	B_t	B_c	Source
Granite	0.62	15.05	2,271	1,722	Kim et al. (2020)
	1.0	2.0	120	90	Souissi et al. (2017)
Limestone	1.0	2.0	120	90	Souissi et al. (2017)
Sandstone	1.0	2.0	120	90	Souissi et al. (2017)
Concrete	1.0	1.0	106	1,000	De Falco et al. (2018)
	0.8	1.25	7,000	395	Mazars et al. (2015)

The Mazars model is well-suited for simulating the behaviour of quasi-brittle materials up to the point immediately following the peak stress (Jirásek 2011). The experimental data was thus pre-processed and the region of the stress-strain curves corresponding to permanent plastic deformation at high values of strain was removed. Following this, the damage parameters were determined by finding the least squares fit of Equation 3.20 separately for the experimental data in tension and compression respectively.

Figure 4.4 shows the parameters obtained for Forsmark rocks in tension and compression. It is worth noting that the parameter values of some samples fall within the range reported in the literature for concrete, with the exception of A_c and B_t, which differ significantly from concrete. This deviation can be attributed to the differences in the elastic properties and the post-failure behaviour between rock and concrete. Furthermore, the range of variability in the parameters calculated for different samples of the same rock is extensive.



Uniaxial tension

Curve	Rock specimen	A_t	B_t
	KFM07A-110-5	0.33	1798
	KFM07A-110-6	13.4	1002
	KFM07A-110-7	17.5	1461
	KFM07A-110-8	0.45	1455
	KFM07A-110-9	0.75	1798
	KFM07A-110-10	0.44	1564

Uniaxial compression

Curve	Rock specimen	A_c	B_c
	KFM02A-113-07	16.5	540
	KFM02A-113-08	1.01	984
	KFM02A-113-11	3.36	824
	KFM07A-113-03	1.63	813
	KFM07A-113-05	2.23	1044
	KFM07A-113-06	1.33	1351

Figure 4.4: Damage model parameters for the Forsmark site derived from uniaxial tension and compression curves. The stress-strain curves for several rock specimens were digitised from SKB reports and colored according to the rock specimen. The tensile data comes from indirect tensile tests (SKB P-05-212 2006), and the compressive data comes from uniaxial compression tests (SKB P-05-211 2005, SKB P-04-224 2004).The black dashed lines show the best fit of the experimental data. The corresponding A_t, B_t, A_c, B_c parameters are listed in the tables below.

4.2.3 Borehole temperature

The ability of the present model to compute the temperature field is validated against the analytical solution for heat conduction in the region outside of a circular borehole with an initial temperature of zero at time $t_0 = 0$. A uniform temperature T_b is applied to a circular borehole of radius R_b, with no external mechanical loads being imposed. The temperature within the domain at a given time t was derived by Carslaw & Jaeger (1986) as:

$$\frac{T - T_0}{T_b - T_0} = 1 + \frac{2}{\pi} \int_0^\infty \exp\left(-\kappa u^2 t\right) \frac{J_0(ur)Y_0(uR_b) - Y_0(ur)J_0(uR_b)}{J_0^2(uR_b) + Y_0^2(uR_b)} \frac{\mathrm{d}u}{u} \tag{4.1}$$

where T_0 is the initial matrix temperature throughout the domain, set to 0°C for the validation case, T_b is the borehole temperature, which is kept constant to 100°C throughout the simulation, κ is the thermal diffusivity defined as $\kappa = \frac{k}{\rho c_p}$ with k being the thermal conductivity, ρ the density and c_p the specific heat capacity of the host rock, and J_0 and Y_0 are the Bessel functions of the first kind and second kind respectively, of order 0, r is the radial distance from the borehole wall, and R_b is the borehole radius.

Figure 4.5a presents the temperature distribution within the numerical domain after 0.1, 1, 10 and 100 days of heating. After 10 days, the temperature pulse has almost reached the domain boundary and the comparison between the analytical and numerical solutions is relevant for times prior this, as the analytical solution assumes an infinite rock domain. Figure 4.5b shows the temperature after 0.1, 1, 10 and 100 days of heating along the line A-B, spanning from the borehole wall to the domain edge. It is observed that the numerical and analytical solutions show nearly perfect agreement, with temperature differences remaining within 1°C at every node throughout the numerical domain and at each time step.

Table 4.2: Average values of the host rock thermal properties at Forsmark (SKB TR-08-05 2007), along with the time step used in the transient simulations for temperature validation.

Property	**Value**	**Time step (dt)**
Thermal Conductivity (κ)	3.68 W/(mK)	10^{-2} if t $\in [0, 10^{-1})$ days
Thermal Expansion Coefficient (α)	7.7 $\times 10^{-6}$ K^{-1}	10^{-1} if t $\in [10^{-1}, 1)$ days
Heat Capacity (C)	765.57 J/(kgK)	10^{0} if t $\in [10^{0}, 10^{1})$ days

Differences between the numerical and analytical solutions occur because in the numerical case heat flows both radially through the surrounding rock and along the borehole axis, whereas the analytical solution assumes unidirectional heat flow from a boundary with a constant temperature.

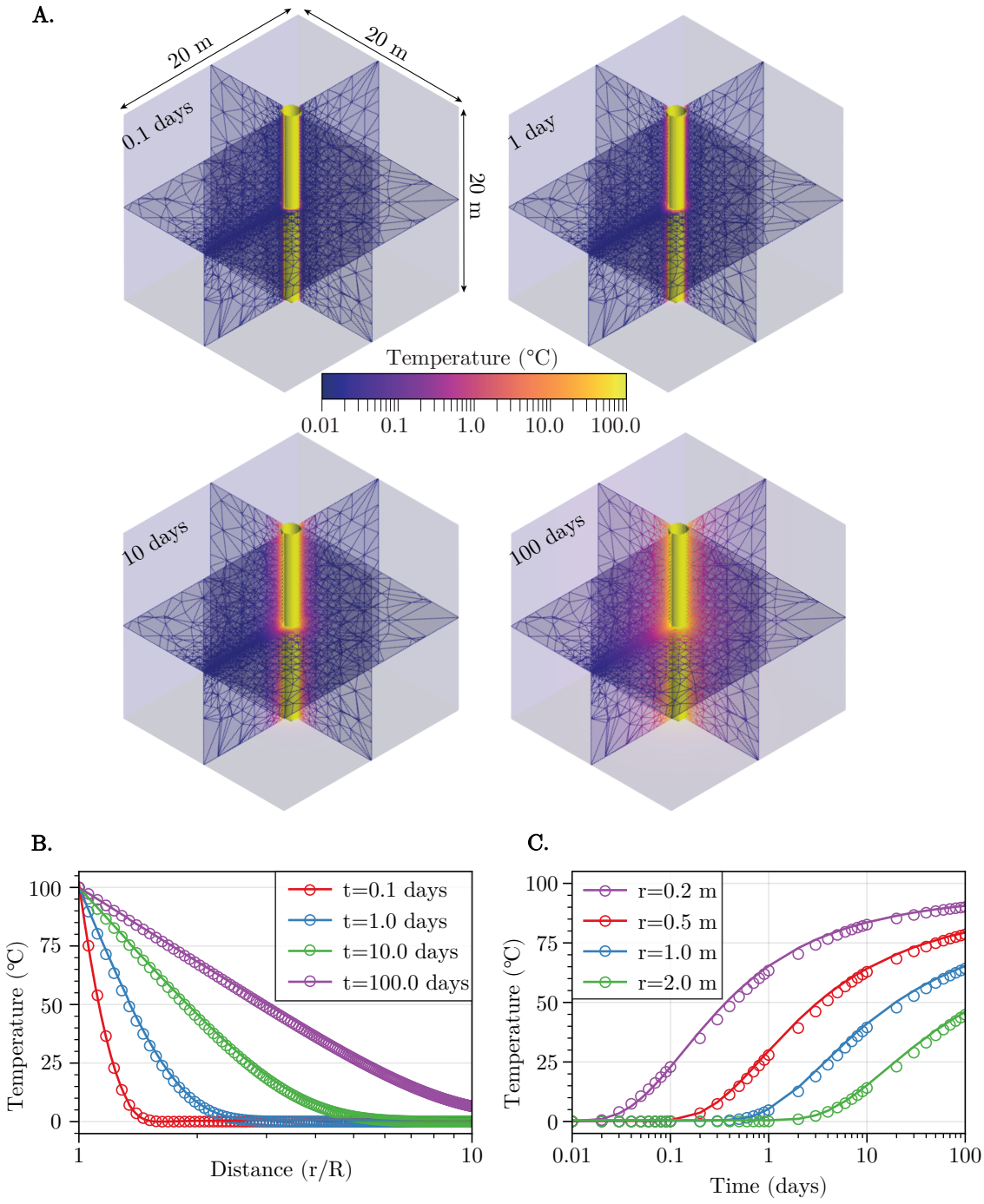


Figure 4.5: **A.** Snapshots of the temperature distribution in a single-borehole model after 0.1, 1, 10 and 100 days of heating. **B.** Temperature measurements taken every 0.1 meters along a radial line extending from the borehole wall to the domain boundaries. Temperature is plotted against the analytical solution (Eq. 4.1) at t=0.1, 1, 10, 100 days. **C.** Temperature curves for nodes located at radial distances r=0.2,0.5,1.0,2.0 m from the borehole wall. Numerical values are plotted as hollow circles and analytical values as solid lines.

4.2.4 Borehole thermal stresses

This section examines the impact of temperature on solid deformation, specifically the displacement and stress fields that result from the temperature changes within the numerical domain. The thermal stresses arising around a cylindrical excavation due to a radially-varying temperature field $T(r,t)$, such as the one shown in Figure 4.5 are (Nowacki 1986)

$$\sigma_{\theta\theta} = \frac{\alpha E}{1-\nu}\frac{1}{r^2}\int_R^r T(r',t)r'\,\mathrm{d}r' - \frac{\alpha E}{1-\nu}T(r,t) \tag{4.2a}$$

$$\sigma_{\mathrm{rr}} = -\frac{\alpha E}{1-\nu}\frac{1}{r^2}\int_R^r T(r',t)r'\,\mathrm{d}r' \tag{4.2b}$$

$$\sigma_{zz} = -\frac{\alpha E}{1-\nu}T(r,t) \tag{4.2c}$$

where $\sigma_{\theta\theta}$, σ_{rr} and σ_{zz} are the tangential, radial and vertical thermal stresses respectively, R is the borehole radius, E is the Young's modulus, ν is Poisson's ratio and α is the coefficient of thermal expansion.

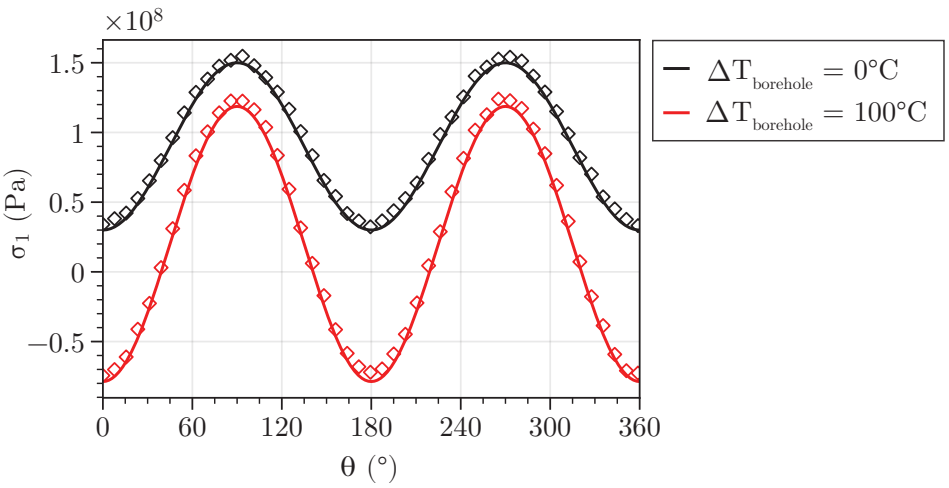


Figure 4.6: Thermo-mechanical stress at the borehole wall when the borehole is heated by $\Delta T = T_{\mathrm{borehole}} - T_{\mathrm{i}} = 100°\mathrm{C}$

Equations 4.2a–4.2c assume uniform temperature distribution along the axial direction (Stephens & Voight 1982, Kumar & Singh 1989). In reality, a three-dimensional cylindrical borehole loses more heat at top/bottom, so the numerical results are compared with the analytical solution at borehole mid-height, where fluctuations in temperature along the borehole axis are relatively negligible compared to those in the radial direction.

Starting from equations 4.2a–4.2c, Stephens & Voight (1982) provided a solution for thermal stresses occurring at the wall of a circular excavation, which only requires knowledge of the temperature change, instead of the full temperature field. They showed that the

maximum thermally induced stress at the borehole wall, due to a temperature change ΔT is constant *w.r.t.* time and equal to

$$\sigma_{\theta\theta} = \frac{\alpha E \Delta T}{1 - \nu} \tag{4.3}$$

While the thermal stress field around an excavation varies depending on the cavity shape and the boundary conditions applied, its maximum always occurs at the excavation wall and is given by Equation 4.3. The borehole stresses are validated in this section for a circular borehole. For validation of the combined thermo-mechanical stress at the borehole wall, the thermal effects are integrated into the Kirsch analytical equations, by adding the thermal stress coefficient (Equation 4.3) to Equations 2.1a–2.1c.

The temperature change $\Delta T = T_{\text{borehole}} - T_{\text{i}} = 100°\text{C}$ at $t = 0$ s introduces additional stresses due to thermal expansion of the rock. The thermal stresses affect the mechanical stress field in the surrounding rock, superimposing upon the initial stress state caused by the triaxial compression. The magnitude and distribution of the thermal stresses are shown in Figure 4.6; for the case of 100°C the curve is shifted downwards as the compressive stresses increase.

4.3 Fracture growth validations

4.3.1 Numerical computation of SIFs

FEM-computed stress fields have been validated in the previous sections in unfractured numerical domains containing one or several co-linear deposition boreholes. In a fractured model, the local stress distribution around newly nucleated fracture disks depends upon the SIFs at the fracture tips. In this work, SIFs are numerically evaluated at each fracture tip node using Nejati et al.'s (2015*a*) virtual integration disk method, which implements a variant of Rice's (1968) $\mathcal{J}$-integral (Walters et al. 2005, Bremberg & Faleskog 2015). The values of K_I, K_{II}, and K_{III} are extracted assuming plane strain conditions close to the fracture tip (Nakamura & Parks 1989, Nejati et al. 2015*a*).

In this section, numerical SIFs are validated against known analytical solutions for a penny-shaped initial fracture disk under uniaxial tension (Equations 4.4a-4.4c) and uniaxial compression (Equations 4.5a-4.5c) respectively. The analytical solutions were derived by Kassir & Sih (1975) for an inclined penny-shaped fracture embedded in an infinite solid, where the initial disk plane makes an angle β with the direction of the uniaxial load σ, as shown in Figure 4.7.

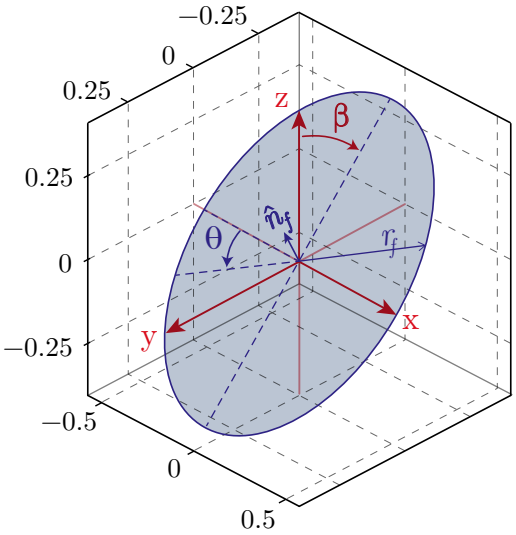


Figure 4.7: Schematic diagram of the initial fracture disk used for SIF validation (Equations 4.4a–4.5c).

The analytical solutions for the three modal SIFs are given by Eqs. 4.4a– 4.4c for uniaxial tension:

$$K_I = 2\sigma\sqrt{r_f/\pi}\sin^2\beta \tag{4.4a}$$

$$K_{II} = \frac{2\sigma\sqrt{r_f/\pi}}{2-\nu}\sin 2\beta\cos\theta \tag{4.4b}$$

$$K_{III} = \frac{2(1-\nu)\sigma\sqrt{r_f/\pi}}{2-\nu}\sin 2\beta\cos\theta \tag{4.4c}$$

and Eqs. 4.5a– 4.5c for uniaxial compression:

$$K_I = 2\sigma\alpha_1\sqrt{r_f/\pi} \tag{4.5a}$$

$$K_{II} = \sigma\frac{2\sqrt{r_f/\pi}}{2-\nu}\cos\theta(\alpha_1+\alpha_2) \tag{4.5b}$$

$$K_{III} = \sigma\frac{2(1-\nu)\sqrt{r_f/\pi}}{2-\nu}\sin\theta(\alpha_1+\alpha_2) \tag{4.5c}$$

where a is the initial disk radius, ν is Poisson's ratio, θ is the polar angle along the fracture front, and the α_1 and α_2 terms accounting for the stick and slip conditions during compression and are given by:

$$\alpha_1 = -2p_0/\sigma \tag{4.6}$$

$$\alpha_2 = 2\left[\mu\left(\sin^2\beta - p_0/\sigma\right) + \tau_c/\sigma\right] - \sin 2\beta - 2(1-\cot\beta)p_0/\sigma \tag{4.7}$$

where p_0 is the fluid pressure inside the fracture, if the fracture is initially open, μ is the coefficient of friction τ_c is the cohesive strength.

Figures 4.8 and 4.9 show the numerical SIFs in tension and compression, respectively. The SIFs are computed along the initial disk front, for a penny-shaped disk centred in a 20×20×20 m domain. The initial disk radius is 0.5 m and it makes a 45° angle with the loading direction. Under uniaxial tension, K_I is positive and constant along the initial disk front. Under uniaxial compression, it is negative and its value depends on the initial fluid pressure p_0 ($K_I = 0$ if $p_0 = 0$). In both cases, K_{II} and K_{III} vary sinusoidally and change sign on diametrically opposite sides of the fracture. The domain boundaries are placed sufficiently far away, so that the SIFs can be compared with the analytical solution for an inclined penny-shaped fracture embedded in an infinite solid. In both cases, there is a good match between the numerical and analytical stress intensity factors, indicating that the numerical model is accurate and can be used to predict the behaviour of the system under the two different loading conditions.

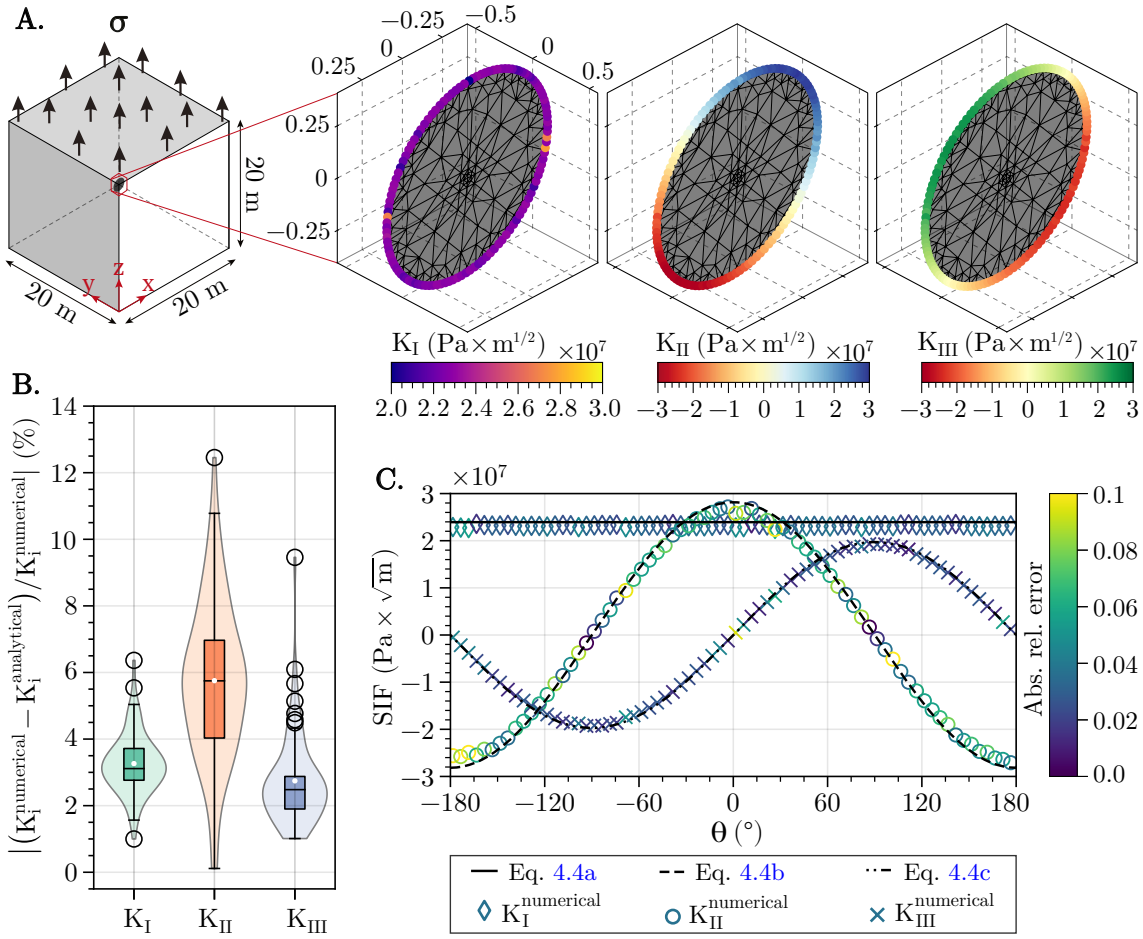


Figure 4.8: **A.** Numerical stress intensity factors around an isolated fracture under uniaxial tension. The fracture front is discretised with 72 tip nodes, and each node is coloured according to the computed SIF value. **B.** Numerical error distribution for each SIF mode. **C.** Numerical SIFs plotted against their corresponding analytical solution. Each data point is coloured based on the percent difference between the numerical SIF and the analytical solution. The set of errors for each failure mode is plotted as a distribution in Figure 4.8b.

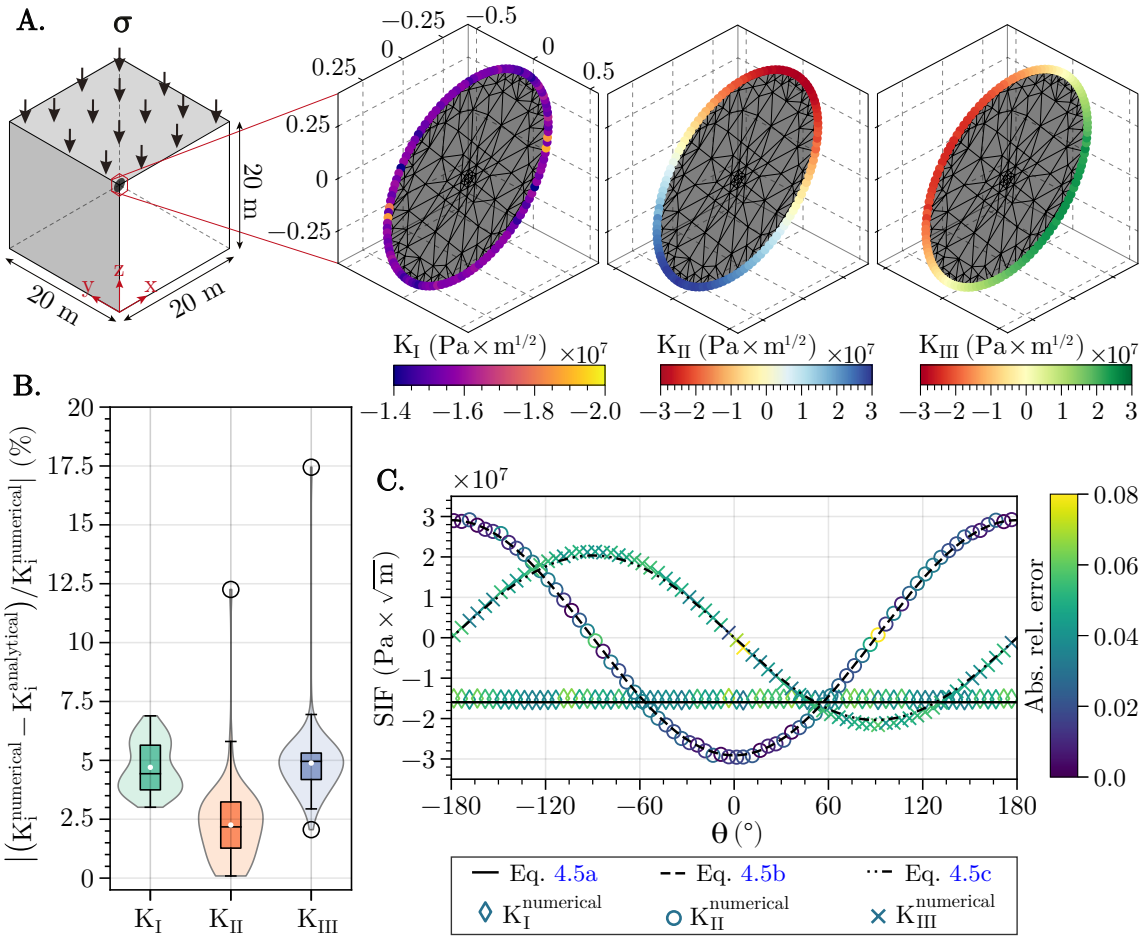


Figure 4.9: **A.** Numerical stress intensity factors around an isolated fracture under uniaxial compression. The fracture front is discretised with 72 tip nodes, and each node is coloured according to the computed SIF value. **B.** Numerical error distribution for each SIF mode. **C.** Numerical SIFs plotted against their corresponding analytical solution. Each data point is coloured based on the percent difference between the numerical SIF and the analytical solution. The set of errors for each failure mode is plotted as a distribution in Figure 4.9b.

4.3.2 Spalling around a single borehole

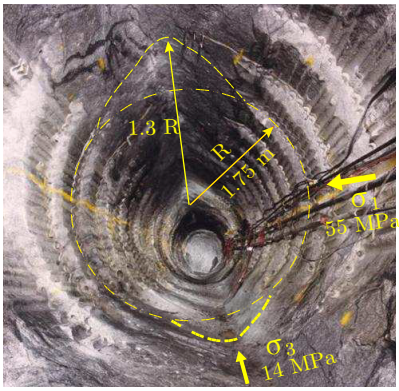
The SIF validations in the previous section demonstrated that the growth mechanism is correctly computed at the beginning of the growth process, under both tensile and compressive loading conditions. As fractures extend and lose the initial penny shape, for which the analytical solutions exist, validation of the numerical growth patterns is further conducted by comparing final fracture patterns (when growth has arrested) with field observations at a specific site, where suitable field data is available.

In this section, the fracture growth methodology implemented in ICGT is validated against the URL Mine-By Experiment, for mechanical spalling. The Atomic Energy of Canada Limited (AECL) carried out the Mine-by tunnel experiment (Read 2004) in order to

characterise spalling around a circular borehole under high stresses. The experiment consisted of drilling a 3.5 m diameter circular tunnel in a relatively unfractured granitic rock. The tunnel was excavated subparallel to the intermediate principal stress direction σ_h, in order to maximise the difference between the minimum and maximum compressive stresses acting on the tunnel boundary. Spalling became apparent in both the roof and the floor of the tunnel (diametrically opposite) after the borehole was cleaned and the spalled fragments removed through scaling (Figure 4.10a). The maximum depth of the spalled zone was approximately 50 cm, with variations along the tunnel length, and the rock mass remained intact beyond this point.

Figure 4.10b shows the simulation parameters for the numerical model pertaining to the validation case. The validation case was set up using the rock properties of the Lac du Bonnet granite, and far-field stresses corresponding to the *in situ* conditions at the 420 m level, where the spalling observations have been recorded: $\sigma_H = 55 \pm 5$ MPa, $\sigma_h = 48 \pm 5$ MPa, and $\sigma_v = 14 \pm 1$ MPa (Read & Martin 1996).

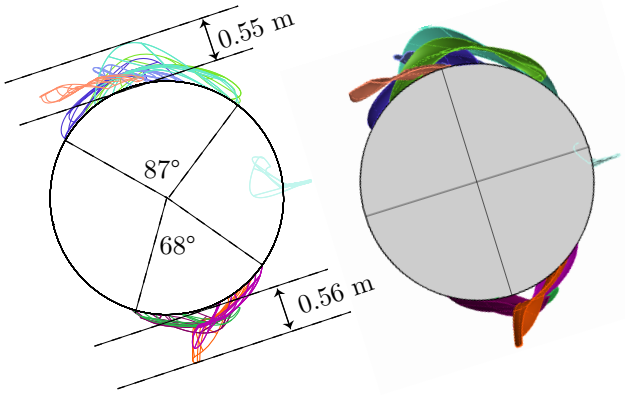
A. Field observations



B. Numerical set-up

Parameter	Value
σ_H	60 MPa
σ_h	48 MPa
σ_v	15 MPa
ν	0.24
E	70 GPa
TS	10 MPa
UCS	220 MPa
A_t	0.73
B_t	1816
A_c	0.73
B_c	1816

C. Fracture patterns: top view



D. Fracture patterns: side view

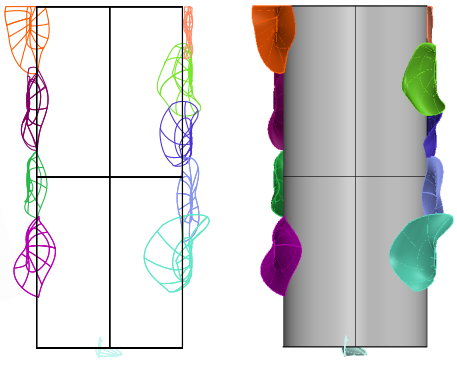


Figure 4.10: **A.** Spalled zone around the AECL's 3.5 m diameter tunnel, modified from Zhao et al. (2010); **B.** Simulation parameters used in the validation case; **C.** Final fracture patterns: radial $(x - y)$ view; **D.** Final fracture patterns: axial $(z - x)$ view.

Figures 4.10c and 4.10d show the final fracture patterns, after the spalling process has stabilised and fracture growth has arrested, in radial and axial view respectively. Each macro-fracture surface that interacts with the borehole wall is regarded as a "fractured zone". When compared with other numerical studies, which model the progressive splitting of the borehole wall through coalescence of smaller fractures (Zheng et al. 1989, Ewy & Cook 1990), or through propagation of active damage planes (Rutqvist et al. 1989), the fractures shown in Figure 4.10 represent the final stage of failure and they inherently encompass all the intermediate stages.

The "spalling" extent is determined from the fractured region around the borehole as follows. For each fracture surface, the "spalling depth" is the maximum distance measured between fracture tip nodes and the borehole wall, and the "spalling width" is the maximum arc length of that fracture around the borehole, as seen from an observation point at the top of the borehole. The maximum measured depths and widths of the two fracture arrays forming the diametrically-opposite notches (Figure 4.10b) are consistent with those observed in the field (Figure 4.10a).

Although nucleation occurs in one stage and a relatively small number of initial fracture disks are initiated, *i.e.*, 10, fractures grow freely, based on the energy in the system, eventually covering the entire length of the borehole and accommodating the whole range of damage that develops in the near-borehole region after the borehole drilling stage. The fracture growth process inherently accounts for nucleation and coalescence of new micro-fractures, by taking into account the stress concentrations at the fracture tip, where new micro-fractures nucleate and coalesce to extend the existing macro-fracture.

Rock buckling and collapse into the borehole are not explicitly modelled, but the loss of integrity of the borehole is accounted for through the damage distribution. This is illustrated in Figures 4.11a–4.11c, where the elastic modulus of the host rock gets degraded

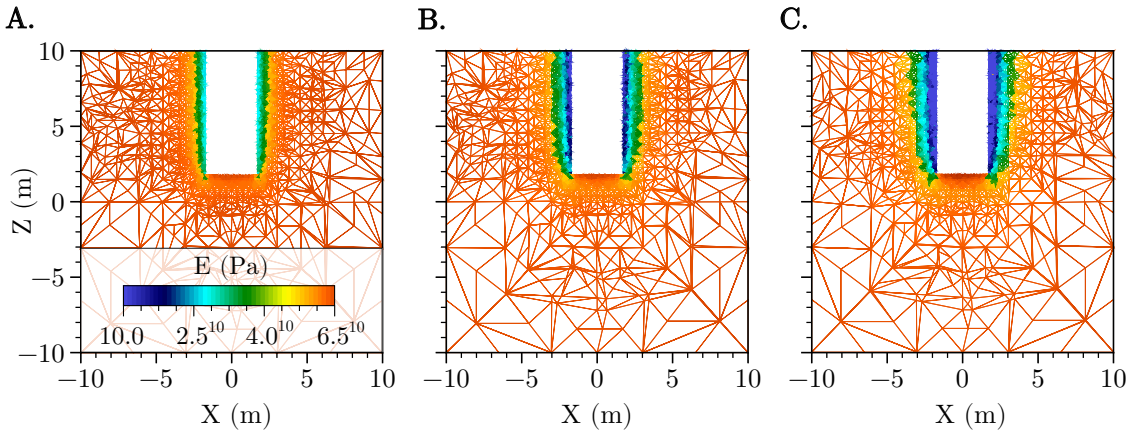


Figure 4.11: Mesh cut planes showing Young's modulus distribution along AECL's circular 3.5 m diameter Mine-by tunnel: **A.** after the tunnel is drilled; **B.** after fracture nucleation; and **C.** after all fractures have stopped growing.

based on Equation 3.29 in the vicinity of the borehole. Prior to nucleation, the damage amounts to a 60% reduction in the intact rock elastic modulus (Figure 4.11a). After the initial fracture disks nucleate, the Young's modulus is reduced completely in the elements adjoining the newly spawned fracture surfaces (Figure 4.11b). Further degradation of the rock mass occurs as fractures grow (Figure 4.11c), covering the whole length of the tunnel. As opposed to the field experiment where the two diametrically opposite spalled zones were asymmetrical, the fractured zones in the numerical model tend to be symmetrical, due to the prescribed homogeneity and isotropy of the numerical domain.

4.3.3 Simulation parameters involved in nucleation and growth

To achieve the fracture patterns shown in the previous section, the following simulation parameters were used for nucleation and growth: number of initial disks = 10; initial disk size = 30 cm, following a normal distribution and scaled with damage, *cf.* Figure 4.12c; minimum fracture spacing = 1.5×initial disk size; maximum extension length Δl_v = 40 cm per growth step; $\beta_f = 0.25$; $\beta_n = 0.75$. These parameters are varied in this section, to assess their influence on nucleation and growth patterns. Their combined effect on fracture growth is explained and a set of recommended parameters will be then used in the subsequent simulations of spalling at the Forsmark site (Chapters 5, 6, 7).

4.3.3.1 Initial disk size and orientation

The size of the initial disks must not affect spalling patterns. This happens for a sufficiently small initial fracture radius. The initial flaw size is controlled by the size of the element in which it nucleates. The initial flaw sizes are normally distributed and scaled with the amount of damage present at the nucleation location. Figure 4.12 shows an example of nucleating 100 initial fracture disks around a circular borehole, where all of them have uniform initial radii of 50 cm (Figure 4.12a), the initial sizes follow a normal distribution, with 50 cm mean radius and 20% of the mean radius as standard deviation (Figure 4.12b) and the initial sizes are normally distributed as in Figure 4.12b, but also scaled according to the damage distribution.

The largest disk size, corresponding to the highest damage present in the rock, is set to 50 cm and decreases as shown in Figure 4.12c, taking as a maximum value the size of the element in which damage is computed. Before nucleation, the area surrounding the borehole walls was refined to enforce a minimum element length of 0.5 m, which reduces as fractures are created and their tips are refined. During nucleation, fractures of radius consistent with the size of their corresponding nucleating elements are created. This translates to initial fractures of 0.5 m maximum radius, reducing with element size

to $2 \times \pi \times 0.5/12 = 0.26$ m, for 12 tips per fracture, and subsequently reducing as fractures get inserted with a minimum radius of 0.01 m.

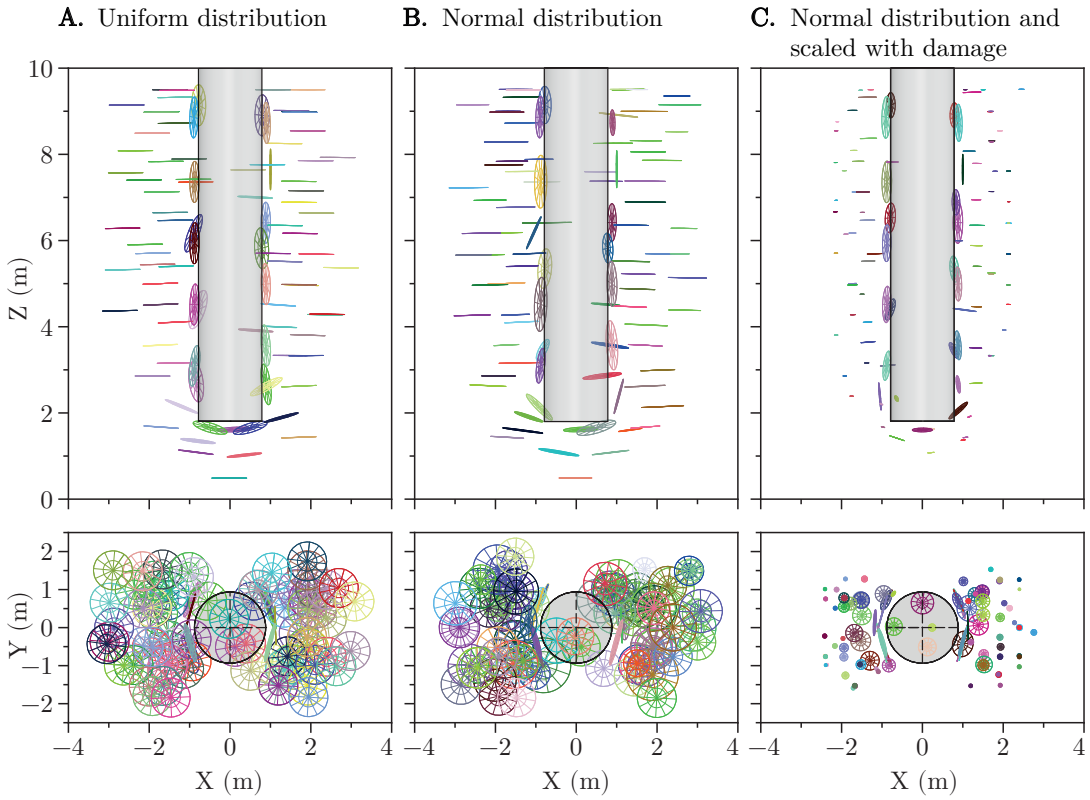


Figure 4.12: Nucleation of 100 fractures in the first 100 most damaged elements around the borehole. **A.** Each fracture disk radius is 50 cm. Improved fracture nucleation patterns are obtained by **B.** defining a normal distribution of initial disk radii, with 50 cm mean and 10 cm standard deviation and **C.** scaling the radii according to the damage in the element, which varies as a function of the distance away from the borehole.

Thus, for a damaged element in which a fracture is being nucleated, the maximum diameter of the fracture will be given by the maximum length of the element in the plane defined by the fracture normal. This can be adjusted to be made to always be contained by the element, and can be adjusted to be a pure material property. A fixed fracture length, consistent with changing element sizes, is implemented throughout the presented simulations, as it better captures spalling fractures that nucleate closest to the borehole wall, while also capturing smaller fractures that nucleate away from the borehole in zones of lower damage, that may not be directly involved in spalling or splitting of the borehole wall (Figure 4.12c). Improved fracture nucleation patterns are thus obtained in Figs. 4.12b and 4.12c. The larger fractures in the highly damaged zone that are oriented parallel to the borehole wall are the ones delineating rock slabs that will eventually spall. As the damage model is isotropic, the initial fracture disks are oriented in the direction of the third eigenvector of the stress tensor.

4.3.3.2 Total number of fractures

As discrete fractures initiate from diffuse damage, the number of initial fracture disks dictates the upper limit for the number of fractures that can nucleate during a simulation. Nucleation occurs in the simulation step immediately following the initial damage computation after the borehole excavation step. Figure 4.13 illustrates the initial and final fracture patterns for 10, 50, and 100 fracture disks that nucleate around a vertical circular borehole. It is apparent that the fractured region around the borehole can be qualitatively divided into three concentric zones once the growth process has stabilized. The innermost zone exhibits the most growth and interaction between fractures. As the radial distance increases, the outer excavation damage zones become progressively less fractured due to the activation of fewer tips by smaller horizontal fractures from these zones, leading to negligible growth. This is quantified as cumulative fracture area as a function of radial distance from the borehole wall.

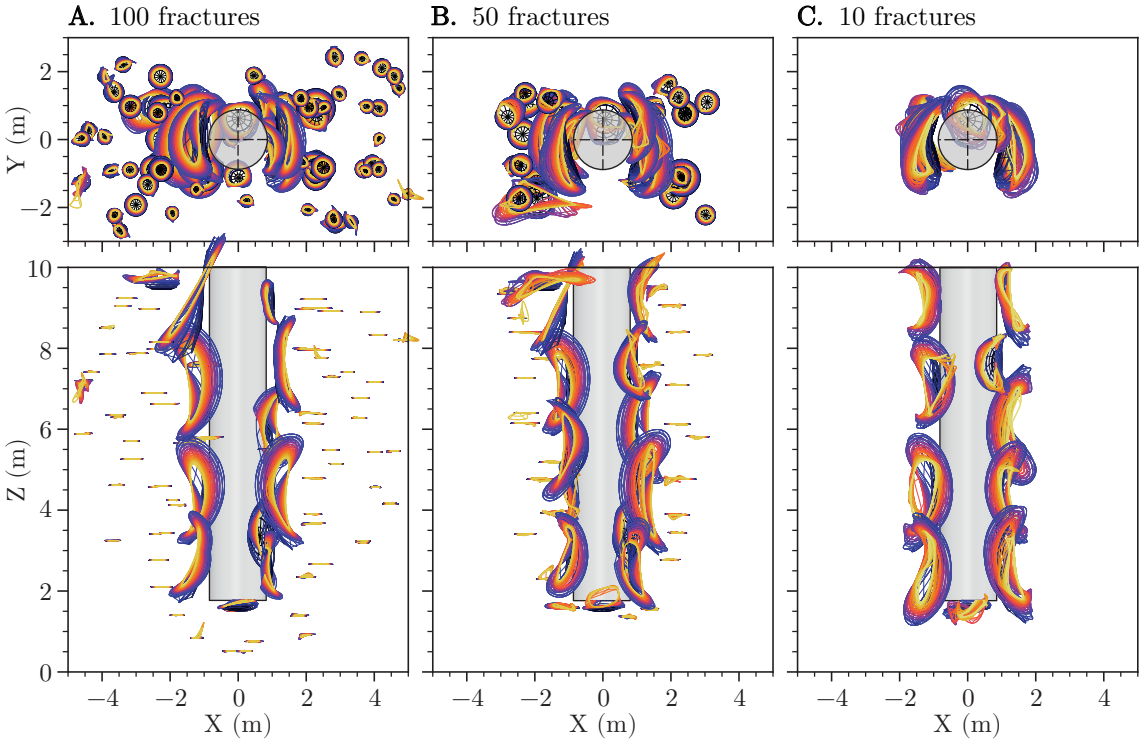


Figure 4.13: Nucleation of 100 fractures in the first 100 most damaged elements around the borehole. **A.** Each fracture disk radius is 50 cm. Improved fracture nucleation patterns are obtained by **B.** defining a normal distribution of initial disk radii, with 50 cm mean and 10 cm standard deviation and **C.** scaling the radii according to the damage in the element, which varies as a function of the distance away from the borehole.

There is only one nucleation event per simulation. While it is possible to have multiple nucleation events, this work assumes that nucleation and growth are two competing processes, and fracture extension can be thought as the nucleation of a new fracture and

coalescence with the existing growing fracture. Irrespective of whether the maximum limit for the number of fractures has been reached or not, additional fractures do not nucleate if the damage criterion is not fulfilled.

The initial number of disks was varied in this section to assess its influence on spalling patterns. While it is possible to introduce as many initial fracture disks as there are elements in the model where the damage criterion is met, the modelling approach is not intended to model the growth of every individual fracture at the borehole wall numerically. Instead, a few initial disks are placed in areas with the highest damage, and they subsequently propagate to locations where the growth criteria are satisfied.

4.3.3.3 Fracture propagation exponents

Multiple studies (Renshaw & Pollard 1994*a*, Olson 1993, 2004, Thomas et al. 2020) have shown that fracture propagation exponents influence the degree of mechanical interaction between fractures that are growing concurrently as part of an array, thereby affecting the resulting fracture patterns in terms of fracture spacing, length, and clustering.

Renshaw & Pollard (1994*a*) developed a criterion for modelling concurrent fracture growth, which relates the specific energy release rate at the crack tip, $\mathcal{G}_n$, to the maximum energy release rate, $\mathcal{G}_{max}$, within a numerical domain containing multiple extending fractures. They numerically simulated the development of a fracture set in a linear elastic solid under constant remote stress, using a fracture mechanics approach and found the fracture spacing, length and clustering to be controlled by the propagation exponent β. The determination of the optimal β value was based on a comparative analysis of fracture tip locations between the numerical model and experimentally generated fractures developing in a brittle coating applied to acrylic polymethyl methacrylate (PMMA) sheets. $\beta = 0.35$ provided the closest agreement between the numerical and experimental fracture tips. Both the numerical and experimental parts of the study reproduced fracture patterns as observed in natural fracture systems.

This section analyses the behaviour of spalling-inducing fractures in three dimensions in accordance with Paris law, and investigates the sensitivity of the fracture growth to changes in the growth exponents. The values of the two propagation exponents β_f (used in Eq. 3.37) and β_n (used in Eq. 3.38) are examined, to explore the effect of growth velocity on fracture growth. Nine cases are simulated, with each growth exponent, β_f and β_n, varied between 0.0, 0.35, and 1.0.

Figures 4.14 and 4.15 show axial and radial views of fracture patterns after 10 growth steps for different combinations of β_f and β_n. The fractures are represented as lofted surfaces, whose isocurves are colored according to the growth step to highlight the evolution of growth during the simulation. A total number of 10 growth steps (including nucleation) are

shown. Larger values of the growth exponents are observed to reduce fracture interactions and reduce growth extent.

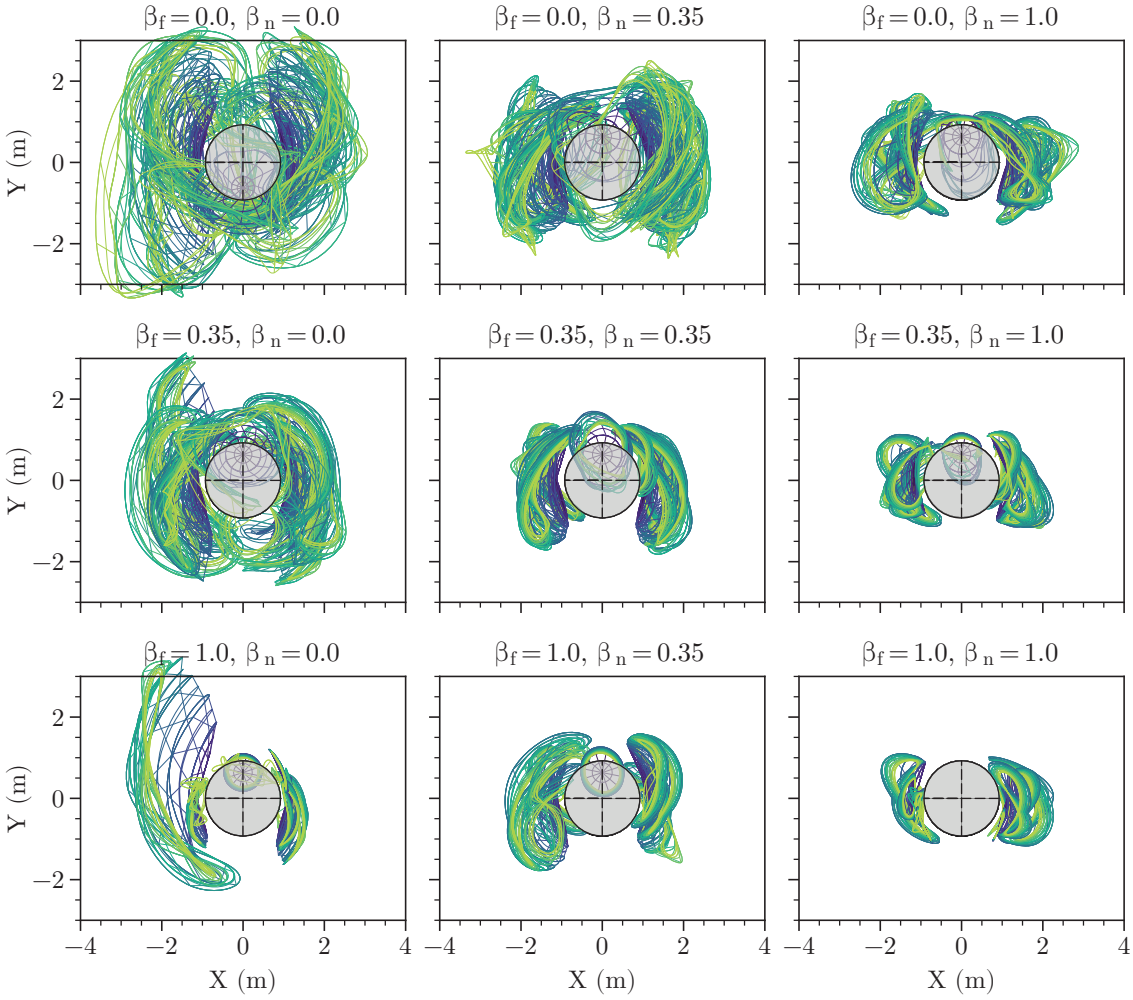


Figure 4.14: Radial views of fracture patterns after 10 growth steps illustrating the effect of the Paris exponents on fracture growth. The lofted fracture surfaces are shown through their isocurves and are colored according to the growth step to highlight the evolution of growth during the simulation. The simulations are performed using rock properties from Forsmark, with the exception of fracture toughness, which is decreased by a factor of 10 to promote growth and enable comparison of patterns from multiple steps.

Figures 4.15 and 4.14 demonstrate that for small values of β_f and β_n, the fracture propagation velocity exhibits limited dependence on the SIF distribution. Consequently, all cracks grow at a similar rate, irrespective of their proximity to other cracks. This is in agreement with Renshaw & Pollard's (1994*a*), who showed that lower propagation exponent means that fractures grow more uniformly, resulting in less clustering. β_f and β_n values of zero mean that extension is independent of the stress intensity factor range, and the tip energy release rate is not taken into account. In this case, all tip nodes from across all fractures extend by the given extension length Δl_v at every growth step. In this case, the effect of β

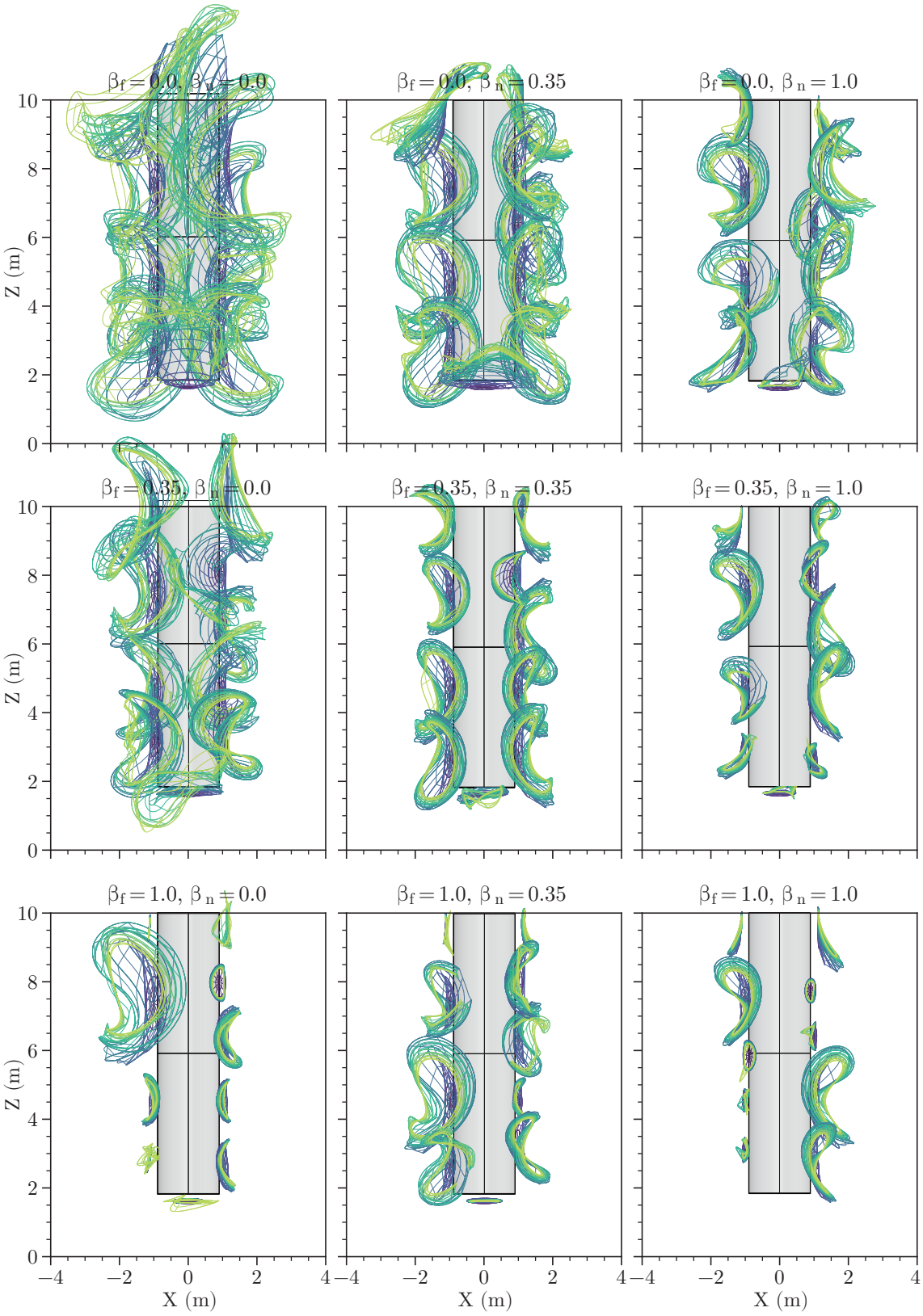


Figure 4.15: Axial views of fracture patterns after 10 growth steps illustrating the effect of the Paris exponents on fracture growth. The lofted fracture surfaces are shown through their isocurves and are colored according to the growth step to highlight the evolution of growth during the simulation. The simulations are performed using rock properties from Forsmark, with the exception of fracture toughness, which is decreased by a factor of 10 to promote growth and enable comparison of patterns for the different β cases.

is not at all simulated and growth is not influenced by the Paris law. Values of $\beta_f \geq 1$ and $\beta_n \geq 1$ mean that the fracture growth rate is directly proportional to the stress intensity factor range and the propagation is governed by the individual fracture and tip energy. The extension per growth step is in this case influenced by variations in the fracture tip energy release rate $\mathcal{G}_n$ across the fracture tips and has been shown to result in fracture patterns where the most energetically favorable fractures and tips activate and propagate (Thomas et al. 2020).

Conversely, for large values of the propagation exponents β_f and β_n, the fracture propagation velocity strongly relies on the SIF distribution. This implies that only tips with the highest SIFs experience rapid growth, while others grow slowly or may even cease to propagate. This is demonstrated in Figure 4.16, which quantifies the fracture surface area during the 10 growth steps, for each individual fracture surface shown in Figures 4.14–4.15.

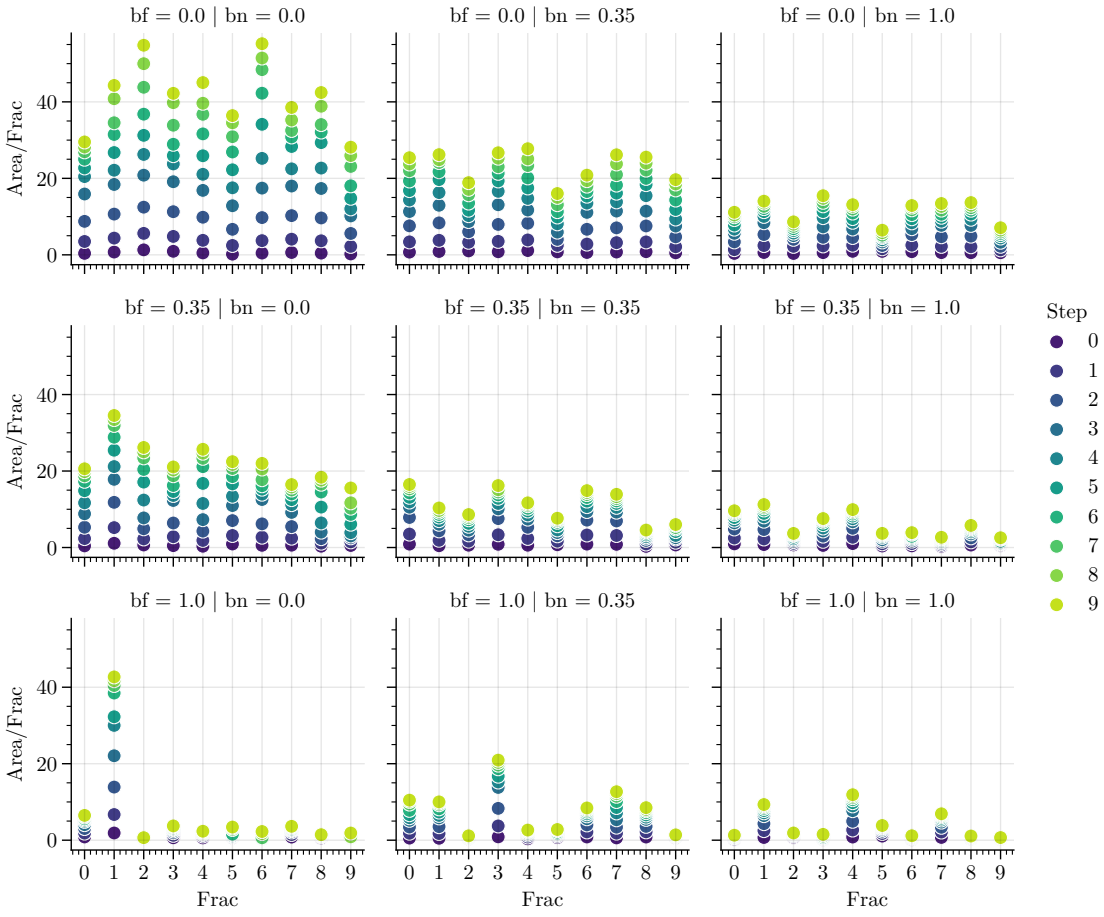


Figure 4.16: Effect of the Paris exponents on fracture growth showing fracture area per growth step for the fractures shown in Figs. 4.14 and 4.15. Each point represents cumulative area up to and including the respective growth step.

Notably, fractures in close proximity to each other have higher SIFs due to mutual inter-

actions, leading to increased stress concentration at the crack tips. As a result, the final fracture array resembles the initial flaw distribution, and the final fracture patterns exhibit significant clustering. This clustering promotes interaction, resulting in some regions with a lot of growth vs other regions with little or no growth.

4.3.3.4 Maximum extension length

Thomas et al. (2020) showed that the scaling of fracture extension by Δl_v (Equation 3.37) is required in models with relatively high values of β_n to accelerate the time required for a fracture array to reach a stable configuration. Fracture growth in cases of high values of the exponent β_n was observed to be more pronounced in the larger, or more favourably oriented initial fracture disks, effectively mimicking high velocity fracture growth.

The scaling of fracture extension by Δl_v (Equation 3.37) results in a minimal augmentation of the fracture surface area for models with elevated values of β_n. Hence, to attain an equivalent fracture surface area, models with high β_n necessitate a greater number of steps compared to those with low β_n.

In this work, the maximum extension length, Δl_v, is employed to scale the calculated fracture extension per growth step. To depict multiple growth increments prior to the fracture surfaces encountering the borehole wall, Δl_v values less than one borehole radius are utilised. The utilisation of larger Δl_v values reduces the number of growth steps required for a fracture array to attain a stable configuration.

4.4 Conclusions

This chapter demonstrated that borehole deformation and ensuing fractures respond realistically to the applied mechanical and thermal loads after borehole drilling and borehole heating. The mechanical and thermo-mechanical responses of the host rock in the vicinity of deep-drilled boreholes prior to fracture nucleation and growth were validated against closed-form analytical solutions and showed good agreement. The damage model is used to characterise progressive damage accumulation, from which the fracture disks causing spalling nucleate. The full separation of spalled rock fragments is not explicitly simulated, but can be inferred from the damage field, and the final patterns of the “spalling” fractures.

The SIFs computation was also validated for a single fracture under uniaxial tension and compression, respectively. For each loading mode, two cases were considered, where the fracture surface was constructed through triangulations, and through lofting, respectively. The numerical SIF error for a single fracture under uniaxial tension was less than 4%,

7%, and 3% for K_I, K_{II}, and K_{III}, respectively and less than 5% for all modalities under uniaxial compression. In addition, the lofted surface improved meshing efficiency. To validate fracture growth in subsequent steps, the spalled zone geometry was compared to fractures observed in field experiments. This step was necessary because once the initial disks lose their elliptical geometry and extend to form complex fracture surfaces, the analytical closed-form solutions for the SIFs are not valid.

Simulation-specific parameters involved in fracture nucleation and growth such as the maximum number of fractures, initial fracture disk size and spacing, propagation exponents and extension length were varied to assess their influence on the final fracture patterns. The initial nuclei number, sizes and spacing do not affect the final patterns, as they grow concurrently and interact during growth, conforming with the new state of the deformation in the numerical domain at every simulation step. These results qualitatively match those of Olson (1993), Renshaw & Pollard (1994*a*), Renshaw (2000). The fracture patterns were also validated quantitatively against field observations by comparing damage, spalling depths and spalling widths with those observed around the well-documented Mine-by tunnel. Fractures that developed in the spalled zone extended up to 55 cm in the radial direction, in line with in situ field observations. Fracture patterns match the ones observed in the field, confirming the reliability of the proposed methodology in modelling spalling.

This section validated the finite element-based discrete fracture growth modelling approach, which presents several advantages over continuum models. One significant advantage is its ability to accurately depict the discrete nature of the fracturing process. The 3D modelling approach considers the growth of fractures and their spatial interactions, influencing the evolution of density and topology of the Excavation Damaged Zones (EDZs) surrounding the underground excavations.

The 2D models of spalling assume plane strain conditions, implying that the boreholes around which EDZs and spalling occurs are infinitely long. However, this assumption does not align with the current nuclear waste disposal concepts, where relatively short (8 m) deposition boreholes are planned to accommodate the spent fuel canisters. The present modelling approach allows for the observation of fracturing behaviour at various locations along the borehole, encompassing the excavation face and borehole bottom face. The following chapters, which model spalling around the prospective boreholes at the Swedish Forsmark site, will showcase how fracture interactions in the third dimension, particularly when the effects of the deposition tunnel are included, significantly influence fracturing behaviour.

Chapter 5

Mechanical Spalling

5.1 Introduction

This chapter focuses on mechanical (M) evolution of spalling-inducing fractures, which are expected to develop in the vicinity of the deposition boreholes and tunnels of a typical repository for nuclear waste. The Swedish Forsmark site is chosen to investigate the effect of *in situ* stresses, heterogeneities, and repository design parameters such as the deposition tunnel and its orientation, borehole geometry and borehole spacing, on the potential damage and fracture extent. Since no deposition boreholes have yet been drilled at Forsmark, this chapter also presents the first numerical predictions of fracture growth which may lead to mechanical spalling at the planned repository site.

5.1.1 Forsmark repository site

The Swedish Nuclear Fuel and Waste Management Company (SKB) has been undertaking site characterisation work nearby the Forsmark nuclear power plant, where Sweden's deep geological repository for spent nuclear fuel will be constructed. Forsmark is located in northern Uppland, approximately 170 km north of Stockholm. The prospective repository will be drilled at 500 m depth, in crystalline host rock that formed during the Svecokarelian orogeny, between ca. 1.89–1.85 Ga (SKB TR-06-09 2006).

During its tectonic history, the bedrock at Forsmark has been subjected to high temperature ductile deformation, which manifests today as large-scale high strain zones, in which the bedrock is strongly foliated, banded, and heterogeneous (SKB TR-06-09 2006). These highly-deformed zones encompass areas in which the bedrock experienced lower levels of ductile strain, named tectonic lenses. The tectonic lenses are lithologically more consistent, as they were subjected to less deformation and folding than the high-strain zones

(SKB TR-06-09 2006). SKB has selected the north-western part of the Forsmark tectonic lens as the target area for the future repository site. The deep geological repository is estimated to occupy an area approximately 6 km long and 2 km wide within the tectonic lens. The Forsmark tectonic lens spans from the coast north-west of the nuclear power plant towards Öregrund, situated in the south-east, and it is approximately 25 km long and 4 km wide (Figure 5.1).

The deep geological repository at Forsmark will involve drilling, excavating, and eventually backfilling a range of underground structures of different geometries and sizes, such as access tunnels, deposition tunnels and deposition boreholes (SKB R-07-31 2007). One of the key issues that remains under investigation is the stability of the underground openings, and more specifically, the impact of stress-induced fractures on the deposition tunnels and boreholes, as well as their effect on the properties of the immediately-surrounding host rock. Understanding how over-stressed rock will behave following the creation of these voids will ensure an effective repository design and its long-term stability and maintenance.

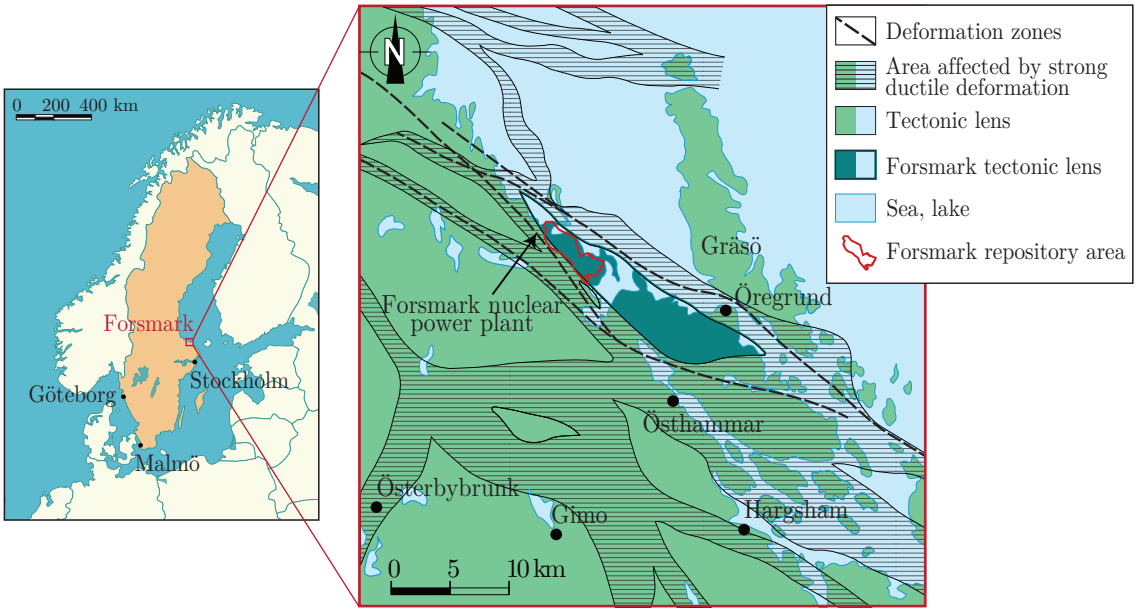


Figure 5.1: Location and general tectonic setting of the planned deep geological repository at Forsmark, showing the future deposition area lying within the Forsmark tectonic lens. Most of the repository will be located onshore, with the northernmost areas close to the Forsmark nuclear power plant extending offshore. Adapted from SKB TR-06-09 (2006).

SKB has drilled several telescopic boreholes at various locations throughout the planned repository area (Figure 5.2), as part of their site investigation work (SKB R-07-26 2007, SKB P-07-166 2007). These were were percussion drilled with a diameter of ca. 200–250 mm in the first 100 m, and core drilled with a diameter of ca. 77 mm in the following 1,000 m. At repository depths, many of the investigation boreholes presented typical breakout patterns (Figure 2.2), with widths and depths in the range of 40-180° and 0.2-67.5 mm

respectively. Although the dimensions and excavation methods of the telescopic boreholes are different from those of the deposition boreholes (SKB R-08-116 2009), which will accommodate the spent fuel, the occurrence of spalling patterns is an indicator of possible stress-induced fracture growth impact on the future deposition boreholes.

The telescopic boreholes also provided additional information on the major deformation zones and host rock lithologies at surface and at repository depth. Figure 5.2 shows a simplified geological map of the Forsmark site and its surroundings. The main host rock lithologies within the future repository site are medium-grained and metamorphic granite and granodiorite (Figure 5.2). These lithologies comprise the bulk of rock domain RFM029, which is the the predominant volumetric domain in the Forsmark tectonic lens. The Forsmark site is described extensively in SKB's Technical Report SKB TR-08-05 (2007), which presents the integrated understanding of the bedrock geology, hydrogeology, rock mechanical and thermal properties, *in situ* stresses, and existing fracture domains and deformation zones.

Figures 5.1 and 5.2 also motivate the assumption of an initially isotropic, homogeneous, and linear elastic brittle rock domain to model spalling in this chapter. This assumption relies on the observation that most of the Forsmark repository area is located within the same geological facies, and the main lithologies comprising this facies are crystalline, *i.e.* the host rock has no porosity and no natural permeability.

5.2 Numerical model set-up

5.2.1 Rock properties

Table 5.1 shows the material properties, *in situ* stresses and simulation parameters used in this chapter to simulate spalling at the Forsmark site. With the exception of Mode I fracture toughness, which corresponds to the Äspö diorite (Andersson 2007), the rock mechanical properties are representative of the metagranite / granodiorite in rock unit RFM029, which is the most frequent lithology throughout the Forsmark repository area (Figure 5.2).

There are currently no measurements of fracture toughness available at Forsmark, but SKB is conducting tests to estimate it. The *in situ* stress magnitudes are the average values found at 500 m depth, where the deposition boreholes will be excavated. σ_h and σ_H are the minimum and maximum far-field horizontal stresses respectively, and σ_v is the vertical stress, corresponding to the weight of the overburden at 500 m depth at Forsmark (SKB R-08-116 2009).

Table 5.1: Rock properties (SKB TR-08-05 2007), damage parameters and *in situ* stress magnitudes (SKB R-08-116 2009) defined for the numerical simulations of deformation, fracture and damage of the Forsmark case.

Simulation parameter	Value
Rock properties	
Density	2730 kg/m^3
Young's modulus	76 GPa
Poisson's ratio	0.23
Uniaxial compressive strength	226 MPa
Tensile strength	13 MPa
Fracture toughness	3.8* MPa/m$^{1/2}$
In situ stresses	
σ_H	41.0 $\pm$ 6.2 MPa
σ_h	23.2 $\pm$ 4.6 MPa
σ_v	13.2 $\pm$ 0.3 MPa
Damage parameters	
ε_0	3.2×10^{-4}
A_c	0.73
B_c	1816
A_t	0.73
B_t	1816
Fracture growth parameters	
Number of fractures	variable
Initial disk radius	variable
K_{IC}/K_{IIC}	0.7540
K_{IC}/K_{IIIC}	1.5881
β_f	0.25
β_n	0.75
Δl_v	0.25

* Mode I fracture toughness value of the Äspö diorite, taken from the APSE experiment (Andersson 2007), as there were no measurments of fracture toughness at the Forsmark site, at the time when this work was conducted.

The Mazars damage parameters used to compute the damage variable d (Equation 3.25) were estimated by fitting the post-peak part of the stress-strain curves from laboratory tests on core samples from Forsmark (Figure 4.4). The experimental data was obtained by SKB through uniaxial compression (SKB P-05-211 2005, SKB P-04-224 2004) and indirect tensile (SKB P-05-212 2006) tests on pegmatite samples. Although the main repository host rock at Forsmark is a granodiorite, the pegmatite approximation should be sufficient, given their similarity. This can be confirmed in future analysis when relevant data from experimental tests on granodiorite becomes available. Section 4.2.2 showed that most

rock samples have comparable damage parameters, since the brittle stress-strain response of the samples in the post-failure stage is similar. Figure 4.4 shows the least-square fit of Equation 3.20 on the compression and tension data respectively. The values given in Table 5.1 are average values from the samples shown in Figure 4.4.

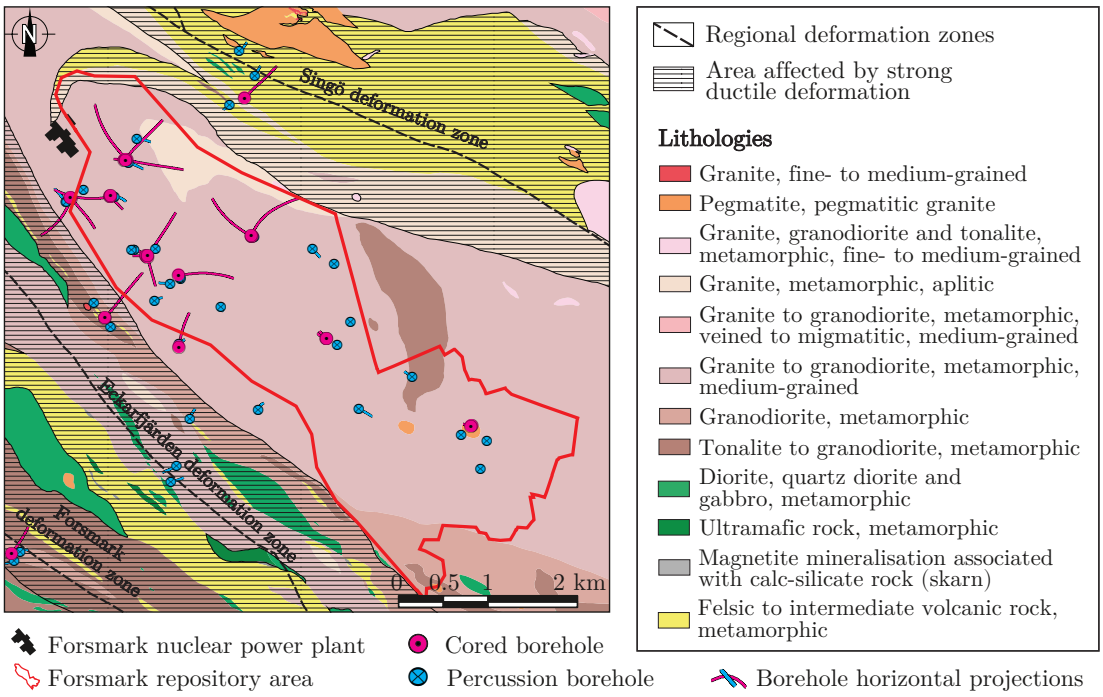


Figure 5.2: Geological map of the Forsmark site, showing the repository area in a less deformed and relatively more homogeneous rock unit, predominantly comprising of granite and granodiorite. The repository area is flanked in the north-east and in the south-west by areas affected by strong ductile deformation. Adapted from SKB TR-06-09 (2006), with some of the infrastructure and map ornaments removed for clarity.

5.2.2 Model geometry and boundary conditions

The borehole (Figure 5.3a) and tunnel (Figure 5.3b) geometries used in this chapter are those currently planned for the final repository (SKB TR-06-09 2006) that will be constructed at the Forsmark site. They are incorporated in the following simulation cases:

- *Single borehole model* (Figure 5.4a) - used in Section 5.3: a 20×20×20 m block model, containing a 1.75 m diameter circular vertical borehole, subjected to a far-field anisotropic triaxial stress. Far-field stresses σ_v, σ_h and σ_H are applied on the top, left and front domain boundary surfaces respectively, and displacements are fixed, for numerical convergence, on the faces and edges symmetrically opposite to the faces and edges where the stresses are applied. Roller boundaries (circle symbols) show the direction in which outer nodes can "move" freely. The corner nodes, where three constrained boundaries intersect one another, are constrained

in all three directions (triangle symbol). The inner nodes belonging to the free excavation surface are not constrained in any direction.

- *Deposition tunnel model* (Figure 5.4b) - used in Section 5.3: a 50×100×50 m block model, with a 50 m long horseshoe-shaped deposition tunnel explicitly inserted as a separate body, and the same circular borehole now emerging from the floor of the tunnel.

- *Simplified borehole and tunnel model* (Figure 5.4c) - used in Sections 5.3 and 5.4: similar to the simple borehole model, but the borehole is attached to a "free" boundary simulating the effect of the deposition tunnel. The "top" domain boundary is split into three surfaces and no vertical forces (σ_v = 0 MPa) are applied on the nodes belonging to the tunnel floor. The "free" surface is illustrated as a 4.2 m wide red-coloured "stripe", which corresponds to the width of the deposition tunnel floor. The rest of the "top" boundary is subjected to the vertical stress estimated at 500 m depth at Forsmark, as triaxial stress conditions return away from the tunnel floor.

- *Modified borehole model* (Figure 5.3a) - used in Section 5.5: The 1.75 m diameter circular borehole is enlarged at the top, in a cone shape and a wedge shape, respectively. Modified borehole geometry can potentially facilitate the emplacement of the spent fuel canister by providing additional space to maneuver the canister during its deposition (Pusch 2008, SKB R-07-31 2007).

- *Multiple borehole model* (Figure 5.4d) - used in Section 5.6: The same as the simplified borehole and tunnel model, with additional boreholes on either side of the central borehole, aligned along the tunnel axial direction. Several borehole spacings are tested, on a three-borehole model, as well as the effect of increasing the number of boreholes in the model to five and seven.

The *single borehole model* (Fig. 5.4a) represents the three-dimensional equivalent of the majority of two-dimensional numerical models of spalling around a single circular borehole, which do not take into account the effect of the deposition tunnel. This case is not entirely realistic; however, it represents an advancement from the most two-dimensional models present in the literature (Hajiabdolmajid et al. 2003, Shen & Barton 2018, Vazaios et al. 2019), as it simulates fracture development in three-dimensions under full triaxial stress conditions. Given the limited number of studies in three-dimensions (Shi et al. 2022), this simpler case may serve as a bridge between existing literature and upcoming, more realistic models of fracture growth under more complex boundary conditions. This case is also representative of spalling at the mid-height of the borehole, where the impact of the deposition tunnel is less prominent, and serves as a benchmark against which the *simplified borehole and tunnel model* (Fig. 5.4c) is compared in Section 5.3 to evaluate the effect of the deposition tunnel.

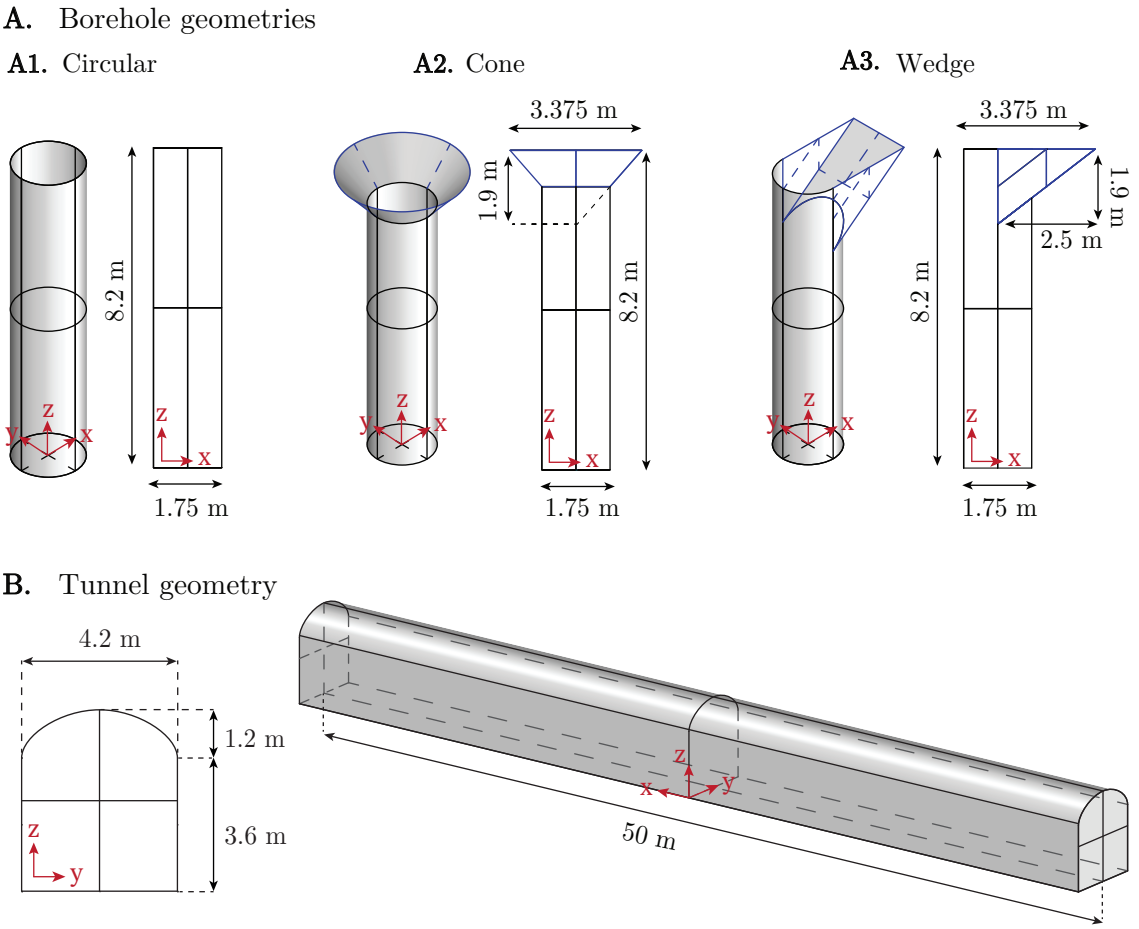


Figure 5.3: Schematic representation of: **A.** several deposition borehole and **B.** deposition tunnel geometries used in the simulation cases presented in this chapter.

In the *single borehole model* (Fig. 5.4a) and the *simplified borehole and tunnel model* (Fig. 5.4c), the excavation of the borehole is performed in a single step, and the resulting damage is calculated along with the nucleation of fractures. Similarly, in the *deposition tunnel model* (Fig. 5.4b), an additional excavation step is introduced for the deposition tunnel, where the excavation of the tunnel is also performed in one step and the displacements, strains, and stresses are calculated in the model that only includes the tunnel. Subsequently, the borehole is excavated in one step and the stresses are recalculated in the full model that includes both the borehole and the tunnel. Finally, fractures are nucleated in the model that comprises both excavations.

In reality, the excavation method for deposition tunnels will be drill and smooth-blast, while for deposition boreholes, it will be full-face down-the-hole drilling. Boreholes have been excavated by SKB at another location (Äspö HRL) using this technique, which resulted in minimal excavation damage to the rock. On average, the total time required to complete a 1.75 m diameter, 8.5 m length borehole was 105 hours, with the fastest

completion time being 30 hours. Stress conditions at Äspö HRL were not conducive to the formation of breakouts, however, based on other field experiments, such as the AECL's Mine-by Experiment, it is known that it may take 4-8 months for the spalling failure process to stabilise at different locations along the tunnel. In this chapter, the borehole is excavated in one step, and fractures are grown quasi-statically, based on the relative duration of borehole drilling compared to fracture growth observed in the different field studies.

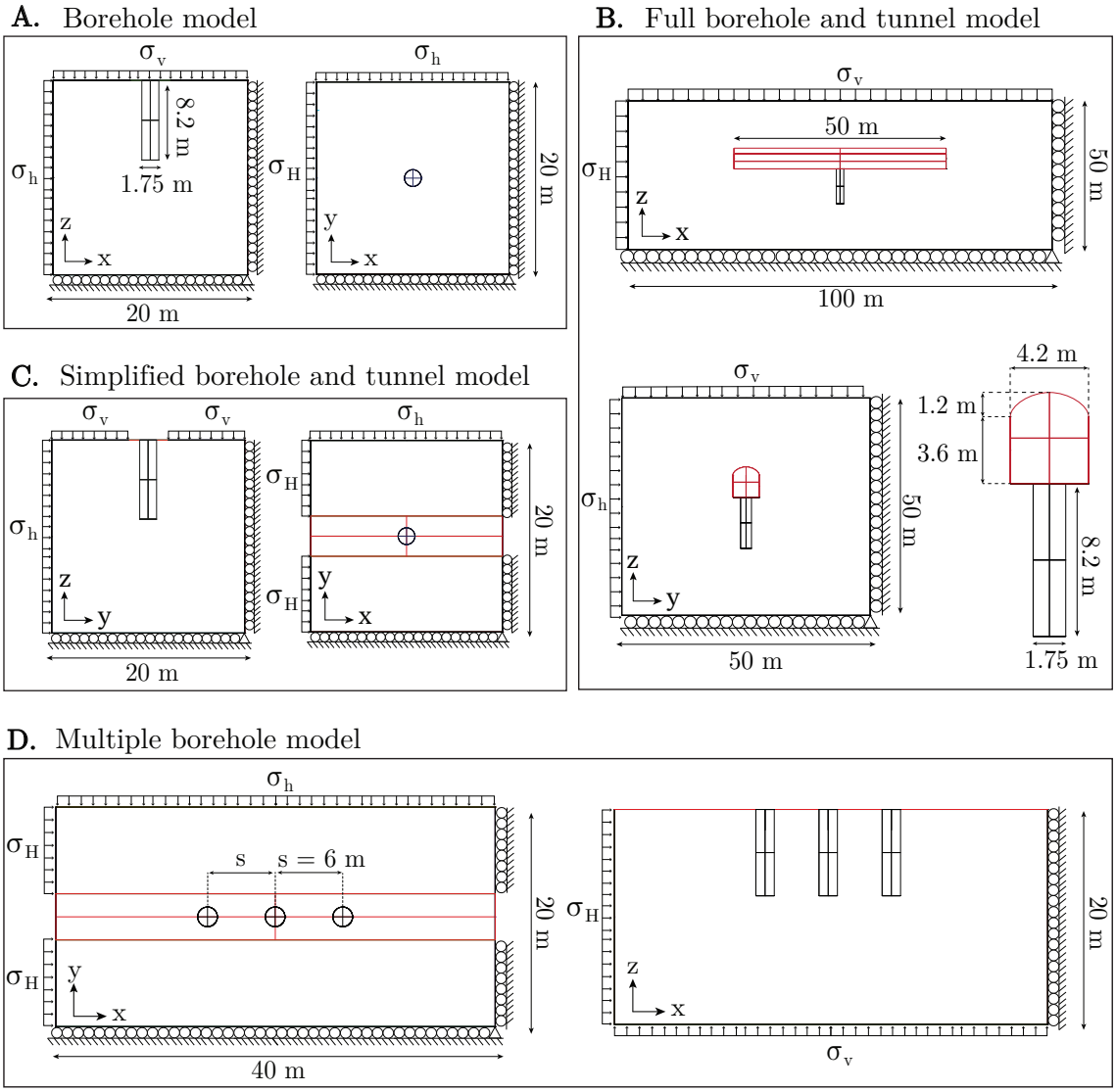


Figure 5.4: Model geometries and boundary conditions for the different simulated cases: **A.** Simple borehole model under triaxial load; **B.** Deposition tunnel model incorporating the full deposition tunnel explicitly; **C.** Simplified borehole and tunnel model with the same geometry as in 5.4a, but modified boundary conditions at the top domain boundary, such as the deposition tunnel floor (red-coloured stripe) is modelled as a free surface. **D.** Multiple borehole model, in which the domain is enlarged in the direction of the tunnel floor, to avoid lateral boundary effects. In all cases, σ_h and σ_H are the minimum and maximum horizontal far-field stresses respectively, and σ_v is the vertical stress, given by the weight of the overburden at 500 m depth at Forsmark.

5.2.3 Model sizes and simulation costs

The motivations for the various simulation cases outlined in Section 5.2.2 are twofold: (a) to model the impact of the deposition tunnel on the growth of fractures leading to spalling in the vicinity of the deposition boreholes, which has not been considered in previous numerical studies (Hajiabdolmajid et al. 2003, Shen & Barton 2018, Vazaios et al. 2019), and (b) to optimise the analysis of various *in situ* stress conditions and borehole geometries by reducing the size of the full borehole and tunnel model (Figure 5.4c) while still preserving the effect of the deposition tunnel.

Figure 5.5a illustrates the increasing mesh complexity as the deposition tunnel is partially and fully incorporated. The meshes correspond to the three different simulation models of spalling around a single borehole (Fig. 5.4a, 5.4b and 5.4c). In each case, the domain boundaries are placed sufficiently far away from the borehole and the tunnel walls, so that the stress field around the excavations is influenced only by the internal boundaries, *i.e.* the tunnel and the borehole walls, and there are no erroneous concentrations due to the effect of the external domain boundaries. The redistributed stress after excavation agrees with the analytical solution at mid-height of a borehole in a semi-infinite medium, and hence the domain boundaries do not have any influence on fracture growth.

As growth progresses, fracture geometry becomes increasingly complex, resulting in the emergence of more refined meshes around the fracture tips. This significantly increases the number of nodes in the full borehole and tunnel model (Fig. 5.5a, **A3**), as compared with the other two models in which only the deposition borehole is fully incorporated (Fig. 5.5a, **A1** and **A2**). The numerical model in which the horseshoe deposition tunnel is modelled explicitly is significantly larger and computationally more expensive to run as fracture growth iterations progress (Fig. 5.5b).

In all models (Fig. 5.5c), the majority of the iteration time is consumed by lofting and meshing the geometry, accounting for 50-75% of the time. This process involves constructing the NURBS fracture surfaces, (re-)meshing the evolving geometry, and mapping the properties from the previous mesh onto the current one. The deformation step, which involves setting up the element contributions, applying initial and boundary conditions, solving for displacements, and computing strains and stresses, takes up approximately 20% of the iteration time. The fastest aspect of the algorithm is the computation of fracture growth, including the calculation of SIFs and tip propagation.

Figure 5.5c motivates the decision to simplify the full borehole & tunnel model in the situations in which spalling around the full deposition tunnel is not of interest, and incorporate the tunnel effect by modifying the boundary conditions at the top of the the simple borehole model with a free surface representing the tunnel floor (Figure 5.4c).

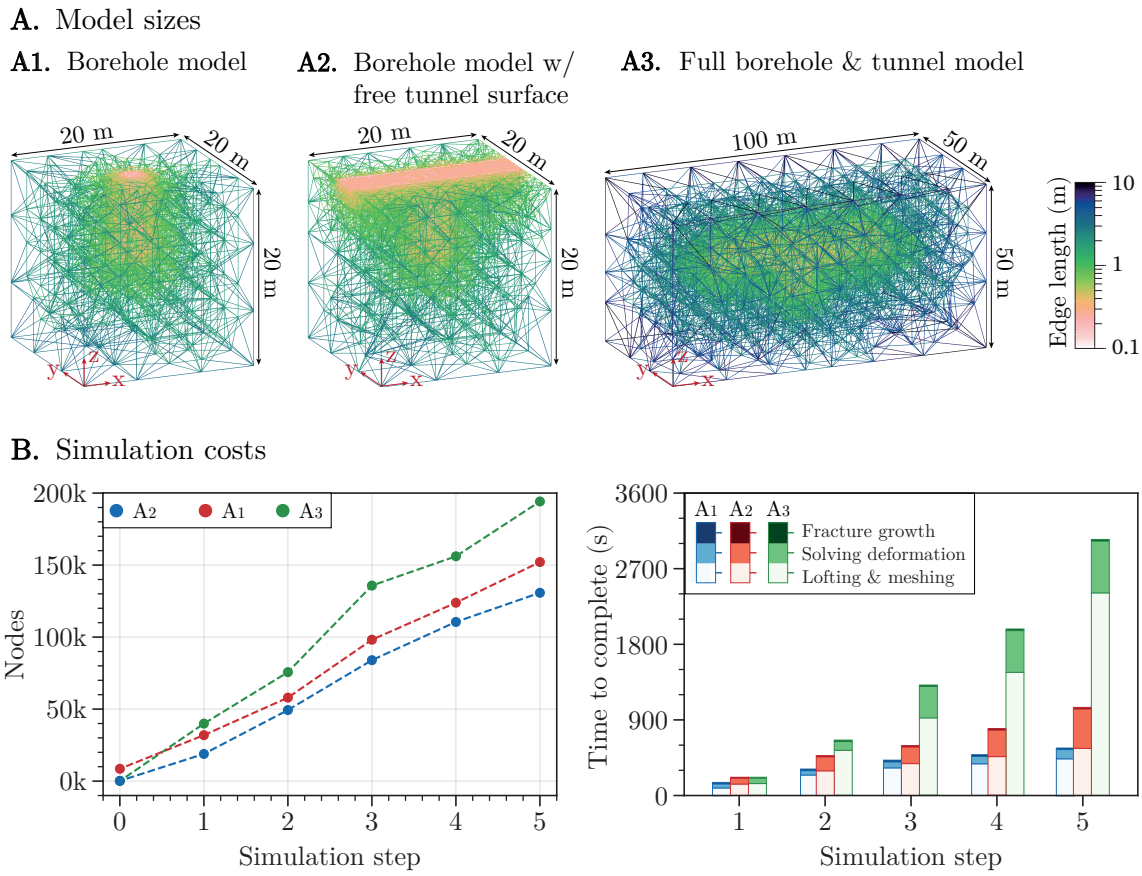


Figure 5.5: Typical simulation sizes showing: **A** Distributions of element sizes, plotted as element edge length in the single borehole model with no tunnel (**A1**), single borehole model with tunnel floor (**A2**) and single borehole model with whole tunnel (**A3**). In each case, the element size at the walls of the excavations is 10 cm. The meshes get progressively coarsened towards the domain boundary. **B** Number of nodes and time to compute iteration.

Figures 5.6a and 5.6b show the principal stress field around the deposition borehole in the *deposition tunnel model* (Fig. 5.4b) and in the *simplified borehole and tunnel model* (Fig. 5.4c), respectively. The stress field is nearly identical in the two simulation models where either the whole tunnel (Fig. 5.6a), or only the tunnel floor (Fig. 5.6b), was simulated. In both cases, the stresses redistribute around the free surfaces, with higher stress concentrations occurring around sharper boundaries.

Figure 5.6c shows the difference between the two models. To compare the two models, stress values were sampled at points the same *(x,y,z)* location in the two distinct grids and the percent difference was calculated between the sampled points at the same physical coordinates *(x,y,z)*. The error is not significant and can be explained mainly by the fact that the *simplified borehole and tunnel model* is not a perfect sub-model of the *deposition tunnel model*. Although the same borehole refinement was used in both models, the meshes are unstructured, resulting in two slightly different grids from where the stress values are sampled.

For a more rigorous comparison, the two models should use structured meshes of same size. This would allow for a one-to-one mapping, in order to compare stress values at the exact nodes. For the purpose of this work, and given that the range of uncertainty in underground stresses is orders of magnitude larger than the differences observed in Figure 5.6c, it is considered that the *simplified borehole and tunnel model*, in which the tunnel effect is modelled implicitly, is a sufficiently accurate approximation of the *deposition tunnel model*.

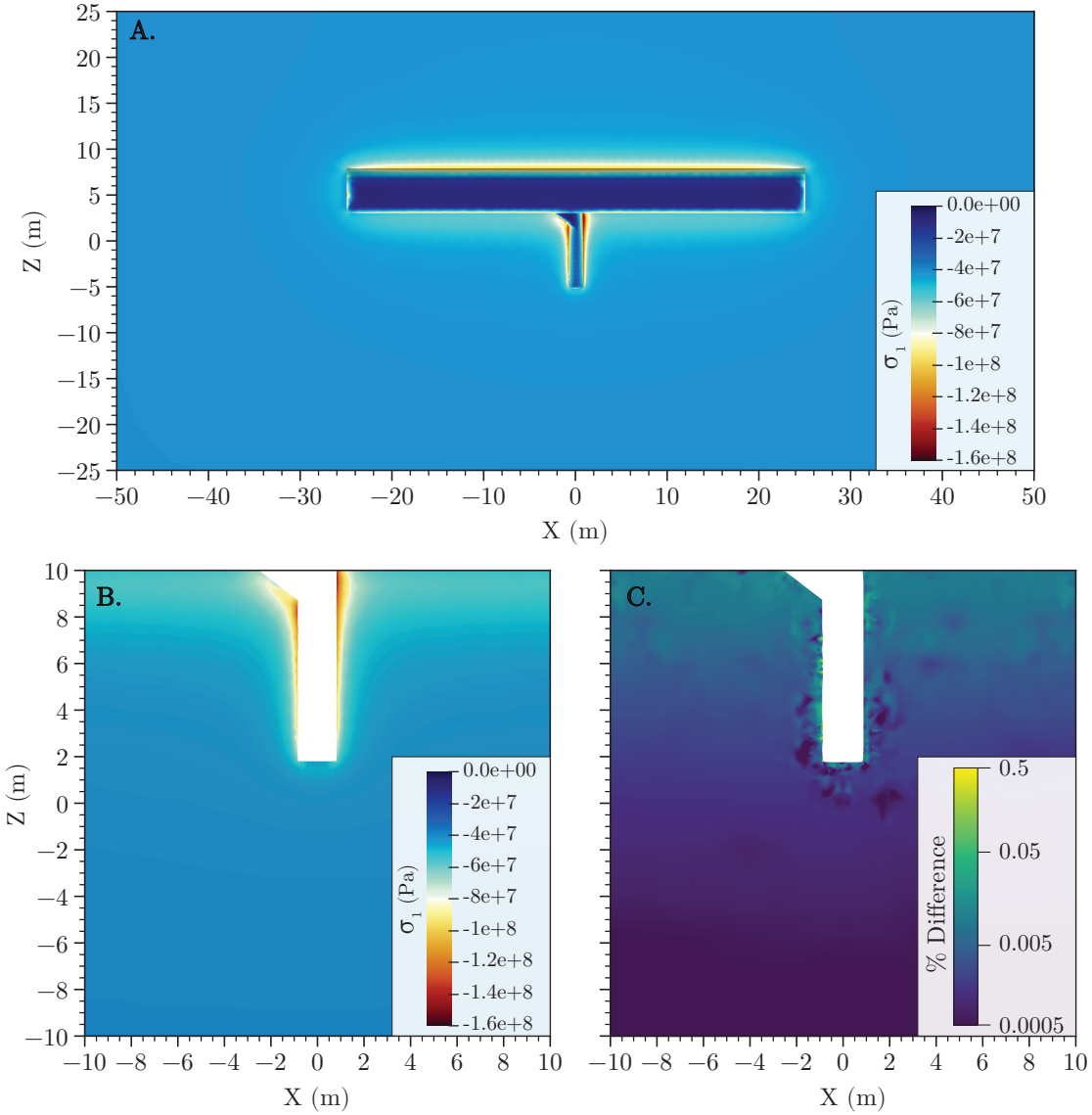


Figure 5.6: A. Maximum principal stress in the *deposition tunnel model* (Fig. 5.4b), in which the tunnel is modelled explicitly; **B.** Maximum principal stress in the *simplified borehole and tunnel model* (Fig. 5.4c), in which the tunnel effect is modelled implicitly; **C.** Percent difference between the nodal stesses computed in the two models.

5.3 Effect of the deposition tunnel

The current design of the deep geological repository at Forsmark comprises of multiple vertical colinear boreholes drilled from the floor of a horseshoe-shaped "deposition tunnel" (Figure 5.3b), whose role is to provide access to the deposition boreholes. The prevailing numerical studies of spalling, or borehole breakouts, focus on simulating the fracturing process around isolated excavations in two dimensions (Shen & Barton 2018, Vlachopoulos & Diederichs 2014, Vlachopoulos & Vazaios 2018, Vazaios et al. 2019) and do not take into account the effect of neighbouring excavations, such as other deposition boreholes, or the deposition tunnel.

The deposition tunnel is expected to affect fracture nucleation and growth patterns, through changing the stress state at the top of the deposition boreholes, where it acts as a free surface. The previous section demonstrated that the tunnel effect on the stress field around a vertical deposition borehole is successfully incorporated in the numerical simulations by either explicitly modelling the deposition tunnel as an individual excavation in a larger domain, or by modifying the boundary conditions at the top surface of the domain to mimic the tunnel floor. The latter option is preferable for computationally more efficient analyses of borehole spalling, as it employs a simplified domain, with a reduced number of nodes and elements (Figure 5.5).

5.3.1 Fracturing around a deposition borehole–deposition tunnel system

Figure 5.7 shows the damage (Equation 3.25) distribution in a full borehole and tunnel model, following the nucleation of the initial fracture disks. The tunnel is excavated in one step and the displacements, strains and stresses are computed in the model containing only the tunnel. Subsequently, the borehole is drilled in one step, and the stresses are re-computed in the full borehole and tunnel model.

Figures 5.7a–5.7c show separate instances of preferred nucleation loci in the full model containing 10, 50 and 100 initial disks respectively. The highest damage concentrations occur at the intersection of the tunnel floor and its sidewalls and at the intersection of the deposition borehole wall and the wedge-shaped access ramp. Numerically, the first fractures to nucleate are those at the edges of the tunnel floor (Figure 5.7a), followed by spalling of the borehole top/access ramp (Figure 5.7b), and finally spalling of the lower curvature surfaces such as the tunnel roof and the rest of the borehole wall (Figure 5.7c). These results are in line with experimental observations where fractures nucleate preferentially around sharp-edged boundaries (Hoek & Brown 1980, Gong et al. 2020).

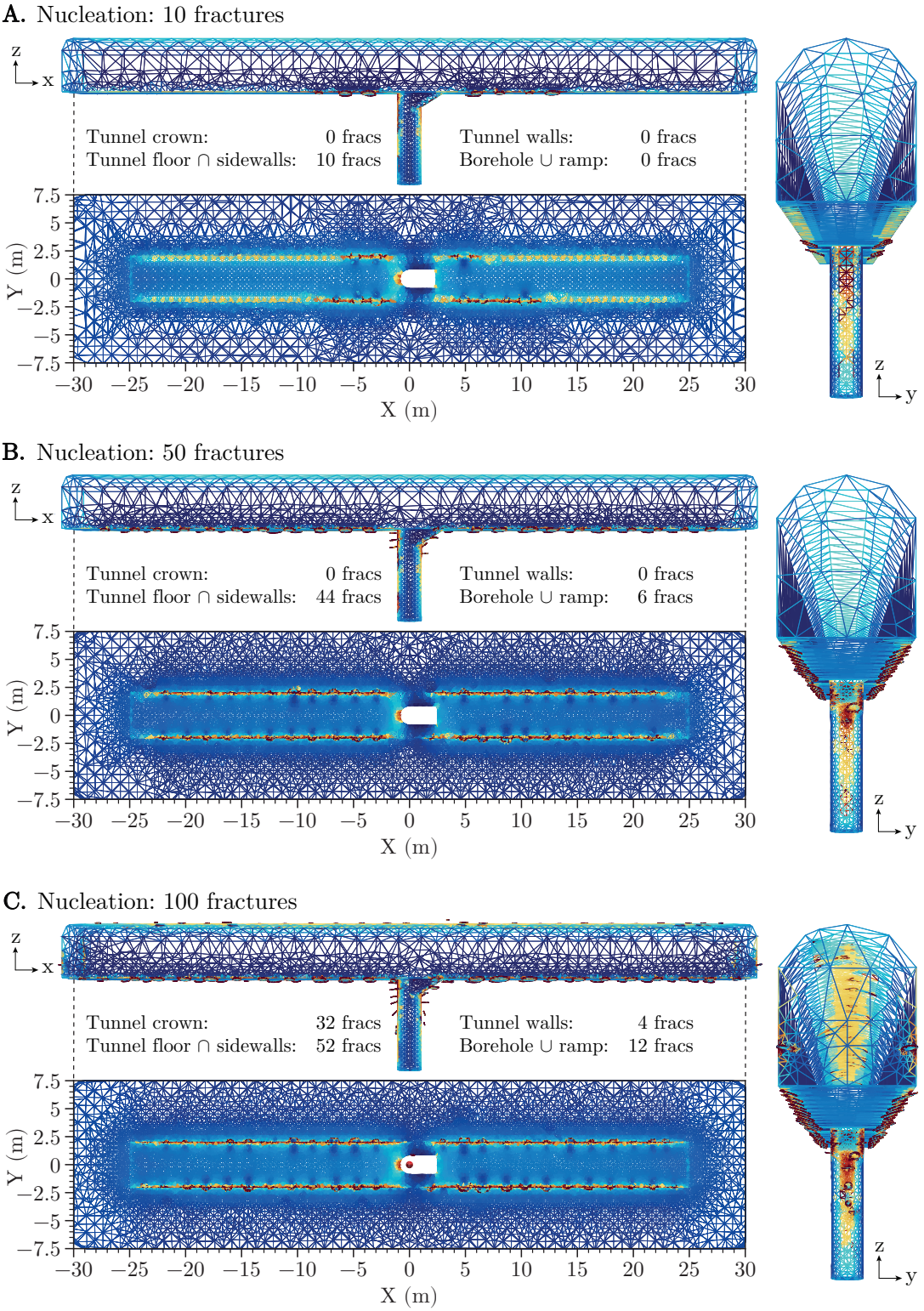


Figure 5.7: Damage and initial fracture disks distribution in the full borehole and tunnel model. First fractures to nucleate are at the tunnel floor/sidewalls (**A.**), followed by those at the borehole top (**B.**), and finally those at the tunnel roof and lower borehole walls (**C.**). The tunnel axis is oriented perpendicular to the maximum *in situ* stress direction. Simulation parameters and boundary conditions are those from Forsmark (Table 5.1).

Figure 5.7 showed an example of the complexity of a full borehole and tunnel model, which required hundreds of fractures to nucleate, in order to capture the complete state of the damage present around both cavities. Figure 5.8 shows an 800 fracture model, stacked in the cross-sectional plane around an excavation system comprising a deposition tunnel and eight deposition boreholes. Initial nucleation in the vicinity of the tunnel roof and side walls creates a swarm of interacting fractures. The fractures reorient during growth to extend sub-parallel to the tunnel roof and sidewalls, and coalesce in an *en-echelon* fashion, delineating sub-parallel rock slabs (Fig. 5.8c). This fracturing behaviour has also been observed by Lisjak & Grasselli (2014) and Gong et al. (2020), who simulated fracture development and spalling around similarly shaped excavations.

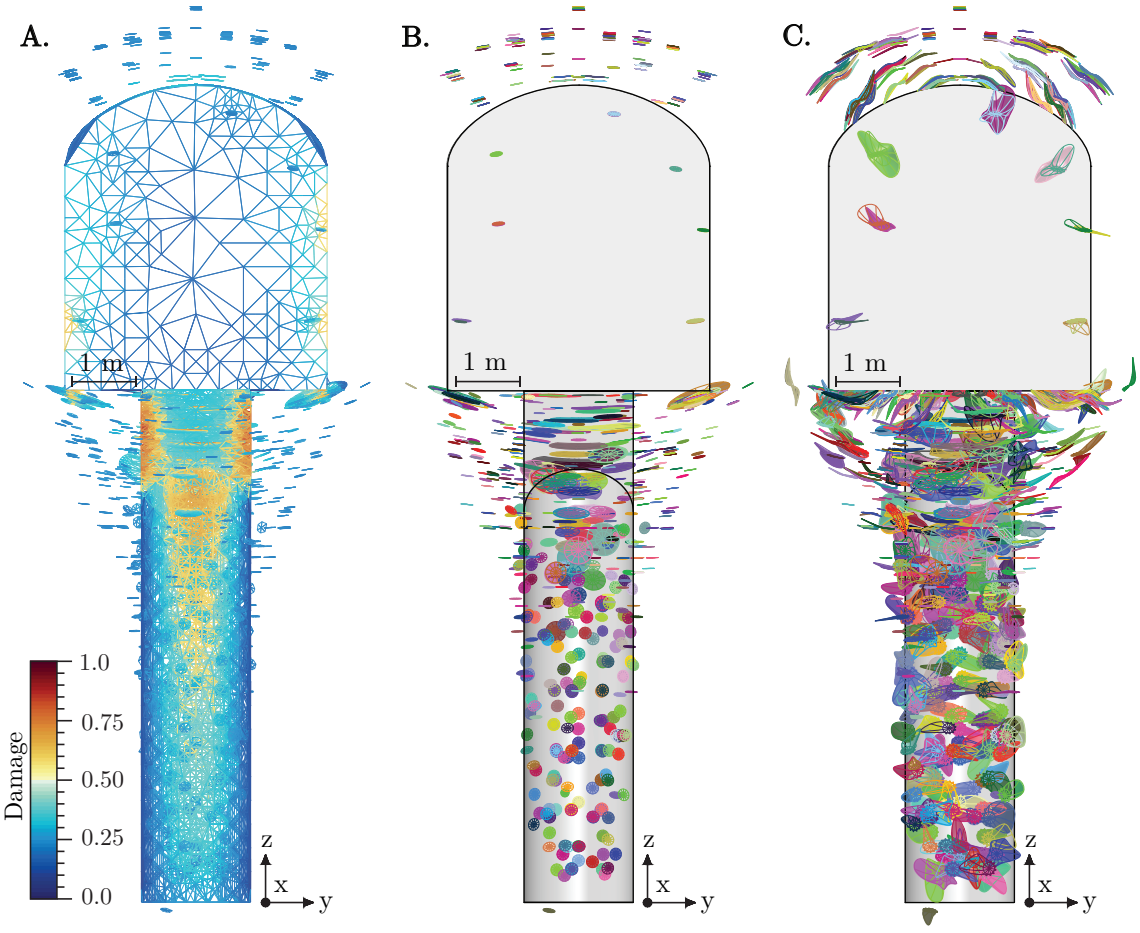


Figure 5.8: Sectional view of damage and fracture development around a horseshoe-shaped deposition tunnel and ramped deposition boreholes showing: **A.** surface meshes of internal interfaces (tunnel, borehole, initial fracture disks) coloured according to the damage value used for nucleation; **B.** rendered geometry from A, showing the initial disks in different colours to highlight their domains; **C.** fracture surfaces after one growth step.

Figure 5.9 shows the initial fracture fronts, each coloured according to the computed SIFs at their respective tip nodes. While there is a mixture of failure modes, only the fracture tips situated directly beneath the the tunnel floor, in the first approximately 0.5 m, and

those located around the roof of the tunnel, particularly near the crown, fail with positive K_I (Figure 5.9a). In these specific regions, tensile fractures open parallel to the tunnel surface. Conversely, the fractures within the borehole damage zone predominantly display negative K_I, with the exception of those developing perpendicular to the borehole wall in the immediate vicinity of the tunnel floor. Negative K_I indicates compressive failure, leading to a shear-dominated fracture growth, as shown in Figures 5.9b and 5.9c.

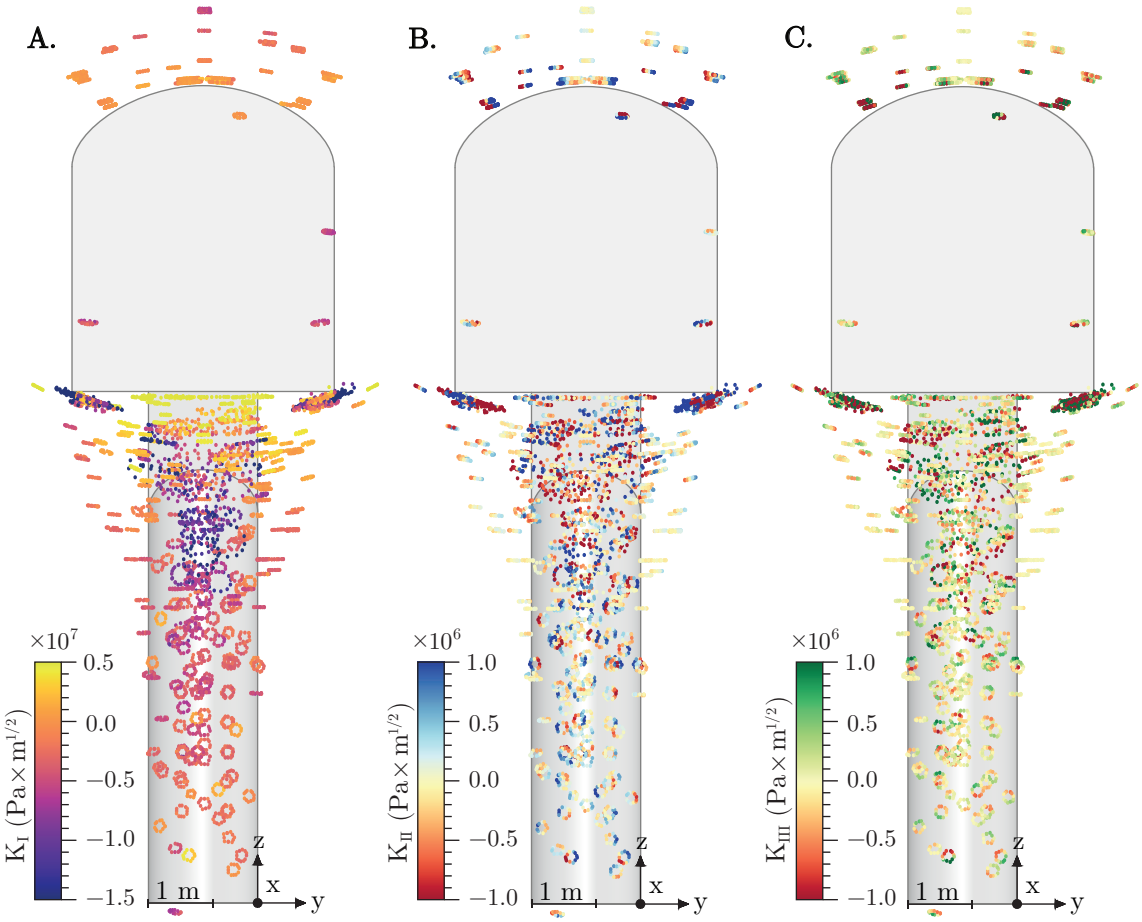


Figure 5.9: Sectional view of stress intensity factors around a horseshoe-shaped deposition tunnel and ramped deposition boreholes in the three principal deformation modes: **A.** opening (K_I), **B.** in-plane shearing (K_{II}), **C.** out-of-plane shearing (K_{III}). The simulation has 800 fractures and each fracture front comprises 12 tip nodes.

The mechanisms of fracture tip failure showcased in Figures 5.9 and 5.10 correlate with the different stress regimes that develop around the system of excavations, as one moves further away from the free excavation boundaries. As noted in several studies, the failure mechanism has been observed to shift from brittle splitting-type failure to shear-dominated failure with the increase of confining stress (Mogi 1972, Haimson & Chang 2000, Zhao et al. 2018).

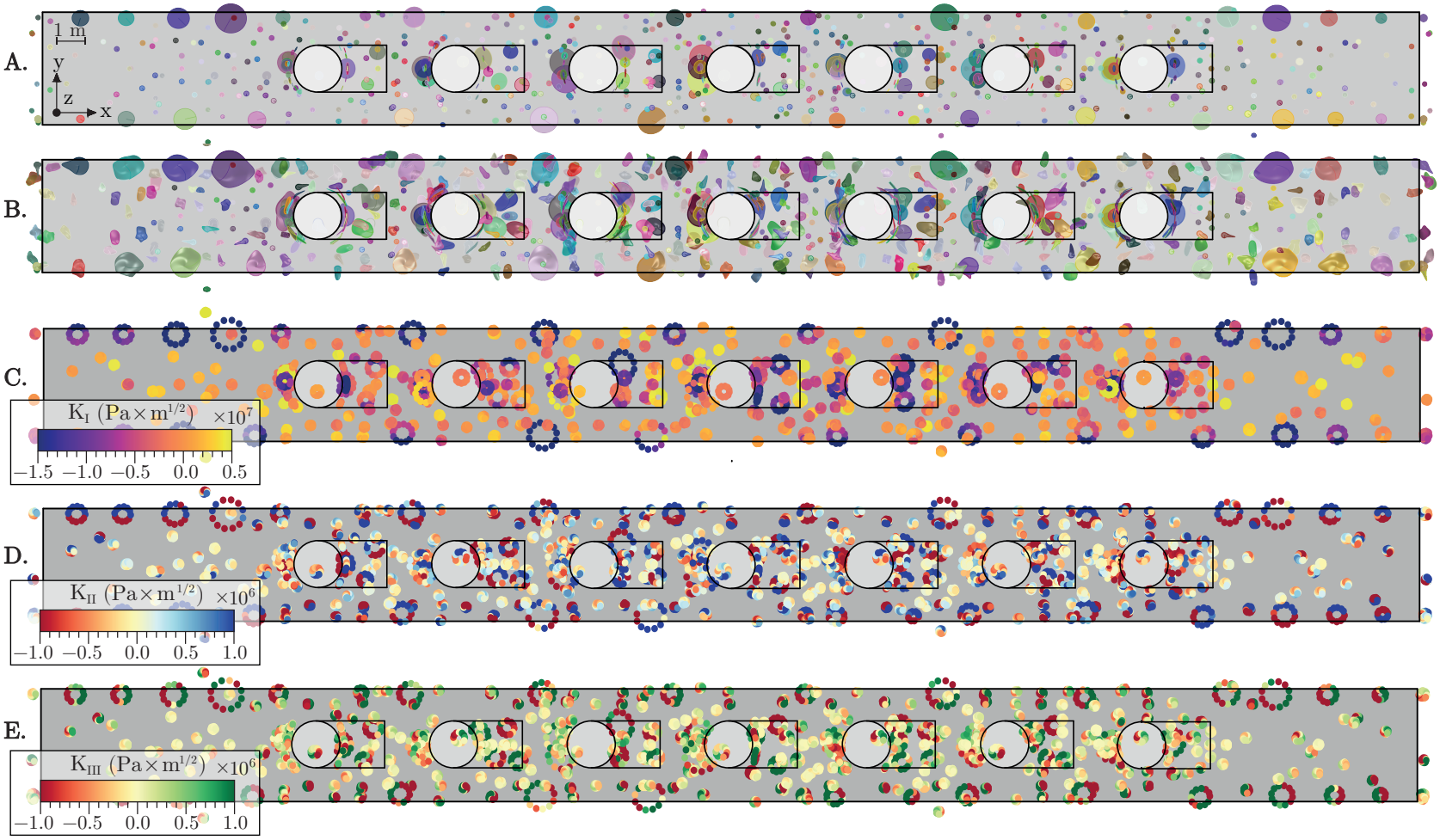


Figure 5.10: Sectional view of fracture development around a horseshoe-shaped deposition tunnel and ramped deposition boreholes showing: **A** rendered geometry of 800 initial fracture disks in different colours to highlight their individual domains; **B** fracture geometry after one extension step; **C**–**E** fracture tip nodes coloured based on computed SIF value.

5.3.2 Fracturing around a single borehole

Figure 5.11 shows the minimum principal stress distribution in a 20×20×20 m single borehole model, with (Fig. 5.11a) and without (Fig. 5.11b) the deposition tunnel effect, after the borehole drilling stage. In the close vicinity of the tunnel floor, the triaxial compressive conditions become biaxial, due to the removal of the vertical stress.

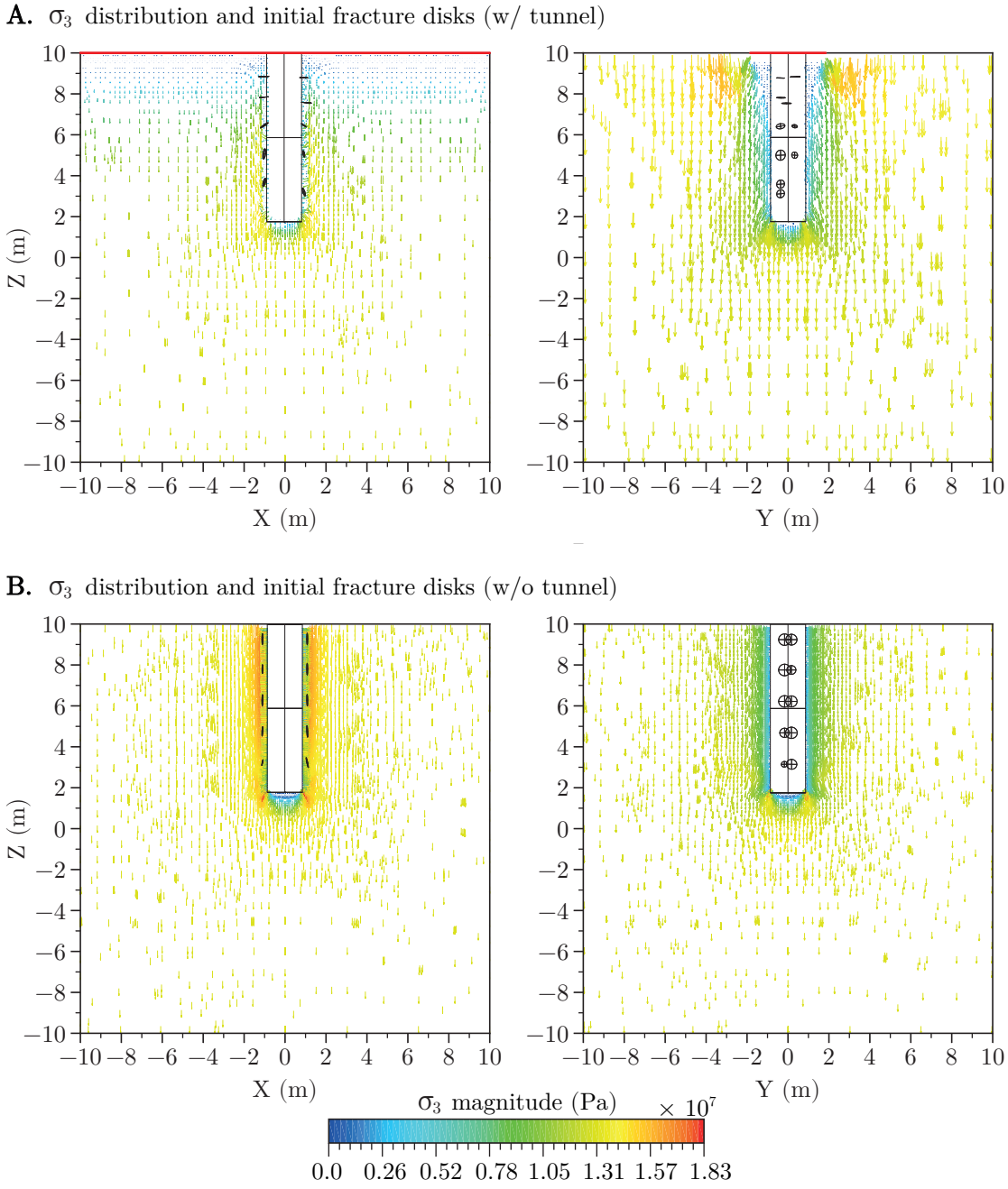


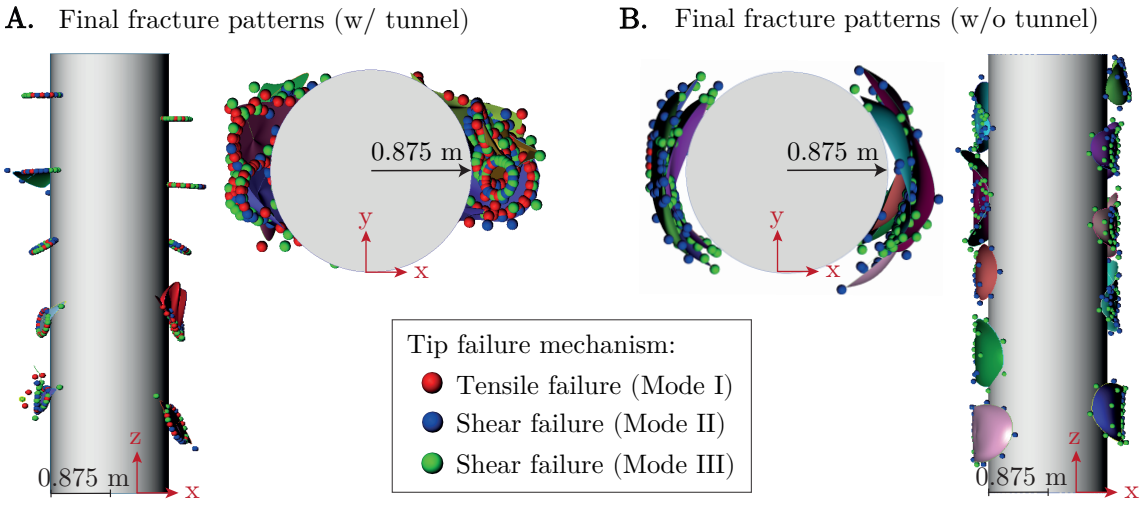
Figure 5.11: Effect of the deposition tunnel on fracture nucleation. Minimum principal stress distribution and initial fracture disks orientations in the 20 × 20 × 20 m single borehole model, with a free top surface acting as the deposition tunnel floor (**A**) and (**B**) the same model, where the tunnel effect is not considered.

The borehole geometry and the initial fracture disks that ensue after nucleation are superimposed, showing fractures nucleating preferentially parallel to the tunnel floor in the first 2-3 m below it (Fig. 5.11a). The initial disks then change their nucleation orientation further down the borehole, conforming with the different stress conditions away from the free tunnel surface. As σ_3 increases further away from the tunnel floor and triaxial conditions return, fractures realign themselves perpendicular to the minimum compressive stress direction, and hence parallel to the borehole wall.

In the case where the presence of the tunnel is not taken into consideration (Fig. 5.11b), the minimum principal stress is magnified at the top of the borehole, and tends to orient perpendicular to the borehole wall. This affects fracture nucleation patterns, since fractures align themselves perpendicular to the direction of the minimum principal stress during nucleation. In this case, there is a higher density of fractures developing at the junction between the borehole and the tunnel, and they will be oriented parallel to the tunnel floor.

Figure 5.12 shows the final fracture geometries after growth has arrested, in the two stress scenarios presented in Figure 5.11. In the case where the tunnel floor is considered (Fig. 5.12a), the fractures at the top of the deposition borehole grow to a lesser extent in the borehole axial direction, and there is overall less interaction with the borehole wall, compared with the case where the tunnel effect is not incorporated. These fractures tend to propagate in the plane of the tunnel floor, appearing to increase spalling depth. However, since there is little growth along the borehole wall, the actual fractured surface area is smaller than in the case where the tunnel floor is not considered (Fig. 5.12b). Because these fractures grow parallel to the tunnel floor, they are more representative of the excavation damage zone of the deposition tunnel. Although they intersect with the deposition borehole, they should not be classified as "spalling" fractures, because they would not induce spalling or splitting of the borehole wall.

Figures 5.12a–5.12b also show fracture tip nodes at all growth steps, coloured according to their dominant failure mode. In both cases, most tips appear to fail under tension in the early stages of the breakout development, but further fracture propagation is mixed mode, and mainly determined by either Mode II or Mode III tip failure. As expected, in the case where the deposition tunnel is considered, more tips fail in tension, since decreasing confining stress promotes tensile fracture conditions.



Frac.	With Tunnel Z [m]	With Tunnel Spalling Depth [m]	With Tunnel Spalling Width [°]	With Tunnel Surface Area [m^2]	Without Tunnel Z [m]	Without Tunnel Spalling Depth [m]	Without Tunnel Spalling Width [°]	Without Tunnel Surface Area [m^2]
F1	0.5	0.43	60.3	1.13	0.5	0.17	50.3	0.50
F2	1.2	0.44	55.1	1.08	1.1	0.15	50.0	0.47
F3	2.4	0.41	63.6	0.98	2.4	0.14	43.7	0.51
F4	2.3	0.15	77.1	1.10	2.3	0.16	57.1	1.10
F5	5.9	0.17	69.5	1.16	5.2	0.14	39.5	1.07
F6	0.4	0.42	40.3	1.12	0.7	0.20	32.0	0.49
F7	0.8	0.40	62.0	0.93	0.8	0.18	52.0	0.55
F8	4.8	0.39	41.2	0.88	4.8	0.18	32.3	0.62
F9	4.6	0.20	54.9	0.95	4.6	0.19	32.9	1.09
F10	6.5	0.23	54.1	1.09	6.5	0.20	44.7	1.05

Figure 5.12: Effect of the deposition tunnel on fracture growth showing: **A.** fracture patterns after growth arrest in the 20×20×20 m single borehole model and **B.** fracture patterns after growth arrest in the 20×20×20 m single borehole model.

5.3.3 Effect of tunnel orientation

Several cases were investigated, in which the tunnel floor was orientated axially parallel to the direction of the maximum horizontal far-field stress, and then rotated in 15 degree increments, until it became perpendicular. Figure 5.13b illustrates simulated fracture patterns in three different cases, in which the deposition tunnel makes an angle of 0°, 30° and 45° respectively with σ_H. The numerical results indicate that tunnel orientation influences the loci where the fractures involved in borehole spalling nucleate, relative to the tunnel floor, but does not influence the depth of the final fractured areas significantly.

The spalling depth, spalling width, and total fracture surface area in each case are listed in Table 5.2. These remain consistent at different tunnel orientations, because the tunnel

floor edges are sufficiently far away from the borehole wall to prevent unstable fracture growth and interaction with tunnel floor/sidewalls. Given the *in situ* conditions at Forsmark, spalling is not predicted to occur in the tunnel axial direction, unless the tunnel is drilled perpendicular to the maximum horizontal stress (Figure 5.13a). Section 5.6.2 shows further examples, deliberately probing this worst-case tunnel orientation scenario, to understand the behaviour for cases where fracture growth and interaction between neighbouring boreholes is modelled.

5.4 Effect of the *in situ* stresses

Three *in situ* stress scenarios are investigated. In the base case, the three principal far-field stresses are assigned their mean expected values at 500 m depth at Forsmark (Table 5.1). In the two other cases, the stress magnitudes are chosen such that, within their given uncertainty range, stress anisotropy is minimised and maximised, respectively. Previous studies have shown that fracture growth is promoted by higher stress differentials at the borehole wall (Shen et al. 2002, Lisjak et al. 2014). Thus, the other two limiting stress scenarios correspond to (1) $\sigma_H - \sigma_h = max.$, $\sigma_H - \sigma_v = max.$ and (2) $\sigma_H - \sigma_h = min.$, $\sigma_H - \sigma_v = min.$

Figure 5.14a shows the maximum principal stress σ_1 at the borehole wall, corresponding to the base case and the two limiting *in situ* stress conditions at Forsmark. Assuming that there are no fluids in the borehole, the tangential stress varies in a sinusoidal fashion as a function of angular distance, matching the analytical solution for a circular hole in a rock mass with prescribed far-field principal stresses (Jaeger et al. 2007). In all cases, the tangential stress exceeds $0.4 \pm 0.05 \times \sigma_{UCS}$, or the "spalling strength" of the rock mass (Diederichs 2007*a*).

Figures 5.14b and 5.14c show how several far-field stress scenarios within the limiting cases dictated by the *in situ* conditions at Forsmark affect the tangential stress magnitude at the borehole wall. For constant far-field maximum stress σ_H (Figure 5.14b), variations of the far-field intermediate stress σ_h cause borehole hoop stress changes within $\pm$ 5 % of its base case value at 90° and 270°, where spalling is expected to occur. Conversely, varying the far-field maximum stress σ_H causes larger σ_1 changes at the borehole wall, covering the entire range between the two limiting stress scenarios (Figure 5.14c).

Figure 5.14 implies that variations of the intermediate *in situ* stress at Forsmark (the minimum horizontal stress σ_h) are less important in affecting the tangential borehole stress, than variations of the maximum *in situ* stress (the maximum horizontal stress σ_H). Since all cases fall within the minimum (red line) and maximum (blue line) stress differential scenarios, subsequent fracturing behaviour will be analysed within these limiting cases. Figure 5.13a shows the simulated fracture patterns for the three different stress

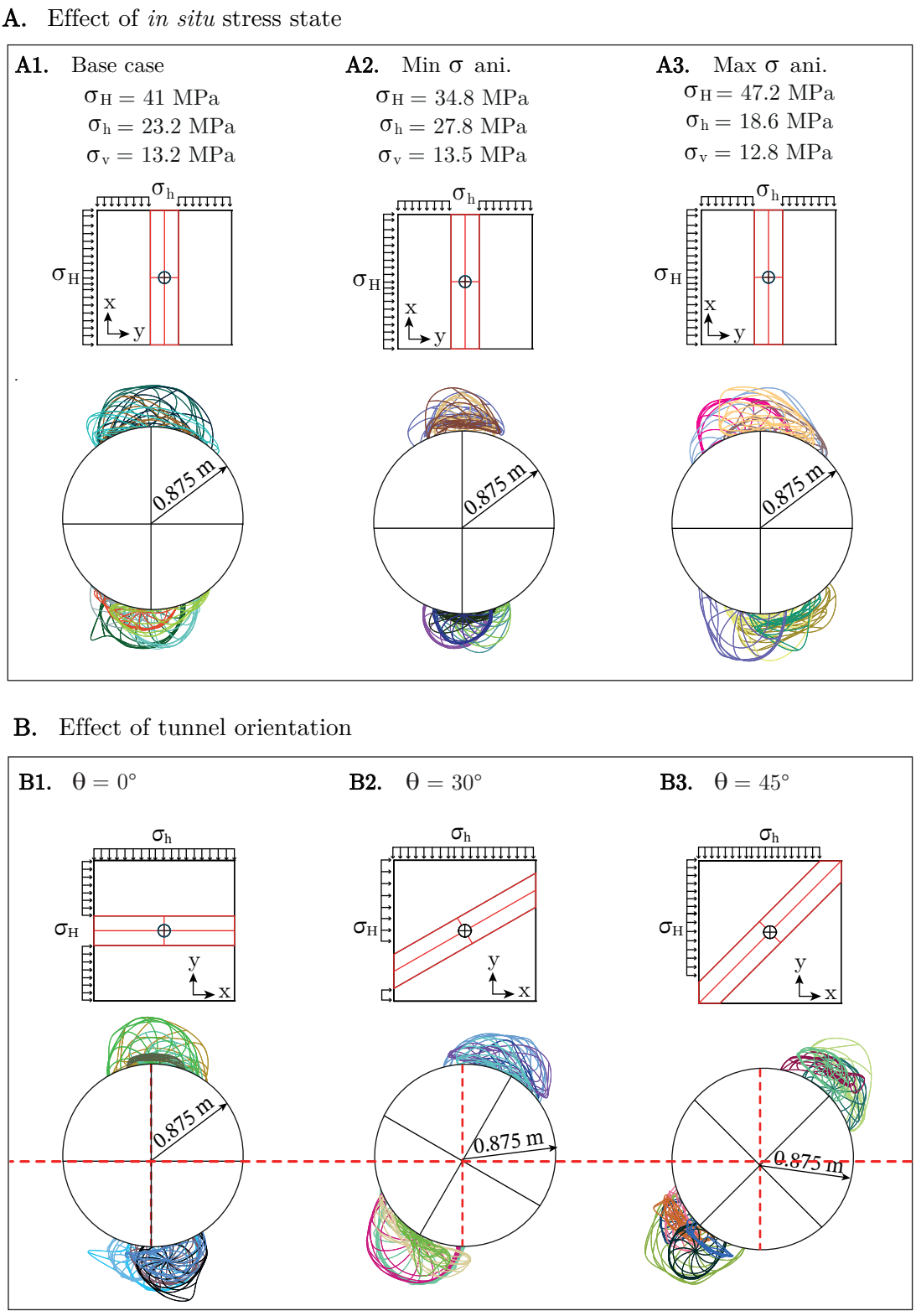


Figure 5.13: **A.** Effect of *in situ* stress magnitude and **B.** Effect of tunnel orientation *w.r.t.* the maximum compressive stress σ_H on simulated fracture patterns, showing final fracture geometries after growth has arrested. The tunnel floor is shown in red. Fracture growth in each case is quantified in Table 5.2. Simulation parameters and boundary conditions are given in Table 5.1.

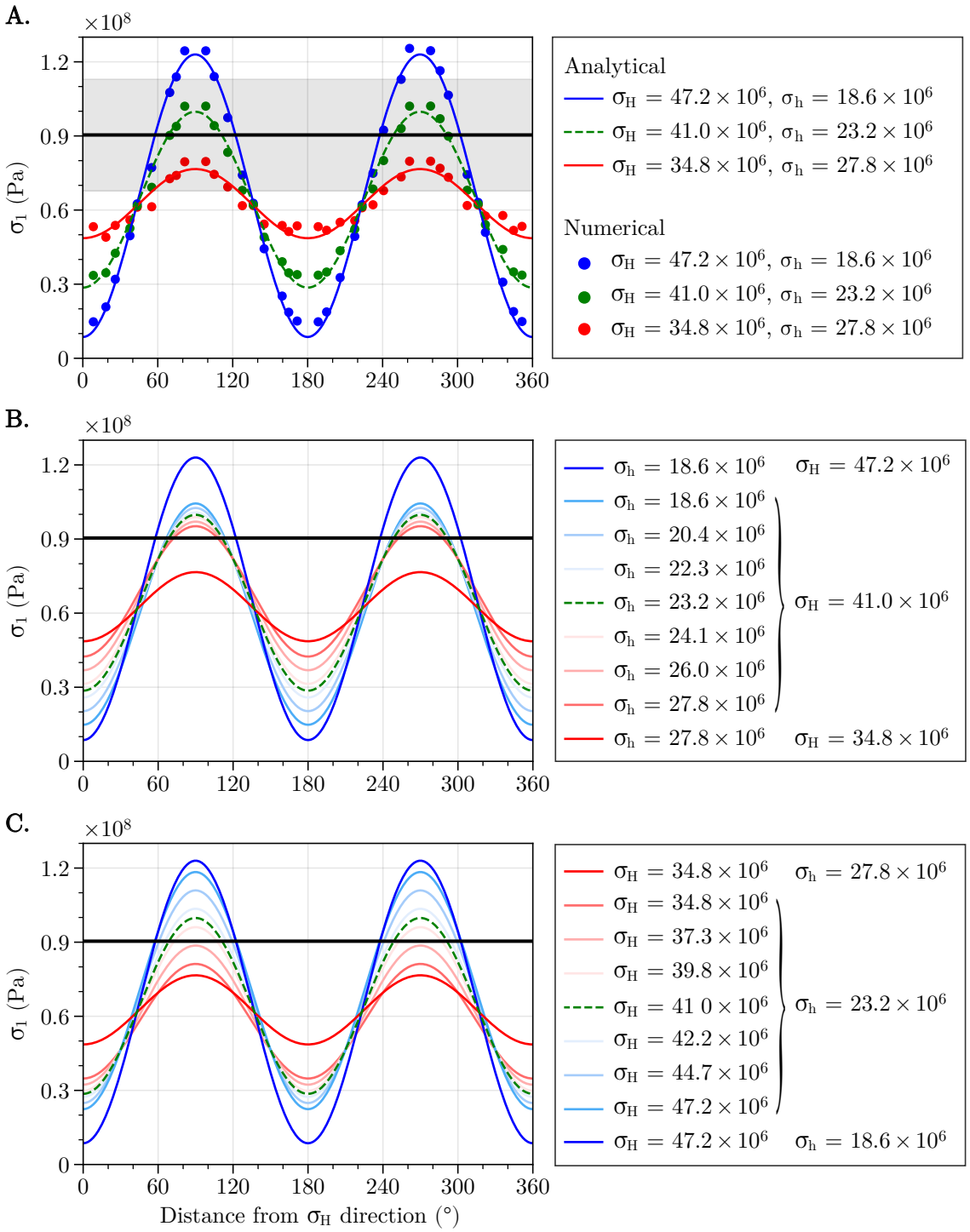


Figure 5.14: Effect of *in situ* far-field stress magnitude at Forsmark on the maximum principal stress at the borehole wall (tangential stress), prior to fracture nucleation (**A**). Effect of varying σ_h, while keeping σ_H constant (**B**) and vice versa (**C**). The horizontal line at 90.4 MPa, corresponds to 0.4×UCS, and the grey shaded area shows the range of stresses favourable to spalling initiation, spanning between 0.3×UCS and 0.5×UCS.

magnitude scenarios (Figure 5.14a), at perpendicular orientation of the deposition tunnel relative to the direction of the maximum compressive stress. Fractures nucleate and grow diametrically opposite around the circular borehole in the direction of the least compressive horizontal stress, as observed in numerous occasions in the field (Read & Martin 1996, Zoback et al. 1985, Barton et al. 1988). Fracture growth is influenced by the relative magnitudes of the stresses applied, with more damage and growth occurring under conditions of higher horizontal stress differential. Fracture growth is quantified in terms of the maximum spalled zone depth, spalled zone angle (width), and total fracture surface area (Table 5.2).

The maximum depths of the fractured zones are comparable with predictions from Martin et al.'s (1999) empirical equation, which relates the ratio of maximum spalling depth and borehole radius to the ratio of maximum tangential stress at the excavation wall and the uniaxial compressive strength of the rock. Given the *in situ* stresses and borehole geometry at Forsmark, Martin et al.'s (1999) empirical relationship predicts spalling depths ranging from a few centimeters in the case of lowest stress differential, up to around 15 cm in the case of highest stress differential.

The simulated numerical results in this chapter are in better agreement with Martin's (2014) empirical relationship in the case where the deposition tunnel is not considered (Table 5.2), but also in the case where the tunnel is considered, for those fractured zones residing in the lower half of the borehole (Figure 5.11). However, fracture nucleation and growth at the top of the borehole is affected by the deposition tunnel, causing a larger apparent maximum spalling depth than the one predicted by Martin (2014) for the Forsmark site specifically. Another reason for the additional fracture growth might be that Martin (2014) looks exclusively at tensile fractures, whereas in this study, spalling fractures initiate in tension, but macro-failure is multi-modal, and generally dominated by shear in the later growth stages.

Since the depths and widths of breakouts in vertical boreholes depend on the relative magnitudes of the major and minor horizontal *in situ* stresses (Amadei & Stephansson 1997), fracture patterns and final breakout metrics are shown in Figure 5.13 only for the base-case and limiting stress scenarios, assuming that any other stress state that falls between the limiting cases will also cause fracturing severity to fall in the expected range.

5.5 Effect of borehole geometry

This section investigates the effect of borehole geometry on numerical predictions of spalling around a typical deposition borehole. The cylindrical borehole is modified at the junction with the tunnel floor to provide an access ramp for the spent fuel canisters. This is a potentially practical modification that could provide additional space to operate

the machines that will lower the spent fuel canisters into the borehole, effectively reducing the requirement of a "tall" deposition tunnel (Pusch 2008). Three cases are investigated, where the borehole top is cylindrical, conical, and wedge-shaped (Fig. 5.3a). Numerical results show that spalling occurs in all cases, and the modified geometries affect fracture nucleation and growth patterns (Figure 5.15).

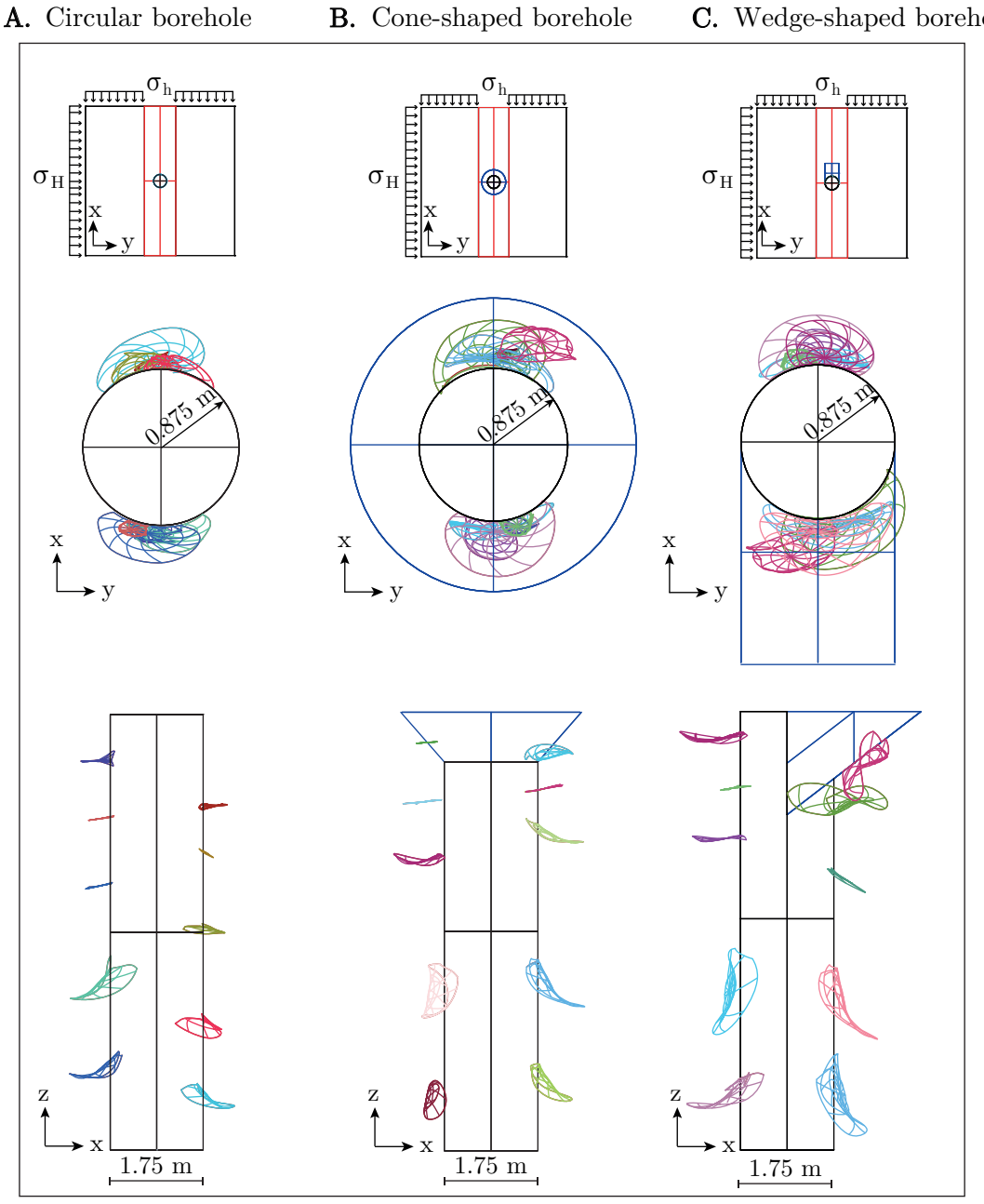


Figure 5.15: Effect of borehole geometry on simulated fracture patterns, showing final fracture patterns for a circular (**A**), cone-shaped (**B**) and wedge-shaped (**C**) borehole. Fracture growth is quantified in Table 5.2. Simulation parameters and boundary conditions are those from Forsmark (Table 5.1).

Fractures nucleate uniformly on either side of the circular borehole (Figure 5.15a), but concentrate at the borehole top in the other two simulated cases, where the top of the borehole is wedge-shaped (Fig. 5.15b), or conical (Fig. 5.15c). The enlargement of the borehole top induces higher stress concentrations at the borehole-tunnel junction at larger radial distances, as well as it introduces additional free surfaces and sharp boundaries, increasing the depth of failure in the top metre of the borehole, where the geometry is modified. Fracture growth is quantified in terms of maximum spalling depths and total fractured surface areas, showing increasing severity from circular, to cone-shaped to wedge-shaped borehole cases (Table 5.2).

Although the maximum absolute spalling depth is the largest in the wedge-shaped borehole case, this only occurs when the tunnel floor is orientated perpendicular to the maximum compressive stress direction. The fractured areas responsible for increased spalling depth on the ramp side are, as shown in Figure 5.15c, involved in the spalling of the ramp itself. However, if the tunnel is orientated parallel to the direction of the maximum compressive stress, the stress conditions required for ramp spalling would not be fulfilled and fractures would nucleate 90° away from the ramp, and grow as in the case of a simple circular borehole. For this reason, the symmetrical cone top is not recommended, as it would increase failure severity in all stress and/or tunnel orientation scenarios.

5.6 Effect of neighbouring boreholes

In all cases presented previously, fracturing processes were localised in the near-borehole region, and the maximum depth of the fractured zones, although variable from case to case, did not exceed one borehole radius. In this section, additional boreholes are added, as shown in Figure 5.4c, at an equal inter-borehole distance, on either side of the central circular borehole. The inter-borehole distance is then gradually decreased, to examine the changes in the displacement and stress fields, and their effects on fracture growth.

5.6.1 Number of boreholes

Chapter 4 demonstrated that the FEM stress field computation is accurate for various borehole separations in a two-borehole model, where several loading cases (longitudinal, transverse, and biaxial tension) were compared with known analytical solutions. In the context of nuclear waste disposal, it is equally important to ensure that the stresses are also accurate when multiple colinear boreholes are present, meaning that the model must be capable of handling both an arbitrary number of boreholes and inter-borehole distances. Analytical solutions for the maximum principal stress at the central borehole wall in the case of an infinite number of boreholes have been provided by Howland (1935),

Horii & Nemat-Nasser (1985), and Isida & Igawa (1991). Figure 5.16 shows maximum, intermediate and minimum principal stress distributions around a three- (Figure 5.16a) and a five-borehole (Figure 5.16b) array, spaced 4 m and 6 m apart, respectively. The three/five aligned boreholes are created simultaneously, and their locations are varied in order to investigate the effect of borehole spacing, as well as the impact of total number of boreholes within an array, on borehole and pillar stress. The applied horizontal stresses are in all cases are $\sigma_H = 41$ MPa and $\sigma_h = 23.2$ MPa, the vertical stress is $\sigma_v = 13.2$ MPa.

Figure 5.16c shows the maximum principal stress magnitude variation along the two pillars, in four different pillar widths scenarios. Comparison of the resulting stress magnitudes in the two pillars shows a 31% pillar stress increase when the inter-borehole distance decreases from 4.0 m to 2.5 m. While borehole spacing is shown to influence stress concentrations in the pillars (Figure 5.16c), the number of boreholes in the model (Figure 5.16d) does not influence stress distribution.

Figure 5.16d shows the maximum principal stress magnitude lateral variation in a three-, five- and seven-borehole model, respectively. In all three simulation models, the borehole spacing is six metres, and the domain was adjusted such as the distance between the outermost boreholes and the domain boundaries remains constant, in order to avoid boundary effects. The purpose of this exercise was to investigate whether increasing the number of neighbouring boreholes has an effect on stress state and fracture patterns around the innermost central borehole(s). It is apparent that regardless of the number of simulated boreholes, provided that the inter-borehole distance remains unchanged and sufficiently large, and the numerical domain is adjusted accordingly, there is no major change in the stress state around the central and outer boreholes. This determines all boreholes to be equally damaged and hence fracture growth amounts to similar fractured area per borehole as well (Table 5.2). This result agrees qualitatively with those obtained by Horii & Nemat-Nasser (1985) and Wang et al. (2003) for larger numbers of co-linear circular openings under uniaxial tension. Their numerical studies also showed that interaction between central and non-central boreholes can be neglected as long as the borehole spacing is large enough to prevent interactions.

Figure 5.16 supports the validity of three-borehole simulation cases extrapolated to the repository scale. The alternative of simulating cm-scale, concurrent fracturing processes around dozens of deposition boreholes per deposition tunnel would not be computationally efficient. For example, in the single borehole case, there are initially 31,911 nodes, which, after the nucleation of ten fractures, increase to 75,704 nodes. For three boreholes, the number of nodes increases from 69,068 in the intact rock domain to 173,942 after the nucleation of thirty fractures, and finally, for five boreholes it increases from 106,920 to 282,170 after the nucleation of fifty fractures. The number of nodes keeps increasing as the fractures continue to grow, adding detailed discretisation to regions of the mesh that were previously coarser.

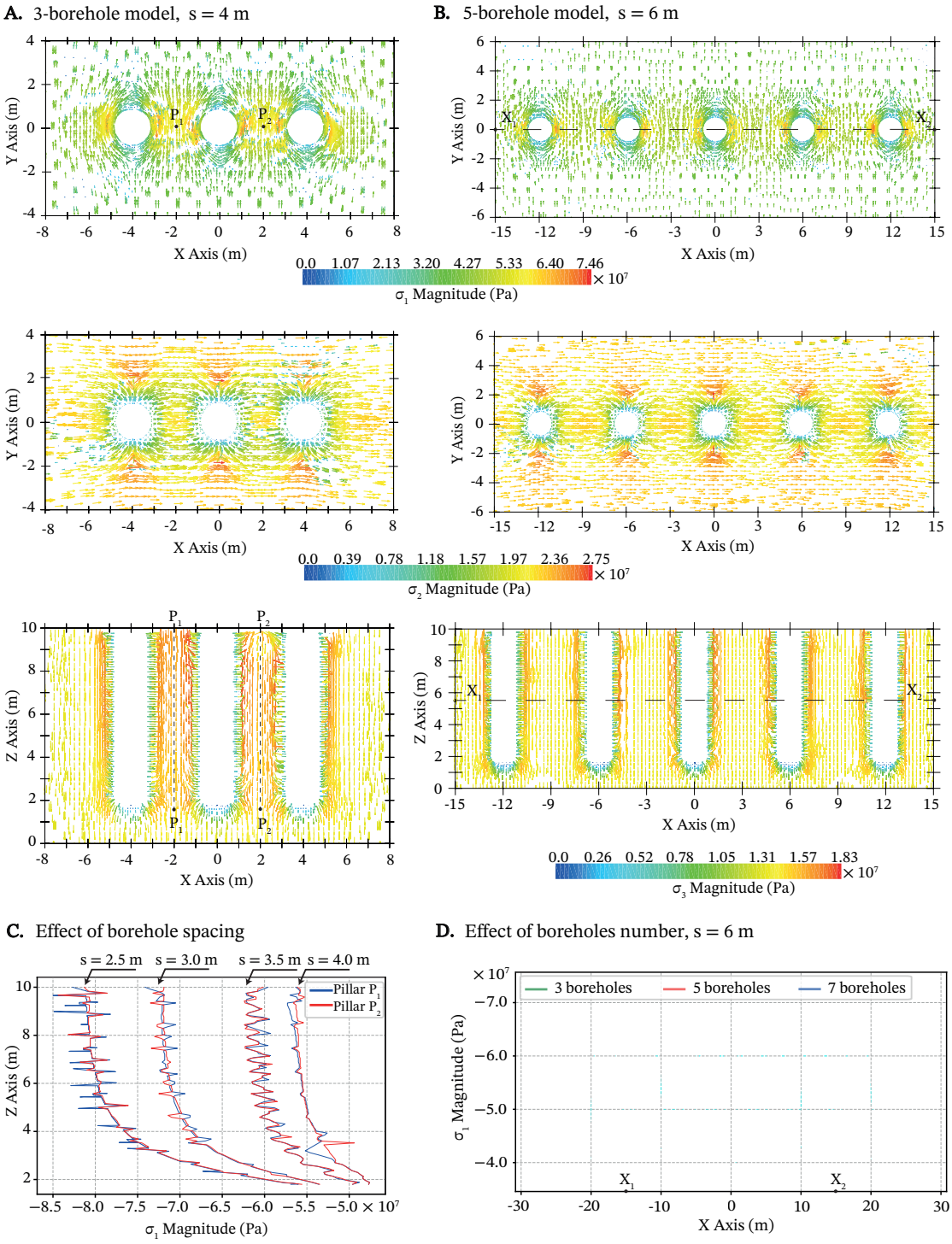


Figure 5.16: Principal stresses magnitudes and orientations around circular boreholes spaced 4 m (**A**) and 6 m (**B**) apart, in a 3- and 5-borehole model respectively. σ_1 magnitude at the centre of the two pillars P_1 and P_2 is plotted for the different borehole spacing cases (**C**). σ_1 magnitude is also plotted over a line X_1X_2 traversing the 5-borehole model laterally, at a depth 4.5 m down the borehole (**D**). Overimposed 3- and 7-borehole models show similar variations of σ_1. Simulation parameters and boundary conditions are those from Forsmark (Table 5.1).

5.6.2 Borehole spacing

The inter-borehole spacing is an important parameter affecting repository design, as it determines the minimum length of the deposition tunnel necessary to accommodate the required number of deposition boreholes. This distance should be optimised to accommodate the maximum number of boreholes along the deposition tunnel, while minimising interaction effects and preserving the structural integrity of the repository. In this section, several borehole spacings are tested to determine its effect on fracture nucleation and growth. The inter-borehole distance, s, is measured between borehole centres, hence the effective pillar width is given by s - $2R_b$, where R_b is the borehole radius.

Figures 5.17 and 5.18 show the elastic modulus distribution and the corresponding fracture patterns, respectively, in a three-borehole model (Fig. 5.4d). The boreholes are evenly spaced, at s = 2.5, 3.0, 3.5 and 4.0 metres apart, resulting in the formation of two overstressed pillars of equal widths, P_w = 0.75, 1.25, 1.75 and 2.25 metres, respectively.

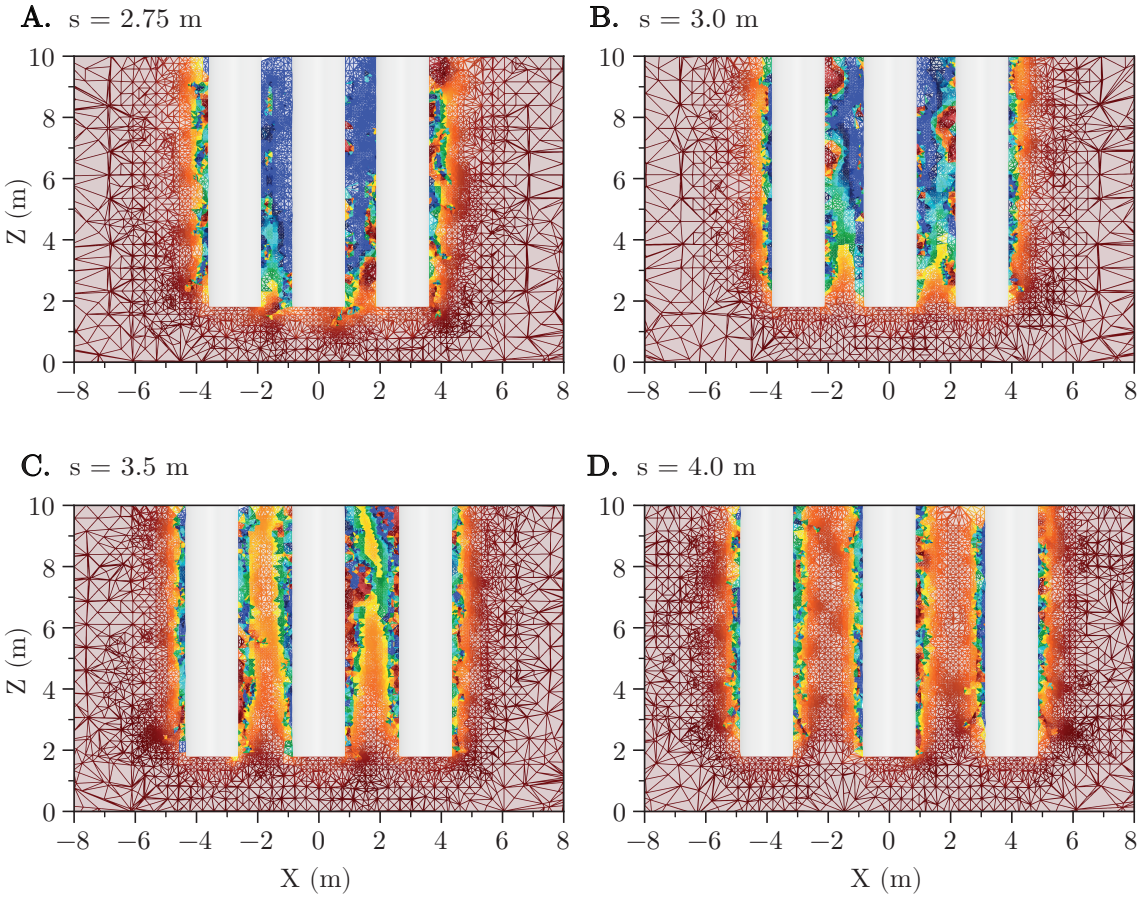


Figure 5.17: Axial cut planes showing the damaged Young's modulus after fracture growth has arrested. The center-to-center borehole distances are: 2.5 (**A**), 3.0 (**B**), 3.5 (**C**) and 4.0 (**D**) m, corresponding fracture geometries shown in Figure 5.18. For closer spaced boreholes, the decrease in Young's modulus due to increased damage is substantial, and correlates to the increase in the fractured area (Table 5.2).

For a borehole spacing of 2.5 m, the two pillars are completely damaged, as shown by the reduction in Young's modulus (Fig. 5.18a). As the inter-borehole distance increases, the damage and corresponding reduction in Young's modulus decreases and becomes more localised to the walls of the boreholes, where the fractures are located. In the case of a 4.0 m spacing (Fig. 5.17d), the centre of each pillar shows a 15% reduction of the original, undamaged Young's modulus, and areas of high damage are localised to the borehole wall.

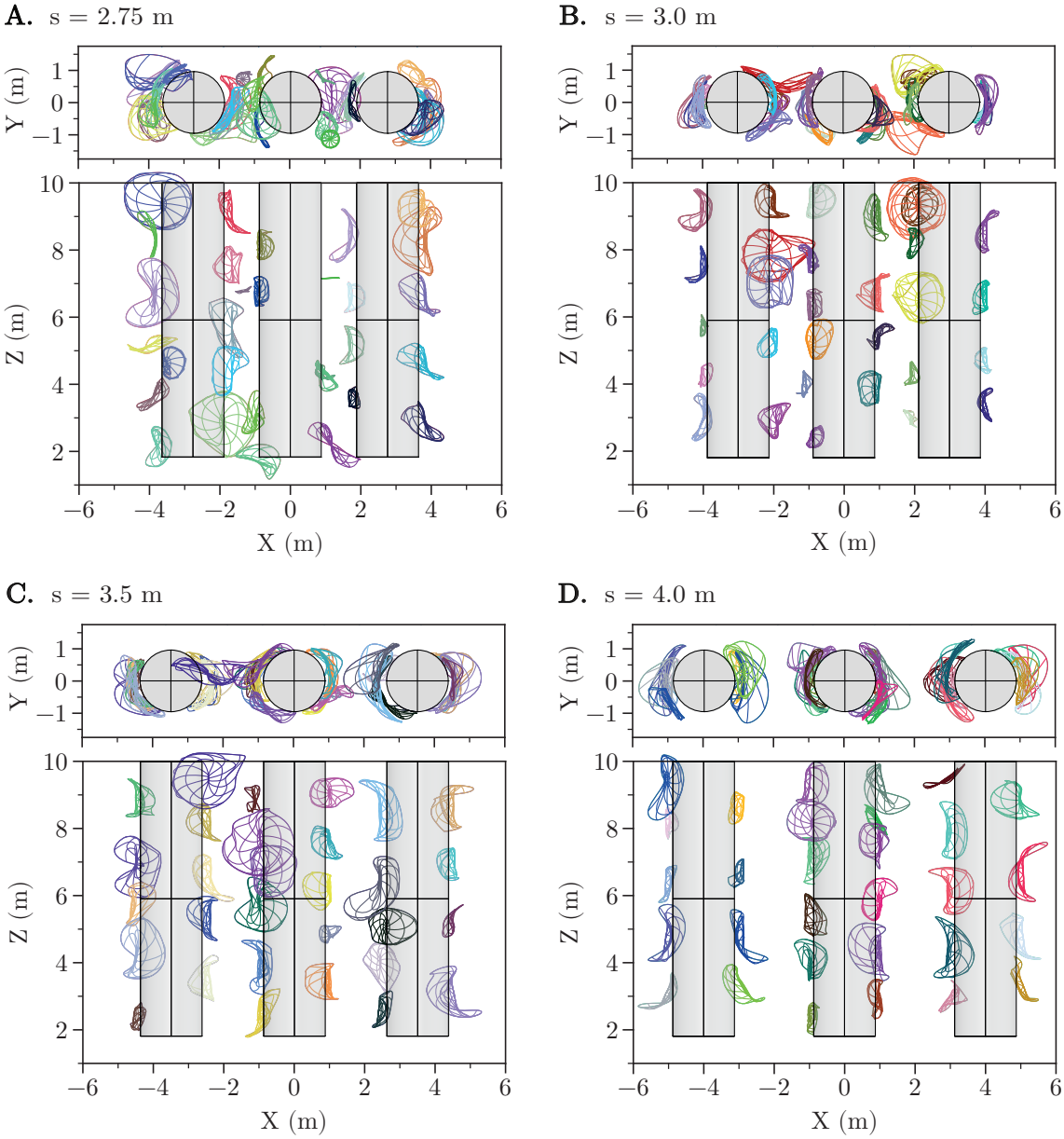


Figure 5.18: Radial and axial views of the final fracture patterns that develop around three interacting boreholes. Four cases are shown, where the center-to-center borehole distances are: 2.5 (**A**), 3.0 (**B**), 3.5 (**C**) and 4.0 (**D**) m. These correlate with the continuum damage shown in Figure 5.17. For closer spaced boreholes, through-going fractures are observed. Simulation parameters and boundary conditions are those from Table 5.1 and Figure 5.4c respectively. The total number of fractures is 30.

For a borehole spacing of 2.5 m, the two pillars are completely damaged, as shown by the reduction in Young's modulus. As the inter-borehole distance increases, the damage and corresponding reduction in Young's modulus decreases and becomes more localised to the walls of the boreholes, where the fractures are located. In the case of a 4.0 m spacing (Fig. 5.17d), the centre of each pillar shows a 15% reduction of the original, undamaged Young's modulus, and areas of high damage are localised in the vicinity of the borehole wall, where the fractured regions reside (Fig. 5.18d). In this case, the three boreholes are not interconnected by a fractured zone and the region between them is largely undamaged. These results are different from the current site-descriptive model from Forsmark, which recommends a preliminary distance of either 6 m (in rock domain RFM029) or 6.8 m (in RFM045) between adjacent boreholes (SKB TR-08-05 2007).

In all four cases, the Young's modulus remains unchanged from about one metre away from the peripheral boreholes, implying that beyond this point the host rock is undisturbed. Figure 5.18 shows the spalling patterns in radial and axial directions corresponding to the four borehole spacing cases in Figure 5.17. Table 5.2 presents the quantified interaction of the three boreholes spaced at 3, 4, 5, and 6 m, noting the maximum observed failure depth, width, and the total fractured surface area in each case.

5.7 Discussion

Geometric fracture growth simulations, based on the finite element method, were conducted to investigate stress-induced fracturing processes leading to spalling around deposition boreholes under different underground conditions. Several scenarios were considered, in which the *in situ* stresses, borehole geometries and spacing were varied to assess their impact on final fracture patterns and damage extent.

In the case of a single circular borehole excavated in a homogeneous and isotropic rock domain, numerical results indicate that spalling failure initiates in areas of high damage close to the borehole wall and continues to develop in the direction of the least compressive stress σ_3, in agreement with experimental observations from laboratory and field studies (Martin & Kaiser 1996, Read 2004, Martin 2014).

When the deposition tunnel floor was incorporated as a free surface, fractures at the intersection between the borehole and the tunnel nucleated preferentially parallel to the tunnel floor, and perpendicular to the borehole wall. Fracture nucleation and growth behaviour around the deposition tunnel is controlled by the higher stress concentrations occurring around sharper boundaries, and in line with similar numerical studies investigating spalling of horseshoe-shaped or rectangular-shaped tunnels (Lisjak & Grasselli 2014, Gong et al. 2020). The preferential nucleation of fractures around the deposition tunnel resulted in larger apparent spalled zones widths, but lower fractured surface area.

Fractures in that case grew more horizontally, in the direction of the tunnel floor, instead of vertically, along the borehole itself. They also showed less interaction with the borehole wall in the borehole axial direction. The tunnel was then rotated at different angles to the maximum horizontal stress, in order to assess the impact of stress orientation on fracture growth. Since the relative stress magnitudes were kept constant regardless of the tunnel orientation, the extent of the fractured zone remained consistent in all orientation cases, for a circular borehole.

Table 5.2: Effect of different repository configurations on the maximum fractured depth, width and surface area. Simulation parameters and boundary conditions are those from Forsmark (Table 5.1).

Case	Maximum spalling depth [m]	Spalling width [°]	Total fractured surface area [m^2]
Deposition tunnel			
w/ tunnel	0.44	63/52	2.0
w/o tunnel	0.19	58/51	13.2
Tunnel orientation			
0°	0.44	63/52	2.0
15°	0.48	23/65	2.34
30°	0.42	90/50	2.60
45°	0.48	27/27	2.11
90°	0.45	52/32	2.28
In situ stress			
base case	0.44	63/52	2.0
max σ anisotropy	0.53	58/51	1.63
min σ anisotropy	0.36	62/55	2.24
Borehole configuration			
circular	0.44	63/52	2.0
cone	0.47	60/62	2.23
wedge	0.49	90/47	2.46
Borehole spacing (3 boreholes)			
3 m	overlap	135/155	120.5
4 m	0.51	68/96	68.7
5 m	0.46	60/63	52.5
6 m	0.44	63/58	35.3
6 m, ramp	0.49	90/47	26.4
Number of boreholes (6 m spacing)			
3	0.44	60/120	35.3
5	0.48	63/109	67.9
7	0.45	62/117	92.3

Another scenario that was examined was the influence of varying *in situ* stress magnitudes. Results showed that damage exceeds the threshold required for nucleation in the near-borehole region, for the expected subsurface conditions at Forsmark. In the case of higher far-field stress differential, the fractures involved in spalling extended deeper into the host rock domain, while lower stress anisotropy caused the fracturing process to stabilise more locally. This observation is in agreement with previous studies have shown that fracture growth is promoted by higher stress differentials at the borehole wall (Shen et al. 2002, Lisjak et al. 2014, Shen & Barton 2018). These are, however, the first simulations of spalling around the future deposition boreholes at Forsmark. Other similar studies focus on modelling spalling generically, or at different locations such as the AECL underground laboratory (Martin & Christiansson 2009, Vlachopoulos & Diederichs 2014, Vazaios et al. 2019).

Finally, the effect of neighbouring boreholes and inter-borehole distance was investigated. Numerical results determined that the maximum stress concentration around flanked boreholes does not change significantly, regardless of the total number of boreholes in the model, provided that the domain boundaries and number of initial disks are adjusted accordingly, and the inter-borehole distance remains constant. The three-, five- and seven-borehole models were fundamentally identical in terms of fracturing behaviour around flanked (inner) borehole(s), and flanking (outer) boreholes. On the other hand, inter-borehole spacing plays an important role in pillar stability. Under the given conditions at Forsmark, circular boreholes need to be spaced at least 4 m apart to maintain pillar integrity under mechanical loading. In the case where access ramps are drilled, the spacing should be increased to at least 6 m, to ensure stability at the top of the boreholes.

5.8 Conclusions

The present approach to model spalling failure and general fracturing around boreholes provides useful and quick information for designing a safe repository for nuclear waste storage. The modelled fracture patterns are consistent with previous studies and field observations, and the computational cost to generate them is low. The extent of the fractured areas around boreholes depends on a number of repository design parameters, some of which can be adjusted to minimise spalling severity and eventually reduce the risk for leaking radionuclides in this highly fractured zone.

Compared with the fracture patterns shown in Chapter 4, where the K_{IC} was reduced by an order of magnitude to enhance growth for validation of numerical parameters, the patterns shown in this chapter are the result of a limited amount of growth. In general, the fractured zones around the boreholes reach a stable configuration in 5-10 simulation steps. This is representative of high velocity “unstable” fracturing observed in brittle rock

under static loading conditions. Moreover, not all fractures intersect the borehole wall, reducing the risk of actual detachment of rock slabs off the borehole wall and subsequent elongation of the borehole diameter.

This chapter showed that the deposition tunnel reduces the interaction of the fractures with the borehole wall along the borehole axis, but enhances fracture development in the radial direction. This implies that the tunnel may decrease the rock burst risk by inducing fractures that are perpendicular to the borehole wall, rather than parallel to it. The parallel fractures are responsible for creating vertical rock slabs that are involved in spalling, whereas the perpendicular fractures do not.

The relative magnitudes of the principal far-field stress components and their effects on borehole stress conditions and fracturing behaviour were also investigated. When the far-field maximum stress σ_H remains constant, changes in the far-field intermediate stress σ_h lead to small variations in the maximum tangential stress at $\theta = 90°$ and $\theta = 270°$, where spalling initiates. Conversely, altering the far-field maximum stress σ_H while keeping σ_h constant resulted in more substantial changes in the borehole tangential stress, thereby affecting the spalling extent. While high far-field stress anisotropy intensifies spalling, this impact is relatively subdued for the range of *in situ* stresses at Forsmark. The fractures developing around a circular borehole concentrated within the $1R_b$–$1.3R_b$ range. For a ramped borehole, spalling became prominent at the sharp edges of the borehole ramp, and these fractures extended to approximately $1.5R_b$.

A minimum spacing of four meters was required to maintain pillar integrity under mechanical loading for circular boreholes, which is two meters lower than SKB's estimates (SKB TR-10-48 2010). Although SKB's estimates were developed to minimise stress interactions between adjacent boreholes by including a higher safety range, the results in this chapter might motivate reducing spacing in parts of the repository where waste which is not emitting heat could be emplaced. Alternatively, this work opens the possibility for future studies on the deposition sequence, such as decreasing the spacing between adjacent boreholes if they are filled with waste that is not heat-emitting waste, or alternating the spacing based on whether boreholes are filled with heat emitting waste or waste that has already been significantly cooled down.

Since there were no measurements of fracture toughness available at Forsmark, at the time this work was conducted, the influence of the new values should be analysed when the new data becomes available. However, taking into account the similarity between the Forsmark granodiorite and the Äspö diorite, and the results shown in Section 6.4, where the fracture toughness was scaled with the heterogeneous Young's modulus, the new fracture toughness data is not expected to have a significant impact on the numerical simulations and the major conclusions drawn from this chapter.

Chapter 6

Thermo-mechanical spalling

6.1 Introduction

The previous chapter addressed the mechanical evolution of the repository host rock, from its pristine state prior to drilling, to its damaged and fractured state, after the redistribution of *in situ* stresses around the deposition boreholes. Following the emplacement of the spent fuel canisters, the host rock will also experience thermal loading, caused by the radioactive decay of the spent fuel. The additional thermal loading will induce stress changes after the mechanical phase of the repository has completed, potentially leading to the formation of new fractures which enhance the permeability of the host rock and create preferential flow paths for water and radionuclide migration (Tsang 1987, Siren et al. 2015). This chapter addresses the impact of thermally loaded deposition boreholes at different stages of the repository on spalling patterns.

The deep geological repository at Forsmark is expected to hold, in its final configuration, thousands of heat-generating spent fuel canisters, and it must be designed so that the maximum temperature limit within the repository does not exceed 100°C at the canister surface (SKB TR-10-48 2010). This design condition prevents the dehydration of the bentonite buffer, which would lead to a reduction of the supporting swelling pressure. To maintain the canister surface temperatures below this limit, SKB has conducted preliminary assessments of the thermal dimensioning of the repository and determined that the canister power, the repository layout, *i.e.* canister spacing and tunnel spacing, rock thermal properties, and initial undisturbed rock temperature, significantly impact the temperature evolution at the deposition borehole-host rock interface, while the conditions inside the deposition borehole, *e.g.* bentonite saturation have a negligible effect on the temperature field developing in the immediate host rock (SKB R-09-04 2009, SKB TR-10-23 2010). These *a priori* results motivate the simplification of the modelling work presented in this chapter, wherein the deposition boreholes are assumed to function ther-

mally as the spent fuel canisters. Consequently, the heat transport characteristics and behaviour of the bentonite buffer are not included in the numerical workflow.

Figure 6.1 shows the Forsmark repository layout, where the deposition boreholes are represented as point sources, and the host rock temperature evolution at the central borehole wall, at several locations within the repository. The boreholes experience a maximum temperature increase of 45-50°C above the undisturbed repository temperature around 30 years after deposition. The temperature increase at the central-borehole wall in the repository region labelled C1 is noticeably lower compared to the other repository regions. This disparity is due to the location of region C1 in rock domain RFM045. RFM045 shares similar thermal properties with rock domain RFM029, where the temperature is sampled for the other repository sections, but the canister spacing in RFM045 is larger, measuring 6.8 meters, whereas in RFM029, it is 6.0 meters. After 10,000 years, the heat

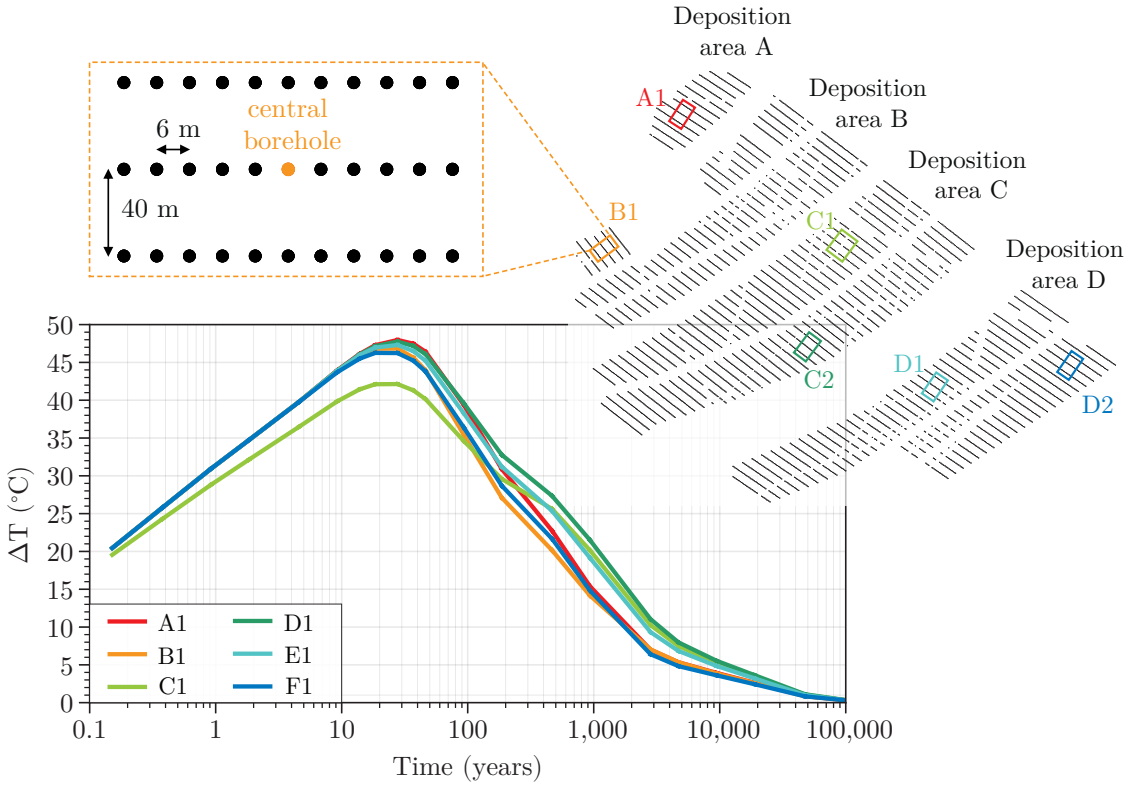


Figure 6.1: Forsmark repository layout and host rock temperature estimations at the central borehole wall in several locations within the repository. The deposition boreholes are represented as point sources, aligned along the deposition tunnels in the axial direction. The major factors affecting borehole temperature are the canister power, repository layout, *i.e.* the borehole and tunnel spacing, and the host rock thermal properties. Modified from SKB TR-10-23 (2010).

generation has declined by approximately 99%, but due to the low heat conductivity of the host rock (Table 6.1), the temperature at the repository depth is still 5-8°C above the initial undisturbed temperature. SKB's preliminary safety assessments, including the temperature evolution shown in Figure 6.1, assume that the spent fuel canisters are de-

posited simultaneously. Previous models of the repository thermal evolution in the near field of individual canisters confirmed that the deposition sequence is not important as long as it is done systematically without long periods between filling neighboring tunnels (SKB TR-10-23 2010). This is the basis for assuming simultaneous deposition spent fuel canisters, which in this work translates as simultaneous heating of the borehole walls in the multiple borehole models.

6.2 Thermo-mechanical spalling of a single borehole

6.2.1 Rock properties

The *in situ* stresses and mechanical rock properties remain the same as in Chapter 5 (see Table 5.1). Additionally, rock thermal properties representative of those encountered at Forsmark (SKB R-08-116 2009, SKB TR-08-05 2007) are given in Table 6.1. As the host rock is a crystalline granodiorite, of low permeability and porosity, heat transport is assumed to occur by conduction and the fractures nucleating in the excavation damage zone are assumed to be dry. Thus, the pore pressure component is not included in the coupled simulations presented in this chapter.

Table 6.1: Average values of the host rock thermal properties at Forsmark (SKB TR-08-05 2007), considered in the thermo-mechanical simulations of spalling in this chapter.

Property	**Value**
Initial temperature (T_{rock})	11.2 °C
Heat Flux ($Q_{borehole}$)	96.24 W/m^2
Thermal Conductivity (κ)	3.68 W/(mK)
Thermal Expansion Coefficient (α)	7.7 $\times 10^{-6}$ K^{-1}
Heat Capacity (C_m)	765.57 J/(kgK)

6.2.2 Model geometry and boundary conditions

The numerical model comprises of a three-dimensional domain with dimensions of 20 $\times$ 20 $\times$ 20 m that contains a cylindrical borehole with a diameter of 1.75 m at its centre. At t=0 s, an instantaneous temperature of $T_{borehole} = 100$°C, corresponding to the repository design limit, is applied to the borehole wall. The temperature prescribed to the borehole wall remains constant throughout the simulation, while the initial repository temperature $T_{rock} = 11.2$°C is maintained at the edges of the domain. The mechanical boundary conditions are the ones described as the mechanical analogue model from Chapter 5, *i.e.*

triaxial compression with far-field stresses $\sigma_H = 41$ MPa , $\sigma_h = 23.2$ MPa, $\sigma_v = 13.2$ MPa (SKB TR-06-09 2006) applied at the domain boundaries (Figure 6.2).

Model geometry:

$$\Omega = (x, y, z) \in \mathbb{R}^3 : -10 \leq x, y, z \leq 10 \tag{6.1}$$

Cylindrical borehole geometry:

$$\mathcal{B} = (x, y, z) \in \Omega : x^2 + y^2 \leq 0.875^2 \text{ and } 1.2 \leq z \leq 10 \tag{6.2}$$

Initial condition for temperature:

$$T(\mathbf{x}, 0) = \begin{cases} 100°\text{C}, & \text{if } \mathbf{x} \in \mathcal{B} \\ 11.2°\text{C}, & \text{if } \mathbf{x} \in \Omega \setminus \mathcal{B} \end{cases} \tag{6.3}$$

Boundary conditions for temperature:

$$T(\mathbf{x}, t) = \begin{cases} 100°\text{C}, & \text{if } \mathbf{x} \in \mathcal{B} \\ 11.2°\text{C}, & \text{if } \mathbf{x} \in \partial\Omega \end{cases} \tag{6.4}$$

where Ω represents the numerical domain, B represents the cylindrical borehole, $T(\mathbf{x}, t)$ represents the temperature at a point $\mathbf{x}$ and at time t in the domain, and $\partial\Omega$ denotes the boundary of the domain.

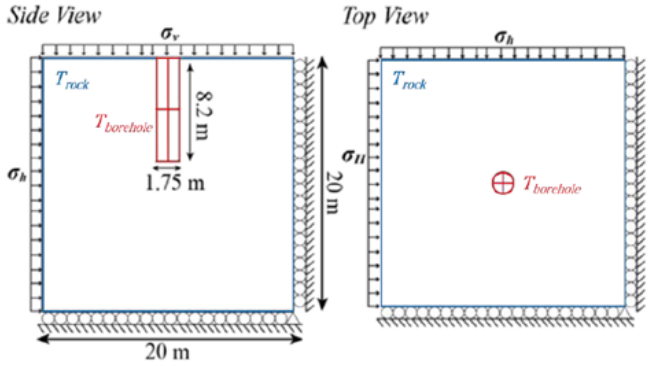


Figure 6.2: Model geometry and boundary conditions corresponding to the single borehole thermo-mechanical case. σ_h and σ_H are the minimum and maximum horizontal far-field stresses respectively, and σ_v is the vertical stress, corresponding to the weight of the overburden at 500 m depth at Forsmark.

6.2.3 Borehole temperature and thermal stress

Figure 6.3 shows the temporal evolution of the temperature field in a single-borehole model, which was subjected to an instantaneous temperature increase of 100°C at its wall, while

the outer boundaries of the domain were kept at the initial temperature of 11.2°C. As time elapses, the temperature diffuses into the adjacent host rock, and the heat continues to propagate outward from the borehole wall. The temperature increase is most significant in the vicinity of the borehole wall and gradually diminishes as the distance from the borehole increases. The slow rate of temperature increase is attributed to the low thermal conductivity of the host rock.

The prescribed geometry and boundary conditions result in the thermal pulse reaching the numerical domain boundaries after approximately 16 weeks of heating, at which point the temperature stabilises and reaches steady state as the domain boundaries are kept at constant temperature (Fig. 6.3).

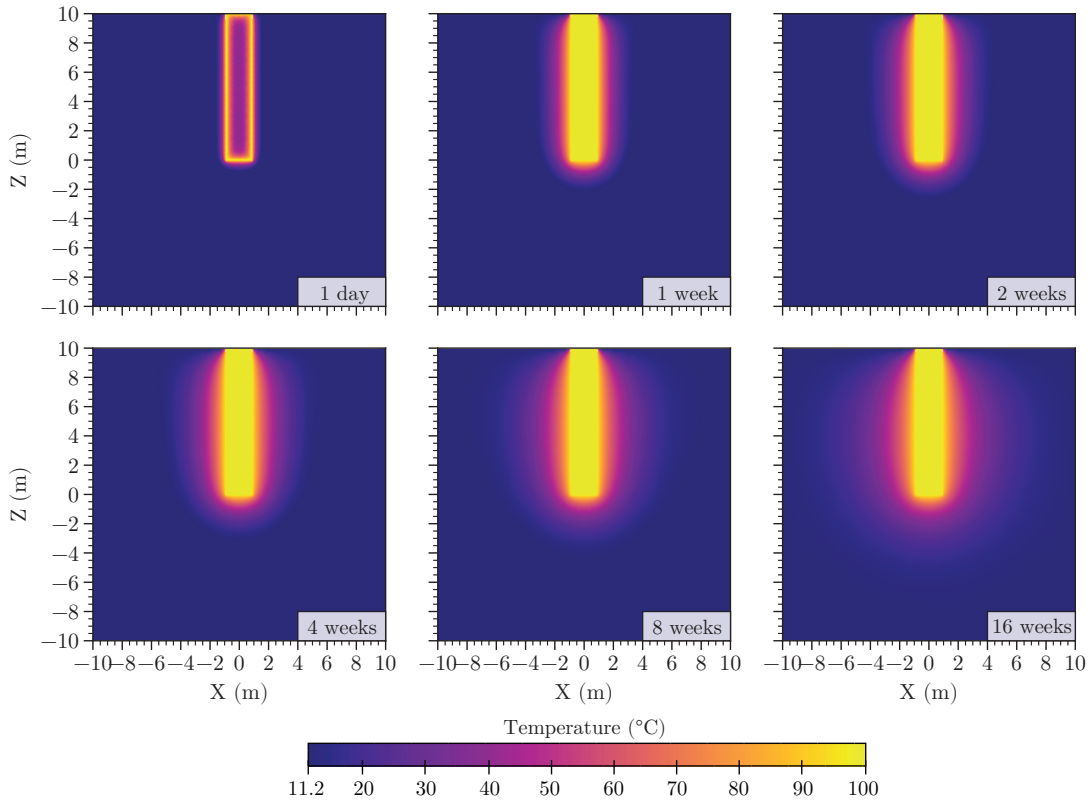


Figure 6.3: A. Temperature field in the single borehole model with a prescribed initial constant temperature of 100 °C showing cut planes after 1 day, 1 week, 2 weeks, 4 weeks, 8 weeks and 16 weeks of heating.

Based on the modeling results from the previous chapter, where mechanical spalling was simulated to occur at distances smaller than 40 cm from the borehole wall, this section assumes that the current boundary conditions adequately capture the temperature evolution in the closest excavation damage zone to the borehole wall, where spalling fractures develop. Therefore, more complex boundary conditions that allow for further dissipation of the heat pulse are not considered.

Figure 6.4 illustrates the profile of the maximum principal stress in the axial direction of the deposition borehole after fracture growth has arrested, for two distinct scenarios: with and without borehole heating. The fracture surfaces can be identified as areas of low stress concentration in the vicinity of the borehole, while the fracture tips exhibit high stress concentrations. As expected, fracture growth and interaction with the borehole wall are more significant in the thermal heating case, where the borehole appears enlarged, and the fracture zones have coalesced. In this case, the fractures show more complex features, and the stress concentration around the borehole is intensified. Figure 6.6 provides a more detailed visualisation of the fracture geometries observed in the two simulated cases, along with a table summarising the spalling depths, widths and areas of each fracture zone that develops around the borehole. Compared with the mechanical spalling case, an increase in temperature promotes fracture growth along the borehole wall, but has a limited effect on spalling depth. In the case of thermal heating, the fracture patterns appear more extensive and spread over a larger area compared to the non-heated case. The differences observed between the mechanical and the thermo-mechanical cases can be attributed to the additional thermal stress near the borehole caused by the temperature increase.

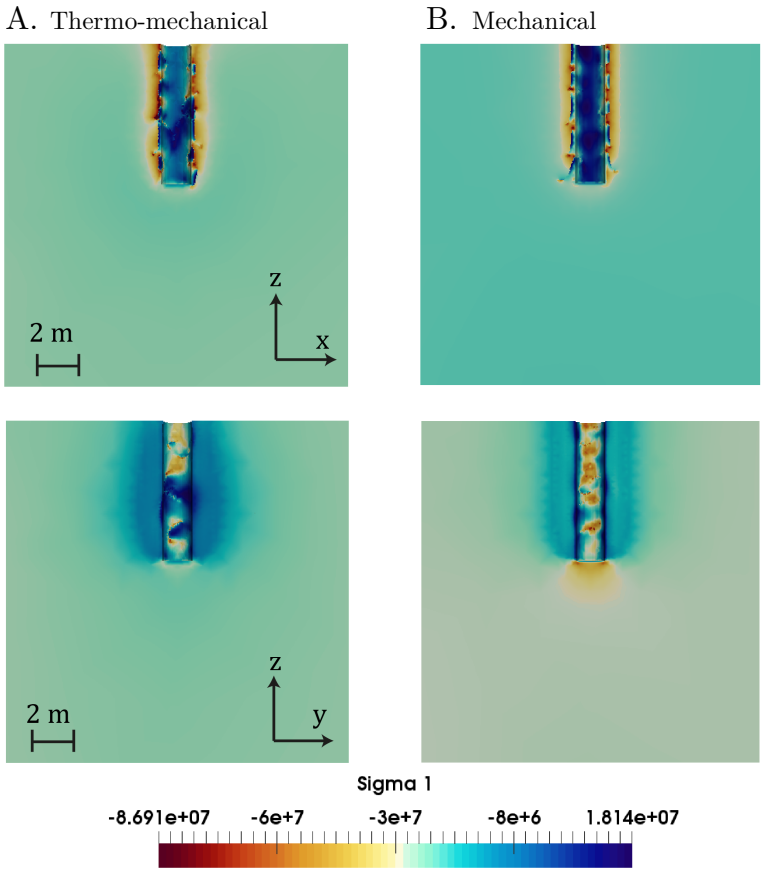


Figure 6.4: Axial cut planes along σ_h and σ_H directions in the single borehole model showing **A.** thermo-mechanical stress after 8 weeks of heating, and **B.** mechanical only stress at maximum fracture growth extent in both cases.

The thermal stress distribution around the borehole is symmetric in all directions, following the temperature distribution (Figure 6.3). Consequently, it causes an equal increase in the magnitudes of both the major and minor horizontal principal stresses at the borehole wall. This results in a reduction of the ratio between the two horizontal stresses and a consequent decrease in the tangential stress with increasing temperature. If fractures were initiated at this stage, they would theoretically extend less compared to the purely mechanical case, due to the lower initial tangential stress, which has been shown in multiple studies to correlate with spalling depth (Martin 2005, Lisjak & Grasselli 2014, Shen et al. 2002). However, a comparison of the fracture patterns between the purely mechanical and thermo-mechanical cases reveals that the spalling depths marginally increase in the case where the borehole is heated to 100°C (Figure 6.6). The primary reason for this is that the thermal effect is not significant enough to overcome the influence of the existing mechanical stress field. Furthermore, the orientation of the initial disks and growth vectors is also primarily dictated by the magnitude and orientation of the mechanical *in situ* stresses, and the effect of thermal stress is secondary to the mechanical stress effect during nucleation and early stages of growth where the fractures extend the most.

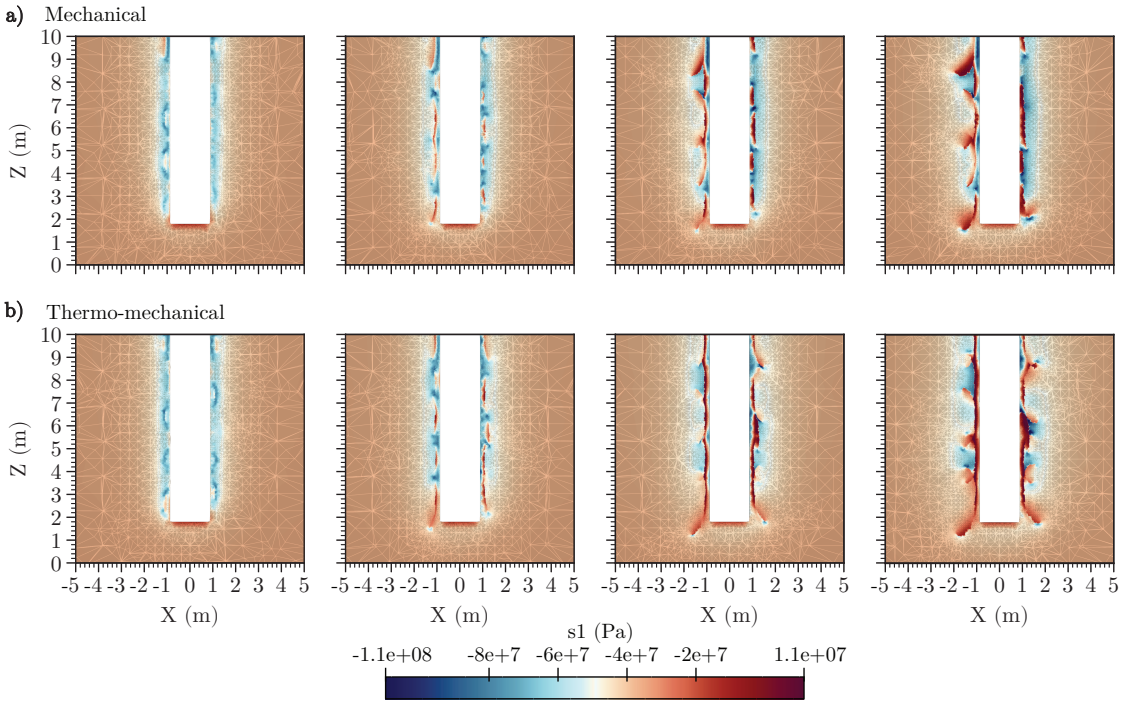


Figure 6.5: Axial cut planes along in the direction of σ_h in the single borehole model showing: **A.** thermo-mechanical and **B.** mechanical only stress at four different growth steps. In the thermo-mechanical case, the four growth steps correspond to stresses after 1 day, 2 weeks, 4 weeks and 8 weeks of heating.

These results suggest that the interplay between thermal and mechanical effects may cause non-intuitive fracturing behaviour, and that the onset of heating relative to the stage of mechanical growth may influence fracture growth. This is further investigated in

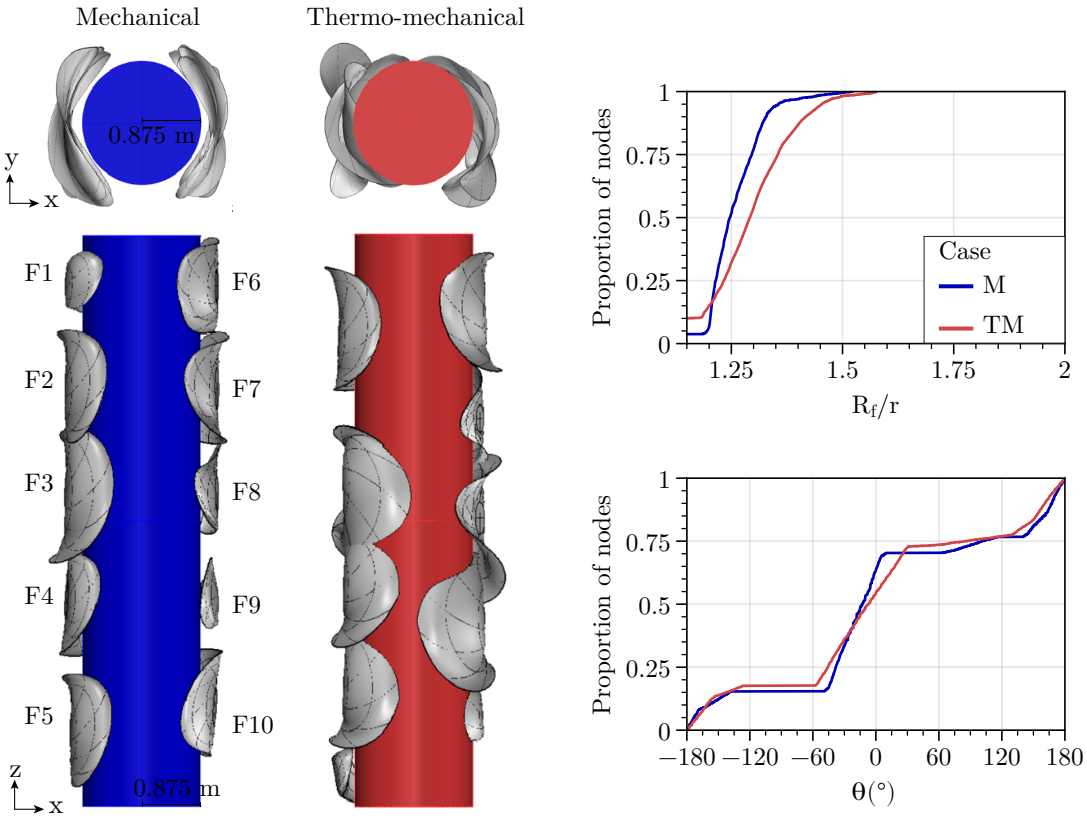
Section 6.3, where a more realistic borehole heating scenario is implemented, based on the decaying heat flux of a spent fuel canister over time.

6.2.4 Fracture patterns and spalling extent

As shown in the previous section, the borehole temperature increases the stress distribution around the borehole, and the thermal effect is most pronounced closer to the borehole wall, in the first 50 cm. The effect of thermal heating on final fracture patterns is more substantial when the borehole wall is heated to 100°C, than in the case where the borehole is not heated at all (Fig. 6.6). In the mechanical case, spalling is limited to the two diametrically opposed spalled zones in the direction of the least horizontal stress. In the thermo-mechanical case, the additional thermal stress promotes spalling in all directions, as the spalling fractures extend towards the springline of the maximum horizontal stress, as if "wrapping" around the borehole (Fig. 6.6). Compared to the base case mechanical spalling, the maximum spalling depth does not increase significantly, but the spalling angle does. The reason for this is that the thermal effect is secondary compared with the mechanical effect of the *in situ* stresses magnitudes (*cf.* Ch. 5).

Figure 6.7 shows fracture development under thermo-mechanical conditions. Ten initial disks nucleate at t = 1 day (Growth step 0) in an initially unfractured rock domain. The initial disks radii are normally distributed around 40 cm average radius with 20% standard deviation, and scaled with initial damage (see Chapter 3, Sec. 3.4). The three subsequent growth steps correspond to t = 2 weeks, t = 4 weeks, and t = 8 weeks, where the temperature distribution in the model follows that shown in Figure 6.3. Fractures are shown as lofted surfaces (Figure 6.7a), emphasising fracture geometry evolution during growth. The fracture array undergoes rapid expansion, with a precedence towards the activation of the larger initial disks. By the second growth step, fractures already begin to interact, and by the third growth step they begin to coalesce along the borehole wall, leading to a gradual reduction in extension during subsequent growth steps, as fracture tips get deactivated once they intersect open fractures.

Figure 6.7b shows surface meshes, showing the evolution of nodal apertures during growth. Fracture apertures are determined based on the interaction between the two sides of the fracture surface: a leader surface and a follower surface, which intersect at the fracture tip. The two surfaces are separated by a normal gap, which is initially zero (Figure 6.7b, Step 0), when the leader and follower surfaces are in contact at every point on the surface. During growth, the differential displacement on either side of the fracture causes the two sides to part, and the fracture opens, incurring aperture. The aperture is determined from the normal gap between the two sides of each fracture and calculated by subtracting the displacements of the leader and follower elements and projecting the gap vector onto the normal vector to the fracture, at every meshed location on the fracture surface:



	Thermo-Mechanical			Mechanical		
Fracture	Spalling Depth [m]	Spalling Width [°]	Surface Area [m^2]	Spalling Depth [m]	Spalling Width [°]	Surface Area [m^2]
F1	0.43	60.3	1.13	0.17	50.3	0.50
F2	0.44	55.1	1.08	0.15	50.0	0.47
F3	0.41	63.6	0.98	0.14	43.7	0.51
F4	0.15	77.1	1.10	0.16	57.1	1.10
F5	0.17	69.5	1.16	0.14	39.5	1.07
F6	0.42	40.3	1.12	0.20	32.0	0.49
F7	0.40	62.0	0.93	0.18	52.0	0.55
F8	0.39	41.2	0.88	0.18	32.3	0.62
F9	0.20	54.9	0.95	0.19	32.9	1.09
F10	0.23	54.1	1.09	0.20	44.7	1.05

Figure 6.6: Spalling patterns and maximum fracture growth extent simulated in the mechanical and thermo-mechanical cases. The maximum spalling depths and widths are reached after 8 weeks of heating in the thermo-mechanical case. The fractures are depicted as lofted surfaces, viewed from radial and axial borehole direction. The locations of the fracture tip nodes are plotted as cumulative distributions for both cases. The distribution plots illustrate the growth extent of the entire fracture array, while the table lists the maximum spalling depth, width, and surface area of each fracture surface individually.

$$a_f = (\boldsymbol{u}_{\text{leader}} - \boldsymbol{u}_{\text{follower}}) \cdot \boldsymbol{n_c} \tag{6.5}$$

where $\boldsymbol{u}_{\text{leader}}$ and $\boldsymbol{u}_{\text{follower}}$ are the nodal displacement vectors of the two faces of the fracture and $\boldsymbol{n}_c$ is the outward unit normal vector to the fracture surface. Aperture is stored at the nodes as a scalar variable (Salimzadeh et al. 2018, Paluszny et al. 2020).

During the growth process (Figure 6.7b Steps 1-3), increased apertures appear at the fracture centres, while apertures at the tips diminish to zero. As fractures interact and merge, the apertures become spatially correlated. This is observable in fractures labeled F1 and F2, which have coalesced by growth step 3 and function mechanically as a single entity. Aperture synchronisation during growth occurs due to local stress perturbations and stress field redistribution around interacting fractures, promoting the concurrent opening or closing of these fractures.

Figure 6.7c summarises the aperture distribution from all fractures displayed in Figure 6.7b, plotting the calculated aperture values at each fracture surface node as a function of radial distance from the borehole wall, and angular distance from the springline of the minimum horizontal stress σ_h. The most significant apertures develop at distances of 1.15-1.5 borehole radii and at borehole azimuths $\theta = 0°$ and $\theta = 180°$, from the direction of the minimum horizontal stress σ_h, demonstrating the aperture correlation within the highly damaged zone, where vertical fractures open parallel to the borehole wall to create spalled slabs.

Figure 6.8 illustrates the maximum principal stress and aperture distribution in an array of 100 fractures, highlighting the impact of initial disk orientation *w.r.t.* the local stress field on fracture growth. Among the 100 fractures, 10 nucleate parallel to the borehole axis, while the remaining fractures are horizontal. Similar to the prior example involving 10 fractures, vertical fractures nearest to the borehole wall experience the most significant extension and opening during growth, owing to their favourable orientation within the redistributed stress field of the borehole.

Vertical fractures interacting along the borehole wall affect each other's growth and apertures by further altering the stress field in the two diametrically opposed fractured zones. Approximately 25 cm from the borehole wall, vertical fractures bend away from the wall and start to close, realigning with the far-field stress as the borehole influence diminishes. In contrast, horizontal fractures undergo minimal extension, and their growth occurs primarily due to shearing in the direction of the maximum principal stress. Apertures for horizontal fractures are generally below 0.5 mm, except for one fracture centered at x=2.4, y=1, z=9.8, which exhibits large apertures at its tips as it intersects the upper boundary of the numerical domain.

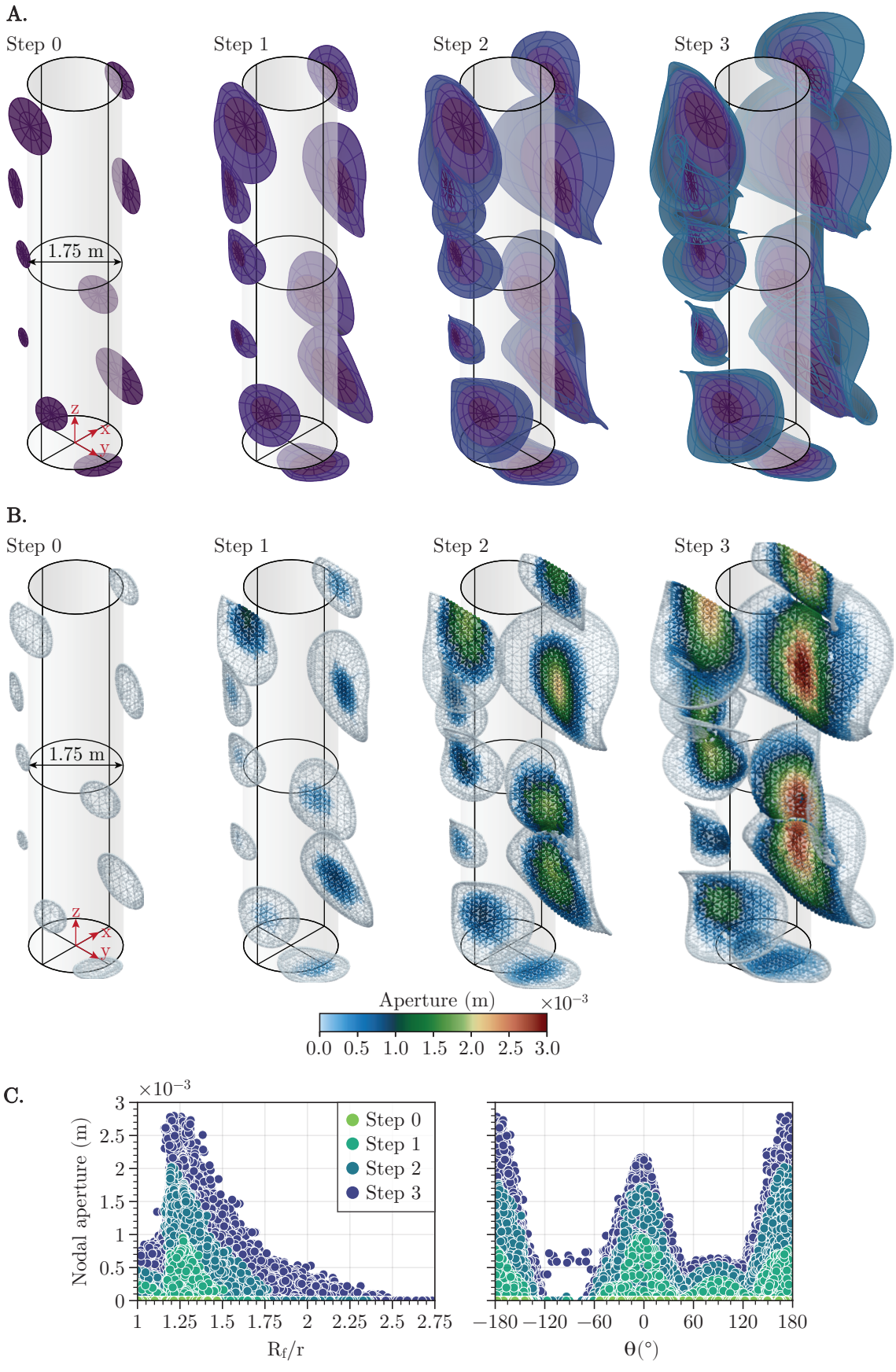


Figure 6.7: Growth of ten spalling fractures in response to thermo-mechanical loading. **A.** Fracture geometries. **B.** Fracture apertures. **C.** Nodal aperture distributions for the whole fracture array plotted against normalised radial distance R_f/R_b and borehole azimuth θ, respectively.

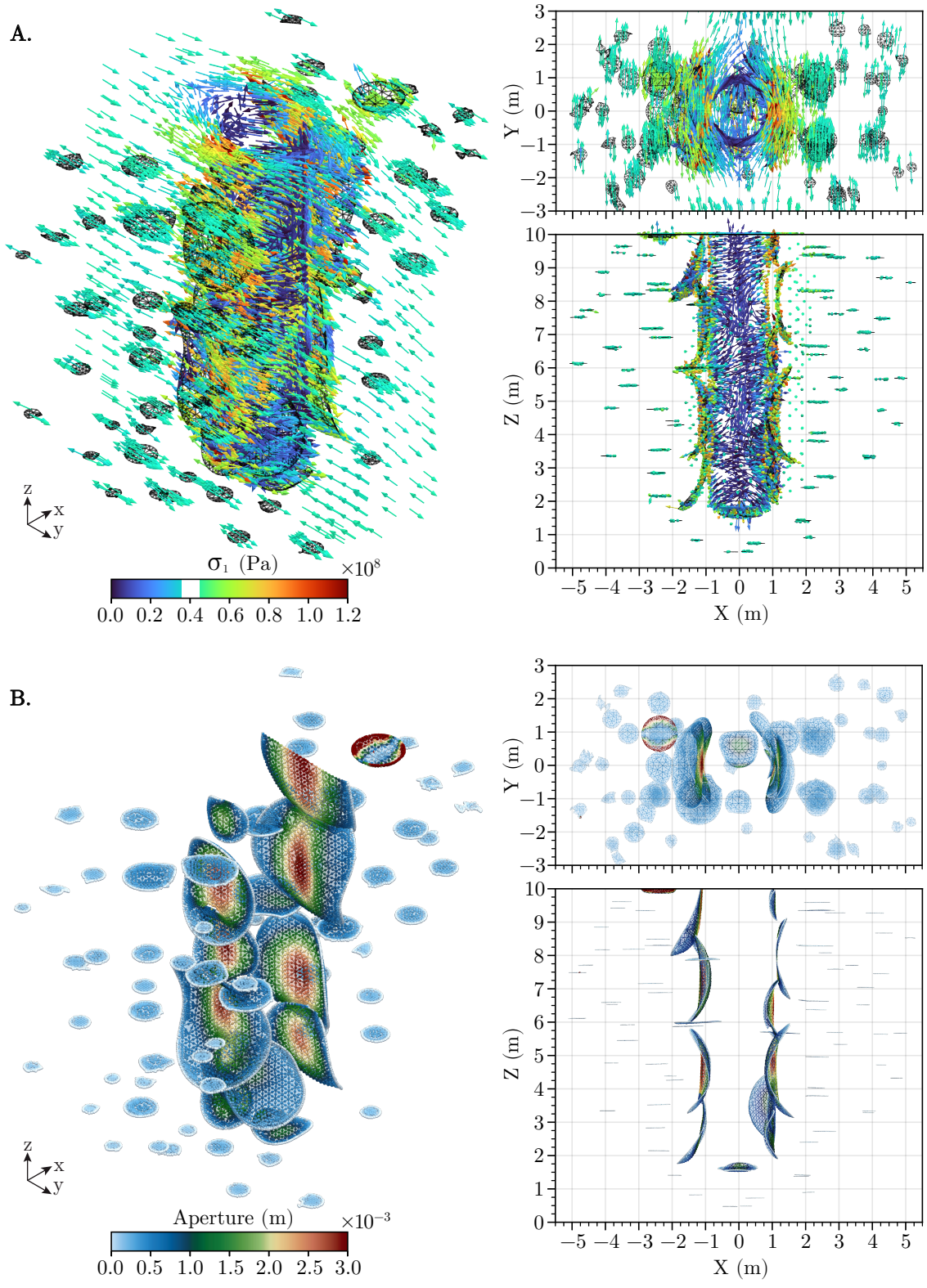


Figure 6.8: Growth of one hundred spalling fractures in response to thermo-mechanical loading. **A.** Maximum principal stress distribution in the fractured zone around the borehole. Values of ±5 MPa around the far-field maximum horizontal stress σ_H are masked to enhance visualisation of the redistributed stress orientation **B.** Fracture apertures distribution within the fractured zone at their maximum.

6.3 Thermo-mechanical spalling of multiple boreholes

The previous section simulated the growth of fractures around a single deposition borehole under coupled thermo-mechanical conditions. The initiation and propagation of spalling fractures are caused by local changes in the stress field due to excavation and thermal heating of the borehole. The influence of temperature on spalling is evaluated by comparing fracture patterns, maximum spalling depths, and widths, which exhibit an increase in the total fractured surface area with increasing temperature. This section implements a realistic heating scenario, based on a typical spent fuel canister decay rate.

In this section, the effect of neighbouring boreholes and a more realistic borehole heating scenario is investigated. A multiple-borehole model is considered, that comprises a 40×20×20 m block of granodiorite. The model includes three circular boreholes with a diameter of 1.75 m, which are subjected to a far field anisotropic triaxial stress. The model geometry and mechanical boundary conditions are identical to the ones used in the 3-borehole mechanical spalling model from the previous chapter. The mechanical and thermal properties of the host rock are the ones listed in Tables 5.1 and 6.1, respectively. These are representative of the Forsmark rock domain FFM01, which is a granodiorite (Rock Type 101057) commonly found at the Swedish repository site. The model geometry and boundary conditions can be summarised as:
Model geometry:

$$\Omega = (x, y, z) \in \mathbb{R}^3 : -20 \leq x \leq 20 \text{ and } -10 \leq y, z \leq 10 \tag{6.6}$$

Cylindrical borehole geometry:

$$\mathcal{B} = (x, y, z) \in \Omega : x^2 + y^2 \leq 0.875^2 \text{ and } 1.2 \leq z \leq 10 \tag{6.7}$$

Initial condition for temperature:

$$T(\mathbf{x}, 0) = 11.2°\text{C}, \quad \forall \mathbf{x} \in \Omega \tag{6.8}$$

Boundary conditions for temperature: Variable heat flux Q_{borehole} at the borehole surface:

$$-k\nabla T(\mathbf{x}, t) \cdot \mathbf{n} = Q_{\text{borehole}}(\mathbf{x}, t), \quad \forall \mathbf{x} \in \partial\mathcal{B} \tag{6.9}$$

Constant temperature at the domain edges:

$$T(\mathbf{x}, t) = 11.2°\text{C}, \quad \forall \mathbf{x} \in \partial\Omega \setminus \partial\mathcal{B} \tag{6.10}$$

where Ω represents the numerical domain, $\mathcal{B}$ represents the cylindrical borehole, $T(\mathbf{x}, t)$ represents the temperature at a point $\mathbf{x}$ in the domain at time t, $\partial\Omega$ denotes the boundary

of the domain, $\partial\mathcal{B}$ denotes the boundary of the borehole, $\mathbf{n}$ denotes the unit outward normal vector to the boundary $\partial\mathcal{B}$, $\nabla T(\mathbf{x}, t)$ is the gradient of the temperature, and k is the thermal conductivity of the host rock.

Two distinct scenarios are examined in this section:

- Case 1 (TM): the boreholes are heated immediately after their excavation, and fractures nucleate and grow under coupled thermo-mechanical (TM) loading, as in the previous section.
- Case 2 (M⇒TM): The boreholes are excavated and mechanical nucleation and growth are modelled as in Chapter 5 following the excavation process. After fracture growth under purely mechanical conditions has arrested, the boreholes are subjected to heating. This scenario thus explores the behaviour of spalling fractures under coupled thermo-mechanical loading, while also accounting for pre-existing "mechanical" damage.

In both investigated scenarios, more practical boundary conditions are employed. Specifically, the boreholes are heated by imposing a heat flux at their walls (Table 5.1), instead of an instantaneous boundary temperature, as in the previous section. Subsequently, the initial heat flux is gradually reduced following the power decay characteristics of a typical spent fuel canister, as illustrated in Figure 6.9b (SKB TR-03-09 2003).

Under these conditions, the host rock undergoes a cyclic process of heating followed by cooling, instead of continuous heating. Additionally, to ensure that the temperature variation in the borehole radial direction is accurately captured, only the temperature at the bottom domain boundary is fixed to the initial rock temperature of 11.2 °C. The temperature on all other boundaries is free to change from the initial value of 11.2 °C, when the thermal pulse reaches them. This also ensures that the system does not reach a "steady state" condition as in the previous section, and the temperature can be validated against SKB calculations at repository scale.

Temperature distribution and its evolution depends on the canister power and host rock thermal properties, as well as the number, and the arrangement of boreholes within the repository. Figure 6.9b shows rock temperature increase at the central borehole mid-height, for several repository layouts. Numerical results from ICGT agree with SKB's analytical calculations for the simpler repository layouts, e.g. where the thermal contributions from one borehole (local canister), or seven co-linear boreholes (local canister and its six closest neighbours) are considered. In the case of more complex repository layouts involving an entire deposition area (approx. 1200 boreholes), it is not practical to model spalling (a cm-scale process) around all thousands deposition boreholes simultaneously. In order to capture the effect of the deposition area, the analytically determined repository

temperature (from the 1200 borehole case) is applied directly as boundary condition to the three-borehole model replacing the canister heat flux as boundary condition.

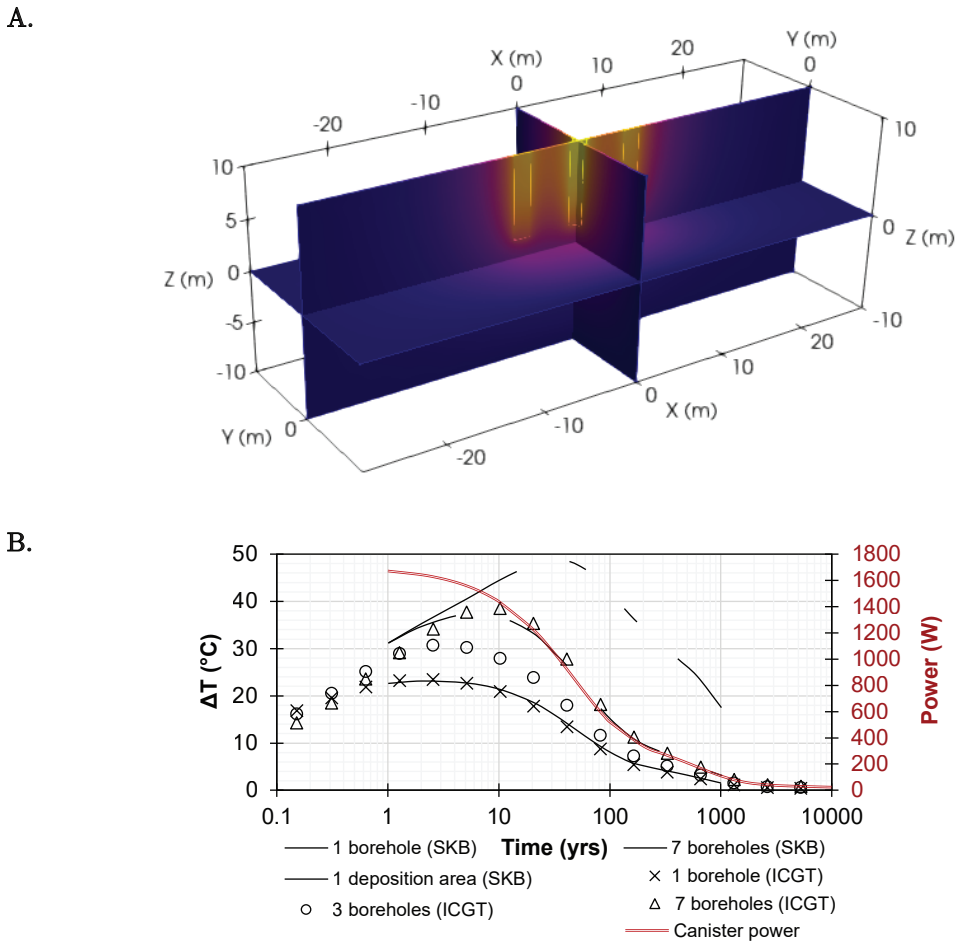


Figure 6.9: Temperature field in a three-borehole repository model. **A.** Temperature field showing cut planes after approximately five years, when the central borehole surface reaches the maximum temperature of 41 °C. **B.** Rock temperature increase at the central borehole mid-height, for several repository layouts and compared with SKB's analytical calculations.

Temperature and stress distributions are considered in the three-borehole model, after approximately five years, when the central borehole surface reaches a maximum temperature of 41 °C, *i.e.*, $T = T_i + \Delta T = 11\ °C + 30\ °C = 41\ °C$. The temperature is shown in Figure 6.9a, and the maximum principal stress distribution is shown in Figure 6.10a. The additional thermal stress amounts to approximately 10 MPa at peak borehole temperature, which promotes fracture growth around and along the borehole, compared with mechanical spalling, but it does not impact the spalling depth significantly. Fracture surfaces appear as zones of low stress concentration in the near borehole region, and fracture tips, conversely, as high stress concentrations. More growth and fracture interaction with the borehole wall occurs in the case of thermal heating immediately after excavation (Figure 6.9).

When the boreholes are heated after mechanical spalling has arrested (Figure 6.10b), the pre-existing spalling fractures do not extend. Additional fracture nucleation is not investigated. The maximum spalling depth, spalling widths of the two diametrically opposite fractured zones, and the total fracture surface area corresponding to the central borehole in the two simulated cases are listed in Table 6.1.

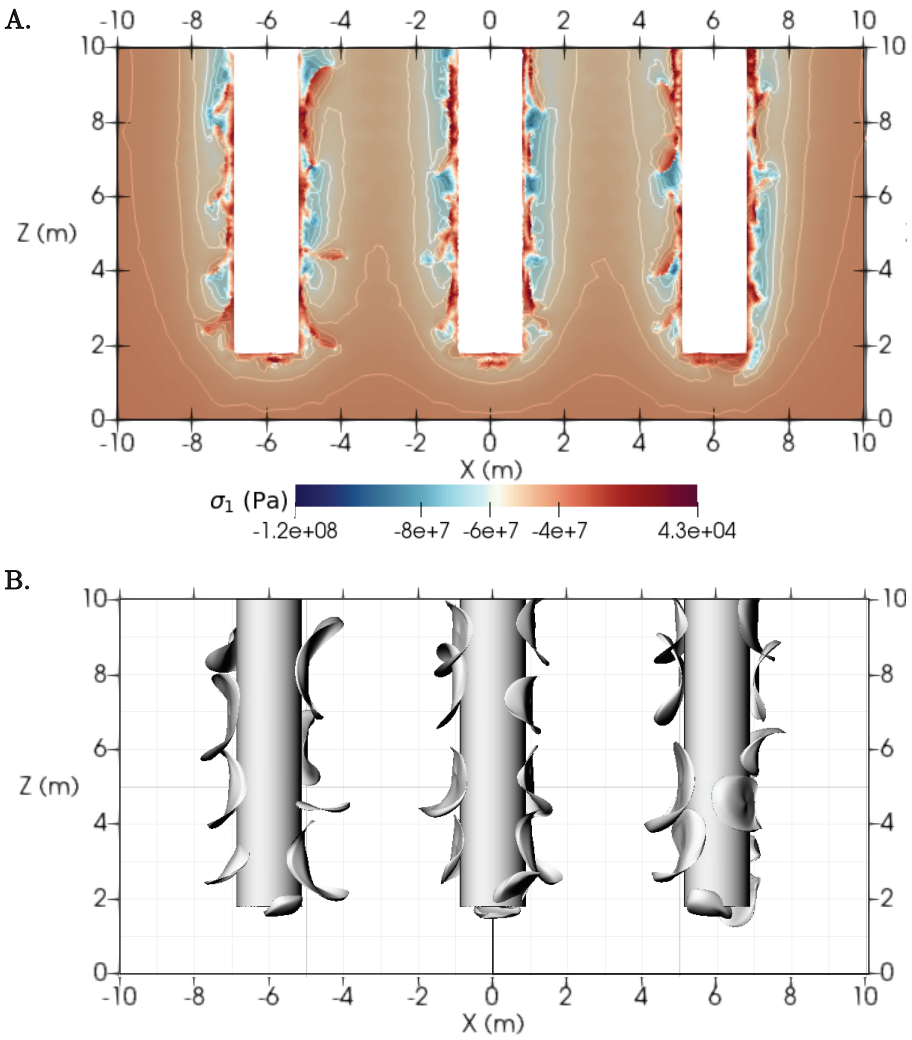


Figure 6.10: Maximum principal stress field in a three-borehole repository model. **A.** Maximum principal stress field in a three-borehole repository model showing cut planes after approximately five years, when the central borehole surface reaches the maximum temperature of 41 °C. **B.** Fracture patterns in three dimensions corresponding to the stress contours shown in **A.**

6.4 Effect of *in situ* heterogeneities

The previous sections presented simulations that were conducted with a homogeneous initial domain. However, the repository planned for Forsmark covers an area of 3-4 km^2 and, despite consisting of largely uniform rock units, an initial heterogeneous domain

would more accurately reflect the actual underground conditions.

It is widely recognised that material heterogeneity, particularly in rock formations, can significantly affect fracture propagation (Zhang & He 2020, Vardon & Nuttall 2009). This section introduces a first level of heterogeneity in the model and investigates its impact on the simulated spalling patterns. In particular, the variation of elastic properties is addressed by using two spatial distribution approaches. In the first, a series of boxes represent the heterogeneities, in the second, clusters of properties represent the variations within the rock. In this approach, variation is assumed to occur at a single scale, comparable to the scale of the borehole.

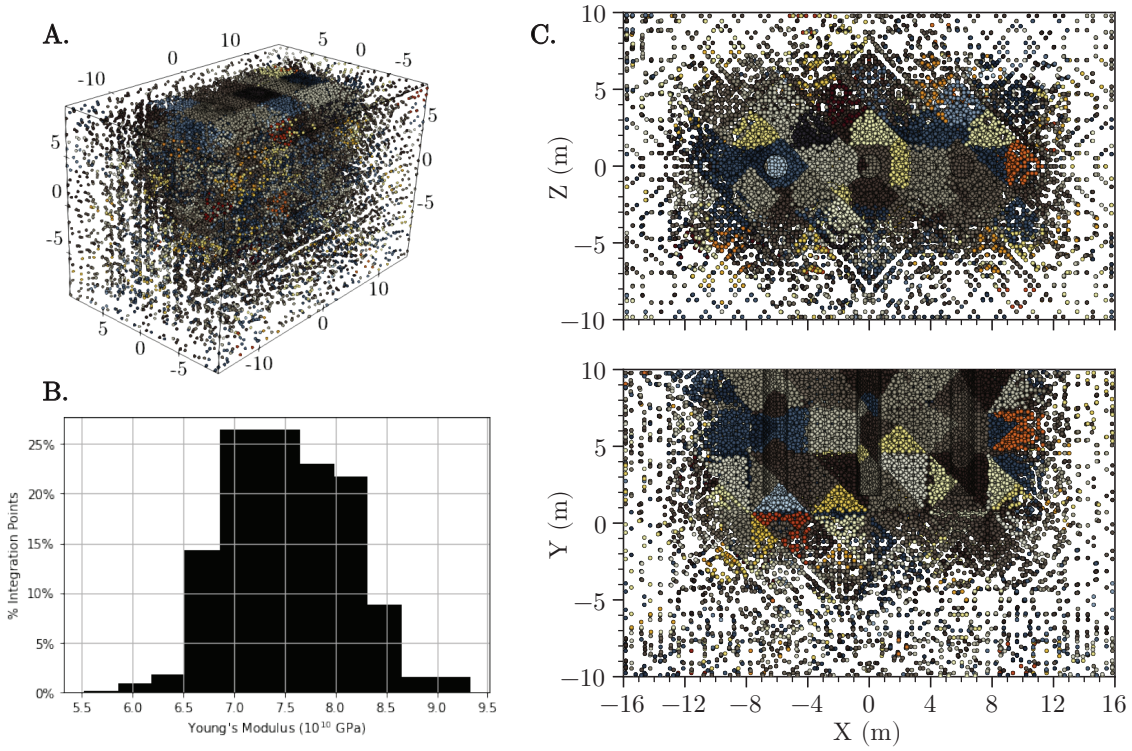


Figure 6.11: Heterogeneous elastic modulus distribution using boxes. Elastic modulus distribution where the integration points have been grouped into boxes of dimensions 4 × 4 × 4 m. The boxes are assigned values of elastic modulus picked randomly from a uniform distribution with average 76 GPa and 5 GPa standard deviation.

To introduce heterogeneity into the initial domain, random uniform distributions of the elastic modulus and fracture toughness are considered, such as those shown in Figures 6.11 and 6.12. All other mechanical and thermal properties are held constant across the numerical domain. The average Young's modulus of the rock is set to 76 GPa, which corresponds to the average value at Forsmark. The heterogeneous cases are generated by introducing random perturbations to the Young's modulus around the average value, with variations of ±5 GP as standard deviation. To examine the impact of the degree of property variation, integration points with similar Young's moduli are randomly grouped into clusters.

The remeshing steps involve mapping at the integration points, where the material properties are defined, to preserve the initial distributions of heterogeneity throughout the simulation.

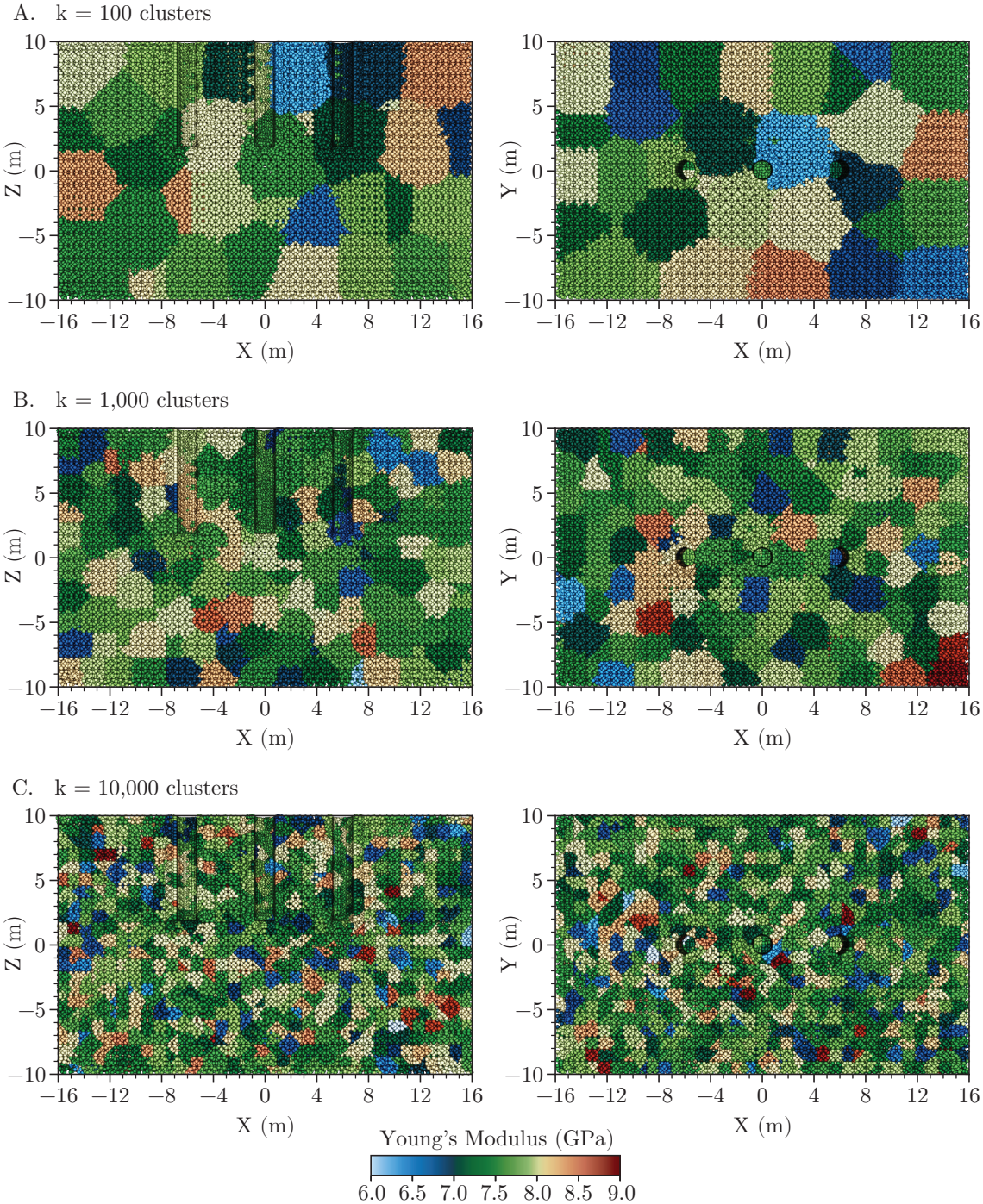


Figure 6.12: Heterogeneous elastic modulus distribution using clusters. Elastic modulus distribution in three heterogeneous initial domains, where the constraint points have been grouped into a number of k clusters based on the distance between the parent element barycentre and the cluster barycentre. The clusters are assigned values of elastic modulus picked randomly from a uniform distribution with average 76 GPa and 5 GPa standard deviation.

A more effective method for representing a heterogeneous domain involves clustering constraint points into k groups based on the distance between the parent element barycentre and the cluster barycentre, as depicted in Figure 6.12. Initially, the cluster barycentres are randomly distributed, and a k-means clustering algorithm is implemented to assign the integration points to their respective clusters (Algorithm 3). The cluster barycenters are subsequently updated, resulting in a wider range of heterogeneity shapes, compared to those illustrated in Fig. 6.11.

Figure 6.11c presents a cross-section of the models displayed in Figure 6.11a. The integration points, where material properties are defined, have been grouped into clusters with a dimension of approximately $4 \times 4 \times 4$ m. Regardless of mesh refinement or coarsening, the clusters maintain a consistent dimension of $4 \times 4 \times 4$ m, and the Young's moduli within each cluster remain constant across the remeshing and remapping steps. The remapping between different meshes is performed at the integration points to preserve the initial heterogeneity distributions throughout the simulation, ensuring that heterogeneity is not influenced by the size of the mesh.

Figures 6.13a and 6.13b present stress contour diagrams in a three-borehole homogeneous and heterogeneous model, respectively. Both figures depict the stress state prior to fracture nucleation. The heterogeneous stress field corresponds to the elastic modulus distribution shown in Fig. 6.11. Fig. 6.13b shows that the local variations of the elastic modulus in the heterogeneous model cause the stress contours to become discontinuous, unlike the continuous contours in the homogeneous model. Additionally, the stress interaction between adjacent boreholes is reduced in the heterogeneous model. Due to the discontinuity in the stress field, there is an approximately 10 MPa decrease in the maximum tangential stress at the central borehole wall in the heterogeneous model compared to the homogeneous model.

Figure 6.13 also displays radial and axial views of the final fracture patterns in the two models, after fractures have initiated and grown to develop spalling patterns. Compared with the homogeneous model, the heterogeneous one displays more variable distribution of fractures along the borehole wall. This is because homogeneous domain accumulates uniform strain at the borehole wall, at all z-locations, due to the effect of stress redistribution. As the domain heterogeneity increases, the damage remains primarily concentrated at the borehole wall, but high strain zones are found at larger radial and azimuthal distances from the borehole wall, increasing the likelihood of fractures nucleating in these areas. In the heterogeneous model, therefore, local concentrations of initial damage causes the fractures to nucleate and develop at locations not predicted by the homogeneous model. However, a qualitive assessment of the fracture patterns reveals that growth in the heterogeneous case is overall more constrained and limited than in the homogeneous case, possibly because of the stress shadowing effect shown in Figure 6.13b.

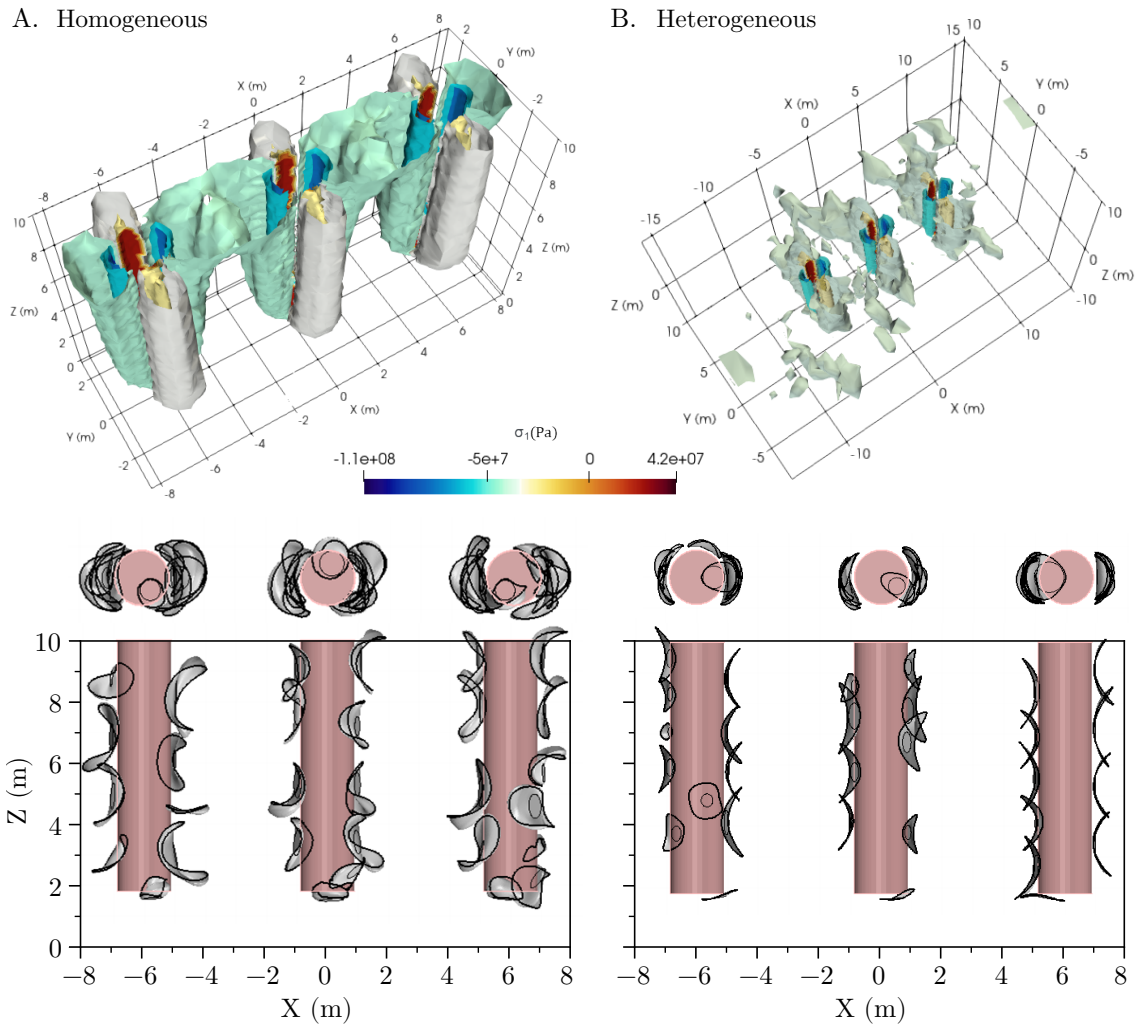


Figure 6.13: Comparison of the maximum principal stress contours and fracture patterns around three boreholes in a homogeneous (**A.**) vs. heterogeneous (**B.**) model. The heterogeneity distribution is the one shown in Fig. 6.11.

6.5 Discussion

The results presented in this chapter align with those observed at the Äspö Hard Rock Laboratory (HRL), where Andersson et al. (2009*a*) investigated the interplay between excavation-induced and thermal-induced stresses around two deposition boreholes in situ. The experiment involved the creation of a 1-meter-thick fractured pillar of diorite positioned between two boreholes with diameters of 1.75 meters, located at a depth of 450 meters, and the application of confining pressure and heating to trigger brittle failure within the rock mass. The resulting spalled zone showed a spalling width of approximately 130° and was formed through tensile fracturing that occurred parallel to the borehole wall. These findings agree with the results presented in this chapter, which demonstrates the enlargement of the width of spalling in scenarios involving thermo-mechanical effects as

compared with purely mechanical loading.

Algorithm 3: Simplified K-means Clustering Algorithm for Heterogeneity

```
Input: k, min_point, max_point
Output: clusters
initializeClusters(k, min_point, max_point)
for i ← 0 to k − 1 do
    Generate random centroid within min_point and max_point
    Create cluster with generated centroid
    Add cluster to clusters list
return clusters
Input: model, clusters
assignElementsToClusters(model, clusters)
foreach cluster in clusters do
    Clear old element IDs from cluster
foreach element in model do
    Find closest cluster centroid to element's barycentre
    Assign element ID to closest cluster
Input: model, clusters
updateClusterCentroids(model, clusters)
foreach cluster in clusters do
    Calculate new centroid as mean of barycentre of all elements in cluster
Input: model, k, max_iterations
Output: clusters
kMeansClustering(model, k, max_iterations)
Initialise clusters with random centroids
for iter ← 0 to max_iterations − 1 do
    assignElementsToClusters(model, clusters)
    updateClusterCentroids(model, clusters)
return clusters
Input: model, average, std_dev
AddHeterogeneityClusters(model, average, std_dev)
Run kMeansClustering(model, k, max_iterations)
foreach cluster in clusters do
    Sample from normal distribution with average and std_dev
    foreach element in cluster do
        Assign sampled value to element's constraint points
```

At Äspö, changes in the magnitude of tangential stress at a level of about 1 MPa were

sufficient to initiate further propagation. This contrasts with the observations of spalling depth in the present chapter, which showed a slight increase in the depth of spalling, but it largely remained unaffected by borehole heating, although the simulated changes in tangential stress were larger than 1 MPa. This discrepancy can be attributed to the fact that the rock pillar in the simulation is thicker than in the experiment (6 m vs 1 m) and that the spalling fractures had already reached a stable state during the mechanical stage of the simulation.

6.6 Conclusions

Thermo-mechanical simulations were conducted to study fracture initiation and growth under coupled conditions around a multiple borehole model of a deep geological repository. The effect of temperature on the nucleation and growth of spalling-inducing fractures, as well as on the reactivation of pre-existing mechanical fractures, was investigated and it was determined that the additional thermal stress enhances spalling if the boreholes are heated before the first fractures nucleate (Fig. 6.6), but it is not sufficient to reactivate pre-existing mechanical fractures (Fig. 6.10b). Overall, the thermal heating from a typical radioactive waste container is predicted to increase spalling depths and widths. Based on simulations presented herein, thermal heating is not considered to be a major factor acting to increase fracture surface area, and is not expected to cause severe borehole instability for the studied repository configuration.

Heterogeneity was introduced in the intact rock domain by perturbing the mechanical (elastic modulus, fracture toughness) properties of the host rock. Spalling initiation and growth was numerically evaluated as a function of host rock heterogeneity. Fracture patterns and their extent were compared with an analogous homogeneous case. Numerical results showed that rock heterogeneity influences the propagation of spalling fractures, and their interaction with the borehole walls, through the creation of stress shadow zones, illustrated as discontinuities in the stress contours.

The chapter presented simulations of three-dimensional fracture initiation and growth under coupled thermo-mechanical conditions and investigated the effect of heterogeneities on borehole stress, damage and fracture patterns. A random heterogeneity configuration was generated with a probability distribution of the elastic modulus, based on its expected frequency distribution at Forsmark. This configuration was then subjected to deterministic fracture growth simulation. Numerical results suggest that heterogeneity may reduce spalling severity. Further work is planned such that, multiple heterogeneity configurations are generated from the same probability distribution of the elastic modulus, which will provide a distribution of simulated spalling depths and widths for a given elastic modulus distribution.

Chapter 7

Effect of glaciation on long-term repository stability

7.1 Introduction

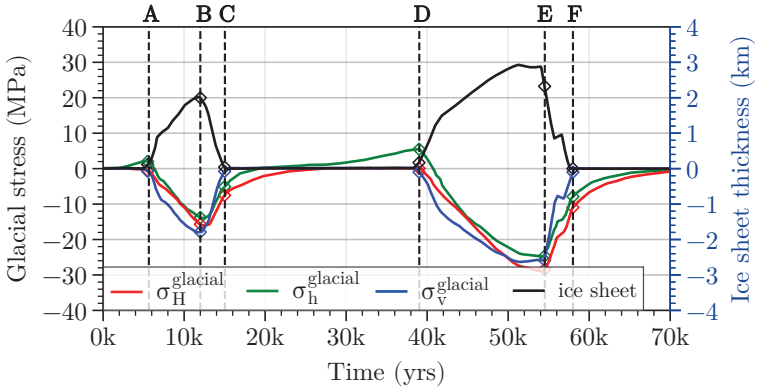
Spalling-inducing fractures initiate in tension and propagate as a response to the mechanical and, if present, thermal loading of the borehole. Fractures interact and coalesce in the vicinity of the borehole, forming excavation damage zones (EDZs), which are classified based on the intensity of the damage (Tsang et al. 2005, Siren et al. 2015). The damaged zone closest to the borehole wall contains interconnected fractures and is generally referred to as highly damaged zone (HDZ). The fractures within the HDZ may cause slabs of rock to spall from the borehole wall, resulting in a distinctive V-shaped notch, i.e. the "spalled" zone, in the direction of the minimum compressive stress (Figure 2.2). Beyond the spalled zone, the host rock becomes progressively less damaged, but the fractures in the outer excavation damage zones still alter host rock properties such as permeability (Siren et al. 2015).

Observations from field studies indicate that mechanical spalling is a common occurrence during the excavation stage of deep-drilled boreholes and tunnels in hard, brittle rock (Read 2004, Martin et al. 1999), and that it will be aggravated during the thermal stage of a deep geological repository (DGR) for nuclear waste disposal (Andersson et al. 2009*b*). DGRs in high latitude regions also have the additional long term risk of being impacted by glaciations (SKB TR-10-23 2010), which may cause new fractures to nucleate in the EDZs, or reactivate pre-existing ones.

During glaciations, the cyclical expansion and contraction of the ice sheet exerts increased mechanical load on the repository, through both the added weight of the ice as overburden, and the flexural response of the Earth's lithosphere. In Sweden, the lithospheric flexure

will induce additional horizontal stresses, that are equal in magnitude to the vertical stress resulting from the weight of the ice (SKB TR-09-15 2009). This will cause fluctuations of the same order of magnitude in the all three far-field stresses at repository depth, as shown in Figure 7.1. The changes in the *in situ* stresses during glaciations can lead to increased fracturing, manifesting as heightened permeability and additional fault slip, as observed in the endglacial faults in Sweden (SKB TR-09-15 2009).

The aim of this chapter is to present a preliminary assessment of the potential impact of glaciations on fracture growth around the future deposition boreholes at the Swedish repository site at Forsmark.



Glaciation Events	
A	1st forebulge
B	1st glacial max.
C	1st edge retreating
D	2nd forebulge
E	2nd glacial max.
F	2nd edge retreating

Figure 7.1: Temporal evolution of the ice sheet thickness and the glacially induced stress components at repository depth, i.e., 500 m depth, at Forsmark (from SKB TR-10-23 (2010)).

7.2 Numerical model set-up

A multiple-borehole model is considered, consisting of a 40 × 20 × 20 m block of granodiorite. The numerical domain contains three 1.75 m diameter circular boreholes, with an access ramp at the top, spaced 6 m apart. The model is subjected to a far field anisotropic triaxial stress, as shown in Figure 7.2a. The domain boundaries are placed sufficiently far away from the boreholes, as to not influence fracture growth in the near borehole region where fracturing occurs. Rock mechanical properties (Table 7.1) are representative of granodiorite, the most frequent lithology at the Swedish site.

Figure 7.2 illustrates the *in situ* stresses that existed during the previous glaciation and their deviation from present-day base values. The horizontal stresses evolution is based SKB's reconstruction of the Weichselian glaciation through ice-crust-mantle simulations (SKB TR-09-15 2009), and the vertical stress is equivalent to the ice load throughout the glaciation.

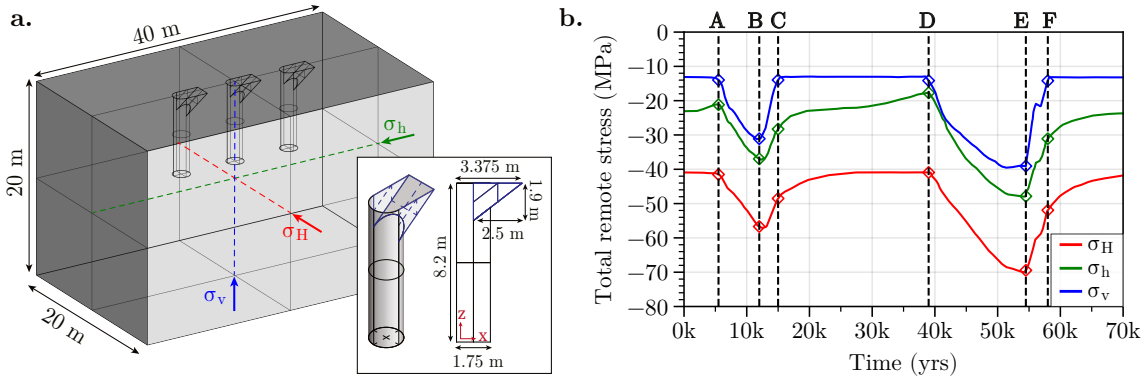


Figure 7.2: **A.** Model geometry and boundary conditions. **B.** Predicted temporal evolution of the total remote stress at Forsmark throughout the next glaciation (SKB TR-10-23 2010).

Table 7.1: Rock properties in the glaciation simulations (SKB TR-08-05 2008).

Property	Value
Density	2.73 g/cm^3
Young's modulus	76 GPa
Poisson's ratio	0.23
UCS	226 MPa
Tensile strength	13 MPa
K_{IC}	3.8 MPa/$\sqrt{m}$

Table 7.2: *In situ* stresses used in the spalling simulations (SKB TR-09-15 2009).

Event	σ_H	σ_h	σ_v
A: 1st forebulge	41.0 MPa	20.5 MPa	13.2 MPa
B: 1st glacial max.	56.7 MPa	36.8 MPa	31.3 MPa
C: 1st edge retreating	48.5 MPa	28.0 MPa	13.2 MPa
D: 2nd forebulge	41.0 MPa	17.5 MPa	13.2 MPa
E: 2nd glacial max.	70.0 MPa	47.8 MPa	39.2 MPa
F: 2nd edge retreating	51.9 MPa	30.9 MPa	13.2 MPa

Six cases are investigated, corresponding to six snapshots in time during the glacial cycle (labeled as events A-F in Table 7.2). Each case comprises different combinations of the principal *in situ* stresses (σ_H, σ_h, σ_v) as listed in the same table. Nucleation and growth are simulated at the six different glaciation events, corresponding to six snapshots in time during the glacial cycle (events A-F). The influence of the *in situ* stresses on fracture nucleation and growth is assessed by simulating each scenario independently from the others, *i.e.* pre-existing damage is not taken into account.

7.2.1 Modelling Assumptions

Mechanical deformation is computed as elastic deformation (Cook et al. 2001) in an initially homogeneous and isotropic numerical domain. The force balance of the system is solved numerically using the finite element method (FEM) to determine the displacement, stress and strain fields. A damage mechanics approach is used to describe the fracture initiation process (Mazars et al. 2015). The nucleation loci of initial fracture disks are found from the equivalent strain, ε, which is the vector norm of the positive part of the strain tensor, and a measure of extensile strain. Fractures nucleate in the elements where ε exceeds the critical nucleation strain ε_c, defined as the ratio of uniaxial tensile strength to elastic modulus. Fractures are grown quasi-statically and growth is driven by stress intensity factors (SIFs), corresponding to the three principal deformation modes (opening, in-plane shear, and out-of-plane shear).

The SIFs are computed using the interaction integral method (Nejati et al. 2015*a*), and incorporated in growth criteria to determine if and by how much fracture tips will extend at every growth step. Richard et al. (2014) mixed-mode propagation criterion, utilising the vales of all three SIFs, is evaluated at each fracture tip to determine the critical SIF at which the tip will extend. Several simplifying assumptions are made in this chapter:

- The thermal transient phase of the repository has completed before the start of the glaciation and the repository temperature has returned to its initial value prior to the emplacement of the spent fuel canisters, *i.e.* 11.2°C (SKB TR-10-23 2010). This assumption is supported by the results from the previous chapter, where the rock wall temperature of deposition boreholes returned to approximately 15°C after 10,000 years, based on the power decay characteristics of a typical spent fuel canister. The previous chapter also demonstrated that large temperature differences are required to observe an effect on fracture patterns and damage extent. Therefore, even though temperature diffusion is a slow process, the thermal phase is not expected influence the *in situ* stress conditions at the beginning of the glaciation.

- The host rock is initially unfractured and has zero porosity. In reality, the ice sheet is expected to elevate the water pressure in the pre-existing fractures within the host rock (SKB TR-10-23 2010). The coupled THM response of the rock to the changes in the *in situ* stresses is within the scope of further study.

- The stress magnitudes during the next glaciation will resemble the Weichselian, which occurred approximately between 115,000-12,000 years ago. The stress boundary conditions (Table 7.2) used in this chapter are selected to represent key events during this 100,000 year period. An additional assumption is that the glacial stress has the same orientation as the initial *in situ* stress. Further work could also con-

sider account the variability of glacially induced stress directions, *i.e.* the relative rotations between the background stresses and the additional glacial stresses.

- Erosion of the overburden occurring as a result of glacial activity, *e.g.* through abrasion, weathering, or dissolution of the overburden as a result of the glacial cycles is not considered in this chapter. These processes are assumed to be secondary, given that modelling results from the previous chapters predicted the fractures to remain localised to the borehole walls under a range of stress conditions, and not become through-going fractures through the pillars separating the deposition boreholes.

7.3 Fracture patterns and spalling extent

Figure 7.4a shows top views (stacked radial planes along the borehole length) of the fracture patterns that develop during the six glacial events. Fractures are represented as lofted surfaces and the surface isocurves are coloured according to the growth step for each glaciation event. The spalling depths and widths are summarised in Figure 7.4b as cumulative distributions for each simulation case, showing the proportion of fracture tips located below given values of radial or azimuthal distance with respect to the borehole wall. The CDF curves encompass fracture tip locations from across all growth steps and from all growing fractures, per glaciation event.

For each fracture tip, θ is defined as the azimuth angle of the tip relative to σ_H direction, and R_f is defined as the distance from the tip to the borehole wall. The presence of a fracture tip at a location (R_f, θ) from the borehole wall does not imply that spalling occurs at that location, but rather that the host rock is fractured. In this work, "spalled zones" refer to the diametrically opposite fractured regions that develop around the borehole in the σ_h direction, assuming material buckling and collapse into the borehole have not occurred yet.

The simulation results show that, despite fractures extending as far as 2.5 m away from the borehole wall, most of the growth is heavily concentrated in the first 30 cm away from the boreholes for both the central and flanking boreholes. In all simulation cases, except case E, the fractures extending beyond 30 cm from the borehole wall are those developing around the ramps of the deposition boreholes. During the second glacial maximum (case E), higher stress concentrations cause fractures to nucleate and extend further from the borehole walls, but there is less overall interaction with the boreholes, as only a small proportion of fracture tips intersect the borehole. This is because the fracturing from prior glaciation events has not been considered.

The decrease in σ_h due to forebulging (cases A and D) leads to an increase in the spalled zones depths, but the extent of spalling fractures is greatest during the early stages of ice

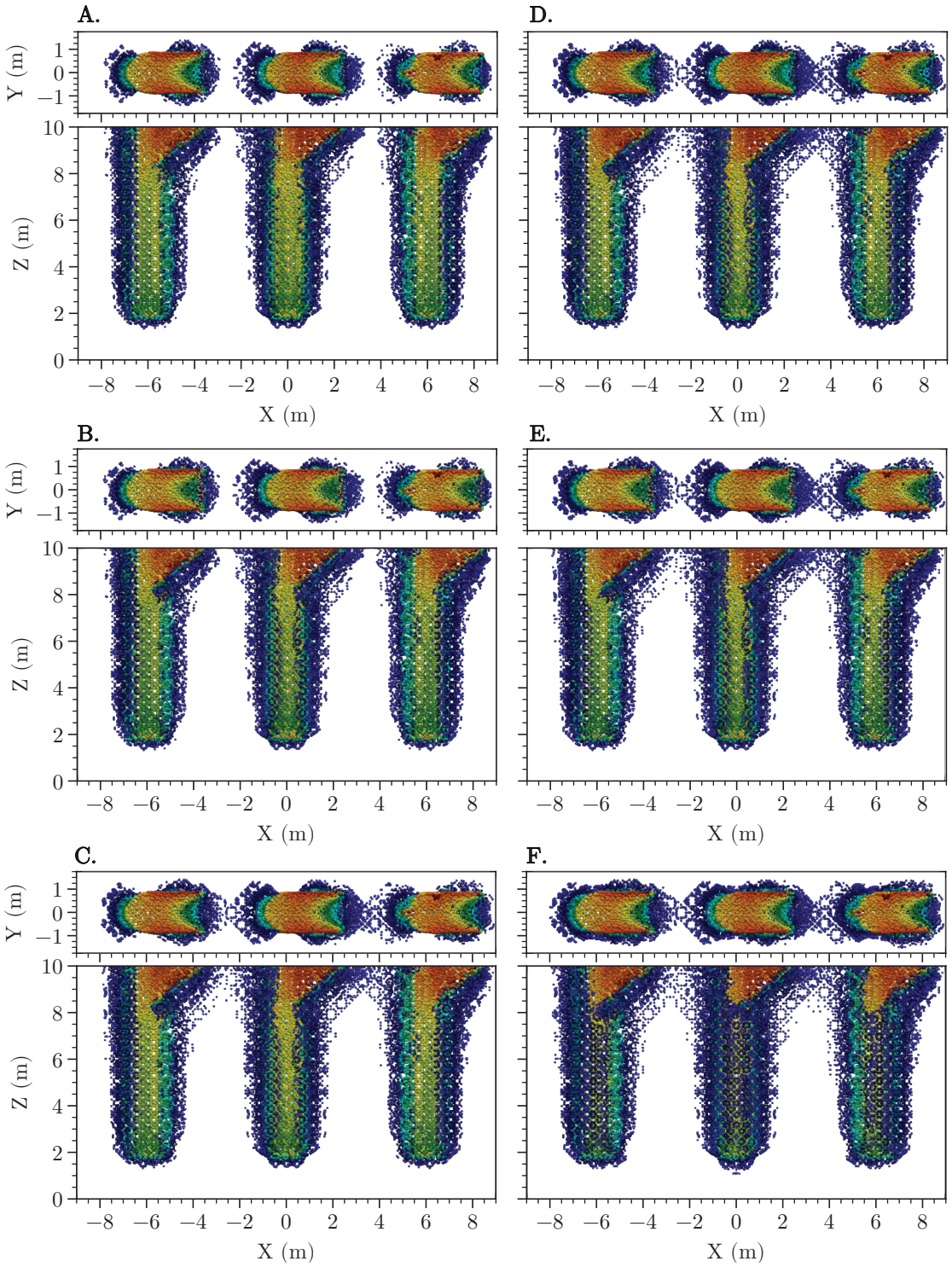


Figure 7.3: Top and side views of the fracture nucleation loci during the selected glacial events A-F. The integration points where the damage threshold for nucleation is exceeded are coloured based on the equivalent strain value of the parent element.

sheet retreat (cases C and F). This can be attributed to the fact that variations in σ_h have a greater impact on the horizontal stresses ratio (σ_H/σ_h), causing higher tangential stresses around the boreholes. Therefore, numerical results indicate that spalling depth is influenced primarily by the relative magnitudes of the *in situ* stresses, rather than the absolute mean stress magnitude, in agreement with other numerical studies investigating the effect of the minimum horizontal stress σ_h (Shen et al. 2002, Shen & Barton 2018, Lisjak & Grasselli 2014, Diederichs 2007*a*).

Regardless of the simulated stress state, no through-going fractures develop in the rock pillars separating the deposition boreholes, suggesting that the repository configuration with borehole spacing of 6 m is stable and the damaged zones where spalling occurs are confined to the close vicinity of their respective borehole.

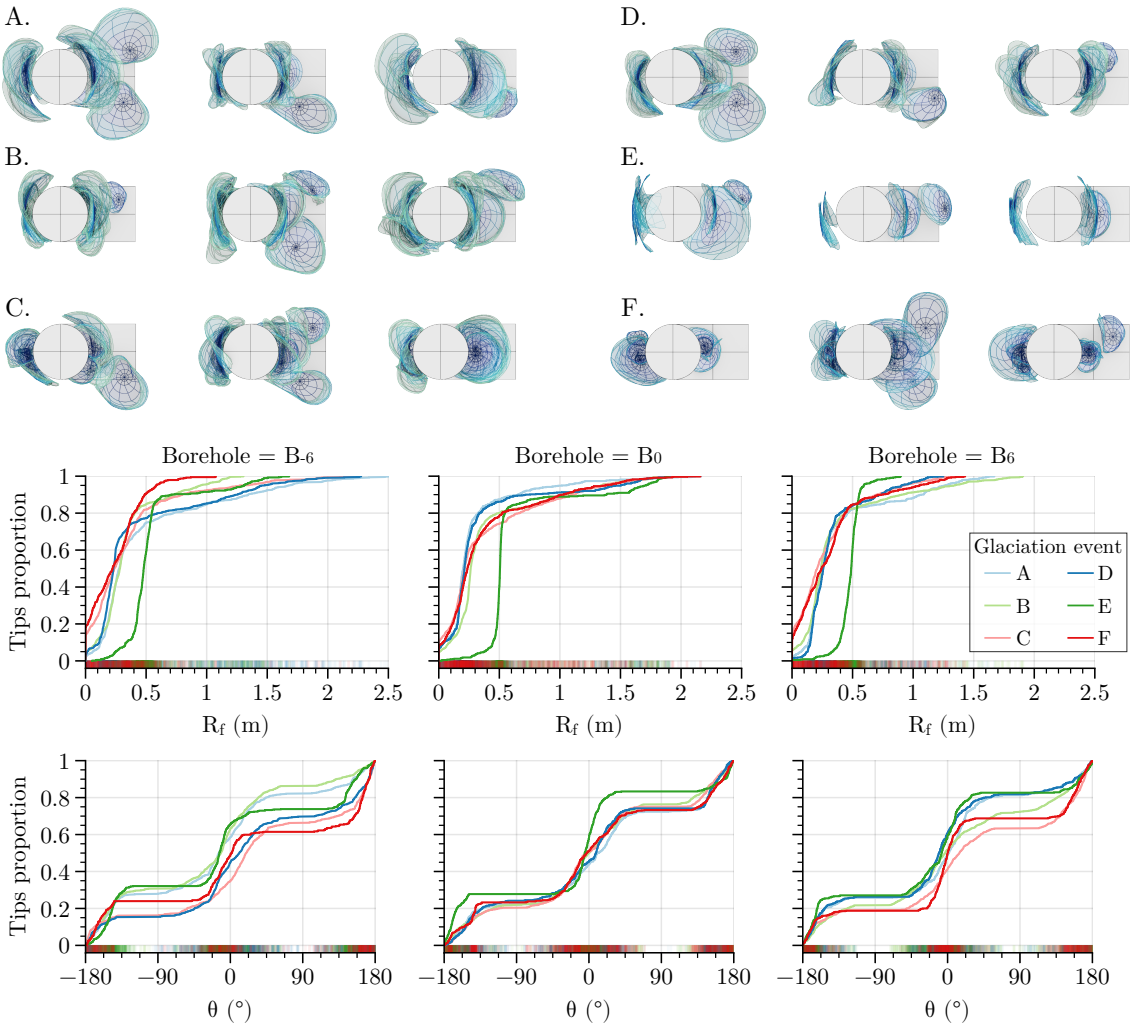


Figure 7.4: **A.** Top and side views of the fracture patterns that develop during the selected glacial events A-F. **B.** Cumulative distributions showing the proportion of fracture tips located below given values of radial or azimuthal distance with respect to the borehole wall.

Figure 7.4b also shows the cumulative distributions of fracture tips plotted against the azimuth angle measured from σ_h direction. The distributions are bimodal, corresponding to the two distinct diametrically opposite fractured zones. The two step upward slopes map to azimuths where fractures are found and are separated by two flat regions where no fracturing occurs. The relative spalling widths can be compared between events by comparing the widths of these regions. Individual tip locations are also marked along the R_f and θ axes to emphasise the density of fracturing at the different locations around the borehole. The central borehole displays larger spalling widths, which are more consistent across the different glaciation events in comparison to the adjacent flanking boreholes. However, it is not evident that there exists a direct correlation between the spalling angle and the glaciation event, as the fracture patterns and tips distributions are distinct for each borehole and respective event.

These results suggest that spalling width are primarily dependent on the 3D fracture interactions along the borehole wall. This agrees with Zheng et al. (1988), who also found that the breakout shapes and sizes are dependent on the stress history of the rock and therefore there might be a non-unique relationship between the in situ stresses and the spalling width. More recently Shen et al. (2014) numerically simulated spalling-type failure in a geothermal reservoir using a fracture mechanics approach in two dimensions. They found that the initial stress distribution at the borehole wall is the main factor that determines the spalling width, and the progressive failure does not significantly influence the spalling width beyond what can be initially determined using the Kirsch equations. This difference may be explained by the inability of the 2D model to account for fracture interactions in 3D.

7.4 Conclusions

Fracture nucleation and growth around the deposition boreholes of a future deep geological repository was simulated in three dimensions using a fracture mechanics approach. Six *in situ* stress scenarios corresponding to glaciation events were investigated, showing their influence on nucleation and growth patterns. In all simulated cases, fracturing was localised to the close vicinity of the boreholes, and there are no inter-borehole interactions.

The simulations presented in this chapter consider fracture nucleation and growth response due to changes in the *in situ* stress magnitude independently, assuming that damage does not get carried forward from previous glaciation events. Further work is planned to take into account pre-existing damage and determine if the stabilised fractures reactivate during subsequent glaciation events.

Chapter 8

Conclusions

This chapter highlights the key contributions of this thesis, and proposes several ideas on how this work could be improved and extended. "Future work" refers to additional studies that can be conducted by readily using the fracture patterns generated in Chapters 5-7, and to specific improvements to the numerical method and simulation workflow.

8.1 Summary of thesis

This thesis described a systematic approach for modelling fracture growth within the excavation damage zone that develops around the deposition boreholes and tunnels of a deep geological repository for nuclear waste.

In Chapter 2, fundamental concepts pertaining to the geological disposal of nuclear waste were presented. The concepts of excavation damage zone and spalling were defined in relation to the existing literature, and the main distinctions between spalling and other forms of borehole failure were discussed. An overview of existing analytical and numerical methods for predicting spalling was provided, and their effectiveness in making predictions was evaluated.

In Chapter 3, a geometric fracture growth methodology was presented as a means to model fracture initiation and growth leading to spalling. The governing equations of elasticity, thermo-elasticity, and linear elastic fracture mechanics, as well as the primary algorithms involved in fracture initiation and progression, were discussed. The process of constructing the geometric model and discretising it, as well as the methods for creating fracture tip loops and lofting the surfaces using non-uniform rational B-splines (NURBS), were also explained. Additionally, numerical procedures for calculating mechanical and coupled thermo-mechanical deformation, damage, contact of the fracture surfaces, stress intensity

factors, and fracture growth, were outlined. Furthermore, this chapter emphasised specific simulation parameters that were subsequently validated for spalling in the ensuing chapter.

In Chapter 4, the validity of the variables computed through the Finite Element Method (FEM), stress intensity factors (SIFs), and patterns of fracture growth, were evaluated in order to assess the efficacy of the modeling approach in reproducing the mechanisms associated with mechanical spalling. This chapter demonstrated that the deformation of the borehole and the resulting fractures respond in a realistic manner to the applied mechanical and thermal loads, following the stages of borehole drilling and heating. Additionally, method-specific and simulation-specific parameters, such as the number of nucleated fractures, their initial disk size, and their spacing, were varied to examine their impact on the final patterns of fractures, and to confirm that the resulting patterns align with observations from field experiments involving tunneling.

In Chapter 5, the mechanical (M) evolution of spalling fractures that are anticipated to occur in the proximity of the deposition boreholes and tunnels of a typical repository for nuclear waste was examined in detail. The Forsmark site in Sweden is selected as the case study location to investigate the influence of *in situ* stresses, the characteristics of the deposition tunnel and its orientation, borehole geometry, and borehole spacing, on the predicted damage and the extent of fractures. As no deposition boreholes have yet been drilled at the Forsmark site, this chapter also provides the initial numerical predictions of fracture growth leading to spalling at the proposed repository location.

In Chapter 6, the impact of borehole heating and cooling on the adjacent host rock and its effect on the initiation and progression of new fractures under coupled thermo-mechanical loading were investigated. This chapter also explored the effect of borehole heating and cooling on pre-existing mechanical fractures, and compared the growth and severity of spalling in these two scenarios. Additionally, a realistic timeline was implemented, in which the borehole heat flux was varied according to a typical spent fuel canister decay rate, and the results for a multiple borehole model were analysed in relation to those presented in Chapter 5.

In Chapter 7, the long-term evolution of the Forsmark repository was evaluated by taking into account the changes in *in situ* stresses that occur over the timescales of a glacial cycle. The results obtained from the previous chapters on mechanical (Chapter 5) and thermal (Chapter 6) phases of the repository were extended in this chapter by analysing several geo-mechanical scenarios corresponding to different *in situ* stress evolution paths at various repository locations relative to the ice sheet during the glacial cycle. It was assumed that the thermal phase of the repository had been completed before the onset of glaciation.

8.2 Future work

The work presented in this thesis focused on fracturing of hard and brittle granitic rocks in the context of deep geological disposal of nuclear waste. This work introduced a novel approach to model fracture nucleation and growth around large-scale boreholes and tunnels of arbitrary shapes, including the effect of both mechanical and thermal deformation. Emphasis was placed on understanding the effect of fracture growth and interaction on the formation of spalling fractures around engineered structures in a geological disposal facility. The methodology and numerical workflow presented in this thesis can be adapted to model fracturing in a range of other scenarios.

In the context of a GDF, extensions of this work can include processes and phenomena such as:

- the analysis of the effect of large fracture networks on permeability and transport away from the tunnel,
- analysis of critical flow pathways and their modification during thermo-chemical deformation,
- effect of vicinal faults on stress reorientation and growth,
- fracture growth due to reactivation of faults,
- interaction with local and vicinal fractures of scale larger than the borehole,
- coalescence of fractures leading to regional-scale fracture growth,
- permeability changes in 100, 1,000 and 10,000 year time-scales, as well as further studies of potential permeability changes during and after glaciation cycles.
- these types of simulations can also serve as numerical twins during the construction phase of the repository, to continue to refine predictions of spalling.

The numerical framework can also be applied in the context of the disposal of fluids in the subsurface, including CO_2 sequestration, hydrogen storage, and seasonal thermal energy storage. In addition, the ability to model fracture growth and coalescence will be greatly beneficial in the context of groundwater flow studies, contaminant transport, and permeability assessment of the subsurface. Current efforts to extract ores by *in situ* leaching of hard rocks may also be a potential future application of the developed methodology.

There are also a number of numerical improvements that can be developed to further enhance the capability of this methodology of capturing more complex scenarios, both geometrically and physically, such as:

- **Nucleation damage model.** Nucleation of the initial disk can be improved by considering a more advanced damage model. An anisotropic damage model with some degree of damage localisation can potentially better inform the sizes and orientations of the initial flaws. The transition between continuum damage and discrete fractures is still a matter of active research, and methods are still being developed and refined to numerically model this process with accuracy.
- **Nucleation frequency.** In the current methodology, fractures only nucleate once at the onset of the simulation. Numerical simulations can be further improved by considering the growth of fractures throughout the entire span of modelled time. This would allow further details of the excavation schedule to be incorporated into the simulations, so as to better analyse potential changes to the spalling patterns as excavation progresses. The sequence of excavation and stress history have been shown to influence the timing of fracture initiation and growth, which in turn affects the overall damage around underground excavations.
- **Include hydraulic effects.** A more realistic and complex extension of the model is to include hydraulic effects, especially when coupled with thermal effects, or associated with changes in *in situ* stresses during a glaciation cycle. The hydraulic effects are expected to influence the fluid pressure and flow in the pre-existing mechanical fractures, which could in turn affect the fracture propagation and spalling extent over larger time-scales.
- **Rock property anisotropy.** The results presented in this thesis assumed isotropic rock properties. The influence of anisotropy on fracture orientation and the ensuing spalling patterns can be investigated by assigning variations in Young's modulus across distinct orientations or as heterogeneity patterns, with different lengths of patches of isotropic properties in different orientations.
- **Model large faults.** Large-scale pre-existing faults can serve both to influence local deformation, while also being subject to deformation and slip due to local variations of stresses. Results described in Section 6.4 show how variations in the elastic modulus have a quantifiable influence on the resultant fracture patterns. The host rock at the Forsmark repository site contains pre-existing, steeply dipping faults, which may influence the stability of those deposition boreholes that are in the immediate vicinity of the large-scale faults. The investigated scenarios may be reconsidered, with several of these faults running through the initial numerical domain, which in this work was considered to be initially unfractured (before the drilling stage).

- **Induced seismicity.** The presented numerical model can also be utilised to evaluate the potential reactivation of these faults, taking into account work developed by other members of the Imperial College Rock Mechanics Research Group during the course of this PhD. Although Sweden is located in a relatively inactive tectonic area, small magnitude earthquakes are still common, raising potential risks related to induced seismicity due to the disturbance of the excavated rock and its long-term deformation after the GDF closure. In addition, it may be of interest to consider the deformation and reactivation of spalling fractures (as presented in Chapters 5-7) following seismic events, as these may get reactivated, grow, and create additional permeability around the GDF facility.

- **Influence of fracture geometry and apertures on host rock permeability.** The final fracture patterns presented in Chapters 5-7 at the end of each modelling stage can be used as starting models for the analyses of permeability, and as initial geometrical input for flow simulations. Further studies can be conducted using the results presented in this work, to determine the permeability of the EDZ and estimate percolation, comparing the 3D results with 2D cases. In particular, these simulations can take into account realistic distributions of fracture apertures, and how these are likely to change during the different storage phases. Such studies are rare, and generally exist only in 2D, limited to constant aperture assumptions, or constrained to disk-shaped apertures with non-physical interaction patterns.

- **Glaciation.** Chapter 7 presented preliminary results of the modelling of the long-term evolution of the repository during a glaciation cycle. A further extension of this work would be to consider sequential glaciation cycles, with progressive fracture nucleation over longer time scales. This is one of the topics that is being investigated in a follow-on post-doctoral project.

- **Validation of fracture apertures.** Chapter 6 showed computed fracture aperture size predictions at Forsmark. These predictions can be further validated by comparing them with actual measurements of the aperture size in situ, once the deposition boreholes as Forsmark have been excavated. The most common methods for measuring fracture aperture size in situ is through direct observation using optical or electron microscopy. Other methods also include using X-ray tomography or petrophysical logs.

References

Abousahl, S., Carbol, P., Farrar, B., Gerbelova, H., Konings, R., Lubomirova, K., Martin Ramos, M., Matuzas, V., Nilsson, K., Peerani, P., Peinador Veira, M., Rondinella, V., Van Kalleveen, A., Van Winckel, S., Vegh, J. & Wastin, F. (2021), Technical assessment of nuclear energy with respect to the 'do no significant harm' criteria of regulation (EU) 2020/852 ('Taxonomy Regulation'), Scientific analysis or review KJ-NA-30777-EN-N (online), KJ-NA-30777-EN-C (print), European Commission, Luxembourg.

Al-Ajmi, A. M. & Zimmerman, R. W. (2005), 'Relation between the mogi and the coulomb failure criteria', *International Journal of Rock Mechanics and Mining Sciences* **42**, 431–439.

Aliha, M., Bahmani, A. & Akhondi, S. (2015), 'Determination of mode III fracture toughness for different materials using a new designed test configuration', *Materials & Design* **86**, 863–871.

Amadei, B. & Stephansson, O. (1997), Borehole breakout method, *in* 'Rock Stress and its Measurement', Chapman & Hall, London, pp. 303–325.

Anderson, T. L. (2017), *Fracture Mechanics: Fundamentals and Applications*, CRC Press.

Andersson, J. C. (2007), Äspö pillar stability experiment: rock mass response to coupled mechanical thermal loading, PhD thesis, Royal Institute of Technology, Stockholm.

Andersson, J. C. & Martin, C. D. (2009), 'The Äspö Pillar Stability Experiment: Part I — Experiment design', *International Journal of Rock Mechanics and Mining Sciences* **46**(5), 865–878.

Andersson, J. C., Martin, C. D. & Stille, H. (2009*a*), 'The äspö pillar stability experiment: Part II — Rock mass response to coupled excavation-induced and thermal-induced stresses', *International Journal of Rock Mechanics and Mining Sciences* **46**(5), 879–895.

Andersson, J. C., Martin, C. D. & Stille, H. (2009*b*), 'The Äspö Pillar Stability Experiment: Part II—Rock mass response to coupled excavation-induced and thermal-induced stresses', *International Journal of Rock Mechanics and Mining Sciences* **46**(5), 879–895.

ANDRA (2005), Phenomenological evolution of a geological repository: Dossier 2005 Granite, Technical report, Agence Nationale pour la Gestion des Déchets Radioactifs.

ANSYS (2020), *ANSYS ICEM CFD User's Manual*, ANSYS, Inc.

Barton, C. A., Zoback, M. D. & Burns, K. L. (1988), 'In-situ stress orientation and magnitude at the Fenton Geothermal Site, New Mexico, determined from wellbore breakouts', *Geophysical Research Letters* **15**(5), 467–470.

Barton, N. & Bandis, S. (1990), 'Review of predictive capabilities of jrc-jcs model in engineering practice', *Rock Joints, Proc. Int. Symp. on Rock Joints* pp. 603–610.

Barton, N. & Shen, B. (2017), 'Risk of shear failure and extensional failure around overstressed excavations in brittle rock', *Journal of Rock Mechanics and Geotechnical Engineering* **9**, 210–225.

Bazant, Z. P. & Kazemi, M. T. (1990), 'Determination of fracture energy, process zone longth and brittleness number from size effect, with application to rock and conerete', *International Journal of Fracture* **44**(2), 111–131.

Bažant, Z. P. (1986), 'Mechanics of distributed cracking', *Applied Mechanics Reviews* **39**, 675–705.

Bažant, Z. P. & Oh, B. H. (1983), 'Crack band theory for fracture of concrete', *Matériaux et Construction 1983 16:3* **16**, 155–177.

Behera, B., Yadav, A., Singh, G. S. & Sharma, S. K. (2021), 'Assessment of excavation damage and spalling potential at a mechanized longwall face: a numerical modeling study', *Geomechanics and Geophysics for Geo-Energy and Geo-Resources* **7**, 1–40.

Bell, J. S. & Gough, D. I. (1979), 'Northeast-southwest compressive stress in Alberta evidence from oil wells', *Earth and Planetary Science Letters* **45**, 475–482.

Belytschko, T. & Black, T. (1999), 'Elastic crack growth in finite elements with minimal remeshing', *International Journal for Numerical Methods in Engineering* **45**(5), 601–620.

Bodansky, D. (1996), *Nuclear Energy: Principles, Practices, and Prospects*, American Institute of Physics.

Boukharouba, T., Elboujdaini, M. & Pluvinage, G., eds (2009), *Damage and Fracture Mechanics*, Springer.

Bremberg, D. & Faleskog, J. (2015), 'A numerical procedure for interaction integrals developed for curved cracks of general shape in 3-D', *International Journal of Solids and Structures* **62**, 144–157.

Burns, R. E., Causey, W. E., Galloway, W. E., Nelson, R. W., Causey, W. E., Galloway, W. E. & Nelson, R. W. (1978), Nuclear waste disposal in space, Technical Publication NASA-TP-1225, George C. Marshall Space Flight Center, National Aeronautics and Space Administration.

Cai, M. & Kaiser, P. (2014), 'In-situ rock spalling strength near excavation boundaries', *Rock Mechanics and Rock Engineering* **47**, 659–675.

Cai, M., Kaiser, P. K., Tasaka, Y., Maejima, T., Morioka, H. & Minami, M. (2004), 'Generalized Crack Initiation and Crack Damage Stress Thresholds of Brittle Rock Masses Near Underground Excavations', *International Journal of Rock Mechanics and Mining Sciences* **41**(5), 833–847.

Carslaw, H. S. & Jaeger, J. J. C. (1986), *Conduction of Heat in Solids*, Clarendo Press.

Chaboche, J. L. (1988*a*), 'Continuum damage mechanics: Part ii—damage growth, crack initiation, and crack growth', *Journal of Applied Mechanics* **55**, 65–72.

Chaboche, J. L. (1988*b*), 'Continuum damage mechanics: Part i—general concepts', *Journal of Applied Mechanics* **55**, 59–64.

Chang, S.-H., Lee, C.-I. & Jeon, S. (2002), 'Measurement of rock fracture toughness under modes i and II and mixed-mode conditions by using disc-type specimens', *Engineering Geology* **66**(1-2), 79–97.

Cook, R. D., Malkus, D. S. & Plesha, M. E. (2001), *Concepts and Applications of Finite Element Analysis*, John Wiley & Sons.

Cundall, P. A. (2001), 'A discontinuous future for numerical modelling in geomechanics?', *Proceedings of the Institution of Civil Engineers - Geotechnical Engineering* **149**(1), 41–47.

Cundall, P. A. & Hart, R. D. (1993), Numerical Modeling of Discontinua, *in* C. Fairhurst, ed., 'Analysis and Design Methods', Pergamon, Oxford, chapter 9, pp. 231–243.

Danowski, C., Gravemeier, V., Yoshihara, L. & Wall, W. A. (2013), 'A monolithic computational approach to thermo-structure interaction', *International Journal for Numerical Methods in Engineering* **95**, 1053–1078.

Davis, B., Wawrzynek, P. & Ingraffea, A. (2014), '3-D simulation of arbitrary crack growth using an energy-based formulation – Part I: Planar growth', *Engineering Fracture Mechanics* **115**, 204–220.

De Falco, A., Mori, M. & Sevieri, G. (2018), Mazars' damage model for masonry structures: a case study of a church in Italy, *in* 'Proceedings of the 2018 COMSOL Conference'.

Defoort, T., Paluszny, A. & Zimmerman, R. W. (2016), Comparison of Fracture Mechanics and Damage Mechanics Approaches to Simulate Three-Point Bending and Double-Notch Shear Experiments on Rock Samples, *in* 'Proceedings of the 50$^{\text{th}}$ U.S. Rock Mechanics/Geomechanics Symposium'. ARMA-2016-670.

Diederichs, M., Kaiser, P. & Eberhardt, E. (2004), 'Damage initiation and propagation in hard rock during tunnelling and the influence of near-face stress rotation', *International Journal of Rock Mechanics and Mining Sciences* **41**(5), 785–812.

Diederichs, M. S. (2007*a*), 'The 2003 Canadian Geotechnical Colloquium: Mechanistic interpretation and practical application of damage and spalling prediction criteria for deep tunnelling', *Canadian Geotechnical Journal* **44**(9), 1082–1116.

Diederichs, M. S. (2007*b*), 'The 2003 Canadian geotechnical colloquium: Mechanistic interpretation and practical application of damage and spalling prediction criteria for deep tunnelling', *Canadian Geotechnical Journal* **44**, 1082–1116.

Dimitri, R., Lorenzis, L. D., Wriggers, P. & Zavarise, G. (2014), 'Nurbs- and t-spline-based isogeometric cohesive zone modeling of interface debonding', *Computational Mechanics* **54**, 369–388.

Ding, X. & Zhang, L. (2014), 'A new contact model to improve the simulated ratio of unconfined compressive strength to tensile strength in bonded particle models', *International Journal of Rock Mechanics and Mining Sciences* **69**, 111–119.

Drucker, D. C. & Prager, W. (1952), 'Soil mechanics and plastic analysis or limit design', *Quarterly of Applied Mathematics* **10**, 157–165.

Edelbro, C. (2010), 'Different approaches for simulating brittle failure in two hard rock mass cases: A parametric study', *Rock Mechanics and Rock Engineering* **43**, 151–165.

Erdogan, F. & Sih, G. C. (1963), 'On the crack extension in plates under plane loading and transverse shear', *Journal of Basic Engineering* **85**, 519–525.

Ewy, R. & Cook, N. (1990), 'Deformation and fracture around cylindrical openings in rock—i. observations and analysis of deformations', *International Journal of Rock Mechanics and Mining Sciences & Geomechanics Abstracts* **27**(5), 387–407.

Fairhurst, C. & Cook, N. (1966), The phenomenon of rock splitting parallel to the direction of maximum compression in the neighbourhood of a surface, *in* ISRM, ed., '1$^{\text{st}}$ ISRM Congress, Lisbon, Portugal', Lisbon, Portugal, pp. 687–692. Paper ISRM-1CONGRESS-1966-115.

Fakhimi, A. & Tarokh, A. (2013), 'Process zone and size effect in fracture testing of rock', *International Journal of Rock Mechanics and Mining Sciences* **60**, 95–102.

Faybishenko, B., Birkholzer, J., Sassani, D. & Swift, P. (2017), International Approaches for Nuclear Waste Disposal in Geological Formations: Geological Challenges in Radioactive Waste Isolation—Fifth Worldwide Review, Technical report, Office of Scientific and Technical Information, United States Department of Energy.

Fordjor, C. K., Bell, J. S. & Gough, D. I. (1983), 'Breakouts in Alberta and stress in the North American plate (oil wells).', *Canadian Journal of Earth Sciences* **20**, 1445–1455.

Frémond, M. & Nedjar, B. (1996), 'Damage, gradient of damage and principle of virtual power', *International Journal of Solids and Structures* **33**, 1083–1103.

Gao, F. Q. & Stead, D. (2014), 'The application of a modified Voronoi logic to brittle fracture modelling at the laboratory and field scale', *International Journal of Rock Mechanics and Mining Sciences* **68**, 1–14.

Geers, M. G., Borst, R. D., Brekelmans, W. A. & Peerlings, R. H. (1998), 'Strain-based transient-gradient damage model for failure analyses', *Computer Methods in Applied Mechanics and Engineering* **160**, 133–153.

Germanovich, L. & Dyskin, A. (2000), 'Fracture mechanisms and instability of openings in compression', *International Journal of Rock Mechanics and Mining Sciences* **37**(1-2), 263–284.

Ghorashi, S. S., Valizadeh, N. & Mohammadi, S. (2012), 'Extended isogeometric analysis for simulation of stationary and propagating cracks', *International Journal for Numerical Methods in Engineering* **89**, 1069–1101.

Gong, F. Q., Wu, X. W. & Tian, B. L. (2020), 'Simulation test of spalling failure of surrounding rock in rectangular tunnels with different height-to-width ratios', *Bulletin of Engineering Geology and the Environment* **79**, 3207–3219.

Gough, D. I. & Bell, J. S. (1982), 'Stress orientations from borehole wall fractures with examples from Colorado, east Texas, and northern Canada.', *Canadian Journal of Earth Sciences* **19**, 1358–1370.

Grassl, P. & Jirásek, M. (2006), 'Damage-plastic model for concrete failure', *International Journal of Solids and Structures* **43**(22-23), 7166–7196.

Griffith, A. (1924), 'The theory of rupture', *International Congress of Applied Mechanics* pp. 163–198.

Griffith, A. A. (1921), 'The phenomena of rupture and flow in solids', *Philosophical Transactions of the Royal Society of London. Series A, Containing Papers of a Mathematical or Physical Character* **221**, 163–198.

Haimson, B. (2007), 'Micromechanisms of borehole instability leading to breakouts in rocks', *International Journal of Rock Mechanics and Mining Sciences* **44**(2), 157–173.

Haimson, B. C. & Song, I. (1993), 'Laboratory study of borehole breakouts in cordova cream: a case of shear failure mechanism', *International Journal of Rock Mechanics and Mining Sciences & Geomechanics Abstracts* **30**, 1047–1056.

Haimson, B. & Chang, C. (2000), 'A new true triaxial cell for testing mechanical properties of rock, and its use to determine rock strength and deformability of westerly granite', *International Journal of Rock Mechanics and Mining Sciences* **37**, 285–296.

Hajiabdolmajid, V., Kaiser, P. K. & Martin, C. D. (2002*a*), 'Modelling brittle failure of rock', *International Journal of Rock Mechanics and Mining Sciences* **39**, 731–741.

Hajiabdolmajid, V., Kaiser, P. & Martin, C. (2002*b*), 'Modelling brittle failure of rock', *International Journal of Rock Mechanics and Mining Sciences* **39**(6), 731–741.

Hajiabdolmajid, V., Kaiser, P. & Martin, C. D. (2003), 'Mobilised strength components in brittle failure of rock', *Geotechnique* **53**, 327–336.

Hamdi, P., Stead, D. & Elmo, D. (2014), 'Damage characterization during laboratory strength testing: A 3D-finite-discrete element approach', *Computers and Geotechnics* **60**, 33–46.

Hamon, F. (2013), *Model of damage of MAZARS*. Code Aster documentation.

Henshell, R. D. & Shaw, K. G. (1975), 'Crack tip finite elements are unnecessary', *International Journal for Numerical Methods in Engineering* **9**(3), 495–507.

Hills, D. A., Kelly, P. A., Dai, D. N. & Korsunsky, A. M. (1996), Introduction to fracture mechanics, *in* 'Solution of Crack Problems: The Distributed Dislocation Technique', Springer Netherlands, Dordrecht, pp. 1–27.

Hoek, E. (1968), Brittle fracture of rock, *in* 'Rock Mechanics in Engineering Practice', Wiley, London.

Hoek, E. & Brown, E. T. (1980), *Underground Excavations in Rock*, CRC Press.

Hollister, C. D., Anderson, D. R. & Heath, G. R. (1981), 'Subseabed disposal of nuclear wastes', *Science* **213**, 1321–1326.

Horii, H. & Nemat-Nasser, S. (1985), 'Compression-induced microcrack growth in brittle solids: Axial splitting and shear failure', *Journal of Geophysical Research* **90**(B4), 3105.

Howland, R. C. J. (1935), 'Stresses in a plate containing an infinite row of holes', *Proceedings of the Royal Society of London. Series A - Mathematical and Physical Sciences* **148**, 471–491.

Hu, X., Su, G., Chen, G., Mei, S., Feng, X., Mei, G. & Huang, X. (2019), 'Experiment on rockburst process of borehole and its acoustic emission characteristics', *Rock Mechanics and Rock Engineering* **52**, 783–802.

Hudson, J. A., Bäckström, A., Rutqvist, J., Jing, L., Backers, T., Chijimatsu, M., Christiansson, R., Feng, X. T., Kobayashi, A., Koyama, T., Lee, H. S., Neretnieks, I., Pan, P. Z., Rinne, M. & Shen, B. T. (2009), 'Characterising and modelling the excavation damaged zone in crystalline rock in the context of radioactive waste disposal', *Environmental Geology* **57**, 1275–1297.

Hudson, J. A. & Harrison, J. P. (2000), *Engineering Rock Mechanics*, Elsevier Science & Technology.

Hughes, T. J., Cottrell, J. A. & Bazilevs, Y. (2005), 'Isogeometric analysis: Cad, finite elements, nurbs, exact geometry and mesh refinement', *Computer Methods in Applied Mechanics and Engineering* **194**, 4135–4195.

Hussain, M. A., Pu, S. L. & Underwood, J. H. (1973), Strain Energy Release Rate for a Crack under Combined Mode I and Mode II, Technical Report AD0768706, U.S. Department of Defense.

IAEA (2012), *Storage of Spent Nuclear Fuel*, number SSG-15 *in* 'Specific Safety Guides', International Atomic Energy Agency, Vienna.

IAEA (2018), *Status and Trends in Spent Fuel and Radioactive Waste Management*, number NW-T-1.14 *in* 'Nuclear Energy Series', International Atomic Energy Agency, Vienna.

IAEA Tecdoc Series (2005), *Disposal Options for Disused Radioactive Sources: Technical Reports Series No. 436*, International Atomic Energy Agency.

Irwin, G. R. (1956), 'Onset of fast crack propagation in high strength steel and aluminum alloys', *Sagamore Research Conference Proceedings* **2**, 289–305.

Irwin, G. R. (1957), 'Analysis of Stresses and Strains Near the End of a Crack Traversing a Plate', *Journal of Applied Mechanics* **24**, 361–364.

Isida, M. & Igawa, H. (1991), 'Analysis of a zig-zag array of circular holes in an infinite solid under uniaxial tension', *International Journal of Solids and Structures* **27**, 849–864.

Jaeger, J. C., Cook, N. G. W. & Zimmerman, R. (2007), *Fundamentals of Rock Mechanics*, John Wiley and Sons Ltd.

Jirásek, M. (2011), 'Damage and smeared crack models', *CISM International Centre for Mechanical Sciences, Courses and Lectures* **532**, 1–49.

Kachanov, L. M. (1999), 'Rupture time under creep conditions', *International Journal of Fracture* **97**, 11–18.

Kaiser, P. K. & McCreath, D. R. (1994), 'Rock mechanics considerations for drilled or bored excavations in hard rock', *Tunnelling and Underground Space Technology incorporating Trenchless* **9**, 425–437.

Kassir, M. & Sih, G. (1975), *Three dimensional crack problems: A new selection of crack problems in three dimensional elasticity*, Mechanics of Fracture, Noordhoff International Publishing.

Khalili, N. & Selvadurai, A. P. (2003), 'A fully coupled constitutive model for thermo-hydro-mechanical analysis in elastic media with double porosity', *Geophysical Research Letters* **30**.

Kim, J.-S., Hong, C.-H. & Kim, G.-Y. (2020), 'Evaluation of mazars damage model of kurt granite under simulated coupled environment of geological disposal', *Journal of Korean Tunnelling and Underground Space Association 2020 22:4* **22**, 419–434.

Koch, K. R. (2009), 'Three-dimensional NURBS surface estimated by lofting method', *The International Journal of Advanced Manufacturing Technology* **49**(9-12), 1059–1068.

Krajcinovic, D. (2000), 'Introduction to damage mechanics', *Damage and Fracture of Disordered Materials* pp. 1–15.

Krajcinovic, D. & Mastilovic, S. (1995), 'Some fundamental issues of damage mechanics', *Mechanics of Materials* **21**, 217–230.

Kruschwitz, S. & Yaramanci, U. (2004), 'Detection and characterization of the disturbed rock zone in claystone with the complex resistivity method', *Journal of Applied Geophysics* **57**, 63–79.

Kumar, P. & Singh, B. (1989), 'Thermal stress analysis of underground openings', *International Journal for Numerical and Analytical Methods in Geomechanics* **13**, 411–425.

Kuppler, S. & Hocke, P. (2018), 'The role of long-term planning in nuclear waste governance', *Journal of Risk Research* **22**, 1343–1356.

Kwon, S., Lee, C. S., Cho, S. J., Jeon, S. W. & Cho, W. J. (2009), 'An investigation of the excavation damaged zone at the KAERI underground research tunnel', *Tunnelling and Underground Space Technology* **24**, 1–13.

Lan, H., Martin, C. D. & Andersson, J. C. (2013), 'Evolution of in situ rock mass damage induced by mechanical–thermal loading', *Rock Mechanics and Rock Engineering* **46**(1), 153–168.

Lan, H., Martin, C. D. & Hu, B. (2010), 'Effect of heterogeneity of brittle rock on micromechanical extensile behavior during compression loading', *Journal of Geophysical Research* **115**(B1).

Lang, P. S., Paluszny, A. & Zimmerman, R. W. (2014), 'Permeability tensor of three-dimensional fractured porous rock and a comparison to trace map predictions', *Journal of Geophysical Research: Solid Earth* **119**, 6288–6307.

Lazarus, V. (2003), 'Brittle fracture and fatigue propagation paths of 3D plane cracks under uniform remote tensile loading', *International Journal of Fracture* **122**(1/2), 23–46.

Lazzari, E. D., van den Boom, S. J., Zhang, J., van Keulen, F. & Aragón, A. M. (2021), 'A critical view on the use of Non-Uniform Rational B-Splines to improve geometry representation in enriched finite element methods', *International Journal for Numerical Methods in Engineering* **122**, 1195–1216.

Lee, M. & Haimson, B. (1993), 'Laboratory study of borehole breakouts in Lac du Bonnet granite: a case of extensile failure mechanism', *International Journal of Rock Mechanics and Mining Sciences & Geomechanics Abstracts* **30**, 1039–1045.

Leeman, E. (1958), 'Some measurements of closure and ride in a stope of the East Rand Proprietary Mines generation at geological boundaries', *Papers of the Association of Mine Managers of South Africa* **1958-1959**, 385–404.

Lei, Q., Latham, J. P., Xiang, J. & Tsang, C. F. (2017), 'Role of natural fractures in damage evolution around tunnel excavation in fractured rocks', *Engineering Geology* **231**, 100–113.

Lemaitre, J. (1984), 'How to use damage mechanics', *Nuclear Engineering and Design* **80**(2), 233 – 245. 4th Special Issue on Smirt-7.

Li, S. J., Feng, X. T., Wang, C. Y. & Hudson, J. A. (2013), 'ISRM suggested method for rock fractures observations using a borehole digital optical televiewer', *Rock Mechanics and Rock Engineering* **46**, 635–644.

Lin, H., Kang, W. H., Oh, J. & Canbulat, I. (2020), 'Estimation of in-situ maximum horizontal principal stress magnitudes from borehole breakout data using machine learning', *International Journal of Rock Mechanics and Mining Sciences* **126**.

Ling, C. (1948), 'On the stresses in a plate containing two circular holes', *Journal of Applied Physics* **19**(1), 77–82.

Lisjak, A., Figi, D. & Grasselli, G. (2014), 'Fracture development around deep underground excavations: Insights from fdem modelling', *Journal of Rock Mechanics and Geotechnical Engineering* **6**(6), 493–505.

Lisjak, A. & Grasselli, G. (2014), 'A review of discrete modeling techniques for fracturing processes in discontinuous rock masses', *Journal of Rock Mechanics and Geotechnical Engineering* **6**(4), 301–314.

Long, J. C. & Ewing, R. C. (2004), 'Yucca Mountain: Earth-science issues at a geologic repository for high-level nuclear waste', *Annual Review of Earth and Planetary Sciences* **32**(1), 363–401.

Macfarlane, A. (2001), 'Interim storage of spent fuel in the United States', *Annual Review of Energy and the Environment* **26**(1), 201–235.

Maiti, S. & Smith, R. (1983), 'Comparison of the criteria for mixed mode brittle fracture based on the preinstability stress-strain field part i: Slit and elliptical cracks under uniaxial tensile loading', *International Journal of Fracture* **23**, 281–295.

Makkonen, J. (2022), 'Trial run of final disposal to start by 2023', Posiva Press Release.

Martha, L. F., Wawrzynek, P. A. & Ingraffea, A. R. (1993), 'Arbitrary crack representation using solid modeling', *Engineering with Computers* **9**(2), 63–82.

Martin, C. & Christiansson, R. (2009), 'Estimating the potential for spalling around a deep nuclear waste repository in crystalline rock', *International Journal of Rock Mechanics and Mining Sciences* **46**(2), 219–228.

Martin, C. D. (1997), 'Seventeenth Canadian geotechnical colloquium: The effect of cohesion loss and stress path on brittle rock strength', *Canadian Geotechnical Journal* **34**, 698–725.

Martin, C. D. & Chandler, N. A. (1994), 'The progressive fracture of Lac du Bonnet granite', *International Journal of Rock Mechanics and Mining Sciences & Geomechanics Abstracts* **31**(6), 643–659.

Martin, C. D. & Kaiser, P. K. (1996), Mine-by Experiment Committee Report Phase 1: Excavation Response Summary and Implications, Technical Report AECL-11382, Atomic Energy Canada Limited.

Martin, C. D., Kaiser, P. K. & McCreath, D. R. (1999), 'Hoek-Brown parameters for predicting the depth of brittle failure around tunnels', *Canadian Geotechnical Journal* **36**(1), 136–151.

Martin, C. D., Read, R. S. & Martino, J. B. (1997), 'Observations of brittle failure around a circular test tunnel', *International Journal of Rock Mechanics and Mining Sciences* **34**(7), 1065–1073.

Martin, D. (2005), Preliminary assessment of potential underground stability (wedge and spalling) at forsmark, simpevarp and laxemar sites, Technical Report Technical report R-05-71, Svensk Kärnbränslehantering AB.

Martin, D. (2014), The Impact of Brittle Behaviour of Rocks on Tunnel Excavation Design, *in* R. Alejano, A. Perucho, C. Olalla & R. Jimenez, eds, 'Rock Engineering and Rock Mechanics: Structures in and on Rock Masses', CRC Press, pp. 51–62.

Martino, J. B. & Chandler, N. A. (2004), 'Excavation-induced damage studies at the underground research laboratory', *International Journal of Rock Mechanics and Mining Sciences* **41**, 1413–1426.

Matthäi, S. K., Geiger, S., Roberts, S. G., Paluszny, A., Belayneh, M., Burri, A., Mezentsev, A., Lu, H., Coumou, D., Driesner, T. & Heinrich, C. A. (2007), 'Numerical simulation of multi-phase fluid flow in structurally complex reservoirs', *Geological Society Special Publication* **292**, 405–429.

Mazars, J. (1984), Application of Continuous Damage Mechanic to Non-Linear Behavior of Concrete Structures (in French), PhD thesis, Paris 6 University.

Mazars, J. (1986), 'A description of micro- and macroscale damage of concrete structures', *Engineering Fracture Mechanics* **25**, 729–737.

Mazars, J. & Grange, S. (2017), 'Simplified strategies based on damage mechanics for concrete under dynamic loading', *Philosophical Transactions of the Royal Society A: Mathematical, Physical and Engineering Sciences* **375**.

Mazars, J., Hamon, F. & Grange, S. (2015), 'A new 3d damage model for concrete under monotonic, cyclic and dynamic loadings', *Materials and Structures/Materiaux et Constructions* **48**, 3779–3793.

Mitelman, A. & Elmo, D. (2014), 'Modelling of blast-induced damage in tunnels using a hybrid finite-discrete numerical approach', *Journal of Rock Mechanics and Geotechnical Engineering* **6**(6), 565–573.

Mogi, K. (1971), 'Effect of the triaxial stress system on the failure of dolomite and limestone', *Tectonophysics* **11**(2), 111–127.

Mogi, K. (1972), 'Effect of the triaxial stress system on fracture and flow of rocks', *Physics of the Earth and Planetary Interiors* **5**, 318–324.

Morton, R. J. & Struxness, E. G. (1956), 'Ground disposal of radioactive wastes', *American Journal of Public Health and the Nations Health* **46**, 156.

NAGRA (2002), Technical Report 02-06, Technical Report 02-06, National Cooperative for the Disposal of Radioactive Waste.

Nakamura, T. & Parks, D. (1989), 'Antisymmetrical 3-D stress field near the crack front of a thin elastic plate', *International Journal of Solids and Structures* **25**(12), 1411 – 1426.

Nejati, M., Paluszny, A. & Zimmerman, R. W. (2015*a*), 'A disk-shaped domain integral method for the computation of stress intensity factors using tetrahedral meshes', *International Journal of Solids and Structures* **69-70**, 230–251.

Nejati, M., Paluszny, A. & Zimmerman, R. W. (2015*b*), 'On the use of quarter-point tetrahedral finite elements in linear elastic fracture mechanics'.

Nejati, M., Paluszny, A. & Zimmerman, R. W. (2016), 'A finite element framework for modeling internal frictional contact in three-dimensional fractured media using unstructured tetrahedral meshes', *Computer Methods in Applied Mechanics and Engineering* **306**, 123–150.

Nowacki, W. (1986), *Thermoelasticity*, III: Comparative Literature; 15, Elsevier Science Limited.

Okada, H., Kawai, H. & Araki, K. (2008), 'A virtual crack closure-integral method (VCCM) to compute the energy release rates and stress intensity factors based on quadratic tetrahedral finite elements', *Engineering Fracture Mechanics* **75**(15), 4466–4485.

Olson, J. E. (1993), 'Joint pattern development: effects of subcritical crack growth and mechanical crack interaction', *Journal of Geophysical Research* **98**.

Olson, J. E. (2004), 'Predicting fracture swarms — the influence of subcritical crack growth and the crack-tip process zone on joint spacing in rock', *Geological Society, London, Special Publications* **231**(1), 73–88.

Paluszny, A. & Matthäi, S. K. (2009), 'Numerical modeling of discrete multi-crack growth applied to pattern formation in geological brittle media', *International Journal of Solids and Structures* **46**(18-19), 3383–3397.

Paluszny, A. & Matthai, S. K. (2010), 'Impact of fracture development on the effective permeability of porous rocks as determined by 2-d discrete fracture growth modeling', *Journal of Geophysical Research* **115**(B2).

Paluszny, A., Matthai, S. K. & Hohmeyer, M. (2007), 'Hybrid finite element-finite volume discretization of complex geologic structures and a new simulation workflow demonstrated on fractured rocks', *Geofluids* **7**(2), 186–208.

Paluszny, A., Thomas, R. N., Saceanu, M. C. & Zimmerman, R. W. (2020), 'Hydromechanical interaction effects and channelling in three-dimensional fracture networks undergoing growth and nucleation', *Journal of Rock Mechanics and Geotechnical Engineering* **12**, 707–719.

Paluszny, A. & Zimmerman, R. W. (2011), 'Numerical simulation of multiple 3D fracture propagation using arbitrary meshes', *Computer Methods in Applied Mechanics and Engineering* **200**(9-12), 953–966.

Paluszny, A. & Zimmerman, R. W. (2013*a*), 'Numerical fracture growth modeling using smooth surface geometric deformation', *Engineering Fracture Mechanics* **108**, 19–36.

Paluszny, A. & Zimmerman, R. W. (2013*b*), 'Numerical fracture growth modeling using smooth surface geometric deformation', *Engineering Fracture Mechanics* **108**, 19–36.

Paris, P. C. & Erdogan, F. (1963), 'A critical analysis of crack propagation laws', *Journal of Basic Engineering* **85**(4), 528.

Parker, F. L., Hemphill, L. & Crowell, J. (1978), Status report on waste disposal in natural salt formations, Report, Oak Ridge National Laboratory, United States Atomic Energy Commission.

Perras, M. A. & Diederichs, M. S. (2016), 'Predicting excavation damage zone depths in brittle rocks', *Journal of Rock Mechanics and Geotechnical Engineering* **8**, 60–74.

Philberth, K. (1977), 'The disposal of radioactive waste in ice sheets', *Journal of Glaciology* **19**, 607–617.

Piegl, L. & Tiller, W. (1996), 'Algorithm for approximate nurbs skinning', *Computer-Aided Design* **28**, 699–706.

Piegl, L. & Tiller, W. (1997), *The NURBS Book*, Springer Berlin Heidelberg.

Potyondy, D. O. & Cundall, P. A. (2004), 'A bonded-particle model for rock', *International Journal of Rock Mechanics and Mining Sciences* **41**, 1329–1364.

Proserpio, D., Ambati, M., Lorenzis, L. D. & Kiendl, J. (2020), 'A framework for efficient isogeometric computations of phase-field brittle fracture in multipatch shell structures', *Computer Methods in Applied Mechanics and Engineering* **372**, 113363.

Pugno, N., Ciavarella, M., Cornetti, P. & Carpinteri, A. (2006), 'A generalized paris' law for fatigue crack growth', *Journal of the Mechanics and Physics of Solids* **54**, 1333–1349.

Pusch, R. (2008), *Repository Concepts for HLW Including Spent Fuel and Waste with Long-Lived Radionuclides*, Springer Berlin Heidelberg, Berlin, Heidelberg, pp. 167–273.

Rabczuk, T. (2013), 'Computational methods for fracture in brittle and quasi-brittle solids: State-of-the-art review and future perspectives', *ISRN Applied Mathematics* **2013**, 1–38.

Rabczuk, T. & Belytschko, T. (2004), 'Application of particle methods to static fracture of reinforced concrete structures', *International Journal of Fracture* **128**(2), 107–133.

Read, R. (2004), '20 years of excavation response studies at AECL's Underground Research Laboratory', *International Journal of Rock Mechanics and Mining Sciences* **41**(8), 1251–1275.

Read, R. S., Chandler, N. A. & Dzik, E. J. (1998), 'In situ strength criteria for tunnel design in highly-stressed rock masses', *International Journal of Rock Mechanics and Mining Sciences* **35**, 261–278.

Read, R. S. & Martin, C. D. (1996), *Technical summary of AECL's mine-by experiment: phase 1: excavation response*, number 95-171 *in* 'COG', Atomic Energy of Canada Limited, Whiteshell Laboratories, Pinawa, Manitoba.

Renshaw, C. E. (2000), 'Fracture spatial density and the anisotropic connectivity of fracture networks', *Geophysical Monograph Series* **122**, 203–211.

Renshaw, C. E. & Pollard, D. D. (1994*a*), 'Numerical simulation of fracture set formation: A fracture mechanics model consistent with experimental observations', *Journal of Geophysical Research: Solid Earth* **99**(B5), 9359–9372.

Renshaw, C. E. & Pollard, D. D. (1994*b*), 'Numerical simulation of fracture set formation: A fracture mechanics model consistent with experimental observations', *Journal of Geophysical Research: Solid Earth* **99**(B5), 9359–9372.

Rhino3D (2020), *Rhino 7*.

Rice, J. R. (1968), 'A path independent integral and the approximate analysis of strain concentration by notches and cracks', *Journal of Applied Mechanics* **35**(2), 379.

Richard, H. A., Fulland, M. & Sander, M. (2005), 'Theoretical Crack Path Prediction', *Fatigue & Fracture of Engineering Materials & Structures* **28**(1-2), 3–12.

Richard, H., Schramm, B. & Schirmeisen, N.-H. (2014), 'Cracks on mixed mode loading – theories, experiments, simulations', *International Journal of Fatigue* **62**, 93–103.

Rutqvist, J., Digby, P., Stephansson, O. & Singh, U. (1989), Simulation of borehole breakouts with a damage material model, *in* 'ISRM International Symposium'. ISRM-IS-1989-172.

Salimzadeh, S., Paluszny, A., Nick, H. M. & Zimmerman, R. W. (2018), 'A three-dimensional coupled thermo-hydro-mechanical model for deformable fractured geothermal systems', *Geothermics* **71**, 212–224.

Salimzadeh, S., Paluszny, A. & Zimmerman, R. W. (2017), 'Three-dimensional poroelastic effects during hydraulic fracturing in permeable rocks', *International Journal of Solids and Structures* **108**, 153–163.

Saroukhani, S., Vafadari, R. & Simone, A. (2013), 'A simplified implementation of a gradient-enhanced damage model with transient length scale effects', *Computational Mechanics* **51**, 899–909.

Scholtès, L. & Donzé, F. V. (2013), 'A DEM model for soft and hard rocks: Role of grain interlocking on strength', *Journal of the Mechanics and Physics of Solids* **61**, 352–369.

Schuster, K., Alheid, H. J. & Böddener, D. (2001), 'Seismic investigation of the excavation damaged zone in opalinus clay', *Engineering Geology* **61**, 189–197.

Setiawan, N. B. & Zimmerman, R. W. (2022), 'Semi-analytical Method for Modeling Wellbore Breakout Development', *Rock Mechanics and Rock Engineering* **55**.

Shen, B. & Barton, N. (2018), 'Rock fracturing mechanisms around underground openings', *Geomechanics and Engineering* **16**, 35–47.

Shen, B., Stephansson, O. & Rinne, M. (2002), 'Simulation of borehole breakouts using fracod2d', *Oil and Gas Science and Technology* **57**, 579–590.

Shen, B., Stephansson, O. & Rinne, M. (2014), 'Modelling rock fracturing processes: A fracture mechanics approach using fracod', *Modelling Rock Fracturing Processes: A Fracture Mechanics Approach Using FRACOD* pp. 1–173.

Shi, J., Shen, B., Khanal, M. & Mallants, D. (2022), 'Analytical and numerical estimation of fracture initiation and propagation regions around large-diameter, deep boreholes for disposal of long-lived intermediate-level waste', *Energies 2022, Vol. 15, Page 2445* **15**, 2445.

Shih, C. F., de Lorenzi, H. G. & German, M. D. (1976), 'Crack extension modeling with singular quadratic isoparametric elements', *International Journal of Fracture* **12**, 647–651.

Simone, A., Wells, G. N. & Sluys, L. J. (2003), 'From continuous to discontinuous failure in a gradient-enhanced continuum damage model', *Computer Methods in Applied Mechanics and Engineering* **192**, 4581–4607.

Siren, T., Kantia, P. & Rinne, M. (2015), 'Considerations and observations of stress-induced and construction-induced excavation damage zone in crystalline rock', *International Journal of Rock Mechanics and Mining Sciences* **73**, 165–174.

SKB (1978), Handling of spent nuclear fuel and final storage of vitrified high level reprocessing waste, Technical report, Svensk Kärnbränslehantering AB.

SKB (2022), 'The government approves SKB's final repository system', *Press Release* .

SKB P-04-224 (2004), Forsmark site investigation. Borehole KFM02. Uniaxial compression test of intact rock, Technical report, Svensk Kärnbränslehantering AB.

SKB P-05-211 (2005), Forsmark site investigation. Borehole KFM07A. Uniaxial compression test of intact rock, Technical report, Svensk Kärnbränslehantering AB.

SKB P-05-212 (2006), Forsmark site investigation. Drill hole KFM07A. Indirect tensile strength test including strain measurement, Technical report, Svensk Kärnbränslehantering AB.

SKB P-07-166 (2007), Forsmark site investigation, Mapping of borehole breakouts, Processing of acoustical televiewer data from KFM08A, KFM08C, KFM09A, KFM09A, KFM09B and KFM90B, Technical report, Svensk Kärnbränslehantering AB.

SKB R-07-26 (2007), Quantifying in situ stress magnitudes and orientations for Forsmark, Forsmark stage 2.2, Technical report, Svensk Kärnbränslehantering AB.

SKB R-07-31 (2007), Rock Mechanics Forsmark: Site descriptive modelling Forsmark stage 2.2, Technical report, Svensk Kärnbränslehantering AB.

SKB R-08-116 (2009), Underground design Forsmark Layout D2, Technical report, Svensk Kärnbränslehantering AB.

SKB R-09-04 (2009), Strategy for thermal dimensioning of the final repository for spent nuclear fuel, Technical report, Svensk Kärnbränslehantering AB.

SKB TR-01-03 (1978), Integrated account of method, site selection and programme prior to the site investigation phase, Technical report, Svensk Kärnbränslehantering AB.

SKB TR-03-09 (2003), Thermal dimensioning of the deep repository. Influence of canister spacing, canister power, rock thermal properties and nearfield design on the maximum canister surface temperature, Technical report, Svensk Kärnbränslehantering AB.

SKB TR-06-09 (2006), Long-term safety for KBS-3 repositories at Forsmark and Laxemar – a first evaluation, Technical report, Svensk Kärnbränslehantering AB.

SKB TR-08-05 (2007), Site description of Forsmark at completion of the site investigation phase. SDM-Site Forsmark, Technical report, Svensk Kärnbränslehantering AB.

SKB TR-08-05 (2008), Site description of Forsmark at completion of the site investigation phase, SDM-Site Forsmark, Technical report, Svensk Kärnbränslehantering AB.

SKB TR-09-15 (2009), Stress evolution and fault stability during the Weichselian glacial cycle, Technical report, Svensk Kärnbränslehantering AB.

SKB TR-10-12 (2010), Design and production of the KBS-3 repository, Technical report, Svensk Kärnbränslehantering AB.

SKB TR-10-23 (2010), THM-issues in repository rock. Thermal, mechanical, thermo-mechanical and hydro-mechanical evolution of the rock at the Forsmark and Laxemar sites, Technical report, Svensk Kärnbränslehantering AB.

SKB TR-10-37 (2010), Counterforce applied to prevent spalling, Technical report, Svensk Kärnbränslehantering AB.

SKB TR-10-48 (2010), Geosphere process report for the safety assessment SR-Site, Technical report, Svensk Kärnbränslehantering AB.

SKB TR-12-01 (2012), KBS-3H Complementary studies, 2008–2010, Technical report, Svensk Kärnbränslehantering AB.

Song, I. (1998), Borehole Breakouts and Code Disking in Westerly Granite: Mechanics of Formation and Relationship to in situ Stress, PhD thesis, University of Wisconsin.

Souissi, S., Miled, K., Hamdi, E. & Sellami, H. (2017), 'Numerical modeling of rock damage during indentation process with reference to hard rock drilling', *International Journal of Geomechanics* **17**.

Spies, T. & Eisenblätter, J. (2001), 'Acoustic emission investigation of microcrack generation at geological boundaries', *Engineering Geology* **61**, 181–188.

Stacey, T. R. (1981), 'A simple extension strain criterion for fracture of brittle rock', *International Journal of Rock Mechanics and Mining Sciences* **18**, 469–474.

Stacey, T. & Wesseloo, J. (2022), 'Design and prediction in rock engineering: The importance of mechanisms of failure, with focus on high stress, brittle rock conditions', *Rock Mechanics and Rock Engineering* **55**, 1–19.

Stephens, G. & Voight, B. (1982), 'Hydraulic fracturing theory for conditions of thermal stress', *International Journal of Rock Mechanics and Mining Sciences & Geomechanics Abstracts* **19**, 279–284.

Stüben, K. (2001), 'A review of algebraic multigrid', *Journal of Computational and Applied Mathematics* **128**(1), 281–309. Numerical Analysis 2000. Vol. VII: Partial Differential Equations.

Szabo, B. & Babuska, I. (2021), *Finite Element Analysis: Method, Verification, and Validation*, John Wiley & Sons.

Tatone, B. S. & Grasselli, G. (2015), 'A calibration procedure for two-dimensional laboratory-scale hybrid finite–discrete element simulations', *International Journal of Rock Mechanics and Mining Sciences* **75**, 56–72.

Thomas, R. N., Paluszny, A. & Zimmerman, R. W. (2017), 'Quantification of Fracture Interaction Using Stress Intensity Factor Variation Maps', *Journal of Geophysical Research: Solid Earth* **122**(10), 7698–7717.

Thomas, R. N., Paluszny, A. & Zimmerman, R. W. (2020), 'Growth of three-dimensional fractures, arrays, and networks in brittle rocks under tension and compression', *Computers and Geotechnics* **121**, 103447.

Tsang, C. F., Bernier, F. & Davies, C. (2005), 'Geohydromechanical processes in the excavation damaged zone in crystalline rock, rock salt, and indurated and plastic clays—in the context of radioactive waste disposal', *International Journal of Rock Mechanics and Mining Sciences* **42**(1), 109–125.

Tsang, C.-F., ed. (1987), *Coupled Processes Associated with Nuclear Waste Repositories*, Academic Press.

Tuckey, Z. (2020), 'Modelling brittle fracture in weak rock with the 3d bonded block method, from laboratory to tunnel scale', *Australian Geomechanics Journal* **55**, 49–64.

Vardon, P. J. & Nuttall, J. D. (2009), 'Fracture growth in heterogeneous geomaterials', *International Journal of Rock Mechanics and Mining Sciences* **46**(3), 478–489.

Vazaios, I., Vlachopoulos, N. & Diederichs, M. S. (2019), 'Assessment fracturing mechanism and evolution of excavation damaged zone of tunnels in interlocked rock masses at high stresses using a finite-discrete element approach', *Journal of Rock Mechanics and Geotechnical Engineering* **11**, 701–722.

Vlachopoulos, N. & Diederichs, M. S. (2014), 'Appropriate uses and practical limitations of 2d numerical analysis of tunnels and tunnel support response', *Geotechnical and Geological Engineering* **32**, 469–488.

Vlachopoulos, N. & Vazaios, I. (2018), 'The numerical simulation of hard rocks for tunnelling purposes at great depths: A comparison between the hybrid fdem method and continuous techniques', *Advances in Civil Engineering* **2018**, 3868716.

Voyiadjis, G. Z. & Kattan, P. I. (2008), 'A comparative study of damage variables in continuum damage mechanics', *International Journal of Damage Mechanics* **18**, 315–340.

Walters, M. C., Paulino, G. H. & Dodds, R. H. (2005), 'Interaction integral procedures for 3-D curved cracks including surface tractions', *Engineering Fracture Mechanics* **72**(11), 1635–1663.

Wang, H., Dyskin, A., Pasternak, E., Dight, P. & Jeffcoat-Sacco, B. (2022), 'Fracture mechanics of spallation', *Engineering Fracture Mechanics* **260**, 108186.

Wang, J., Crouch, S. & Mogilevskaya, S. (2003), 'A complex boundary integral for multiple circular holes in an infinite plane', *Engineering Analysis with Boundary Elements* **27**, 789–802.

Wesseloo, J. & Stacey, T. R. (2016), 'A reconsideration of the extension strain criterion for fracture and failure of rock', *Rock Mechanics and Rock Engineering* **49**, 4667–4679.

Xia, Y., Wang, H., Zheng, G., Shen, G. & Hu, P. (2022), 'Discontinuous galerkin isogeometric analysis with peridynamic model for crack simulation of shell structure', *Computer Methods in Applied Mechanics and Engineering* **398**, 115193.

Yadav, A., Godara, R. K. & Bhardwaj, G. (2020), 'A review on xiga method for computational fracture mechanics applications', *Engineering Fracture Mechanics* **230**, 107001.

Zeller, E. J., Saunders, D. F. & Angino, E. E. (1973), 'Putting radioactive wastes on ice', *Bulletin of the Atomic Scientists* **29**, 4–52.

Zhang, C., Chu, W., Liu, N., Zhu, Y. & Hou, J. (2011), 'Laboratory tests and numerical simulations of brittle marble and squeezing schist at jinping ii hydropower station, china', *Journal of Rock Mechanics and Geotechnical Engineering* **3**, 30–38.

Zhang, W. & He, X. (2020), 'The effect of heterogeneity on multiple fracture interaction and on the effect of a non-uniform perforation cluster distribution', *Geomechanics and Geophysics for Geo-Energy and Geo-Resources* **6**(4), 427–442.

Zhao, J., Feng, X. T., Zhang, X. W., Zhang, Y., Zhou, Y. Y. & Yang, C. X. (2018), 'Brittle-ductile transition and failure mechanism of jinping marble under true triaxial compression', *Engineering Geology* **232**, 160–170.

Zhao, X., Cai, M. & Cai, M. (2010), 'Considerations of rock dilation on modeling failure and deformation of hard rocks—a case study of the mine-by test tunnel in Canada', *Journal of Rock Mechanics and Geotechnical Engineering* **2**(4), 338–349.

Zheng, Z., Cook, N. G. W. & Myer, L. R. (1988), Borehole Breakout And Stress Measurements, *in* 'Proceedings of the 29$^{\text{th}}$ U.S. Symposium on Rock Mechanics (USRMS)'. ARMA-88-0471.

Zheng, Z., Kemeny, J. & Cook, N. G. W. (1989), 'Analysis of borehole breakouts', *Journal of Geophysical Research* **94**(B6), 7171.

Zhou, S. (1994), 'A program to model the initial shape and extent of borehole breakout', *Computers & Geosciences* **20**(7-8), 1143–1160.

Zienkiewicz, O. C., Taylor, R. L. & Fox, D. (2013), 'The finite element method for solid and structural mechanics: Seventh edition', *The Finite Element Method for Solid and Structural Mechanics: Seventh Edition* pp. 1–624.

Zimmerman, R. (1991), Approximate expressions for stress concentrations in elastic solids containing multiple holes or notches, *in* 'Proceedings of the ASME winter annual meeting', ASME, Atlanta, GA.

Zimmerman, R. W. (2000), 'Coupling in poroelasticity and thermoelasticity', *International Journal of Rock Mechanics and Mining Sciences* **37**, 79–87.

Zoback, M. D., Barton, C. A., Brudy, M., Castillo, D. A., Finkbeiner, T., Grollimund, B. R., Moos, D. B., Peska, P., Ward, C. D. & Wiprut, D. J. (2003), 'Determination of stress orientation and magnitude in deep wells', *International Journal of Rock Mechanics and Mining Sciences* **40**, 1049–1076.

Zoback, M. D., Moos, D., Mastin, L. & Anderson, R. N. (1985), 'Well bore breakouts and in situ stress', *Journal of Geophysical Research: Solid Earth* **90**(B7), 5523–5530.

Zoback, M. D., Paul, P. & Lucier, A. (2010), 'Utilizing observations of borehole failure in deviated wellbores to constrain the full stress tensor in deep wells and mines: Application to two complex case studies', *Rock Stress and Earthquakes - Proceedings of the 5th International Symposium on In-Situ Rock Stress* pp. 69–76.